

**3-D VSP ELASTIC KIRCHHOFF PRE-STACK
DEPTH MIGRATION – VINTON DOME,
LOUISIANA**

A Dissertation
Presented to
the Faculty of the Department of Geosciences
University of Houston

In Partial Fulfillment
of the Requirements for the Degree
Doctor of Philosophy

By

Mariana Gherasim

August 2005

TABLE OF CONTENTS

1. Introduction	1
1.1. Introduction of surface seismic, ocean bottom-cable (OBC), and VSP acquisition.....	1
1.2. Review scalar and elastic seismic migration.....	3
1.3. Limitation of current technology to the imaging of Vinton Dome, Louisiana.....	7
1.4. Dissertation objectives.....	8
1.5. Dissertation outline.....	9
2. Geologic background	11
2.1. Northern Gulf of Mexico continental margin geology.....	11
2.2. Vinton Salt Dome geology.....	21
3. 3-D 3-C VSP Data Processing	32
3.1. Introduction.....	32
3.2. 3-D 3-C VSP Vinton Dome acquisition overview.....	35
3.3. Pre-processing of 3-D 3-C VSP Vinton Dome data.....	38
3.4. Rotation of horizontal geophones.....	53
3.5. Deconvolution of VSP Vinton Dome data.....	60
3.6. Up-going and down-going wavefield separation.....	69
4. VSP subsurface illumination	76
4.1. Introduction.....	76
4.2. 2-D Velocity model building.....	76
4.3. 2-D VSP subsurface illumination via ray-tracing.....	79
4.4. 2-D VSP subsurface illumination via elastic pseudo-spectral modeling.....	90
4.5. 3-D VSP subsurface illumination via acoustic pseudo-spectral modeling.....	101
5. 3-D 3-C VSP Kirchhoff pre-stack depth migration	107
5.1. Introduction.....	107
5.2. 2-D scalar synthetic VSP Kirchhoff pre-stack depth migration.....	109

5.3. 2-D elastic synthetic VSP Kirchhoff pre-stack depth migration.....	134
5.4. 3-D scalar synthetic VSP Kirchhoff pre-stack depth depth migration.....	153
5.5. 3-D 3-C VSP elastic Kirchhoff pre-stack depth migration – Vinton Dome, Louisiana.....	162
5.6. Traveltime and take-off angle estimation using wavefront construction.....	188
6. Fort Worth Basin – 2-D Elastic synthetic depth modeling.....	196
6.1. Summary.....	196
6.2. Introduction.....	196
6.3. Geologic framework.....	198
6.4. 2-D 3-C field data.....	199
6.5. Model construction and synthetic generation.....	199
6.6. Data Interpretation.....	202
6.7. Conclusions.....	204
7. Conclusions.....	219
Appendix A.....	225
References.....	234

1. INTRODUCTION

1.1. Introduction of surface seismic, OBC, and VSP acquisition

The seismic method is one of the geophysical methods that help us understand the structure of the earth. There is a distinction between seismic exploration and seismology, with the first one dealing with seismic waves artificially generated while the second one uses seismic waves naturally produced by earthquakes.

The reflection method can provide reflected energy from the upper 10 km of the earth and has proven its efficacy in hydrocarbon exploration. Seismic data are generated by explosive or other types of energy sources and are recorded on-shore and off-shore by geophones and/or hydrophones.

Seismic exploration for hydrocarbons began in 1920s and has driven the development of the new types of sources and receivers used throughout this time. More sophisticated acquisition and processing techniques were required to unravel the complicated structures in which the hydrocarbons were trapped. Simple acquisition methods like 2-D 1-C (vertical geophone) surface lines were replaced over the years with 3-D 3-C (vertical and two horizontal geophones) or 9-C surveys, which provided data necessary for shear-waves analysis. During the 1990s, marine acquisition took the advantage of the existence of the multicomponent phones by upgrading the methodology from 2-D streamer to 3-D 4-C (hydrophone, vertical geophone and two horizontal geophones).

In surface acquisition, an explosive source or mechanical vibrator is used to generate the seismic waves which penetrates the subsurface and reflects back to the surface where are recorded by receivers (geophones). The geophones can be single or multicomponent. A multicomponent geophone is composed of three-geophones, typically one vertical and two horizontal phones. The horizontal phones have perpendicular axis and were originally designed to record S-waves. Quite recently, manufacturers have developed “vector” 3-component piezoelectric accelerometers sensors that fit neatly in a small package.

In off-shore acquisition, air-guns are used to generated P-waves that travel through the water and subsurface and are reflected back into the water where they are recorded by hydrophones placed inside a neutrally buoyant cable called streamer. The Ocean Bottom Cable technique was introduced to take advantage of the presence of the S-waves generated by the conversions at the water bottom and in the subsurface. In this method, groups composed of a hydrophone, a vertical geophone and two horizontal phones are placed inside nodes or cables similar to a streamer and dragged into place on the ocean bottom.

The VSP (Vertical Seismic Profiling) (Figure 1.1.1), technique deals with two kinds of settings of sources and geophones. In a normal VSP, the sources are fired at the surface generating wavefronts that are recorded by the geophones placed in the well. In a Reverse VSP, the locations of sources and receivers are interchanged.

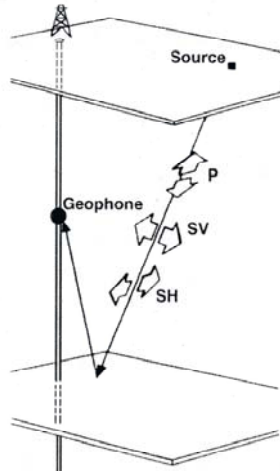


FIG. 1.1.1. VSP acquisition. The source is located at the surface and the receivers in the well. The P, SV and SH polarizations are displayed along the seismic ray (after Hinds *et al.*, 2001).

1.2. Review of scalar and elastic seismic migration

Migration involves repositioning data elements to the locations of the associated reflector or diffraction points (Sheriff and Geldart, 1995). Migration methods can be classified into time and depth domain migrations, scalar and elastic migration methods. Each one of these problems can be next solved using Kirchhoff, one-way wave equation, or reverse time (two-way wave equation) algorithms.

Hagedoorn (1954) was the first to perform seismic migration using an analogue device. His method finds the reflectors as an envelope of equal traveltimes curves defined by events on a seismic trace and is the forerunner of digital Kirchhoff migration (Schneider, 1978) and Kirchhoff inversion (Bleistein, 1987) techniques.

Schneider (1978) discussed the mathematical formulation of migration as a solution to the scalar wave equation in which surface seismic observations are the known boundary values. He treated that solution of this boundary value problem using standard techniques, with the migrated image expressed as a surface integral over the known seismic observations when areal or 3-D coverage is available. Derogowski and Brown (1983) examined how the integral method can be extended to employ nonhyperbolic one-way traveltimes.

Since then, geophysicists tried to improve the method in order to be able to image very complicated structures (Wiggins, 1984; Miller *et al.*, 1987; Bevc, 1997; Chang *et al.*, 1998; Zhao *et al.*, 1998; Guo and Yang, 1998; Dellinger *et al.*, 1999; Dellinger *et al.*, 2000; Calandra *et al.*, 2001; Gray *et al.*, 2001; Gray *et al.*, 2002; Stolk *et al.*, 2002).

Stolt (1978) introduced the Fourier-transform migration for a 2-D constant velocity case. Gazdag (1978) developed the phase-shift method for a 2-D case with vertical variable velocity and Gazdag and Sguazzero (1984) developed the phase-shift plus interpolation migration for a lateral variable velocity medium.

Another frequency-wavenumber domain migration method is phase-screen migration, which was first described by Wu, *et al.* (1992) and later applied to synthetic data generated over the Marmousi model (Hildebrand *et al.*, 1997).

Claerbout and Doherty (1972) introduced the finite-difference method of wave-equation migration, which is based on the downward continuation of the seismic wavefield. It utilizes the continuity property of fields, which implies that we can calculate the field over an arbitrary surface if we know the field completely over one surface, provided that the field satisfies Laplace's equation.

All the migration methods discussed above were first performed commercially in time and later, due to the necessity of improving the accuracy of subsurface images in the presence of lateral velocity variation, in depth.

Elastic migration of multicomponent seismic data attempts to generate images of PP, PS, SP and SS reflections. We can either attempt to image each mode separately using a modified scalar migration algorithm, or simultaneously using a fully elastic propagator.

There are several different methods to separate P- and S-waves described by Tatham and Goolsbee (1984), Dankbaar (1985, 1987), Devaney and Oristaglio (1986), Foster and Gaiser (1986), Dillon *et al.*, (1988), Leaney (1989), Wapenaar *et al.*, (1990), Amano (1995), Amundsen and Reitan (1995), and Sun *et al.*, (2004).

The separated P- and S-waves are then migrated (Dillon *et al.*, 1988; Vanderfeen, 1988; Whitmore and Marfurt, 1988; Wang and Nemeth, 1997; Sun and McMechan, 2001).

Another set of migrations separates the P- and S-waves after migration (Jackson *et al.*, 1991; Hou and Marfurt, 2002). The two-components are migrated using P- and S-wave velocities and then rotated to obtain the P and S images. The rotation requires a take-off angle that can be calculated via ray-tracing or a polarization angle calculated using the histogram technique developed by DiSiena (1981).

Elastic migration uses two-component (typically vertical and inline horizontal) data simultaneously without separating P- and S-waves. Kuo and Dai (1984) first developed the Kirchhoff multicomponent migration for the case of noncoincident source and receiver based on the Kirchhoff-Helmholtz type integrals developed by Pao and Varatharajulu (1976) for elastic waves in a medium in which velocity is a function of depth. Keho and Wu (1987) applied elastic Kirchhoff migration to a synthetic VSP data set generated using paraxial ray tracing developed by Keho and Beydoun (1988). Wapenaar and Haime (1990) derived the Kirchhoff-Helmholtz integrals for vertically inhomogeneous anisotropic solids for extrapolating P- and S-waves as a part of a new way of processing elastic data proposed by Berkhout and Wapenaar (1988).

Hokstad (2000) presented an elastic and viscoelastic type of Kirchhoff multicomponent migration based on Claerbout's survey-sinking concept and the viscoelastic Kirchhoff integral for the displacement field. He tested the method on synthetic and field VSP data. Zhe and Greenhalgh (1997) proposed an elastic migration by displacement potential extrapolation, which is a mixed function-blocked vector wavefield migration algorithm. They introduced a new wavefield extrapolation method for inhomogeneous media and developed a new imaging condition based on the time consistent principle.

1.3. Limitation of current technology to the imaging of Vinton Dome, Louisiana

In the previous section, I gave an overview of the VSP prestack depth migration methods. There are different ways we can classify these methods. One of them is to group them into scalar and elastic migration methods.

Scalar migration requires wavefield separation prior to migration, separation that can be accomplished by making some assumptions about acquisition geometry, velocity and wavefield propagation. Most of the P-/S-wave separation methods require constant velocity along the receiver line, which is not the case in the real world. Other methods consider that the wavefield propagates only from one side of the borehole and that the borehole is vertical, which again is not true.

In some cases, a more careful rotation of the horizontal geophones separates the P and S wavefields. This method is proven to give good results in horizontally stratified media (Yan *et al.*, 2004) but it cannot provide good results in the Vinton Dome area.

To overcome these assumptions, the geophysicists started paying more attention to the elastic type of migration. The elastic migration takes into account the full recorded wavefield, without requiring the wavefield separation, and the results obtained until now are encouraging. Unfortunately, most of the elastic methods are mostly developed for the 2-D VSP case and are mostly tested on the synthetic data.

The 3-D 3-C VSP data set recorded in the Vinton Dome area allows us to make a step forward and try to create new techniques. Due to the presence of rapid lateral velocity variations, we need to focus our attention on the depth type of migration rather than time migration.

1.4. Dissertation objectives

The main objective of my dissertation consists of generating a salt flank image of the Vinton salt dome, Louisiana. Considering the limitations of the current techniques presented in the previous section, I focused on developing a method that will help me achieve my goal.

The novelty of my dissertation consists of designing a new 3-D elastic Kirchhoff prestack depth migration algorithm, which uses the complete wavefield recorded by the three components as input. This way, I avoid all the assumptions considered in conventional VSP migration and take advantage of the full information content in the vector recording. The particular structure presented in the Vinton area, e.g. the salt dome, requires special attention when designing the pre-processing and migration workflow.

My method is somehow similar with Wang's method (2004) in the sense that we are both using the dot product to project the data onto the expected polarization. The difference is that I use the direction cosines to calculate the expected polarization and generate separate P and PS images while he generates separate images for vertical, inline and crossline horizontal geophones.

Another new algorithm enclosed in my dissertation consists of designing a special type of stacking, called semblance weighting stacking, which removes the incoherent migrated events based on calculating the semblance inside common-image gathers. I use semblance weighting as a more complex tool to replace the well-known "surgical mute" typically used in VSP imaging.

1.5. Dissertation outline

In Chapter 2 of my dissertation I present an overview of the geology from the Gulf of Mexico area, reviewing the tectonic provinces of the Northern part of the Gulf and focusing on the structure and stratigraphy of Vinton Dome area.

Chapter 3 is dedicated to the 3-D 3-C VSP data processing. Each processing step is discussed in detail for each component and followed by examples from the field data set. I paid special attention to the rotation of horizontal geophones and wavefield separation.

Chapter 4 is reserved to the VSP subsurface illumination study. I performed 2-D acoustic and elastic VSP modelling based on ray-tracing and elastic pseudo-spectral methods, and 3-D VSP modelling based on an acoustic pseudo-spectral technique. I emphasize the impact of acquisition geometry on subsurface illumination and data aliasing on pre-stack depth migration. I sustain my point by presenting a set of wavefield snapshots recorded for both 2-D and 3-D data.

I dedicated Chapter 5 to the Kirchhoff migration methods. I begin with a short introduction about scalar and elastic pre-stack VSP Kirchhoff depth migration methods, then I continue with sections dedicated to 2-D VSP scalar Kirchhoff pre-stack depth migration of synthetic ray-traced data and 2-D VSP elastic Kirchhoff pre-stack depth migration of synthetic elastic pseudo-spectral data. Next, I describe the calibration of the 3-D scalar Kirchhoff pre-stack depth migration using a 3-D VSP data set computed by using 3-D acoustic pseudo-spectral technique. After calibrating my algorithm using 2-D

and 3-D synthetic data, I move on to 3-D 3-C VSP Kirchhoff pre-stack depth migration of Vinton Dome field data.

Chapter 6 is reserved for a special modeling project that is based on the 2-D 3-C surface seismic line shot in Fort-Worth Basin. I list the steps performed in creating the depth model and the modeling programs used to generate the synthetic seismic data. The final part is reserved for the interpretation of the synthetic data and their correlation to the field data.

I end my dissertation with a chapter of conclusions.

2. GEOLOGIC BACKGROUND

2.1. Northern Gulf of Mexico continental margin geology

During the past decade, traditional models of a passive margin with vertical rooted salt stocks and massifs with intervening steep growth faults has been replaced by one of a complex mosaic of diachronous detachment fault systems and variously deformed allochthonous salt sheets (Jackson *et al.*, 1995).

Hydrocarbon exploration in deeper water provided data that has helped us better understand the Cenozoic tectonics of the Northern Gulf of Mexico continental margin in the 1980s. The modern history of Gulf Coast structural studies began with the recognition of the Sigsbee escarpment as a salt overthrust at the toe of the slope (Amery, 1969). As a consequence, Humphris (1978) proposed a large-scale basinward flow of salt away from the continent by downbuilding of slope sediments deposited on top of the moving salt mass. Martin (1978) reviewed the stratigraphic and structural framework of the Gulf Coast with the contemporary understanding of margin progradation over autochthonous Louann salt. He found attendant rooted vertical stocks and steep growth faults apparently related to flow of deeply buried shale and salt masses. Worrall and Snelson (1989) used qualitative palinspastic reconstructions to show how Humphris' (1978) model for basinward salt flow can be applied to large-scale growth fault systems of the Texas shelf.

Martin (1978) and Worrall and Snelson (1989) consider the Gulf Coast salt structures to begin with low-relief structures at the updip basin margin, followed by high-

relief salt stocks of coastal Louisiana and then more complex leaning stocks and allochthonous salt wings and sheets of the outer shelf and slope. Figures 2.1.1 and 2.1.2 shows a tectono-stratigraphic province map, which illustrates eight distinct regions defined by adjacent areas of similar structural style (Jackson *et al.*, 1995).

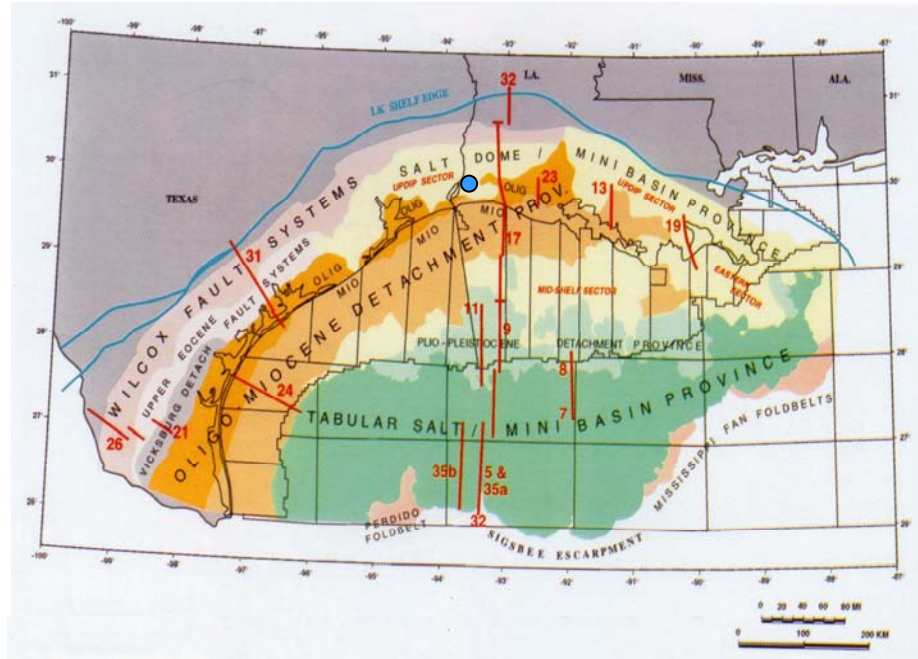


FIG. 2.1.1. Tectono-stratigraphic provinces of the northern Gulf of Mexico Basin (after Jackson *et al.*, 1995). The location of the Vinton Dome is indicated by the light blue solid circle.

The eight provinces from Figure 2.1.1 are, from bottom up, (1) a contractional foldbelt province at the toe of slope (coral), (2) a tabular salt-minibasin province on the slope (green), (3) a Pliocene-Pleistocene detachment province on the outer shelf (light green), (4) a salt dome-minibasin province (beige), (5) an Oligocene-Miocene detachment province onshore and on the shelf (light brown), (6) an Oligocene Vicksburg

detachment province onshore Texas (purple), (7) an upper Eocene detachment province (light purple), and (8) the Wilcox growth fault province of Paleocene-Eocene age (pink).

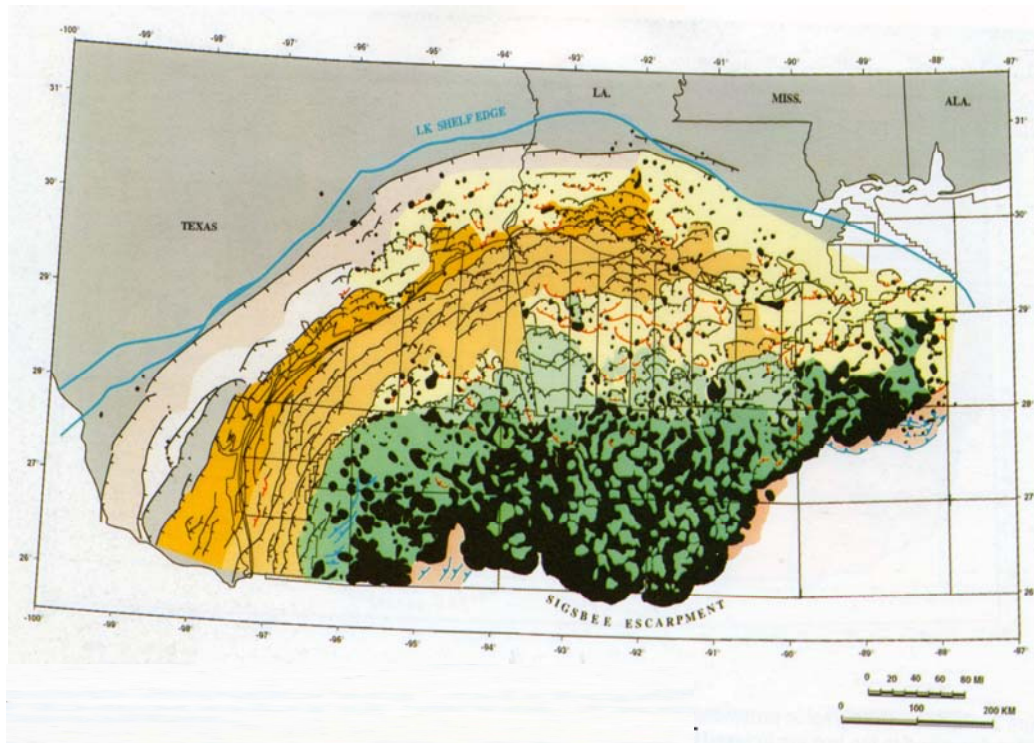


FIG. 2.1.2. Structural summary map of the northern Gulf of Mexico Basin. Tectono-stratigraphic provinces are color coded same as in Figure 2.1.1. The black represents the deeper parts of the escarpment (after Jackson *et al.*, 1995).

Contractional Foldbelt Province

The contractional foldbelt provinces include the Perdido foldbelt of Oligocene age in Texas (Weimer and Buffler, 1992) and the Mississippi Fan foldbelt of Miocene-Pliocene age in eastern Louisiana (Wu *et al.*, 1990). These salt-floored fold and thrust systems formed at the basinward margin of autochthonous salt. Their ages are different and are separated geographically by a wide zone without contractional deformation.

Tabular Salt-Minibasin Province

The tabular salt-minibasin province covers most of the continental slope along the northern Gulf of Mexico margin, stretching from Mexico to eastern Louisiana between the shelf margin and the Sigsbee escarpment at the toe of the slope (Jackson *et al.*, 1995). Allochthonous salt tongues and tabular salt with intercalation of sediment-filled minibasins represent the dominant structural style of this province, where the term “tabular salt” refers to the laterally extensive salt bodies with flat tops.

The most important features that can be observed include the prominent Sigsbee escarpment, which is considered to be a large salt body overriding the abyssal plain, the Mississippi Canyon (MC) and the upper part of the Mississippi Fan (Figure 2.1.3).

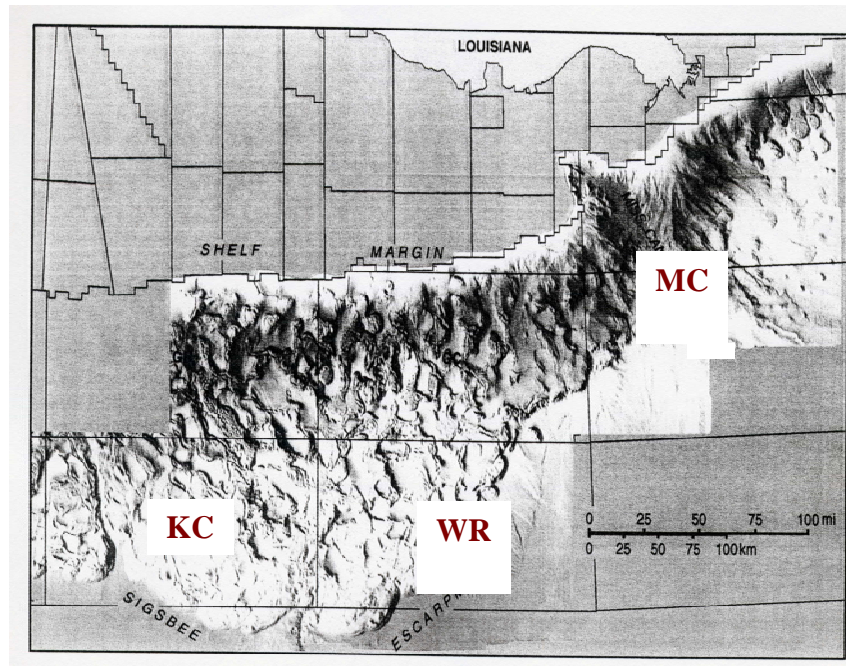


FIG. 2.1.3. Artificial illumination of seafloor structure, Louisiana slope. KC – Keathley Canyon; WR – Walker Ridge; MC – Mississippi Canyon (after Jackson *et al.*, 1995).

A contiguous canopy of united allochthonous salt underlies the western Keathley Canyon area and the southern part of the eastern Keathley Canyon (KC) and Walker Ridge (WR). A thin sedimentary cover forming incipient polygonal minibasins above allochthonous salt and separated by crestal grabens on salt ridges covers the western part. The dominant features of the central part of the Louisiana slope are the deep sediment minibasins surrounded by interconnected shallow salt bodies.

In general, there is a gradual transition from isolated minibasins bordered by adjacent salt in the lower slope to isolated salt bodies surrounded by interconnected fault-bounded minibasins near the shelf margin. This transition suggests progressive deformation during progradation of the margin across allochthonous salt.

Pliocene-Pleistocene Detachment Province

Sumner *et al.* (1990) divided the Pliocene-Pleistocene detachment province into separate regions of “organized” and “disorganized” *roho* systems. The *roho* term refers to the characteristic discontinuous, high-amplitude seismic reflections caused by remnant salt along welds (Jackson and Cramez, 1989), also called *salt-evacuation surfaces* or *salt-withdrawal surfaces*.

The organized systems appear in the western and eastern parts of the area and are underlain by extensive salt welds, or *rohos*. The disorganized systems occur in the central area where a combination of residual salt wings, evacuation surfaces and gaps between salt bodies forms a more complicated structure (Sumner *et al.*, 1990). Organized *roho* areas of the outer shelf show large amounts of extension by listric down-to-the-basin growth faults that expand Pliocene-Pleistocene sediments above the salt welds. Although some contractional structures exist locally, they do not balance the cumulative extension. Palinspastic reconstruction suggests that extension is balanced by withdrawal of tabular salt originally present near the seafloor (Jackson *et al.*, 1995).

Salt Dome-Minibasin Province

The salt dome-minibasin province is divided into updip, eastern and midshelf sectors (Jackson *et al.*, 1995). All sectors share the same structural style, salt stocks and intervening shelf minibasins bounded by large-displacement, arcuate, and counter-regional growth faults.

Updip and Eastern Sectors

The landward edge of the Oligocene-Miocene detachment is considered to be the updip limit of a continuous Paleogene salt canopy, but isolated allochthonous salt bodies occur in the updip and eastern sectors of the salt dome-minibasin province.

Predominantly down-to-the-basin listric growth faults of the detachment province formed in areas of coalesced allochthonous salt, but isolated minibasins formed during evacuation of isolated allochthonous salt bodies of the updip and eastern sectors (Jackson *et al.*, 1995).

Two distinct structural styles – salt-based detachments and stepped counter-regional fault systems – formed during shelf margin progradation in southern Louisiana. Salt-based detachment systems developed in the places where allochthonous salt merged to form a continuous canopy and salt-floored minibasins and marginal salt domes formed where salt bodies were isolated (Jackson *et al.*, 1995).

Mid-Shelf Sector

The structural style of the mid-shelf sector of the salt dome-minibasin province is similar to the updip and eastern sectors of the province. The mid-shelf minibasins generally contain younger deltaic sediments and the deep structure is obscured by deep burial. The counter-regional faults form a linked network across much of the shelf. Salt-based detachment systems terminate basinward either in minibasins bounded by counter-regional faults or in thrust complexes related to the forward edge of a salt sheet (Sumner *et al.*, 1990; Schuster, 1995).

Oligocene-Miocene Detachment Province

The Oligocene-Miocene detachment province covers most of the slope and parts of coastal onshore Texas and Louisiana (Jackson *et al.*, 1995). This is a region of large-displacement, dominantly down-to-the-basin listric growth faults that sole on a regional detachment above the Paleogene section. Another characteristic of this province is the great thickness of deltaic sediments above the detachment, usually exceeding 5 km.

Thermal and isostatic subsidence alone cannot account for more than 6 km of shallow-water sediment deposited in the late Tertiary on a passive margin where rifting occurred in the Jurassic, but subsidence can be balanced isostatically with salt withdrawal. Jackson, *et al.* (1995) discuss a technique that estimates the amount of the salt withdrawal but does not indicate the level of the evacuation surface. End-member models show two possibilities, the salt was withdrawn from the autochthonous Louann

level or the detachment for listric growth faults represents a salt weld that formerly contained a thick, allochthonous salt body (Jackson *et al.*, 1995).

Oligocene Vicksburg Detachment System

A large shale-based detachment system is recognized onshore in southern Texas, in the lower Oligocene Vicksburg productive trend (Combes, 1993). Onshore Texas, this system contains sand-prone Vicksburg deltaic sediments greatly expanded by a listric down-to-the-basin fault system that stands in Eocene Jackson shale. This fault system shares some similarities with the salt-withdrawal detachment systems, which include the presence of expanded deltaic sediments above listric normal faults that sole into a subhorizontal detachment surface. The main difference consists of the fact that the expanded sequences are younger landward in contrast to salt-based examples (Jackson *et al.*, 1995).

Unlike the salt-withdrawal fault systems, the shale-based Vicksburg detachment is an example of extreme extension. The oldest units in the Vicksburg example were translated horizontally more than 16 km. In contrast, the oldest sediments in the salt-withdrawal example show about 3.2 km of horizontal translation.

Upper Eocene Detachment Province

The upper Eocene detachment province includes several listric detachment-based fault systems expanding in the upper part of the Eocene section (Jackson *et al.*, 1995).

Wilcox Growth Fault Province

The oldest Tertiary growth fault system in the northern Gulf of Mexico Basin is the Paleocene-Eocene Wilcox fault system (Jackson *et al.*, 1995). The most prominent feature of the trend is the great expansion of Wilcox deltaic strata confined to narrow depotroughs. These depotroughs are characterized by the absence of Cretaceous strata, which are present outside the troughs. The complex imbricate fan of down-to-the-basin growth faults merges downward into major fault planes that end at the Jurassic Louann salt level, apparently directly overlain by Paleogene strata. The basinward edge of the Eocene-filled depotroughs is bounded by counter-regional faults that extend to the Louann salt level and have Cretaceous strata on their footwalls (Jackson *et al.*, 1995).

2.2. Vinton Salt Dome geology

The Vinton salt dome is located in Southwest Louisiana, Calcasieu Parish, 3 ½ miles Southwest of the town of Vinton (Figure 2.2.1). According to the Jackson *et al.* (1995) classification, Calcasieu Parish, Louisiana, should be situated within the salt dome minibasin province.



FIG. 2.2.1. Location of the Vinton salt dome.

Vinton was the first of the salt dome oil fields in which oil was found on the flank of the salt dome. The first well was drilled in May 1901, near the bank of the east side of the Gray lake (Thompson and Eichelberger, 1928).

Surface geology

The layers exposed at the surface belong to the Port Hudson series, of Pleistocene age, which in Texas is known as the Beaumont clay. These series are composed of sands and clays (Thompson and Eichelberger, 1928; Wilson and Noel, 1983).

Subsurface geology

Vinton is a characteristic salt dome with a core of massive salt and a well-defined cap-rock. The cap-rock consists of limestone, followed in depth by gypsum and anhydrite, which are cavernous in places and filled with sulphur water. Samples of old cores picked up on the north part of the dome showed a characteristic fine-grained cap-rock limestone permeated by a network of fine solution channels (Thompson and Eichelberger, 1928).

The salt core is approximately 4200 ft (1280 m) wide from North to South (Figure 2.2.2) and 5000 ft (1524 m) long from East to West (Figure 2.2.3). The highest elevation at which it has been found is 925 ft (282 m) below sea level near the north end of Gray Lake.

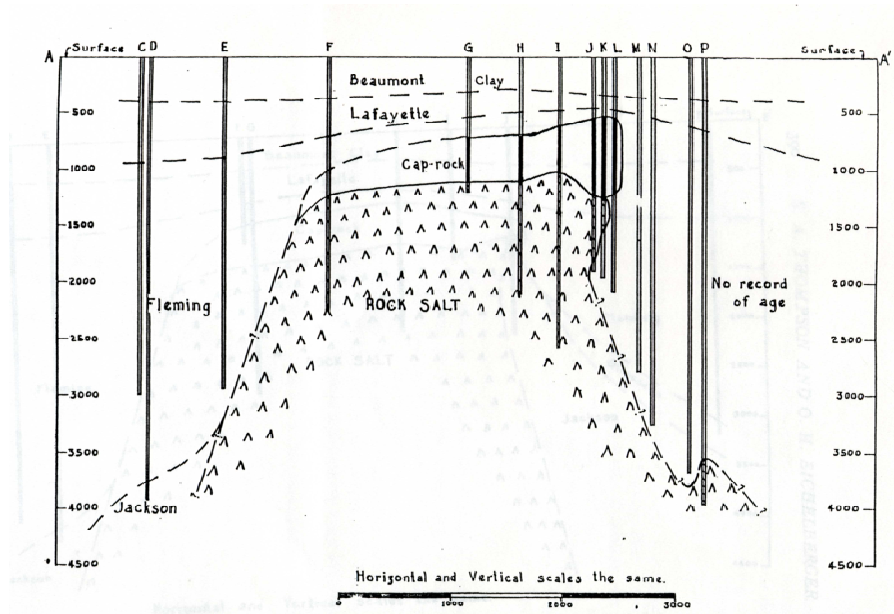


FIG. 2.2.2. North-South section of Vinton salt dome (after Thompson and Eichelberger, 1928).

The uppermost portion consists of Pleistocene sands, gravels and clays. On the flanks of the dome these Pleistocene sands and gravels have a very gentle slope. The sediments off the dome are composed of sand and shale.

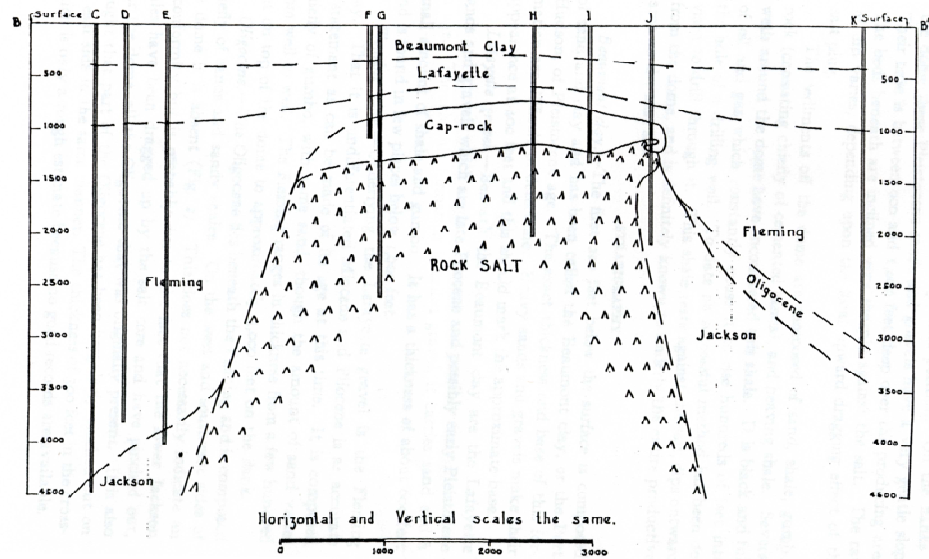


FIG. 2.2.3. East-West section of Vinton salt dome (after Thompson and Eichelberger, 1928).

Beneath the Pleistocene deposits is a sequence of sandstones and shales that are considered to be post-Anahuac of age ranging from Miocene to Pliocene (Wilson and Noel, 1983). Below these layers are the Anahuac and Frio groups, which are underlain by the Oligocene Vicksburg formation.

Stratigraphy of the area

The stratigraphic column of Gulf of Mexico is presented in Figure 2.2.4

STRATIGRAPHIC COLUMN GULF REGION—UNITED STATES (Northwest Mexico Equivalent*)					
ERA	SYSTEM	SERIES	GROUP	FORMATION	
CENOZOIC	QUATERNARY	REGENT		Undifferentiated	
		PLEISTOCENE	HOUSTON	Beaumont Lizie Willis	
			PLIOGENE	Goliad	
	TERTIARY	MIOCENE	FLEMING	Lugarito Oakville Catahoula	
		OLIGOCENE	UPPER	Anahuac	
			MIDDLE	Frio	
			LOWER	Vicksburg	
		EOCENE	JACKSON	Whitsett Mc Elroy Caddo Moody Branch	
				CLAIBORNE	Cockfield-Yagua Oak Mountain Sparta Waches Queen City Hicklow
			WILCOX	Cerrito Sabineblow Rockdale Sagin	
	PALEOCENE		MIDWAY	Wills Point Kinard	
	MESOZOIC	UPPER CRETACEOUS	GULF	NAVARRO	Upper Navarra (Kemp, Escondido) Nacatoch (Olmes)
				TAYLOR	Upper Taylor (San Miguel) Pecan Gap (Anacapa) Wolf City Lower Taylor (Gober)
AUSTIN				Austin Sub-Glorhville	
EAGLEFORD				Eagleford	
WOODBINE			Woodbine		
LOWER CRETACEOUS		COMANCHEAN	WASHITA	Auda Del Rio Georgetown Weno Denton Fort Worth Duck Creek	
			FREDERICKSBURG	Kiamichi Edwards Comanche Peak Walnut	
			TRINITY	Paluxy	
				Upper (Ferry Lake Anhydrite) Middle (Rodessa) Lower (Pearson) Lames (Caw Creek) Travis Peak (Pine Island)	
COAHUILA		Silgo Hasten			
JURASSIC		SABINAS	COTTON VALLEY (LA CASITA*)	Schuler Bossier	
				Haynesville Rockner (Divida*) Smackover (Zuloaga, La Gloria*) Norphlet	
	LOWER		Louann Salt (Mines Viejas*) Werner		
TRIASSIC			Eagle Mills (La Boca*)		
PALEOZOIC	PERMIAN			Undifferentiated Deformed & Metamorphosed Rocks	

FIG. 2.2.4. Stratigraphic column of Gulf of Mexico (after Halbouty, 1972)

Thompson and Eichelberger in 1928 provided the first basic stratigraphic description of the Vinton dome area.

Beaumont clay

The first 200 ft (61 m) below the surface is composed of sand and clay and has been called the Beaumont clay, or the Port Hudson, of Pleistocene age. Heavy sands and gravels appear at 400 ft (122 m) and this should mark the approximate base.

Lafayette gravel

Beneath the Beaumont clay are the Lafayette sands and gravels that are late Pliocene and possibly early Pleistocene in age. Though this formation is called gravel, it carries sand and a small amount of shale. It has a thickness of about 600 ft (183 m) and is found in few places below 1000 ft (305 m).

Fleming clay

Underlying the Lafayette gravel is the Fleming clay. It is undifferentiated Miocene and Pliocene age, composed chiefly of gumbo, with sand varying in thickness from place to place. The Fleming ranges in thickness from a few hundred ft on top of the dome to approximately 3000 ft (915 m) on the flank.

Oligocene

The Oligocene lies beneath the Fleming and is composed chiefly of sands and sandy shale. It is absent on the West and Southwest sides of the dome (Figure 2.2.2). This does not necessarily indicate an unconformity but is probably due to the fact that the lower Jackson shale has been dragged up by the salt core and has pinched out, near the dome, all the Oligocene that was originally present. It is also thought that part of the Oligocene has been irregularly pinched out on the east side in the same manner. The thickness of 300 ft (92 m) in the cross-section is only a rough estimate. Since the deepest section wells have penetrated in the study area is of Oligocene age, I will present a more detailed discussion on the stratigraphy of sediments.

The **Anahuac Formation** is considered to be located at the top of Oligocene interval, containing shale and sands deposited in marginal to shallow marine environments (Wilson and Noel, 1983). Also, dark, greenish gray, calcareous shale with beds of sand and calcareous sand and occasional thin lenses of limestone are considered be present (Warren, 1957). The unit becomes calcareous Eastward and turns into a unit that is completely formed of reef and detrital limestone except for trace amounts of shale and sand. The Anahuac Formation is approximately 2700 ft (820 m) thick and it thickens downdip. In some areas the unit has thickness greater than 3500 ft (1065 m).

The **Frio Formation** underlies the Anahuac formation and consists of sands and shale representing a variety of environments (Wilson and Noel, 1983). Jackson and

Galloway (1984) describe the Frio Formation as a combination of two major delta systems and an interdelatic wave-dominated shore-zone system, all fronted by the shelf margin and continental slope. They define three paleomargin sequences that illustrate depositional and structural features typical for an unstable progradational margin. These sequences are filled with deltaic and upper slope sediments. Structure includes also major bounding growth faults and deep salt domes.

The **Hackberry wedge** is a deep-water marine wedge that extends from the eastern flank of the Houston delta system into Western Louisiana. The Hackberry consists of a lower sequence containing sands and an upper sequence dominated by shale. The unconformity displays considerable channeling and local truncation of underlying Frio section that exceeds 1000 ft (600 m). Hackberry sandstones occur mainly within the incised canyons and are a current exploration target.

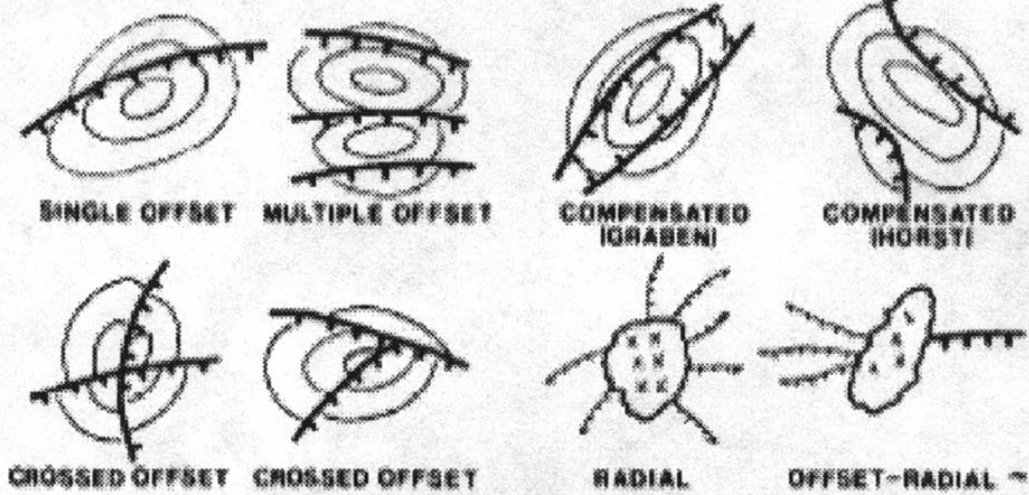
The **Vicksburg Formation** is composed mainly from dark-gray to brown, fossiliferous and calcareous marine shales of early Oligocene age. The strata vary in thickness from 200 ft (60 m) to more than 300 ft (90 m).

Tectonics of the area

The salt activity and its impact on the structural evolution in the Gulf area have been studied since early 60s. Fails (1990) reviewed the work done by his predecessors and proposed a fault pattern classification for the salt structures based on the analysis of over 200 salt domes in the coastal basin area of offshore Texas and Louisiana. He considers three groups: Single or multiple offset, Compensated, and Crossed offset, shown in Figure 2.2.5. He also grouped the salt domes in three classes: Penetrant (shallow piercement), Semipenetrant (intermediate piercement), and Nonpenetrant (deep-seated), displayed in Figure 2.2.6.

His studies indicated that penetrant and semipenetrant salt domes are heavily faulted with a complex pattern. He found that penetrant and semipenetrant domes reveal similar characteristics such as counter basinward faulting and that radial faults are specific only to penetrant domes.

BASIC FAULT PATTERNS - COASTAL SALT BASIN DIAPYRIC STRUCTURES



SINGLE PHASE Fault Patterns are shown above.

MULTIPLE PHASE Fault Patterns are combinations of:
Offset plus Compensated or Crossed Offset plus Compensated Basic Patterns

FIG. 2.2.5. Fault pattern classification for Coastal Salt Basin diapiric structures, including salt domes (after Fails, 1990). The basic single phase fault patterns are:
Offset: one or more semiparallel major faults downthrown in the same direction.
Compensated: two or more semiparallel major faults downthrown in opposite directions, to form a graben or a horst.
Crossed offset: two or more major faults in crossed orientation.
Multiple phase fault patterns consist of combinations of superimposed offset plus compensated or crossed plus compensated single phase patterns. The less common radial pattern is restricted to penetrant salt domes, while the relatively uncommon offset radial pattern occurs on all salt dome types.

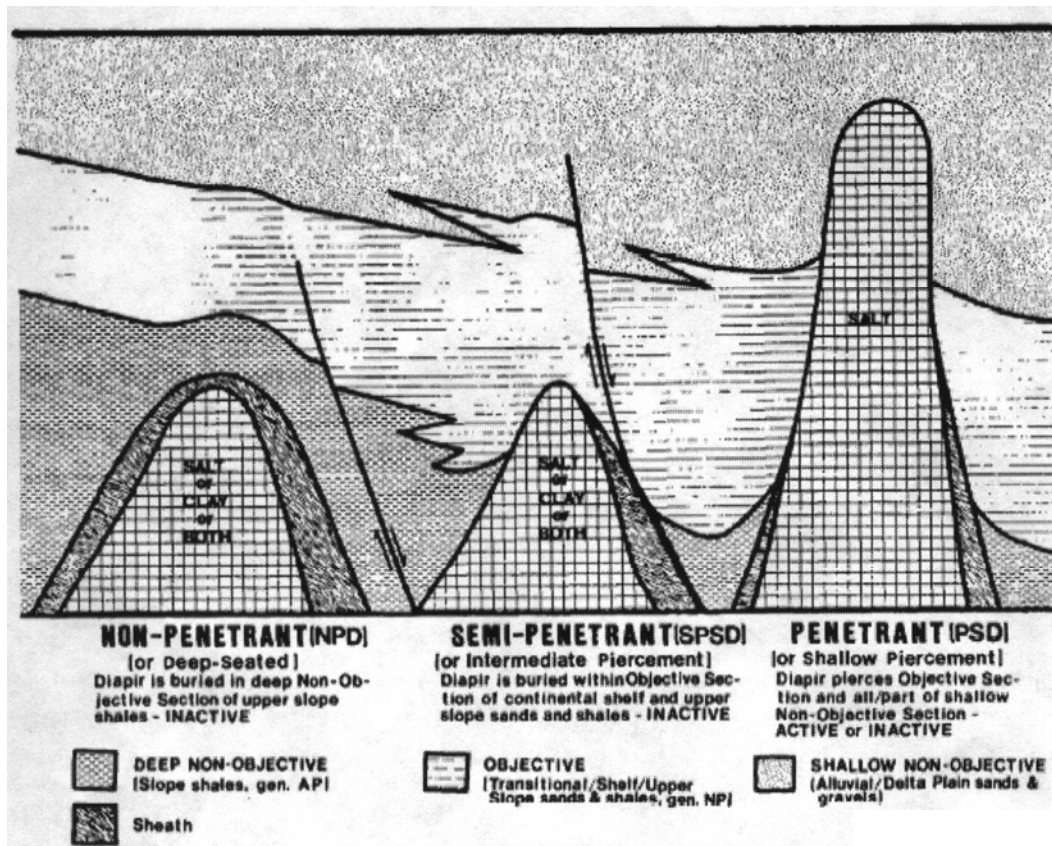


FIG. 2.2.6. Salt dome classification (after Fails, 1990)

3. 3-D 3-C VSP DATA PROCESSING

3.1. Introduction

Vertical seismic profile (VSP) surveys utilize sources located at the surface of the earth and receivers located inside the borehole. Due to the acquisition geometry, we are able to record both up-going and down-going wavefields as they pass through the recording surface in contrast with the conventional surface seismic acquisition where the upgoing and downgoing wavefields are coupled at the recording surface.

VSPs can be categorized as near- or far-offset (Hinds *et al.*, 2001) and can be deployed in both vertical and deviated wells (Figure 3.1.1).

The term *near-offset VSP* or *zero-offset VSP* (Cassell, 1984) refers to a geometrical setting where the source and receiver locations are vertically aligned (Figure 3.1.1.a). Near-offset VSPs are usually used to tie surface seismic data to the subsurface geology and to differentiate primary reflections from surface-generated and interbed multiples (Hinds *et al.*, 2001).

The term *far-offset VSP* or *offset VSP* (Cassell, 1984) refers to a geometrical configuration where the source and receiver locations cannot be considered vertically aligned during processing (Figure 3.1.1.b). Far-offset geometries are common for deviated boreholes. Offset VSPs are usually recorded in areas with complex structures because they provide high frequency images around the borehole.

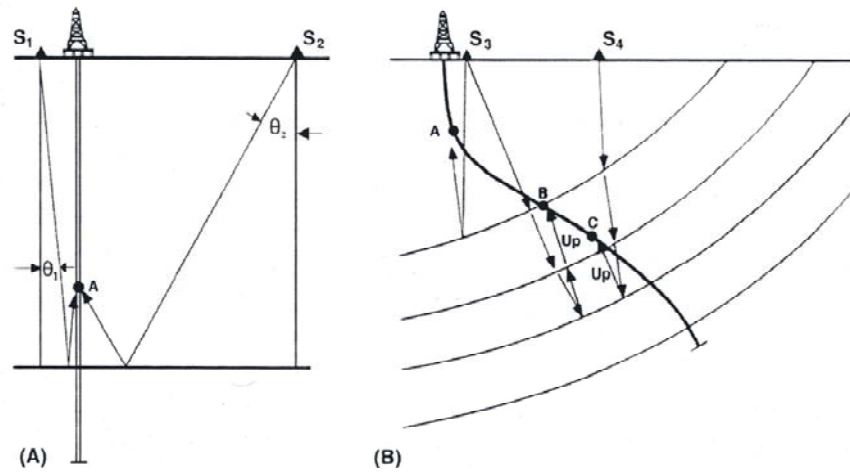


FIG. 3.1.1. Near-offset VSP geometry (A) and far-offset VSP geometry (B). S_1 , S_2 , S_3 , and S_4 denotes the sources; A, B, and C marks the geophones in the wells; θ_1 and θ_2 represents the angle between the downgoing ray and the vertical (after Hinds *et al.*, 2001).

Since the 1980s, multicomponent receivers have been used to acquire VSP data. DiSiena *et al.* (1981, 1984), Gaiser *et al.* (1982) and Toksoz and Stewart (1984) discussed the polarization (hodogram) method of using time invariant rotation angles to extract the partitioned P-, SV-, and SH-wave energy from the X, Y, and Z components. Dupal and Miller (1985) and Jones and Fung (1988) used multiple offset VSP data for carbonate reef interpretation. Stewart and DiSiena (1989) reviewed the contribution of VSP in understanding corresponding geologic logs and providing additional seismic interpretational insight. Coulombe *et al.* (1991, 1992) and Coulombe (1993) illustrated the processing and analysis of AVO effects in VSP interpretation.

Chopra *et al.* (2004) presented a history of VSP acquisition (Table 1) and described the complete VSP processing sequence, the problems encountered and the ways to overcome them.

Year	Company	Location	Receiver	Components
1986	AGIP	Brenda	8 levels	1
1989	Philips Pet., Norway	Ekofisk-K17	8 levels	1
*				
1993	Shell	Brent	5 levels	3
1994	Philips Pet., Norway	Eldfisk	5 levels	3
1995	Philips Pet., Norway	Ekofisk-K6	5 levels	3
1995	Norsk Hydro	Oseberg	5 levels	3
1995	Philips Pet., Norway	Ekofisk-K3	5 levels	3
1995	PanCanadian	Blackfoot	5 levels	3
1996	AGIP, Luisella	-	-	-
1996	Petrozeit, Egypt	-	-	-
1997	British Petroleum	Magnus Field	8 levels	3
1997	Philips Pet., Norway	Ekofisk-C11a	12 levels	3
1998	Chevron	Lost Hills Field, California	40 levels	3
1999	Output Expl. Inc.	S. Louisiana, Salt Basin	80/40 levels	3
1999	PanCanadian	Weyburn, Saskatchewan	80 levels	3
1999	Unocal	Indonesia	65 levels	3
2000	Crestar Energy	Coyote, Alberta	80 levels	3
2000	-	Bakersfield, California	80 levels	3
2000	PanCanadian	Christina Lake	23 levels, overall 80 levels	3
2001	-	West Texas	80 levels	3
2001		Wyoming	80 levels	3
2001		California	80 levels	3
2002	British Petroleum	Alaska	80 levels	3
2002	British Petroleum	Gulf of Mexico	36 levels	3

Table 1. History of VSP acquisition (after Chopra *et al.*, 2004)

3.2. 3-D 3-C VSP Vinton Dome acquisition overview

A 3-C VSP measures the complete seismic wavefield (downgoing and upgoing) in the subsurface and is, therefore, an ideal tool for a detailed stratigraphic and lithological interpretation (Ahmed *et al.*, 1986; Ahmed, 1987). Simultaneous acquisition of surface 3-D and subsurface 3-C VSP data provides a comprehensive data set for imaging the subsurface. Since no extra sources are used, this method is considered to be a cost-effective means to acquire 3-D VSP data. The combination of surface seismic and VSP also provides an opportunity to add extra control for the determination of seismic velocities (Constance *et al.*, 1999) and estimate the source wavelet.

Because the location of the salt was well known, the Vinton Dome acquisition program used a radial receiver grid on the surface, two multilevel downhole 3-C arrays, and concentric source lines (Figure 3.2.1).

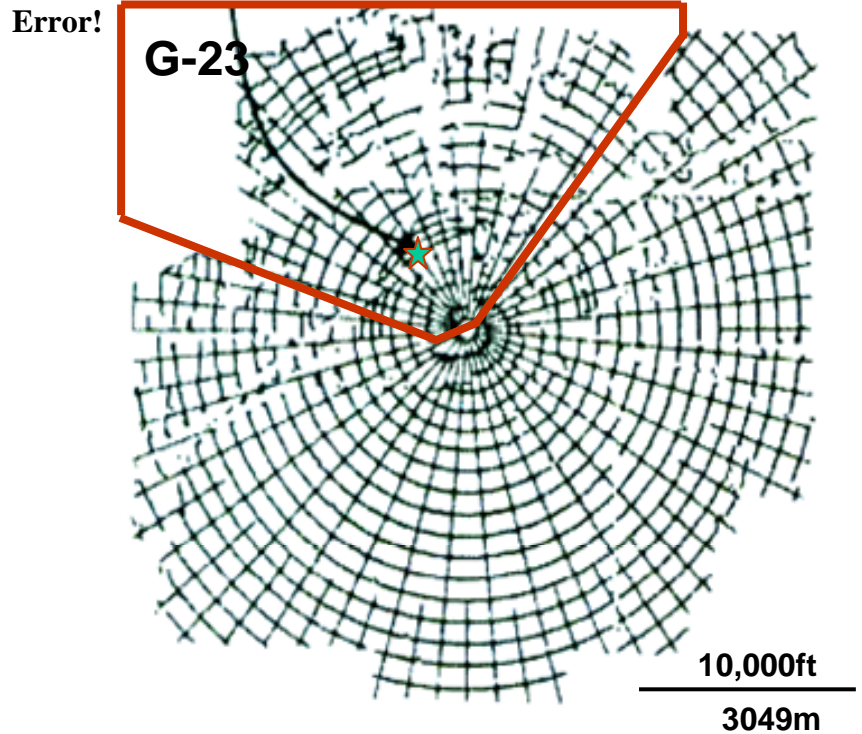


FIG. 3.2.1. Acquisition at Vinton Dome. Receivers are along radial lines, sources on concentric arcs. The VSP in well G-23 used sources included in the shaded polygon (after Constance *et al.*, 1999).

The polygon in Figure 3.2.1 indicates the sources recorded by the 3-C geophones located in well G-23. Concentric circles approximate source locations, with shot spacing 165 ft (50 m) along an arc. The seismic sources consisted of 5.5 lb. pentolite charges set off at 60 ft. depth (18 m). The receiver line interval on the surface is variable, ranging from approximately 900 ft to 1200 ft (275 to 365 m), with alternating long and short line segments spaced at 5° increments. The receiver station spacing is 165 ft (50 m) along a receiver line segment. At each station, a 6-element array was deployed using 10 Hz

geophones. Cultural obstacles in the Northern and Western portions of the survey area, such as houses, wells, canals, pipelines, and a 4-lane super highway (US Interstate 10) produced irregularities from the original planned source grid. The active recording spread consisted of 19 receiver lines, which represent a 90° wedge of the 360° coverage produced by the radial receiver line distribution. Typically, 1400 to 2000 channels were active in the surface spread.

While the approximate Northern half of the surface seismic survey was acquired, two abandoned boreholes were used to deploy 3-C arrays in the subsurface. The Western well, G-23, has 80 levels of 3-C geophones cemented in place at 50 ft (15.24 m) spacing, located between 943 and 4893 ft (287 to 1492 m). The last 19 groups were damaged during deployment and were not operational for recording. The Eastern well, G-24, has only 40 3-C geophones with the same spacing between groups and located between 350 and 2350 ft (107 to 716 m). These phones were temporarily deployed using a coiled tubing/bladder technique. The seismic data recorded by the VSP well G-23 shows better quality due to the cementation of the geophones in the well and will be the data used in my dissertation. Figure 3.2.2 shows the mapview of 1176 sources recorded by G-23 generated in Seisup. Sources are color-coded based on shot depth. The size of the survey is around 18700 ft (5702 m) NS and 30000 ft (9147 m) EW.

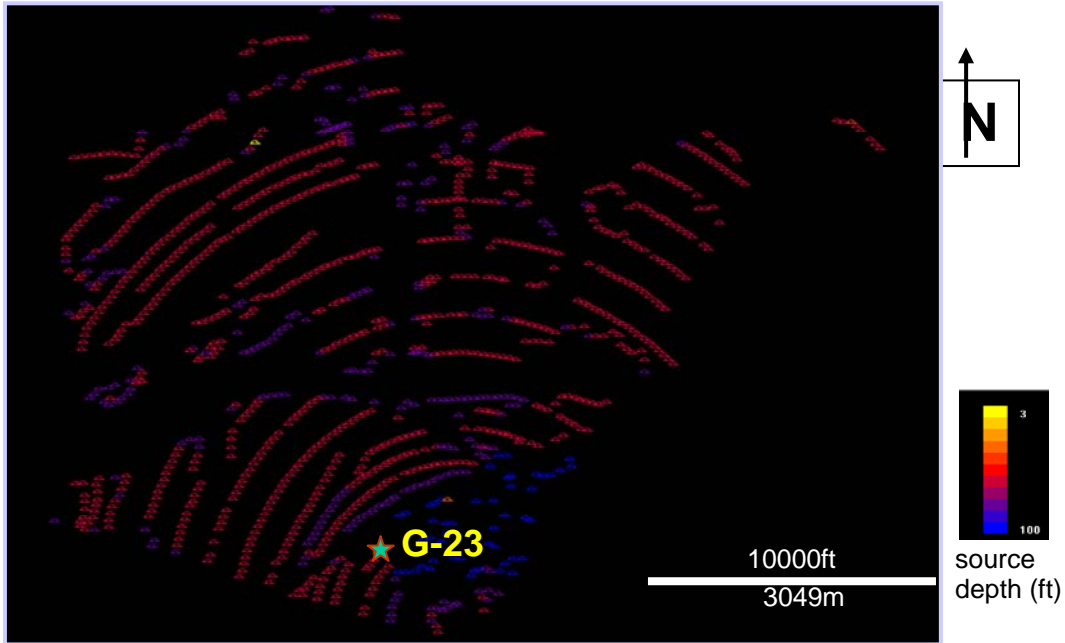


FIG. 3.2.2. Mapview of sources recorded in VSP well G-23. Color bar is shown on the lower right corner of the mapview.

3.3. Pre-processing of 3-D 3-C VSP Vinton Dome data

Since 3-D multicomponent surveys are relatively rare, no single commercial processing package contains all the necessary tools. I therefore use both Focus and Seisup where appropriate.

My first step during the pre-processing stage was to re-number and re-arrange the traces in a regular order inside the common-shot gather. Each common-shot gather has 240 traces. The traces were numbered twice from 1 to 120 instead of 1 to 240 and the 120 traces coming from the deeper groups were recorded before the 120 traces coming from

the shallower groups. In general, the normal order of channels is 1,2,3,1,2,3 with trace number 1 corresponding to Vertical phone (Z), trace number 2 to Horizontal (X) component and trace number 3 to Horizontal (Y) component. Due to mechanical characteristics of the recording instruments, the order of the 3-C components was mixed (Figure 3.3.1-3.3.3). The channel number was recalculated based on the depth of the group and all traces were resorted. More sobering, the component number was not stored in the SEG Y trace headers. Considerable effort was invested in discovering which components were which!

Next, I sorted the data into Vertical (Z) and Horizontal (X, Y) components (Figures 3.3.4-3.3.6). Notice the noisy 19 traces at the bottom due to crushed phones that were later eliminated. Using two different types of geophones in the same well generated another technical problem fixed during processing. The shallower 41 groups used 30 Hz geophones while the deeper 39 groups used 10 Hz geophones. I designed a filter based on the characteristics of these two types of geophones in order to match the data from 10 Hz to those using the 30 Hz phone. I show the spectral characteristics of a near offset common-shot gather, vertical component, in Figure 3.3.7. I transform selected data via FFT into the frequency domain and display them in two forms. I plot frequency as a function of time in the upper portion of the display and as a function of amplitude in the lower portion of the display. In the upper display, the amplitudes for each analyzed frequency are contoured and plotted in a two dimensional array. Vertical axis represents the time and horizontal axis represents the frequency. The lower display is a conventional amplitude spectrum, with the vertical axis representing amplitude and the horizontal axis representing frequency. Scales along the frequency axis for both displays are equal.

Next, I needed to balance the traces in order to correct the amplitudes. Trace balancing is a *time-invariant scaling* of amplitudes (Yilmaz, 2001). This operation was performed in Focus 5.0.

Focus 5.0 routine “BALAN” is the first of three modules that together perform surface-consistent amplitude or energy balancing on pre-stack seismic data sets. It is designed to analyze a gate of data from each input trace and write a balancing factor corresponding to each trace into a file. A basic assumption of BALAN is that the amplitudes within the design gates represent the true trace character. BALAN computes the mean of either the absolute amplitude or energy (amplitude squared) within the time window of each input seismic trace and stores the logarithms of these values. We selected the option of mean of absolute amplitude.

Focus 5.0 program “BALSOL” reads the file created by BALAN and reduces the trace amplitude information to surface-consistency in two passes. Bad traces, identified during the initial pass, are excluded from consideration during the second iteration. The surface-consistent scale factors for each trace are written into a file read by Focus 5.0 module “BALAPP”, which applies the scale factors to the seismic data. In Figures 3.3.8-3.3.9 I compare a representative common-shot gather before and after trace balancing. I show common-shot gathers for near, mid and far offset after trace balance in Figures 3.3.10-3.3.18 for each component.

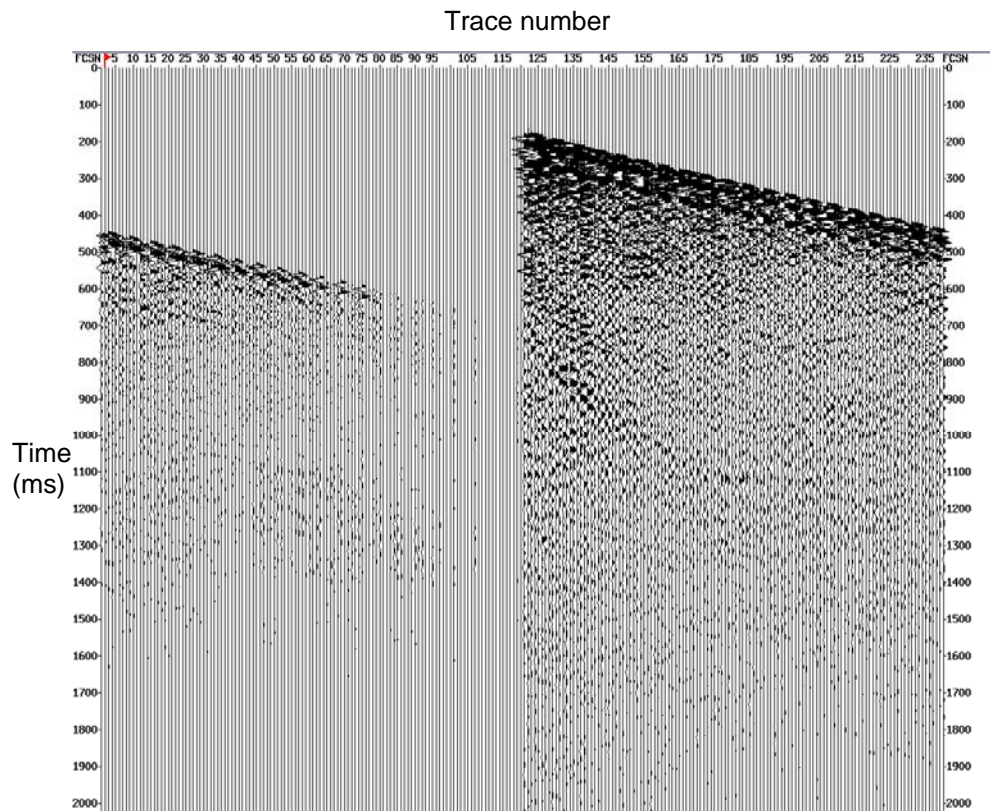


FIG. 3.3.1. 3-C near-offset common-shot gather (240 traces) as stored on the input tape in the field. The traces corresponding to the deeper 40 groups were recorded before the traces corresponding to the shallower 40 groups. Shot no. 3024, offset = 553 ft (169 m). No AGC applied.

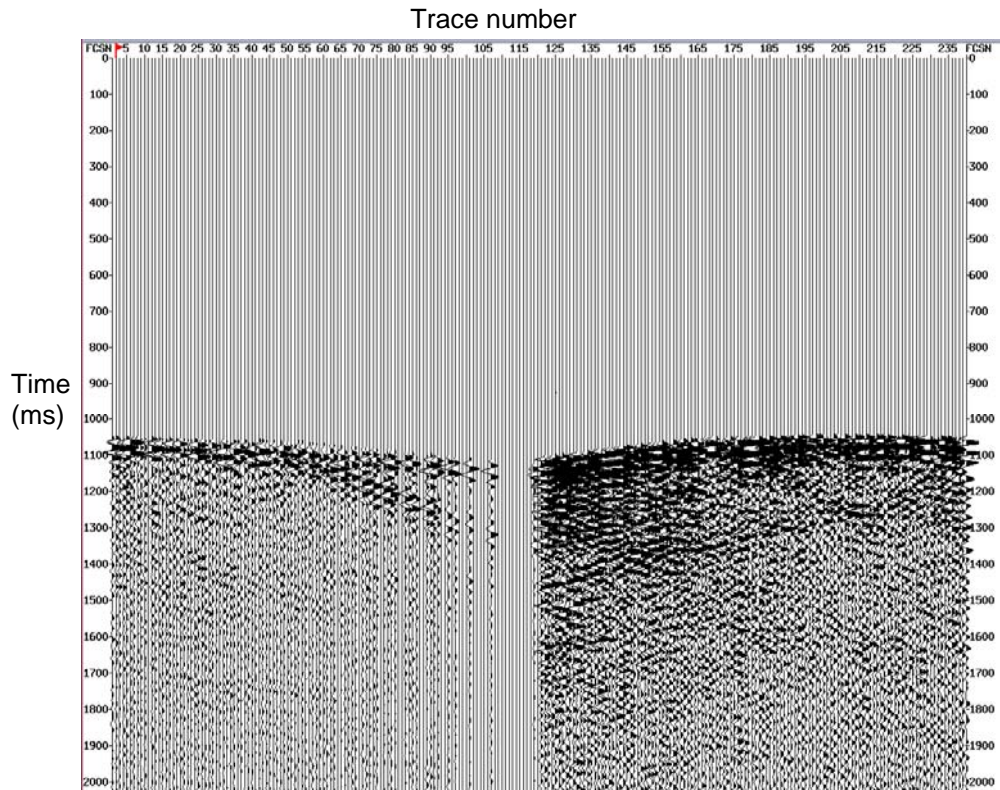


FIG. 3.3.2. 3-C mid-offset common-shot gather (240 traces) as stored on the input tape in the field. The traces corresponding to the deeper 40 groups were recorded before the traces corresponding to the shallower 40 groups. Shot no. 3082, offset = 6590 ft (2009 m). No AGC applied.

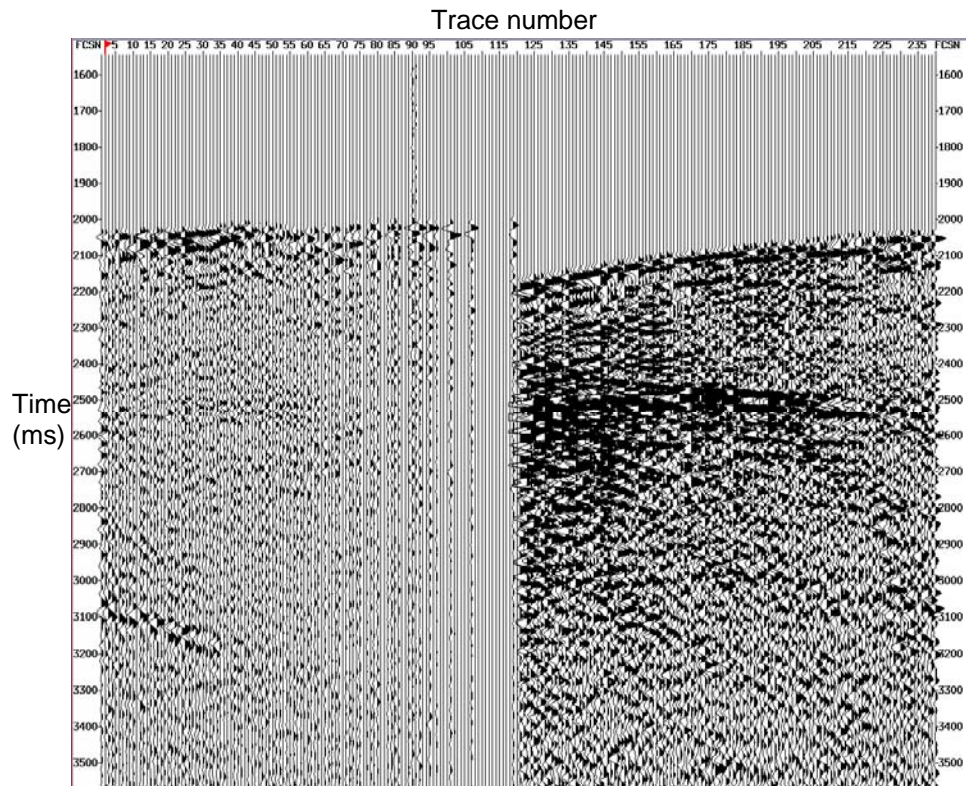


FIG. 3.3.3. 3-C far-offset common-shot gather (240 traces) as stored on the tape in the field. The traces corresponding to the deeper 40 groups were recorded before the traces corresponding to the shallower 40 groups. Shot no. 3126, offset = 14450 ft (4405 m). No AGC applied.

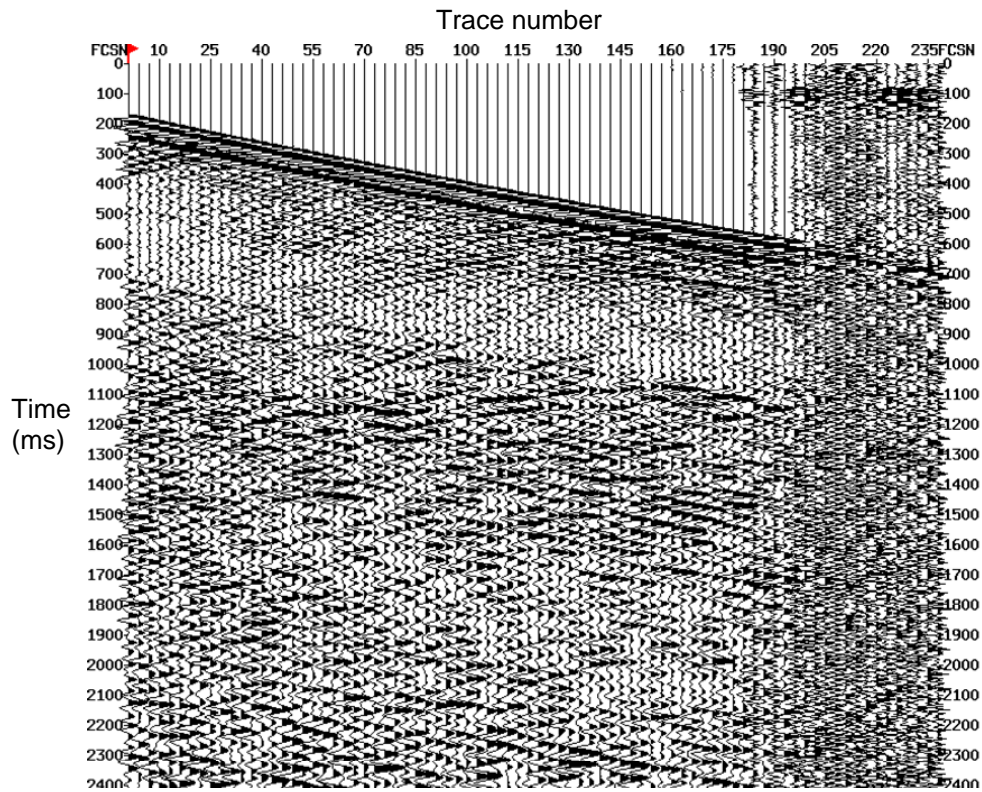


FIG. 3.3.4. Vertical component near-offset common-shot gather after renumbering and sorting (80 traces). Notice the bad 19 traces at the end due to crushed geophones at the bottom of the well. Shot no. 3024, offset = 553 ft (169 m). AGC applied.

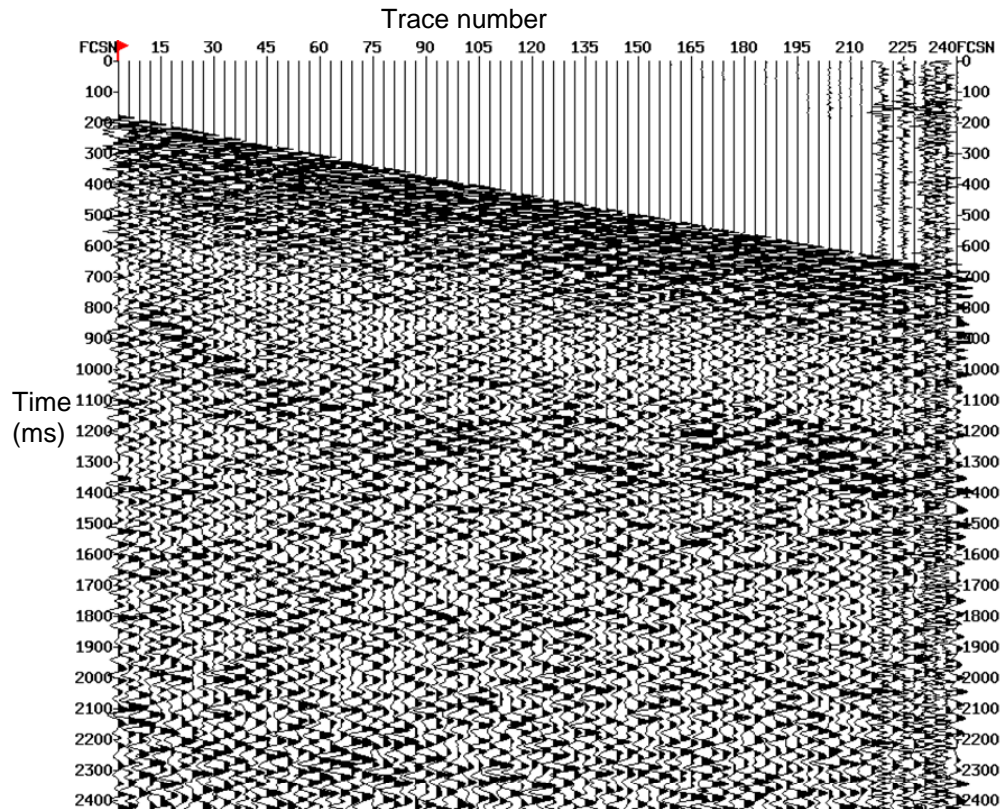


FIG. 3.3.6. Horizontal component (Y) near-offset common-shot gather after renumbering and sorting (80 traces). Notice the bad 19 traces at the end due to crushed geophones at the bottom of the well. Shot no. 3024, offset = 553 ft (169 m). AGC applied.

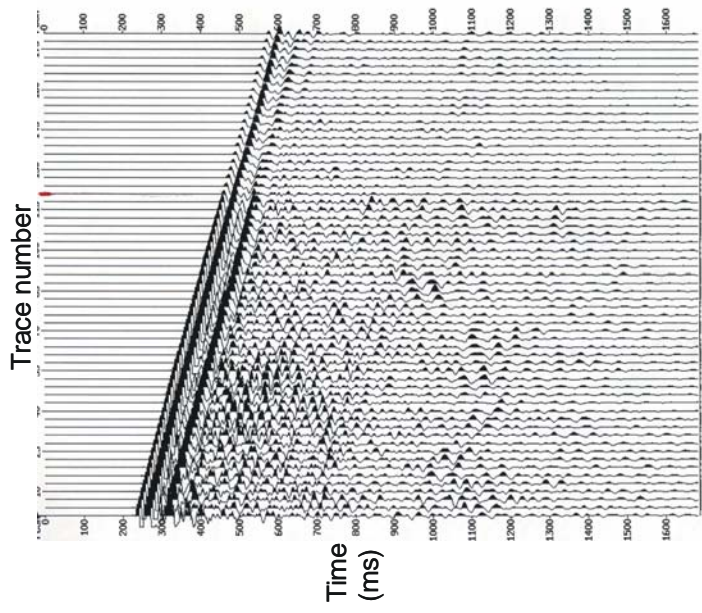


FIG. 3.3.8. Vertical component, near -offset common-shot gather before trace balancing. Last 19 bad traces were removed. Shot no. 2953, offset = 550 ft (168 m). AGC applied.

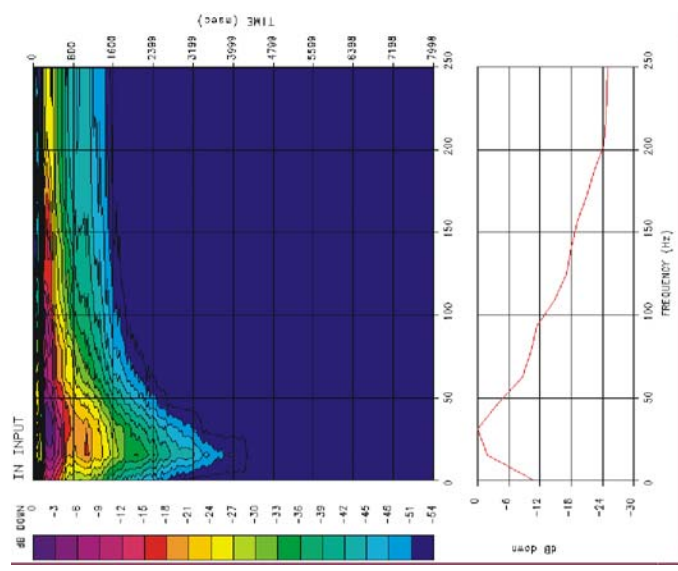


FIG. 3.3.7. Amplitude spectrum of vertical component, near-offset common-shot gather. Peak signal occurs at 30 Hz. Shot no. 2953, offset = 550 ft (168 m).

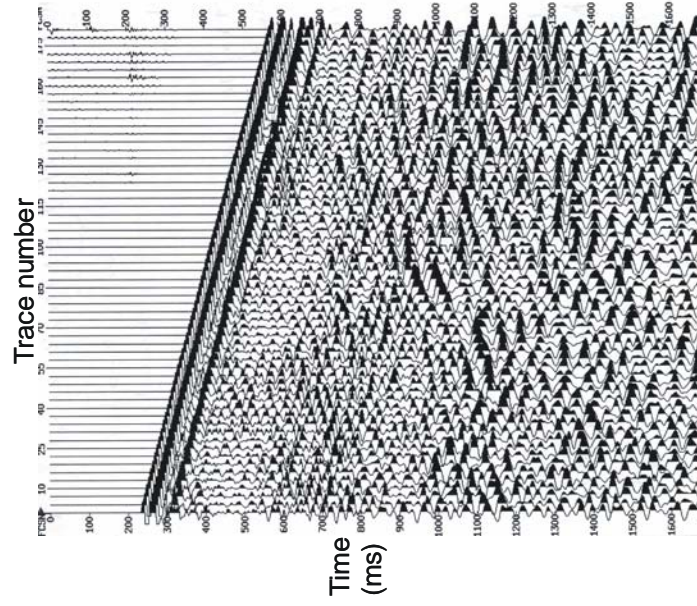


FIG. 3.3.9. Vertical component, near -offset common-shot gather shown in Figure 3.3.8 after trace balancing. Last 19 bad traces were removed. Shot no. 2953, offset = 550 ft (168 m). AGC applied.

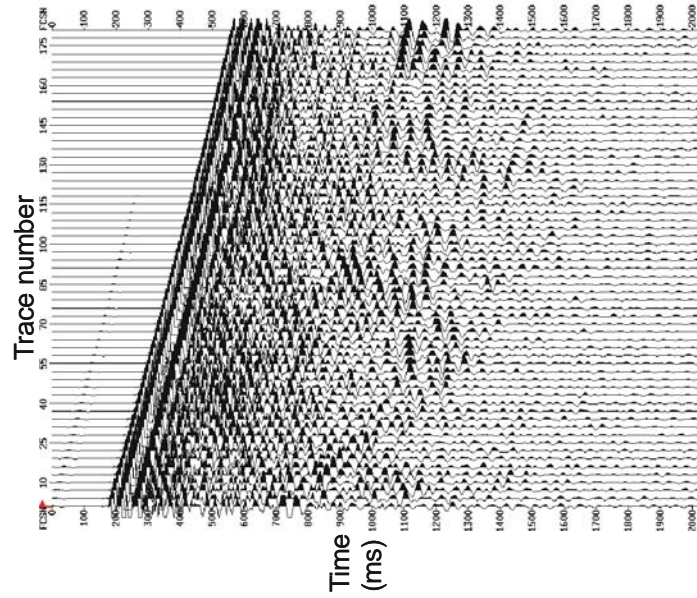


FIG. 3.3.10. Vertical component, near -offset common-shot gather (61 traces). Shot no. 3024, offset = 553 ft (169 m). No AGC applied.

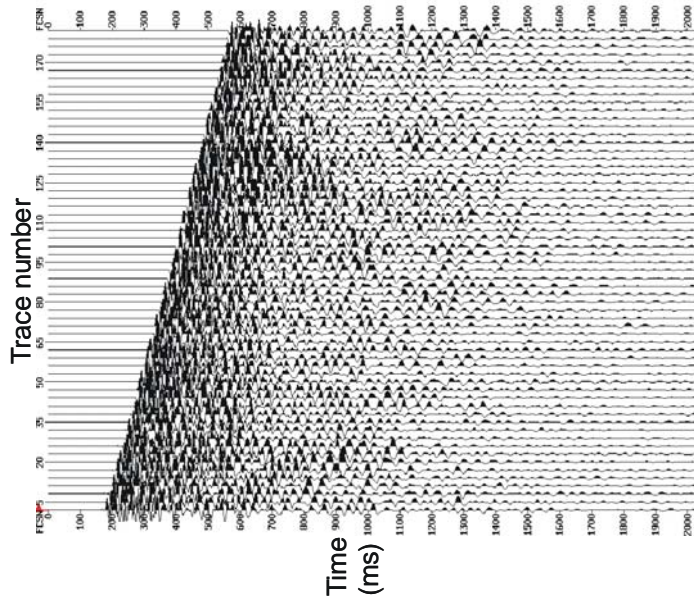


FIG. 3.3.11. Horizontal (X) component, near-offset common-shot gather (61 traces). Shot no. 3024, offset = 553 ft (169 m). No AGC applied.

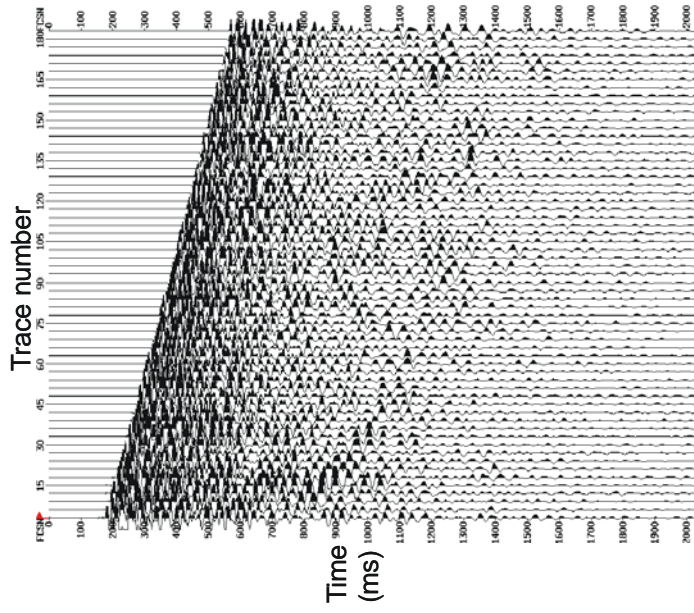


FIG. 3.3.12. Horizontal (Y) component, near-offset common-shot gather (61 traces). Shot no. 3024, offset = 553 ft (169 m). No AGC applied.

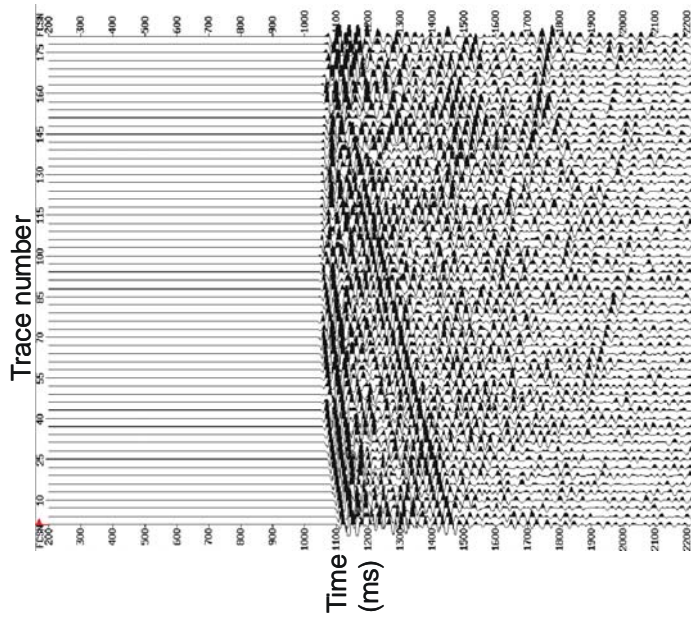


FIG. 3.3.13. Vertical component, mid-offset common-shot gather (61 traces). Shot no. 3082, offset = 6590 ft (2009 m). No AGC applied.

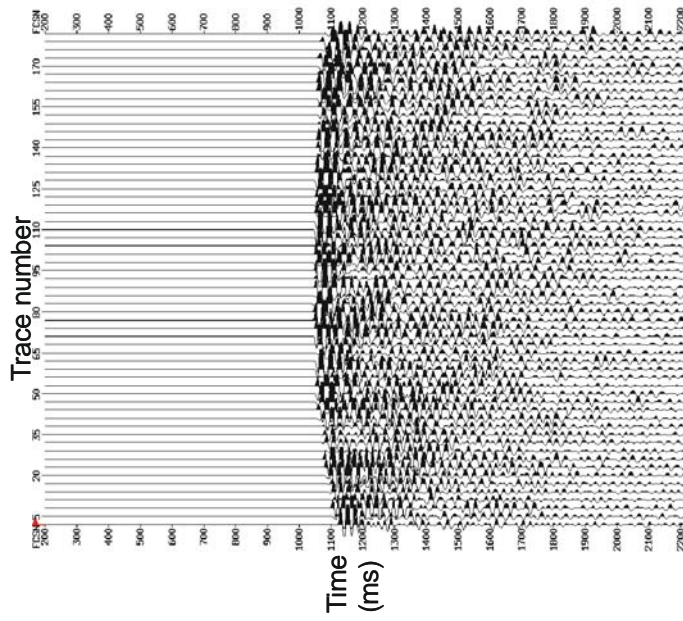


FIG. 3.3.14. Horizontal (X) component, mid-offset common-shot gather (61 traces). Shot no. 3082, offset = 6590 ft (2009 m). No AGC applied.

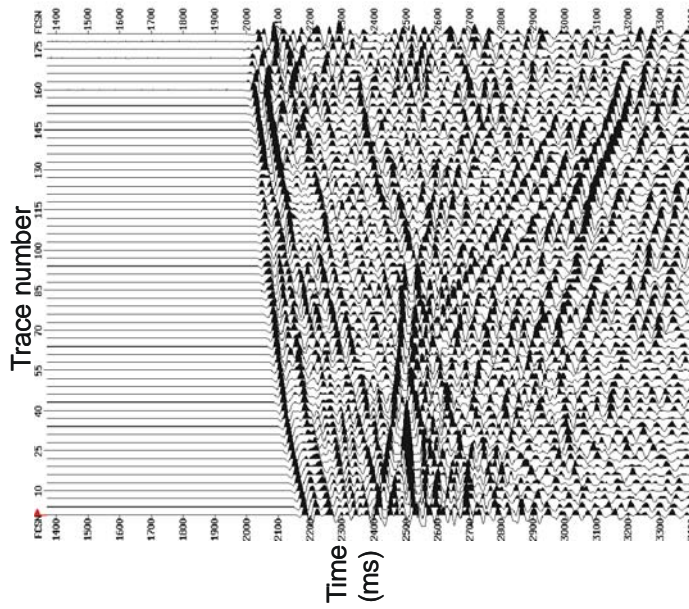


FIG. 3.3.16. Vertical component, far -offset common-shot gather (61 traces). Shot no. 3126, offset = 14450 ft (4405 m). No AGC applied.

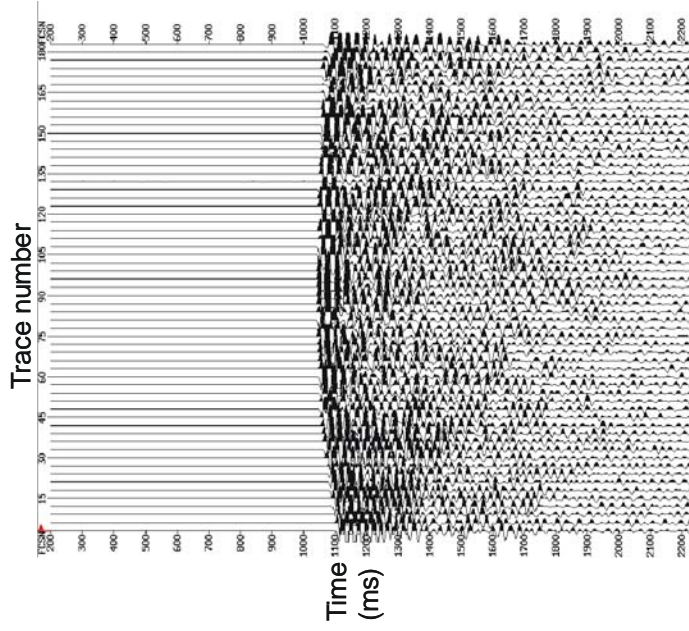


FIG. 3.3.15. Horizontal (Y) component, mid-offset common-shot gather (61 traces). Shot no. 3082, offset = 6590 ft (2009 m). No AGC applied.

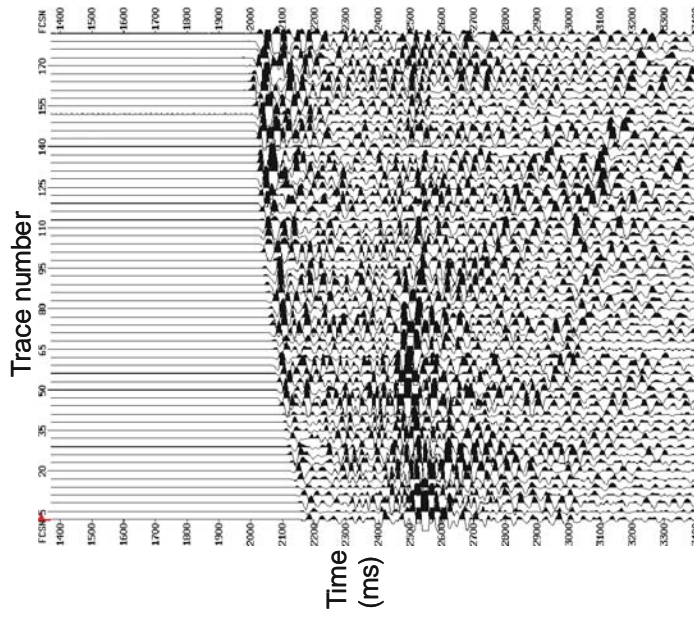


FIG. 3.3.17. Horizontal (X) component, far-offset common-shot gather (61 traces). Shot no. 3126, offset = 14450 ft (4405 m). No AGC applied.

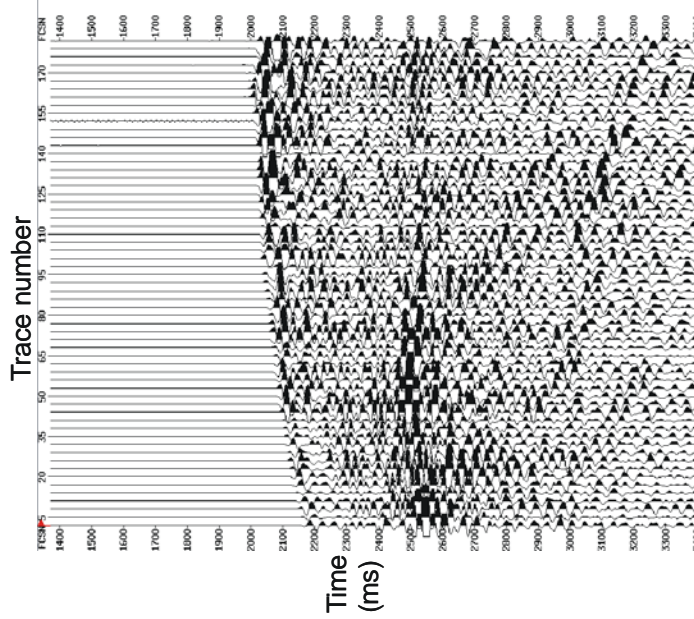


FIG. 3.3.18. Horizontal (Y) component, far-offset common-shot gather (61 traces). Shot no. 3126, offset = 14450 ft (4405 m). No AGC applied.

3.4. Rotation of horizontal geophones

Accurate geophone orientation is essential in multicomponent seismology, since this will allow separating P from S-waves (Guevara and Stewart, 2001). Usually, gyroscopes are not used to determine downhole orientation of the horizontal geophones. Instead, a predefined geophone orientation is assumed, which implies careful geophone deployment during acquisition. An alternative is to obtain orientation directly from the field data. Polarization of first arrivals has been used successfully to obtain geophone orientation in both VSP (DiSiena *et al.*, 1984), (Figure 3.4.1), and marine multicomponent data (Gaiser, 1999). Gulati *et al.*, (1998) proposed to use first break polarization to obtain geophone orientation in land 3-C data.

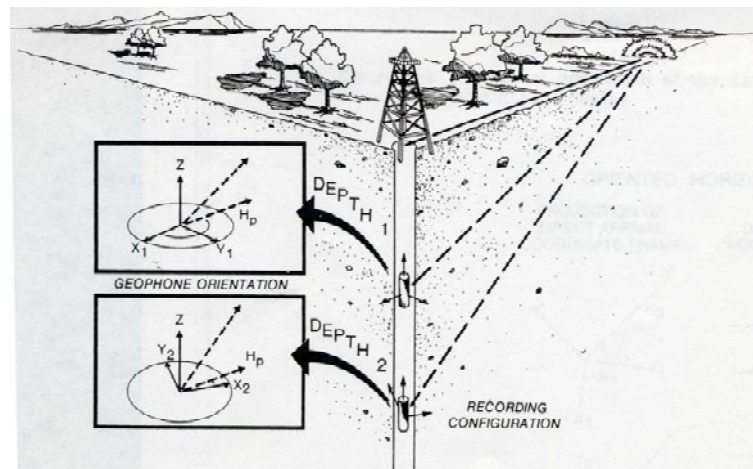


FIG. 3.4.1. Schematic of the vertical seismic profile geophone orientation problem (after DiSiena *et al.*, 1984).

For my study, I have selected a hodogram method to orient my data. For analysis of time-variant signals, hodograms display the terminus of a moving vector as a function of x, y and time. They allow the simultaneous analysis of amplitude, polarization and relative orientation (DiSiena *et al.*, 1984). For this purpose, I selected a few common-shot gathers with similar offset but different azimuths. I then sorted data into common-receiver gathers and built the hodograms by cross-plotting the samples from a time window along the first breaks of the X and Y horizontal components. With help from Dr Zhou, I checked the hodograms of the first-arrival wavelets (Figure 3.4.2) and estimated the rotation angle of X and Y components with respect to the x-axis at each depth level. Receiver number 41 had a strange behavior and its (x,y) coordinates had to be switched before rotation. Dr. Zhou suggested that this particular 3-C receiver might be placed upside-down in the borehole.

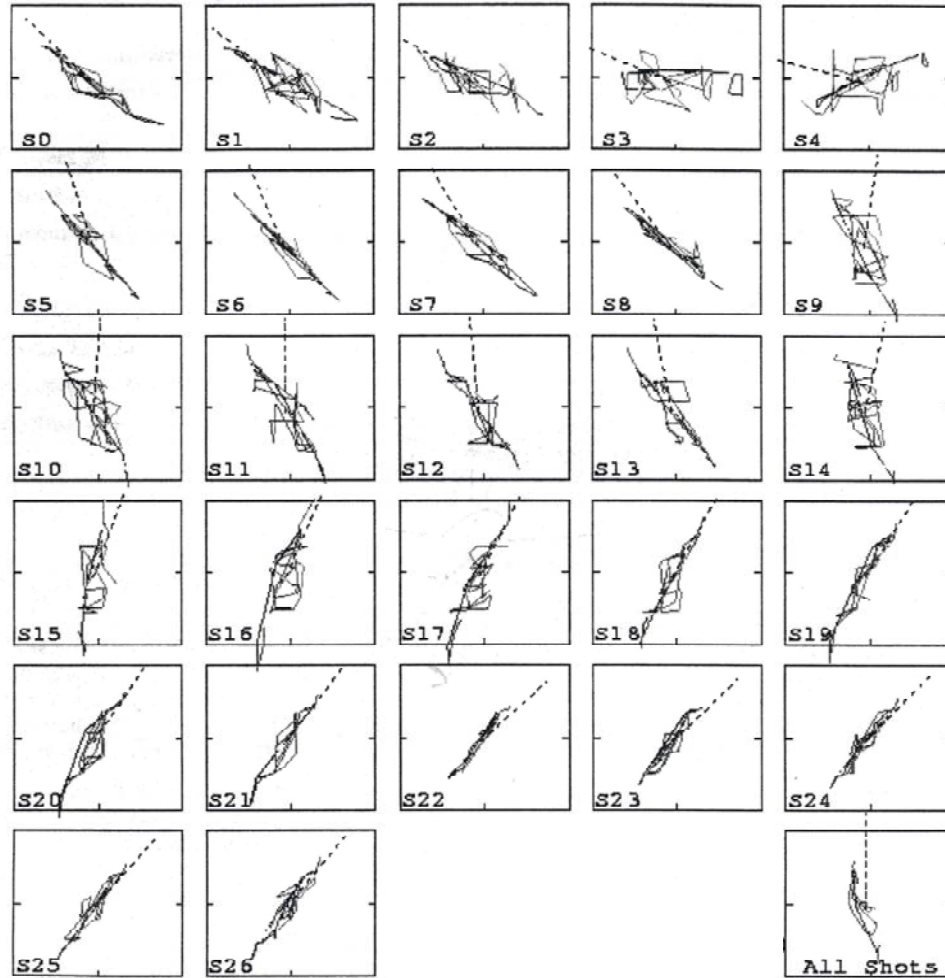


FIG. 3.4.2. First break hodograms of 27 shots having a similar offset and different azimuth for receiver #1 at a depth = 943 ft (287.5 m). In each hodogram, the dashed line indicates the direction from the shot to the receiver and the curve represents the hodogram track. The last hodogram in the lower right corner is a composite of all 27 shots. All the hodograms have been rotated by a positive 90 degrees and the final rotation angle is 105 degrees (after Zhou, 2002).

Since the source-receiver azimuth was measured with respect to North, all the angles were re-calculated to be measured in exactly the same way. Then, a geometrical rotation has been applied to the horizontal (X,Y) geophones (Figures 3.4.3 – 3.4.8).

$$E = X \cos\phi + Y \sin\phi \quad (1)$$

$$N = -X \sin\phi + Y \cos\phi \quad (2)$$

where N is the north component and E is the east component, and, ϕ is the rotation angle measured from North.

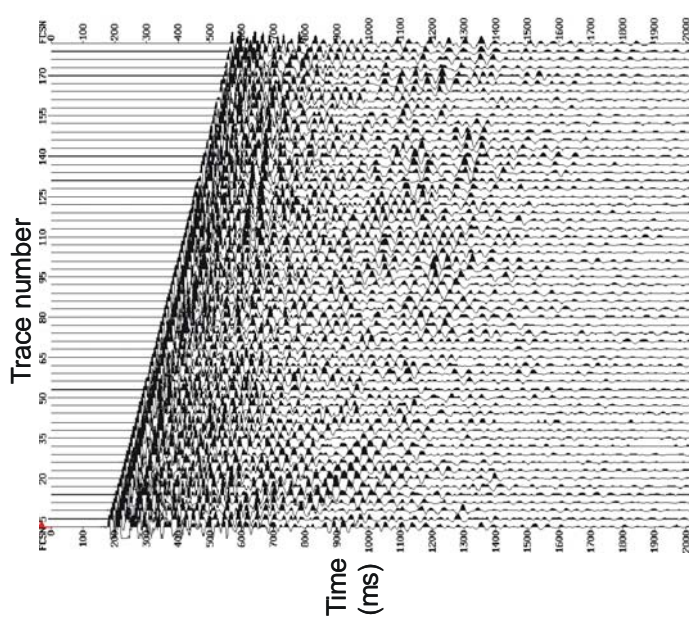


FIG. 3.4.3. East component, near-offset common-shot gather derived from figures 3.3.11 and 3.3.12. Shot no. 3024, offset = 553 ft (169 m). No AGC applied.

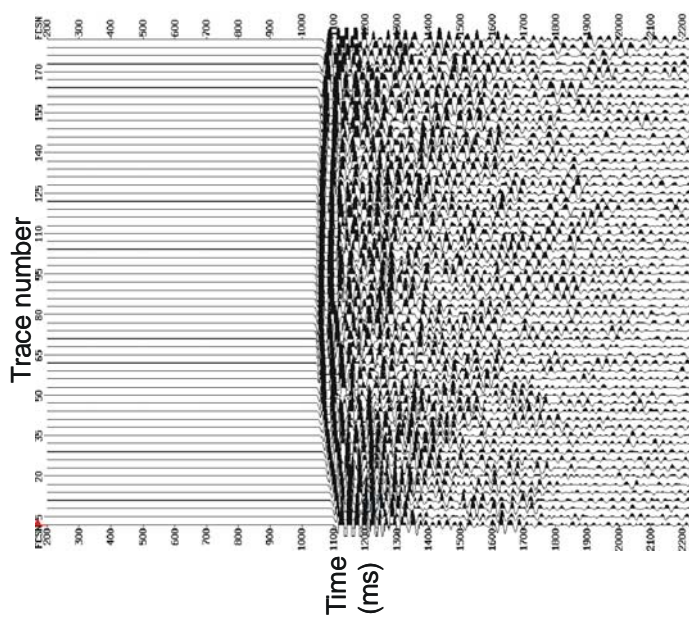


FIG. 3.4.5. East component, mid-offset common-shot gather derived from figures 3.3.13 and 3.3.14. Shot no. 3082, offset = 6590 ft (2009 m). No AGC applied.

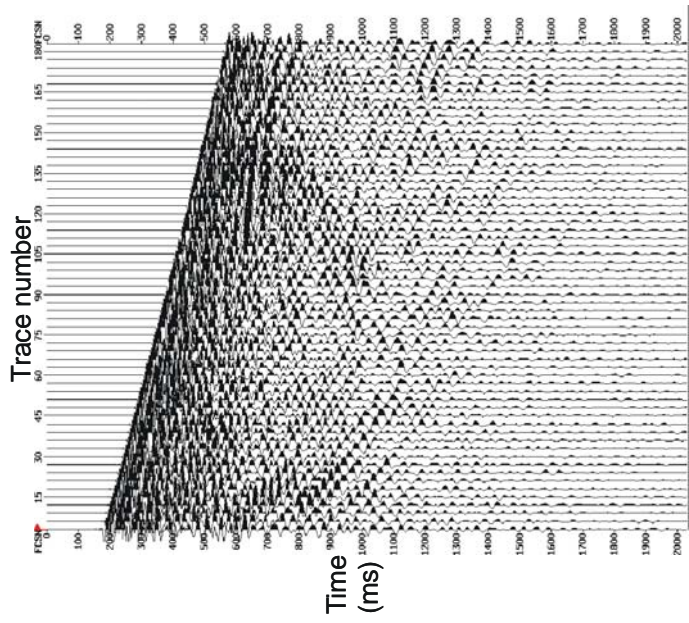


FIG. 3.4.4. North component, near-offset common-shot gather derived from figures 3.3.11 and 3.3.12. Shot no. 3024, offset = 553 ft (169 m). No AGC applied.

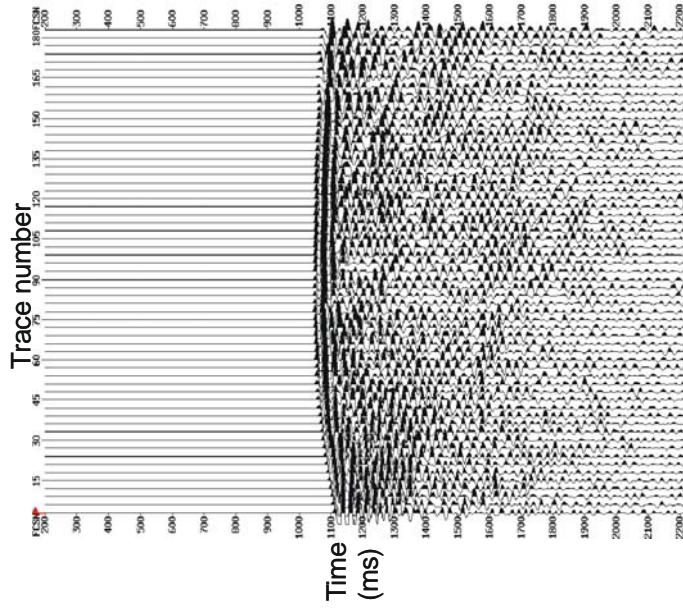


FIG. 3.4.6. North component, mid-offset common-shot gather derived from figures 3.3.13 and 3.3.14. Shot no. 3082, offset = 6590 ft (2009 m). No AGC applied.

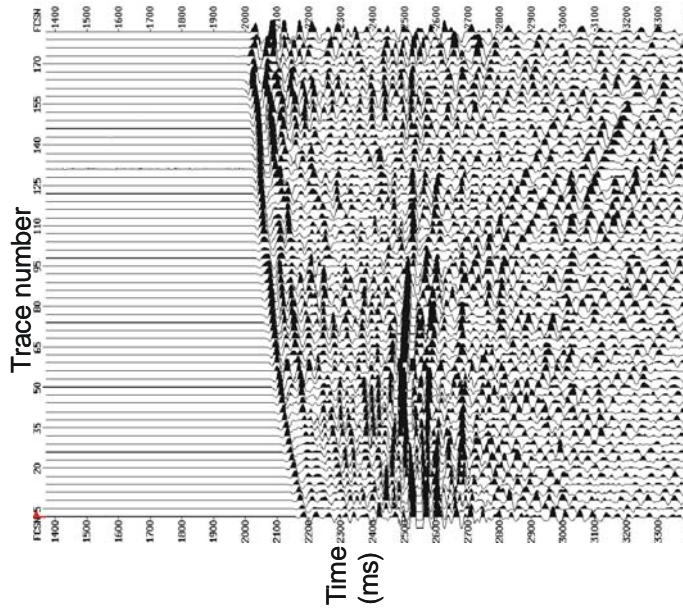


FIG. 3.4.7. East component, far-offset common-shot gather derived from figures 3.3.15 and 3.3.16. Shot no. 3126, offset = 14450 ft (4405 m). No AGC applied.

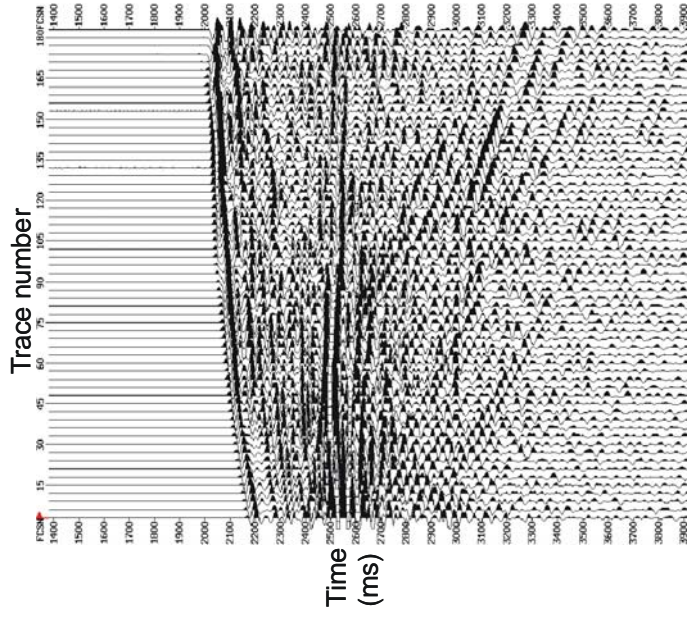


FIG. 3.4.8. North component, far-offset common-shot gather derived from figures 3.3.15 and 3.3.16. Shot no. 3126, offset = 14450 ft (4405 m). No AGC applied.

3.5. Deconvolution of VSP Vinton Dome data

The process of convolving with an inverse filter is called deconvolution (Sheriff and Geldart, 1995). Deconvolution has two goals – to shape the wavelet and balance the frequency bandwidth, and to suppress multiples. For VSPs, we calculate the deconvolution operator from the downgoing waves (Hinds *et al.*, 2001).

In this process I first pick the first arrivals on a common-shot gather, flatten the first arrivals, apply a median filter to enhance the downgoing waves and suppress the upgoing waves. Finally, I sum all the traces to generate a statistically robust wavelet.

In Figures 3.5.1-3.5.2 I show the shot gather 3068 before and after statics. The output of the 9-points median filter enhances the downgoing events having the same slope as the first break and attenuates the upgoing events (Figure 3.5.3). In Figure 3.5.4.a I present the result of summing the traces into single trace. Next, I select a window between 100 and 140 ms for zero-phase wavelet shaping (Figure 3.5.4 b), which was later used to deconvolve the shot gather. Figure 3.5.5 shows the zero-phase wavelet. In Figure 3.5.6 I display the vertical component common-shot gather shown in Figure 3.5.1 after deconvolution. The result is a somewhat more coherent, less ringy image.

Since wavefronts suffer a decay of amplitudes due to spherical divergence, I applied a simple time-scaling gain. To prevent overcorrection of amplitudes of multiple reflections, we usually select a velocity-independent scaling function, such as

$$g(t) = t^\alpha \quad (1)$$

where α is typically equal to 2.

I present examples of shot-gathers after this correction in Figures 3.5.7 – 3.5.9.

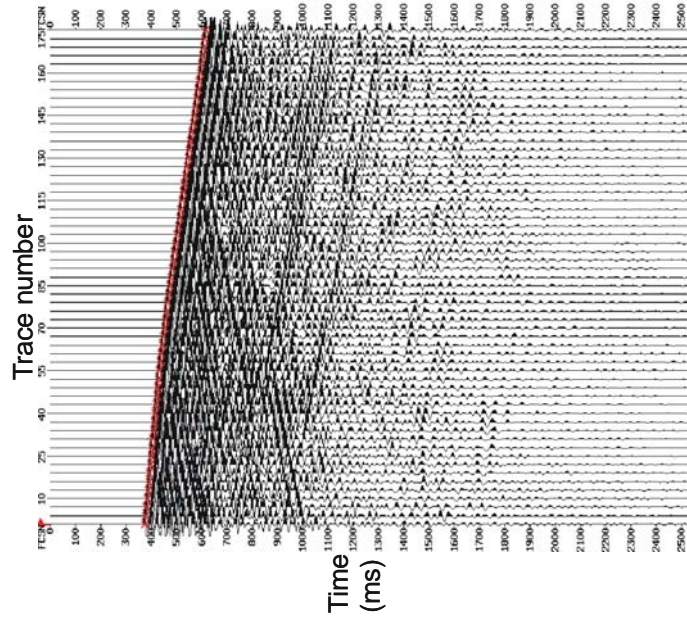


FIG. 3.5.1. First break picks on vertical component, near-offset common-shot gather. First break picks are shown in red. Shot no. 3068, offset = 1989 ft (606 m). No AGC applied.

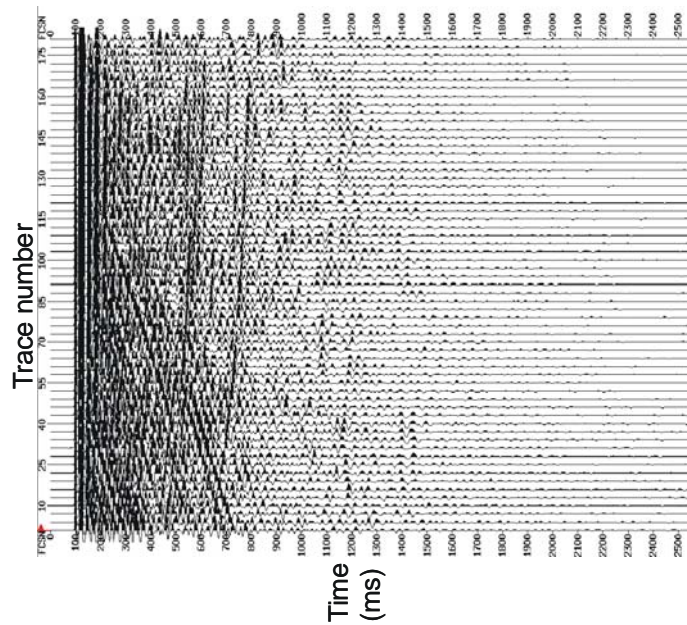


FIG. 3.5.2. Vertical component, near-offset common-shot gather from Figure 3.5.1 after flattening on the first breaks. Shot no. 3068, offset = 1989 ft (606 m). No AGC applied.

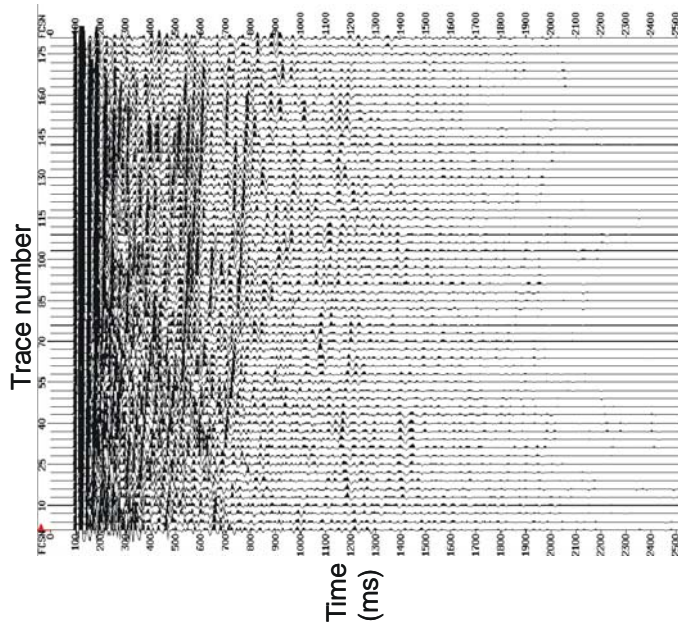


FIG. 3.5.3. Result of a 9-point median filter applied to the common-shot gather from Figure 3.5.2. Note that the up-going are attenuated. Shot no. 3068, offset = 1989 ft (606 m). No AGC applied.

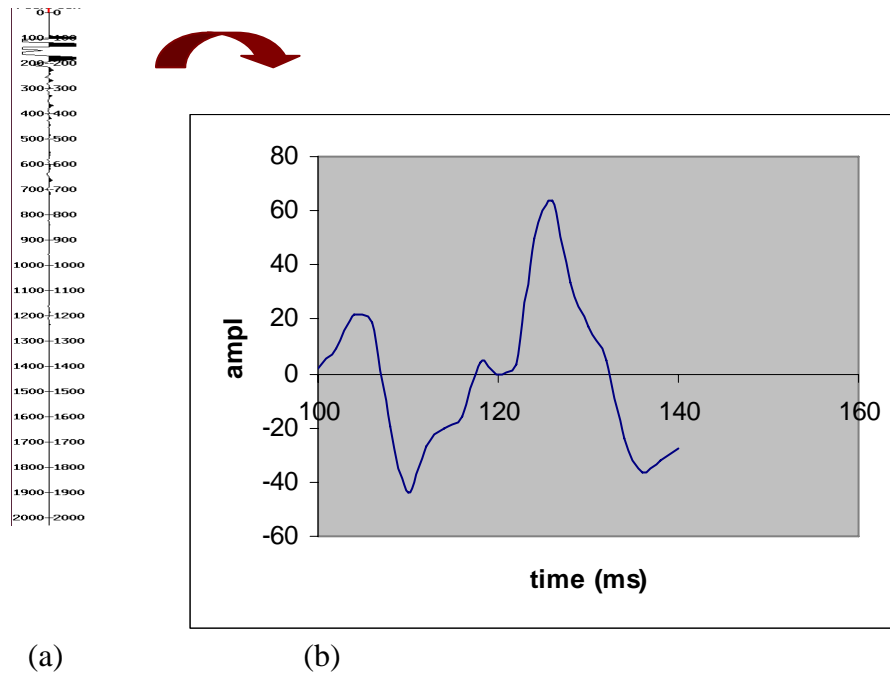


FIG. 3.5.4. (a) Summed trace of the flattened median filtered output shown in Figure 3.5.3 and (b) extracted wavelet for zero-phase shaping.

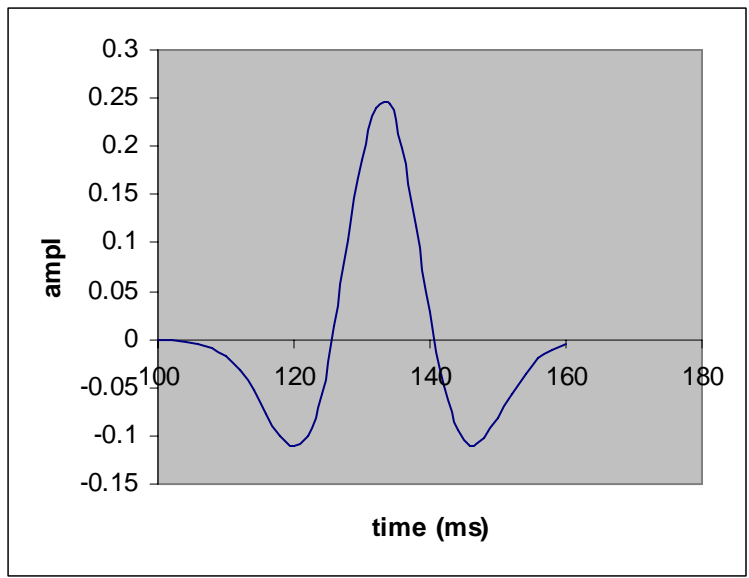


FIG. 3.5.5. Zero-phase wavelet used for deconvolution.

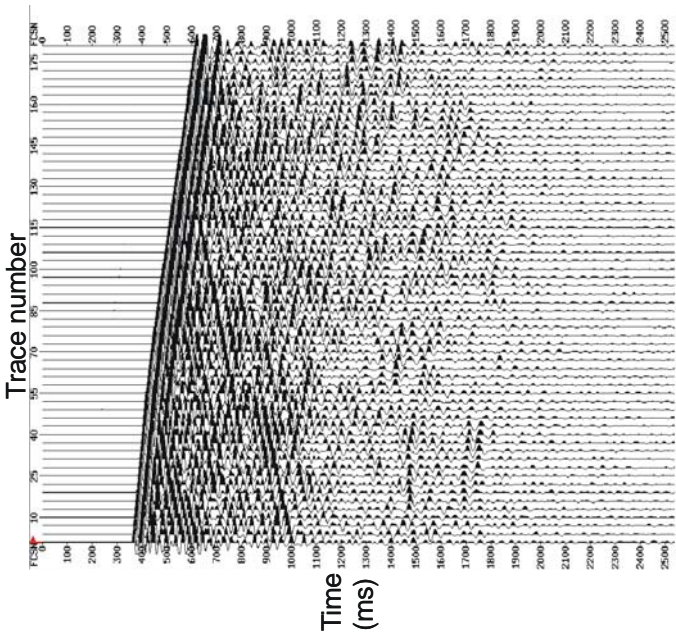


FIG. 3.5.6. Vertical component, common -shot gather after deconvolution. Shot no. 3068, offset = 1989 ft (606 m). No AGC applied.

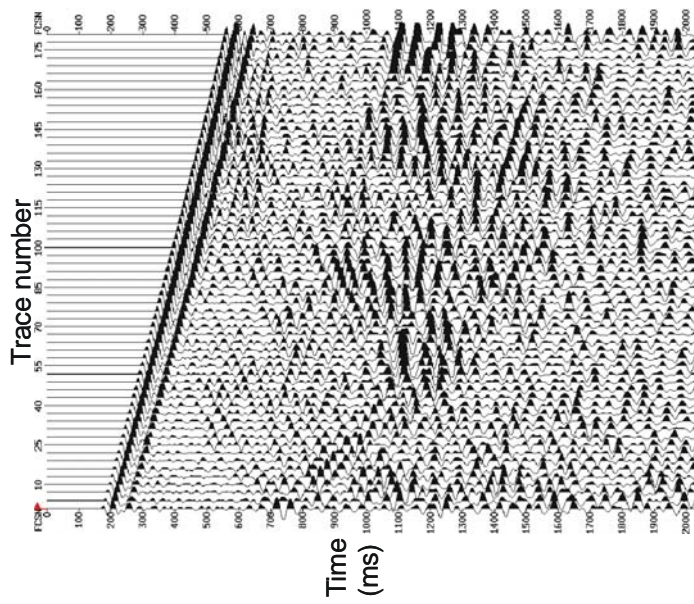


FIG. 3.5.7.a. Vertical component, near -offset common-shot gather after time scaling. Shot no. 3024, offset = 553 ft (169 m).

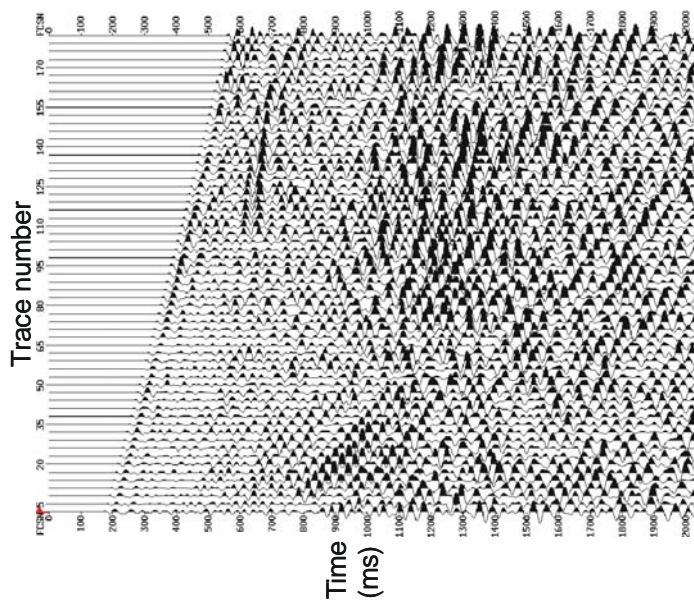


FIG. 3.5.7.b. East component, near -offset common-shot gather after time scaling. Shot no. 3024, offset = 553 ft (169 m).

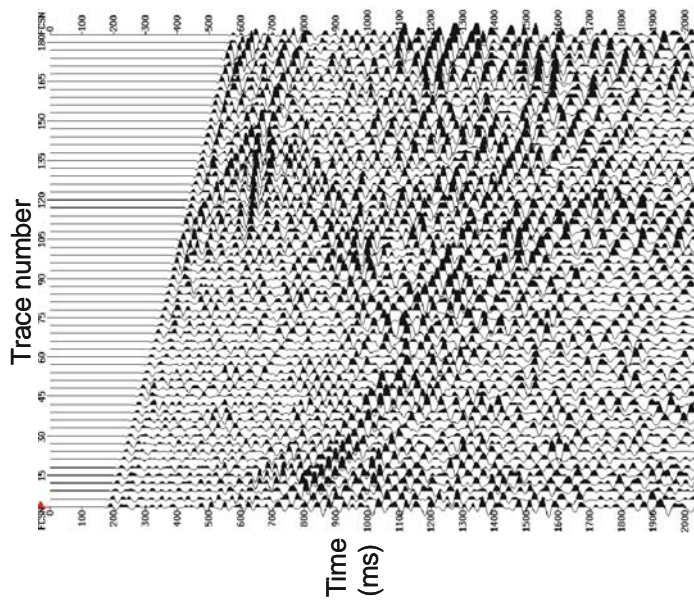


FIG. 3.5.7.c. North component, near-offset common-shot gather after time scaling. Shot no. 3024, offset = 553 ft (169 m).

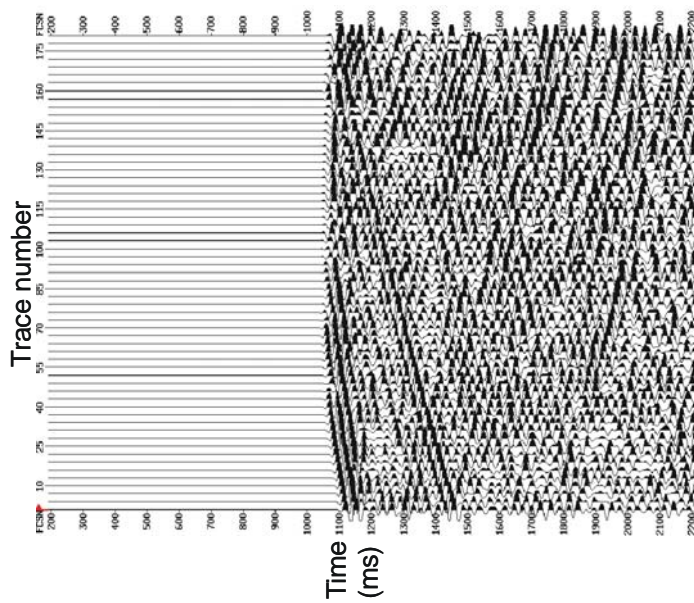


FIG. 3.5.8.a. Vertical component, mid-offset common-shot gather after time scaling. Shot no. 3082, offset = 6590 ft (2009 m).

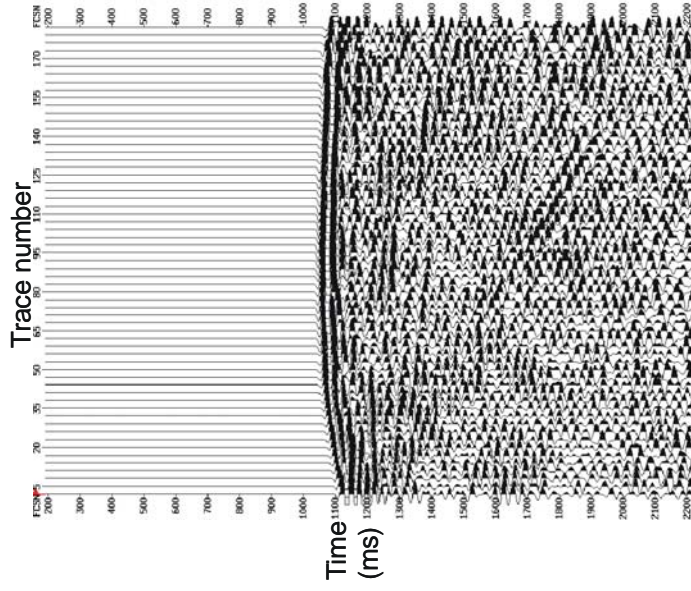


FIG. 3.5.8.b. East component, mid-offset common-shot gather after time scaling. Shot no. 3082, offset = 6590 ft (2009 m).

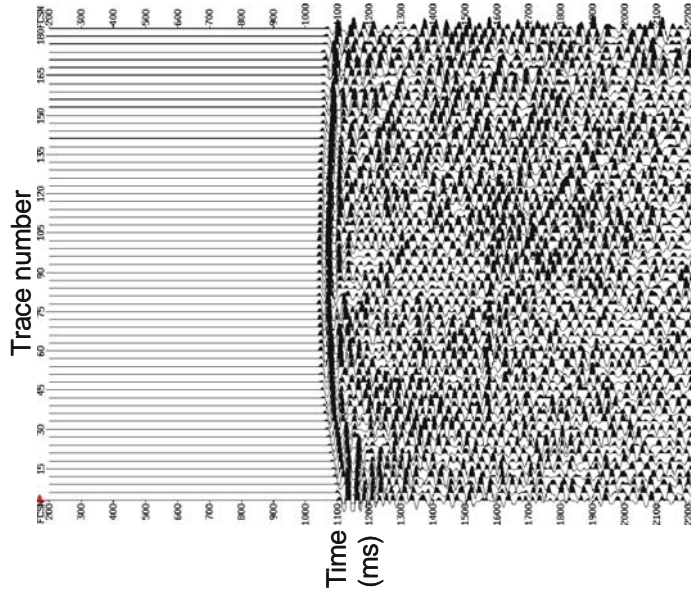


FIG. 3.5.8.c. North component, mid-offset common-shot gather after time scaling. Shot no. 3082, offset = 6590 ft (2009 m).

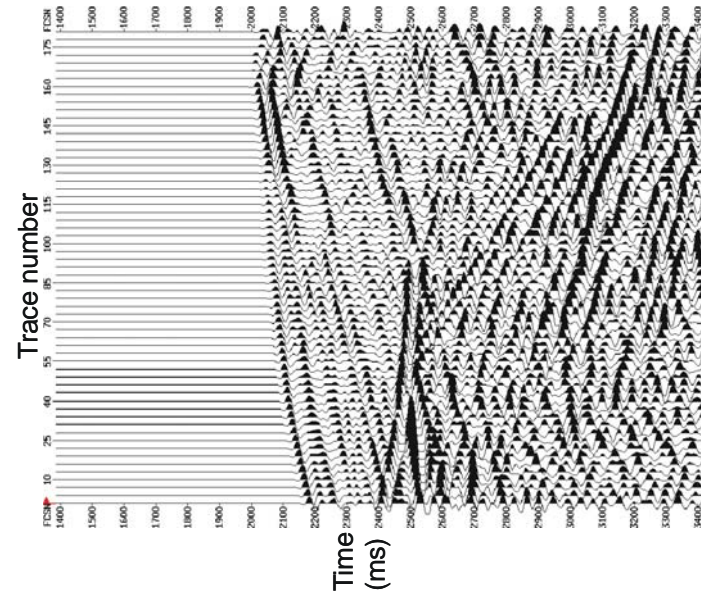


FIG. 3.5.9.a. Vertical component, far-offset common-shot gather after time scaling. Shot no. 3126, offset = 14450 ft (4405 m).

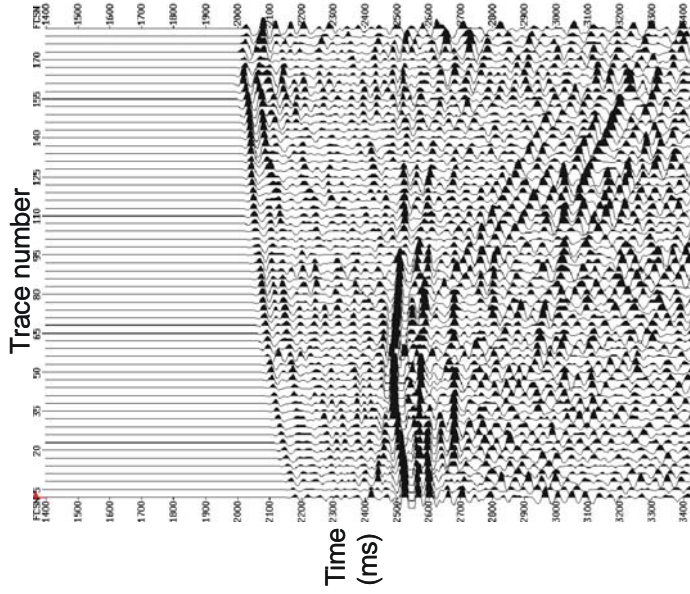


FIG. 3.5.9.b. East component, far-offset common-shot gather after time scaling. Shot no. 3126, offset = 14450 ft (4405 m).

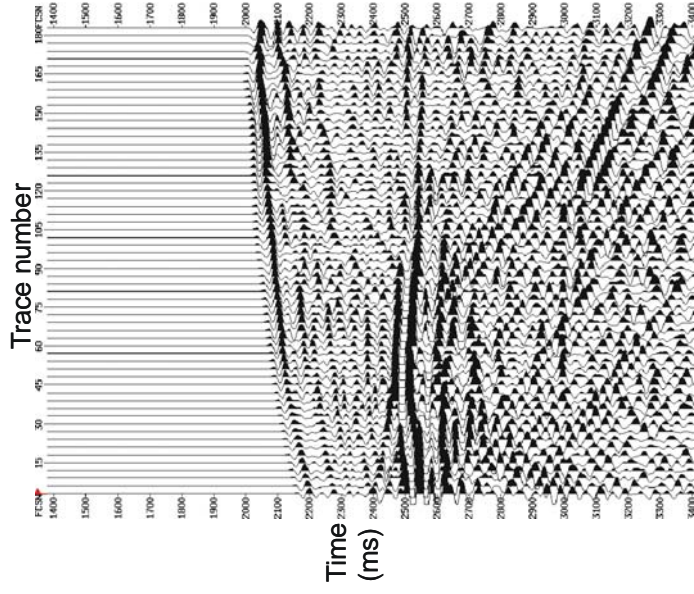


FIG. 3.5.9.c. North component, far-offset common-shot gather after time scaling. Shot no. 3126, offset = 14450 ft (4405 m).

3.6. Up-going and down-going wavefield separation

One important step during VSP processing is the separation of up-going and down-going events. The down-going waves are used to extract the source wavelet necessary for deconvolution of the up-going waves. Normally, in the case of a horizontal or slightly dipping layered medium, all reflections from the subsurface boundaries are up-going events. Since we are mainly interested in reflected energy, we should perform the separation of these events (Foster, 1988; Moon *et al.*, 1986).

At Vinton Dome, our case is different. The subsurface structure is more complicated due to the presence of the salt dome, which could modify the characteristics of reflections from the salt flank. To understand more about the implications in seismic wave propagation in the presence of steep dips, we performed a modeling study (Hoelting *et al.*, 2003). This study was based on a previous model built using a 2-D dip line through the time migrated seismic volume obtained from the surface data (Gherasim *et al.*, 2002). The dip line is oriented NW-SE including the well G-23 and the center of the salt dome (Figure 3.6.1).

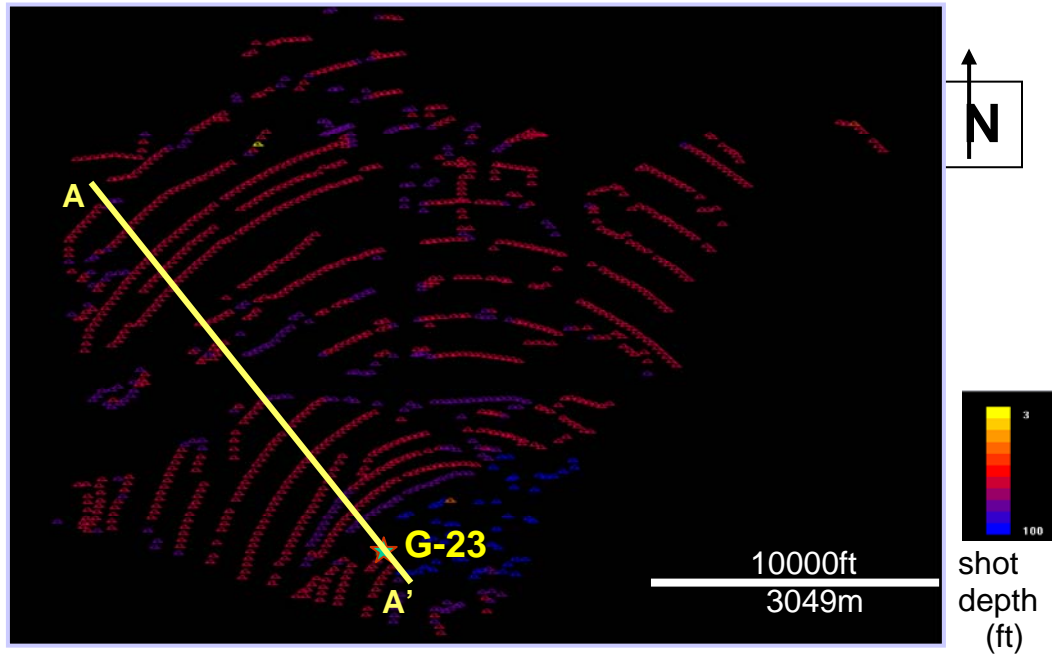


FIG. 3.6.1. Mapview of sources recorded in well G-23. AA' represents the 2-D dip line selected from the 3-D time migrated surface data to generate the depth model.

There are more than 500 wells in this area, which provide formation tops, and helped identify horizons and salt in the 3-D time migrated surface data (Figure 3.6.2).

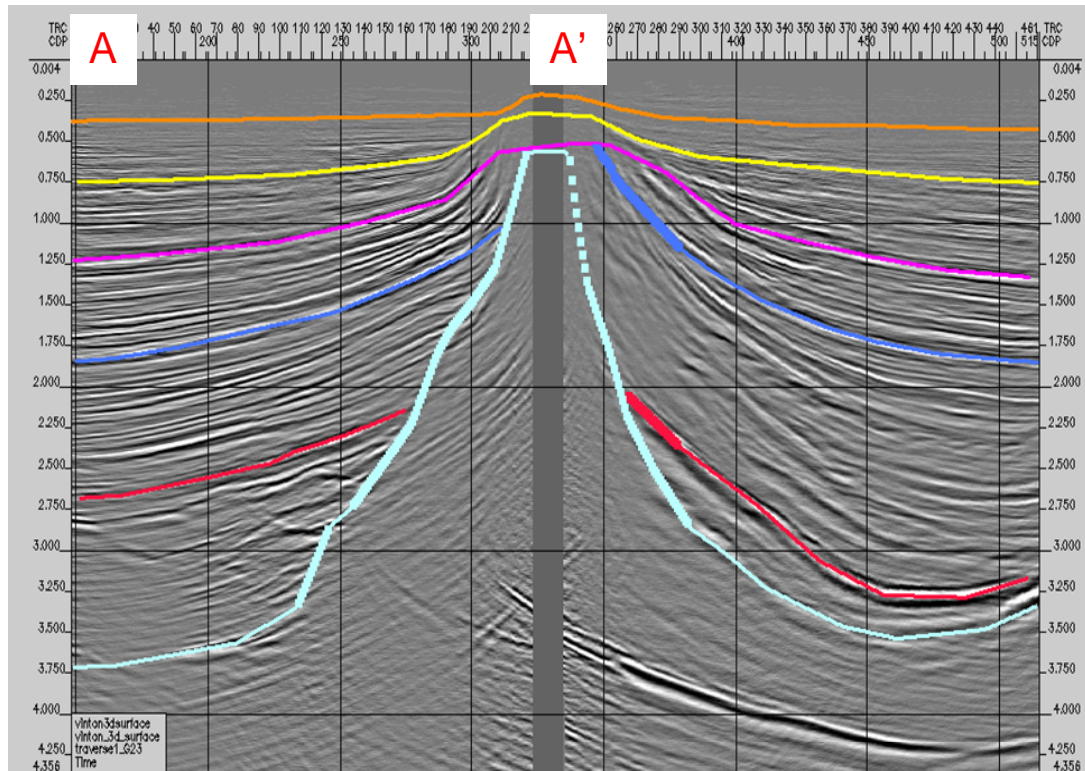


FIG. 3.6.2. 2-D seismic section along the dip-line. Picked horizons are displayed in color: Upper Miocene (orange), Upper mid-Miocene (yellow), Mid-Miocene (purple), A sand (blue), Hackberry (red), and Salt (light blue).

I exported the picks shown in Figure 3.6.2 in ASCII format and then imported into the seismic modeling software, GX-II. I calculated interval P-wave velocities from check-shot velocities. I used Castagna's equations to estimate S-wave velocities and densities. No velocity gradient has been applied. I then used these velocities to convert the time horizons from Figure 3.6.2 to depth horizons displayed in Figure 3.6.3.

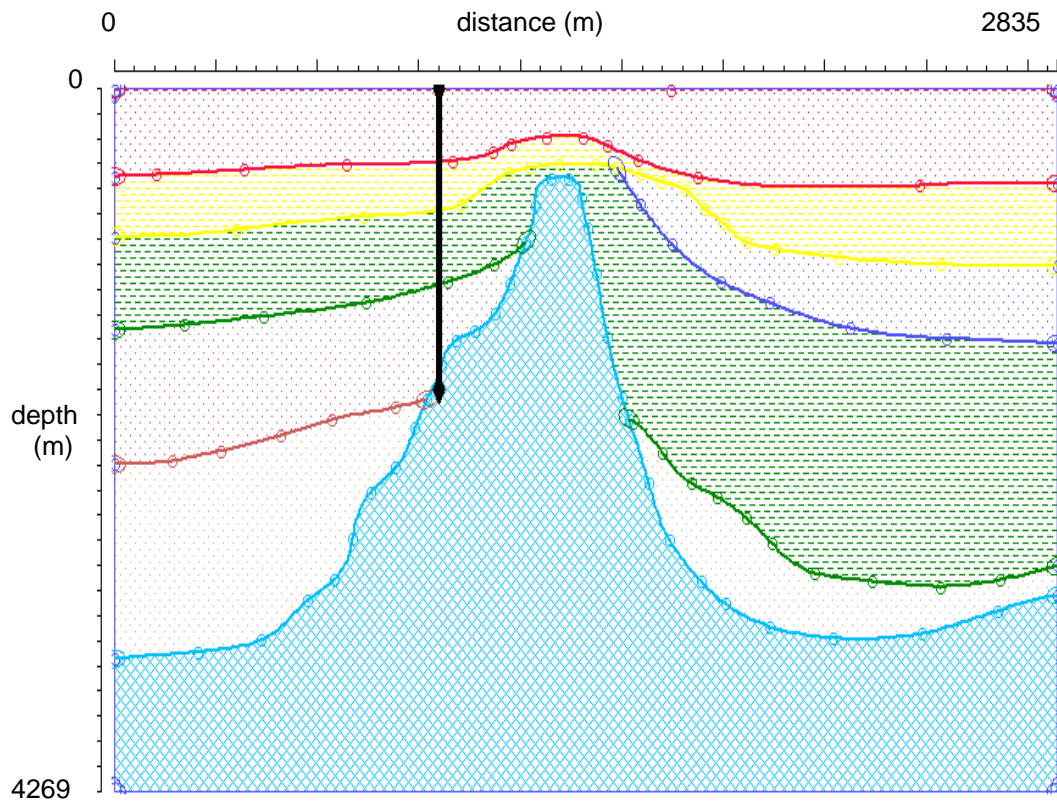


FIG. 3.6.3. 2-D depth model generated in GX-II based on the time horizons displayed in Figure 3.6.2 .

Although the salt flank has been picked on the time migrated data and there are uncertainties regarding the correct location, I can assume that our model is accurate in some part. I have information that the VSP well entered in salt around depth of 6000 ft (~1830 m), which helped me to calibrate the model. Sources were placed 60 ft (18.3 m) below the top-boundary of the model and 61 receivers were placed in the well. Common-shot gathers for vertical and horizontal components were generated in GX-II.

An interesting observation was that PP events from the salt flank are better observed on the horizontal component and PS events on the vertical component, an observation that contradicts the conventional supposition that PP reflections are observed mainly on the vertical phone and PS reflections on the horizontal phone (Figures 3.6.4 - 3.6.7).

The modeling results indicate that the salt reflection is composed of both, up-going and down-going events such that the separation into up- and down-going waves is inappropriate. The up-going/down-going separation is only necessary in case of sedimentary layers imaging.

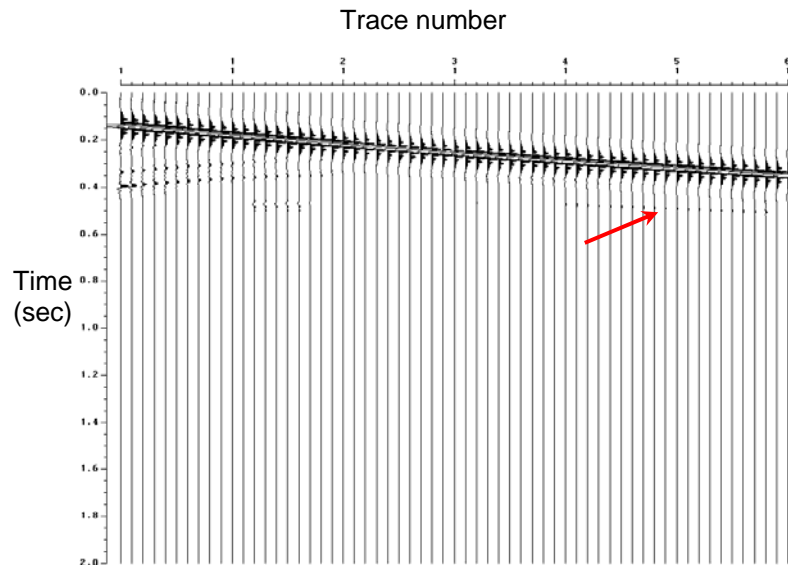


FIG. 3.6.4. Near offset common-shot gather vertical component (P and PP events only). Note the weak PP salt reflection on the deeper traces around 0.5 seconds (red arrow).

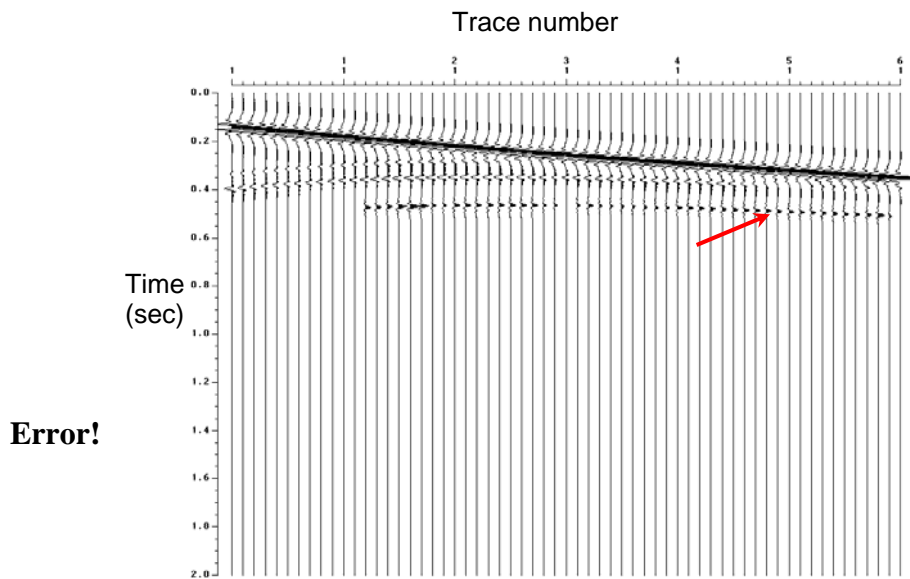


FIG. 3.6.5. Near offset common-shot gather horizontal component (P and PP events only). Note the strong PP salt reflection around 0.5 seconds (red arrow).

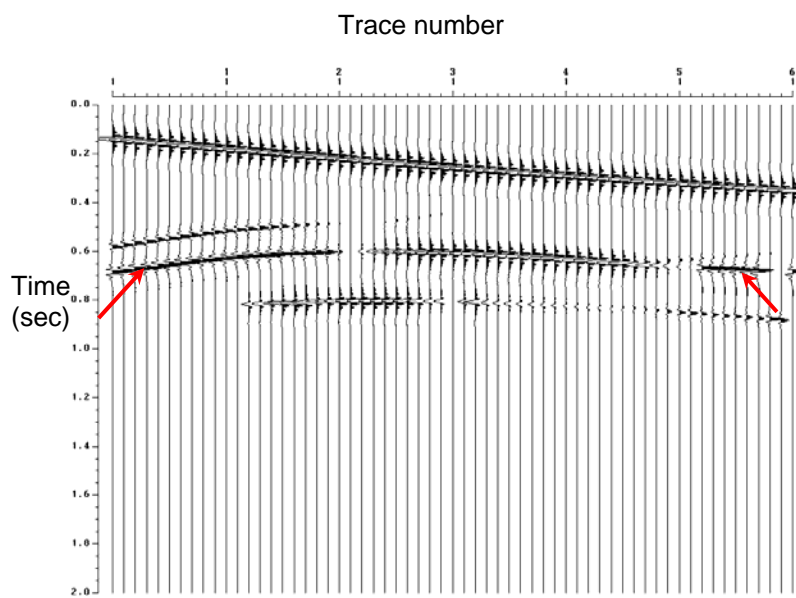


FIG. 3.6.6. Near offset common-shot gather vertical component (P and PS events only) Note the strong PS salt reflection coming around 0.7 sec (red arrows).

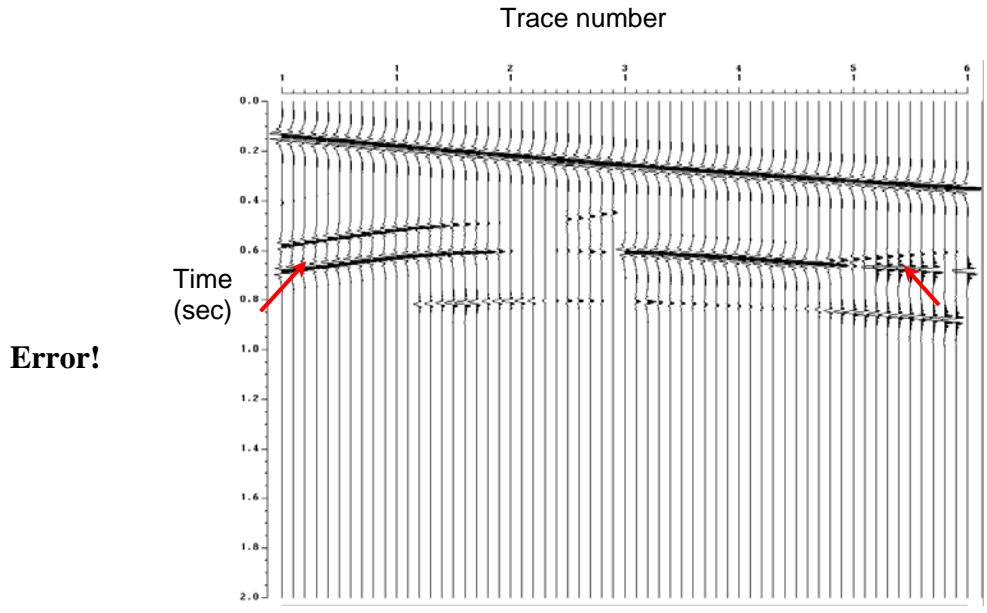


FIG. 3.6.7. Near offset common-shot gather horizontal component (P and PS events only). Note the weak PS salt reflection coming around 0.7 sec (red arrows).

4. VSP SUBSURFACE ILLUMINATION

4.1. Introduction

Seismic modeling represents an important step in data processing because it helps us understand the wavefront illumination of the subsurface. In this chapter, I describe the steps involved in building the 2-D and 3-D synthetic velocity models corresponding to the Vinton Dome area. The goal of this modeling project is to understand the impact of the acquisition geometry on subsurface illumination and migration.

4.2. 2-D Velocity model building

The first step in the modeling process consists of analyzing the 3-D surface pre-stack depth migrated data (Duncan, 2005) and interpreting three major horizons and the salt flank. I display a mapview of the shallowest interpreted horizon in Figure 4.2.1 indicating the VSP area by the maroon square. I also display a 2-D vertical section through the migrated volume (Figure 4.2.2) marked by the blue line in Figure 4.2.1 that passes through the VSP well.

The second step consists of modeling the structure using a commercial modeling package based on the previous information we have about the study area, which indicates the presence of the salt dome at the southeast end of the VSP survey. The 2-D model consists of 4 sedimentary layers onlapping the salt dome. I selected the P-wave velocity

values based on a velocity model provided by my colleague, Warren Duncan (Duncan, 2005). I derived the S-wave velocity and density values from the V_p values using Castagna's and Greenberg's relations. V_p , V_s and density values are constant in each layer.

For sandstone:

$$V_s = -0.856 + 0.804 \cdot V_p, \text{ and} \quad (4.2.1.a)$$

$$\rho = 0.200 \cdot V_p^{0.261}. \quad (4.2.1.b)$$

I show V_p and V_s velocity models in Figure 4.2.3 - 4.2.4. The 2-D model is 18000 ft (5488 m) long and 8000 ft (2439 m) deep.

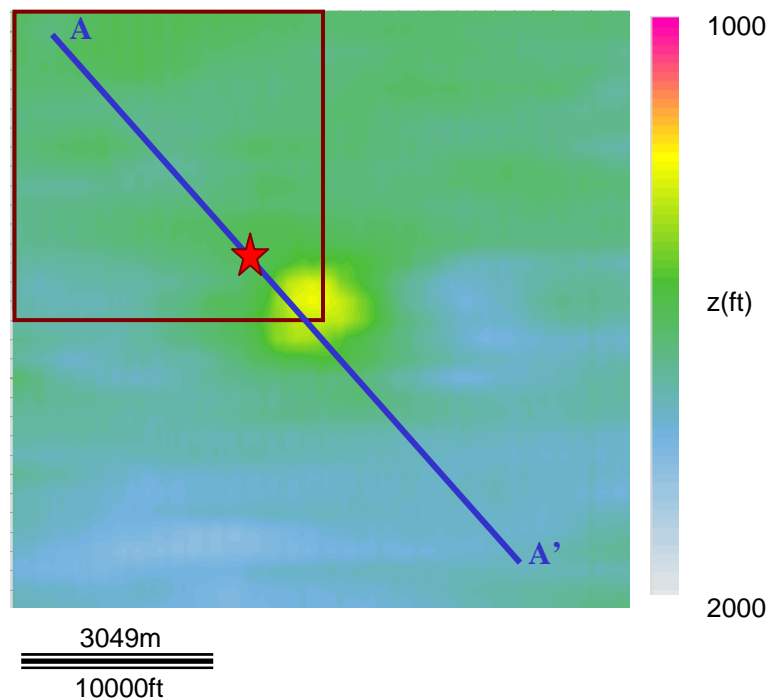


FIG. 4.2.1. Mapview of the shallowest picked sedimentary boundary, colored by depth. The maroon square marks the location of the VSP Vinton survey, the red star indicates the VSP well and the blue line marks the location of the 2-D vertical section displayed in Figure 4.2.2.

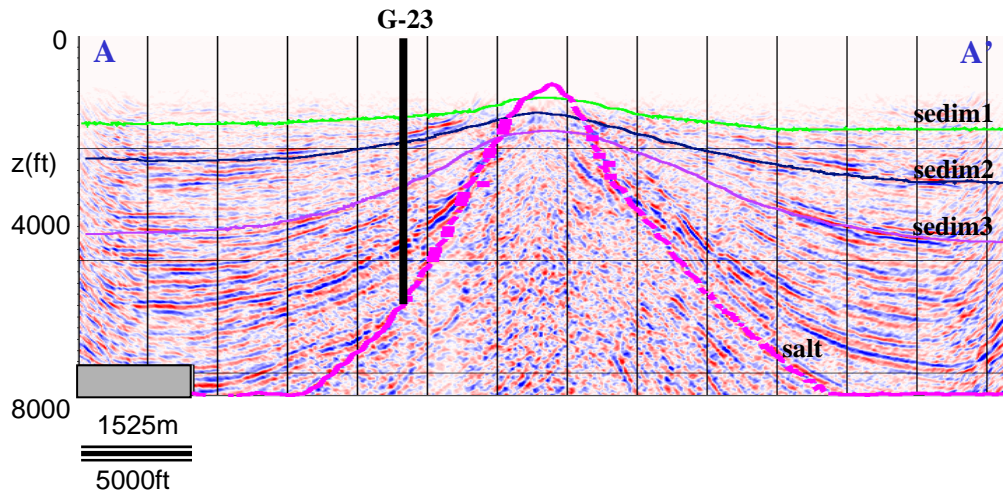


FIG.4.2.2. 2-D vertical section through the 3-D surface pre-stack depth migrated volume. I display four interpreted horizons: three sedimentary boundaries and the top of salt.

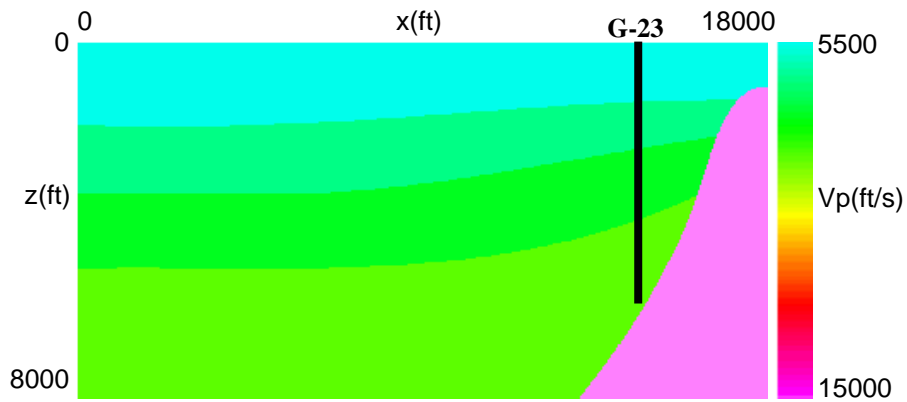


FIG. 4.2.3. 2-D P-wave velocity model, colored by P-wave velocity. The solid black line indicates the VSP well location.

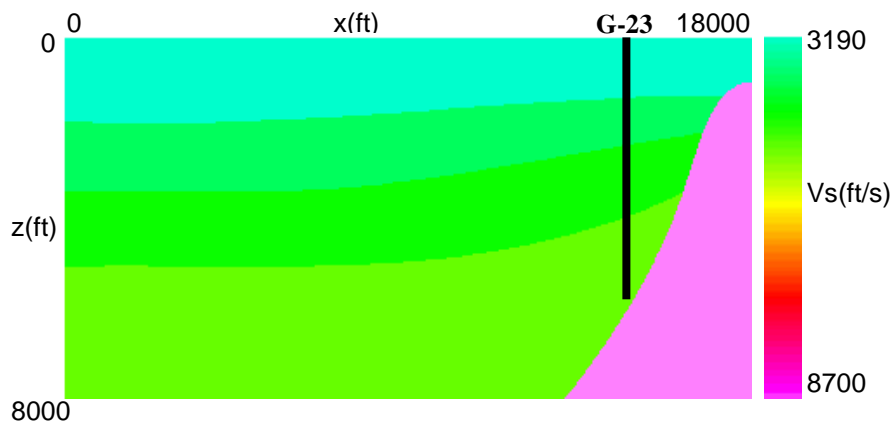


FIG. 4.2.4. 2-D S-wave velocity model, colored by S-wave velocity. The solid black line indicates the VSP well location.

4.3. 2-D VSP subsurface illumination via ray-tracing

A near-offset VSP only provides illumination limited to the well location. For this reason, walk-away VSPs were designed to improve lateral subsurface illumination (Dillon, 1988).

The first part of the VSP subsurface illumination study consists of modeling synthetic data via ray-tracing. I generated 2-D VSP synthetic shot-gathers to simulate geometry that mimicks field data. The Vinton VSP data were recorded using shots located on concentric circles over the salt dome. A quick examination of the Vinton survey acquisition map indicates that the sources, marked by triangles, are very closely spaced along the circular arcs and quite coarsely spaced along the radial direction (Figure 4.3.1).

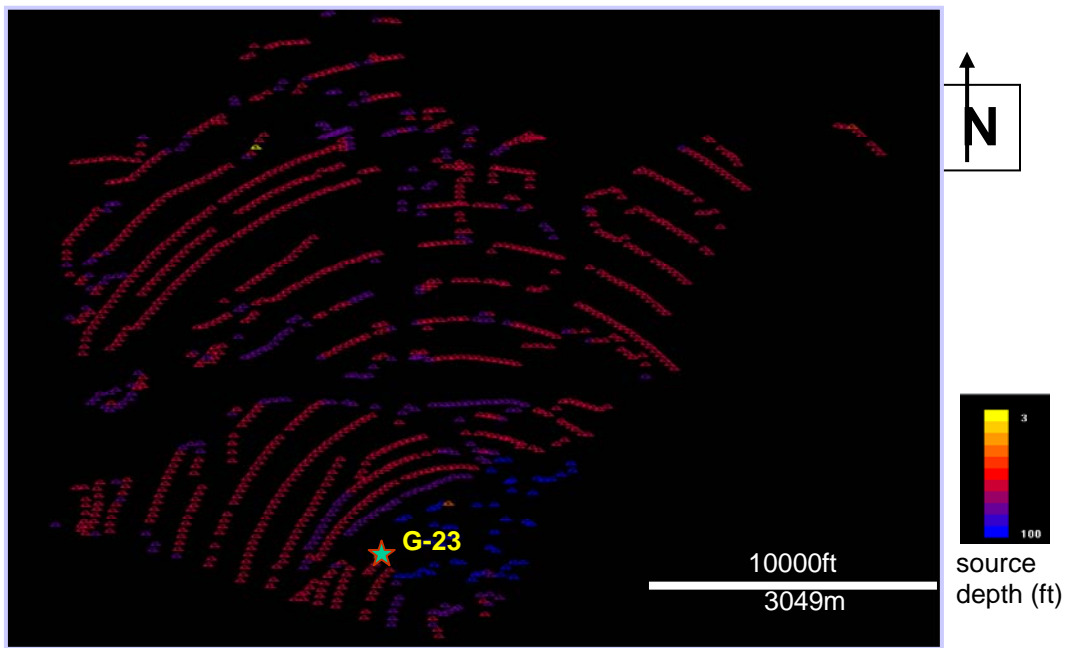


FIG. 4.3.1. Mapview of sources recorded in VSP well G-23. Color bar is shown on the lower right corner of the mapview.

Since the 2-D velocity model follows a radial line with respect to the dome, I used a set of 14 sources coarsely spaced, 1000 ft (304 m) apart, to generate the synthetics. I display the source locations on the 2-D velocity model in Figure 4.3.2.

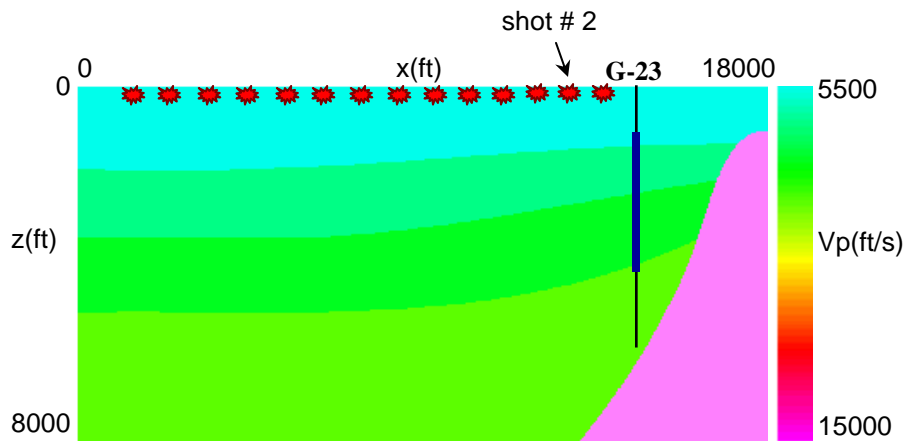


FIG. 4.3.2. Source locations used to generate the synthetics. There are 14 sources marked by the red stars, 1000 ft apart. The solid blue line indicates the receiver location in the VSP well.

I modeled PP and PS reflections for vertical and horizontal components for shot no. 2. Shot no. 2 is the 2nd closest one from the well. There are 61 receivers in the well, located between 943 ft (287 m) and 3943 ft (1202 m), with 50 ft (15 m) group spacing. Figures 4.3.3 – 4.3.4 show the PP and PS reflection rays overlaying the velocity model. I immediately recognized that PP and PS rays illuminate only a small portion of the sedimentary boundaries around the well. However, I noticed a quite good illumination of the salt flank partially due to the steepness of the boundary. A careful examination of the results indicates that PS reflections provide a slight better salt flank illumination than the PP reflections.

Ray tracing indicates that the salt flank reflection is composed of both up- and down-going events, which indicates that the up-/down-going wave separation is inappropriate prior to migration.

Next, I modeled a group of 14 shots (Figure 4.3.2) having 1000 ft (305 m) shot spacing, which improved the lateral illumination of the sedimentary boundaries. As we can see from Figures 4.3.5 – 4.3.6, the PP and PS rays cover a larger area around the VSP well compared to the single shot case. Note the smaller subsurface illumination provided by the PS rays.

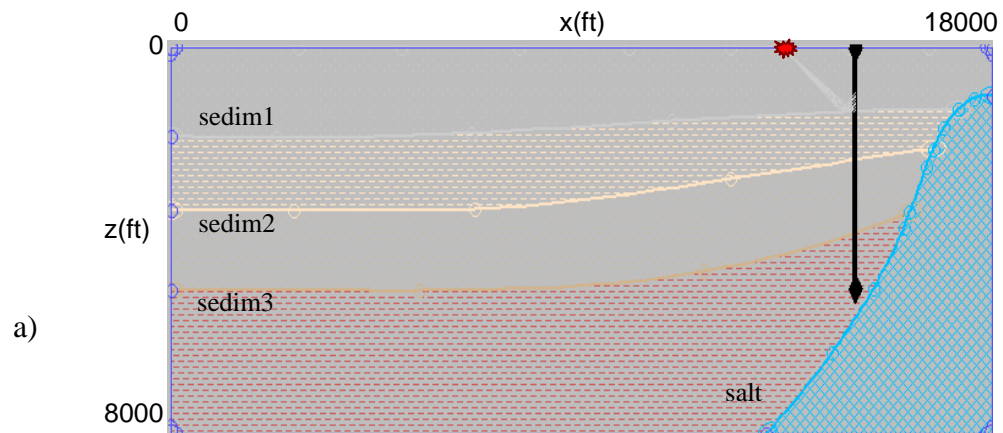


FIG. 4.3.3. PP reflection rays corresponding to shot no. 2, offset = 1605 ft (490 m). Note how only the geophones placed above the boundary intercept the reflected rays. Also note the good salt flank illumination compared to the more limited sediment illumination.

a) Reflections corresponding to the first sedimentary boundary (sedim 1); b) Reflections corresponding to the second sedimentary boundary (sedim 2); c) Reflections corresponding to the third sedimentary boundary (sedim 3); d) Reflections corresponding to the salt flank (salt).

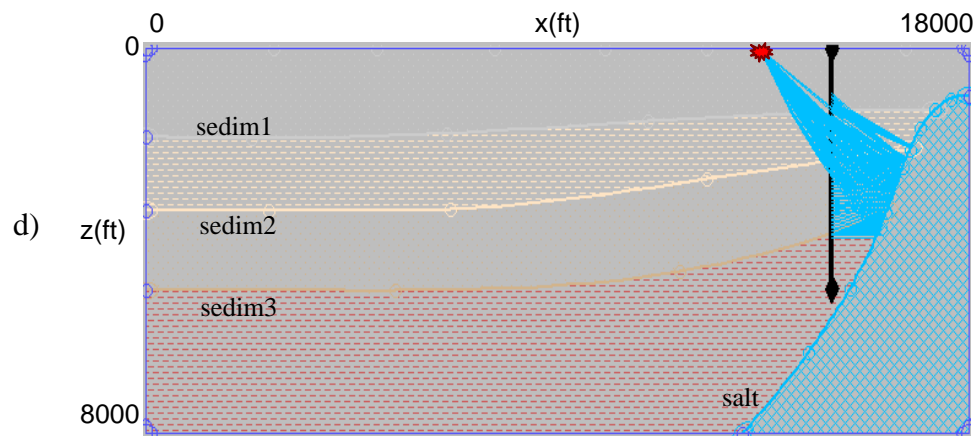
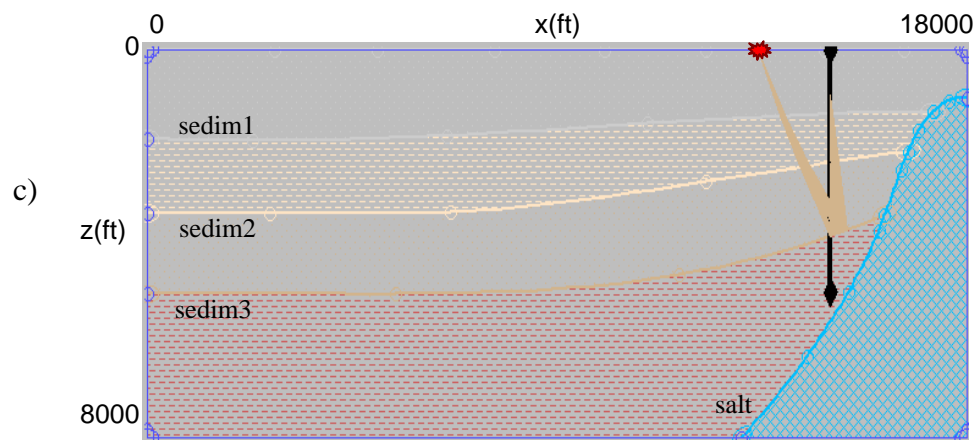
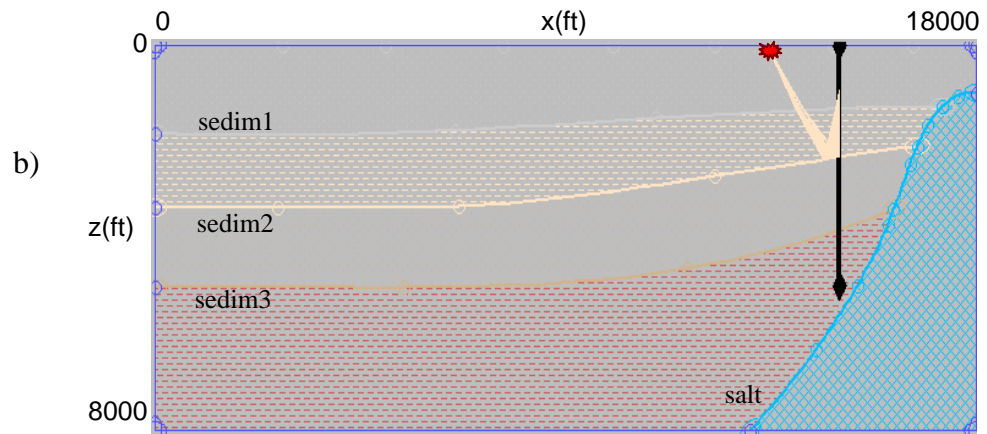


FIG. 4.3.3. (continued)

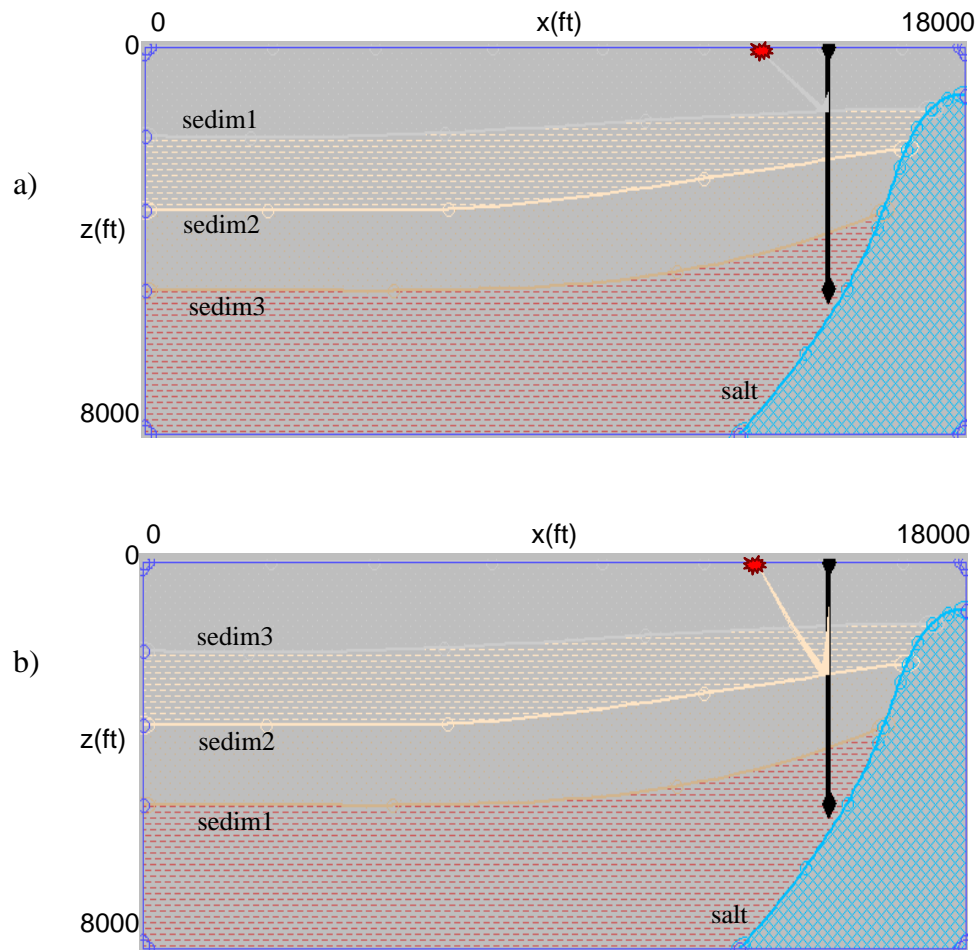


FIG. 4.3.4. PS reflection rays corresponding to shot no. 2, offset = 1605 ft (490 m). Note how only the geophones placed above the boundary intercept the reflected rays. The lateral extent of boundary illumination is much smaller than for the PP case. Also, note the PS salt flank illumination is slightly improved compared to the PP rays case. a) Reflections corresponding to the first sedimentary boundary (sedim 1); b) Reflections corresponding to the second sedimentary boundary (sedim 2); c) Reflections corresponding to the third sedimentary boundary (sedim 3); d) Reflections corresponding to the salt flank (salt).

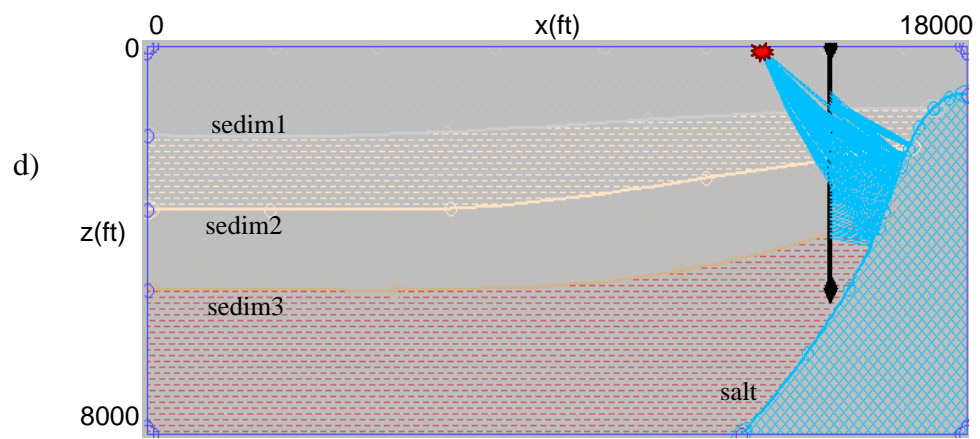
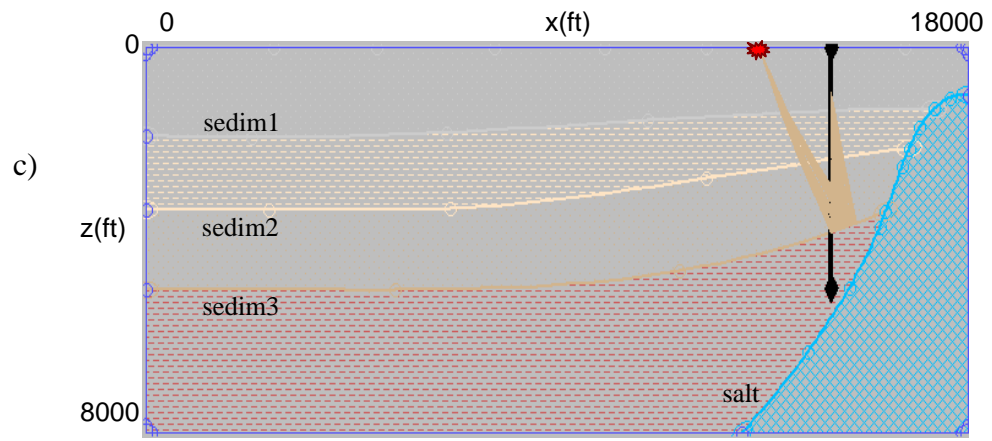


FIG. 4.3.4. (continued)

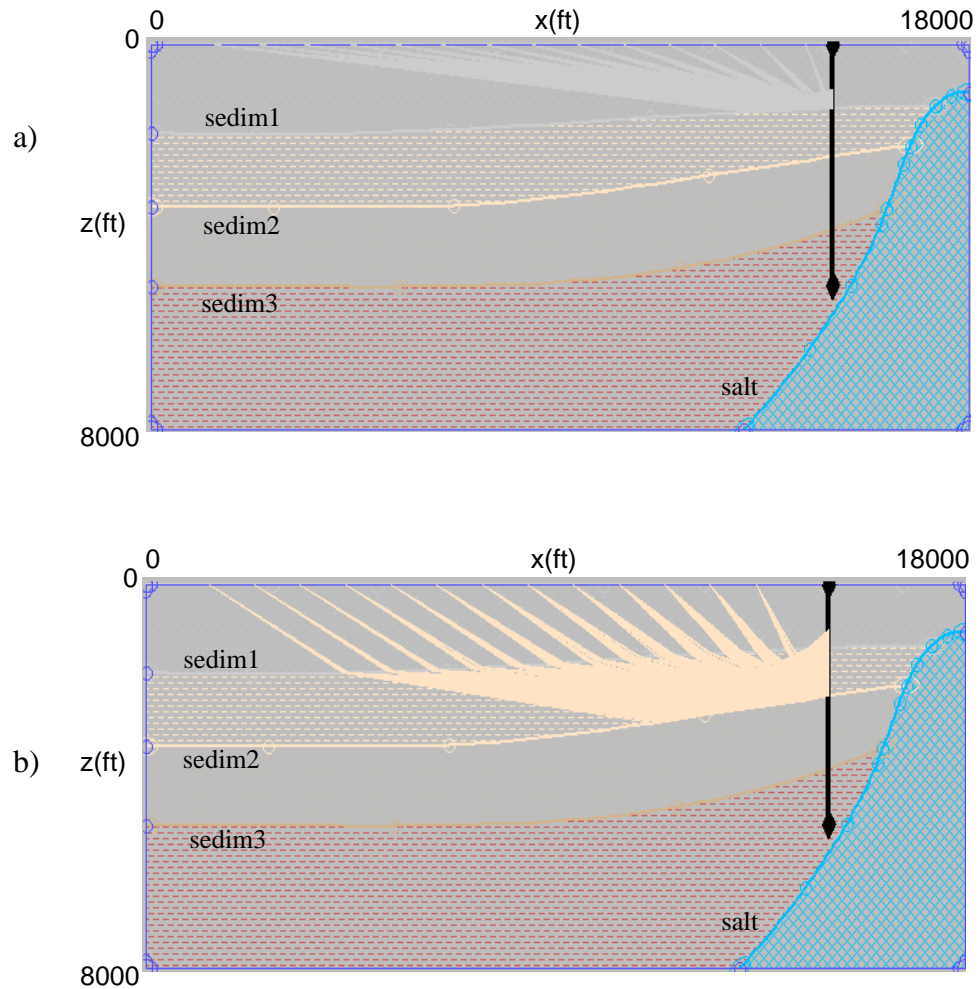


FIG. 4.3.5. PP reflection rays corresponding to a group of 14 shots. Note how the extent of subsurface illumination is greatly improved.

a) Reflections corresponding to the first sedimentary boundary (sedim 1); b) Reflections corresponding to the second sedimentary boundary (sedim 2); c) Reflections corresponding to the third sedimentary boundary (sedim 3); d) Reflections corresponding to the salt flank (salt). Note how the farthest shot refracts through the lowermost layer (sedim 3) at a very high angle in order to reach the salt flank (salt). Red circle marks the refraction point. For this reason, imaging the salt flank from long offset shots will be very sensitive to an incorrect velocity depth model.

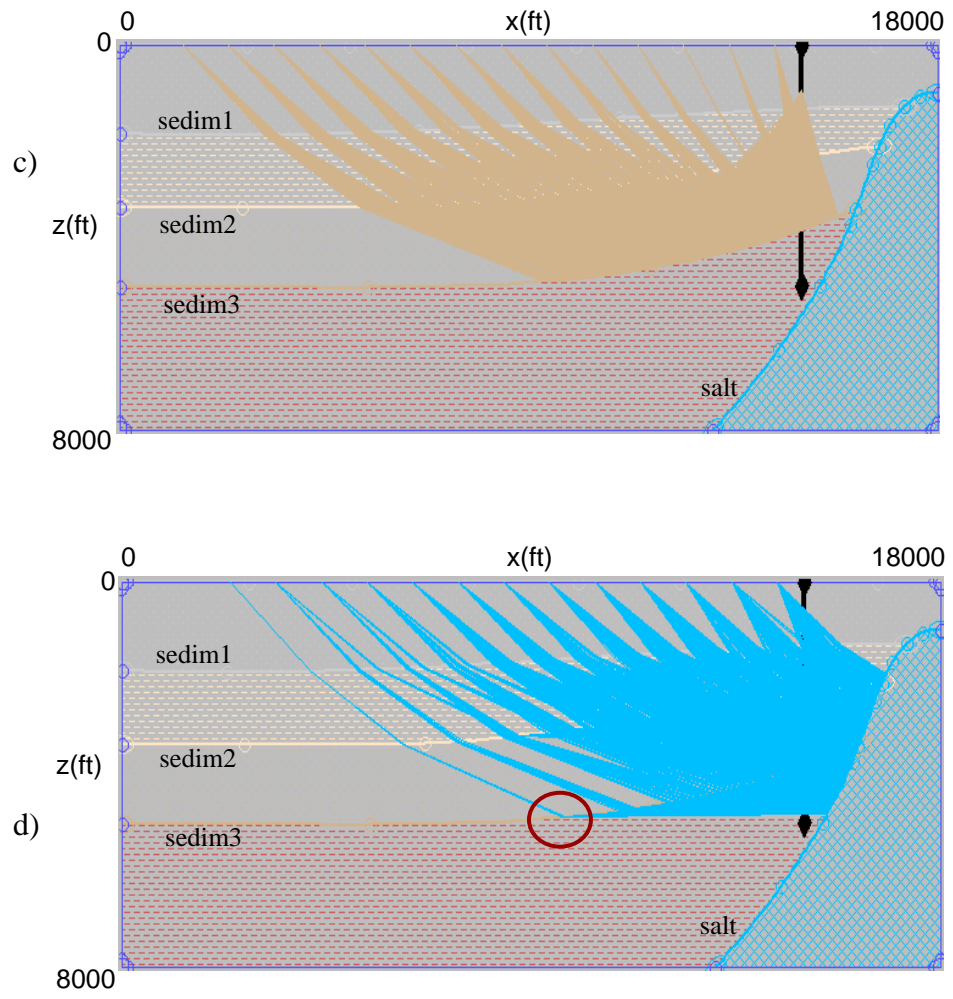


FIG. 4.3.5. (continued)

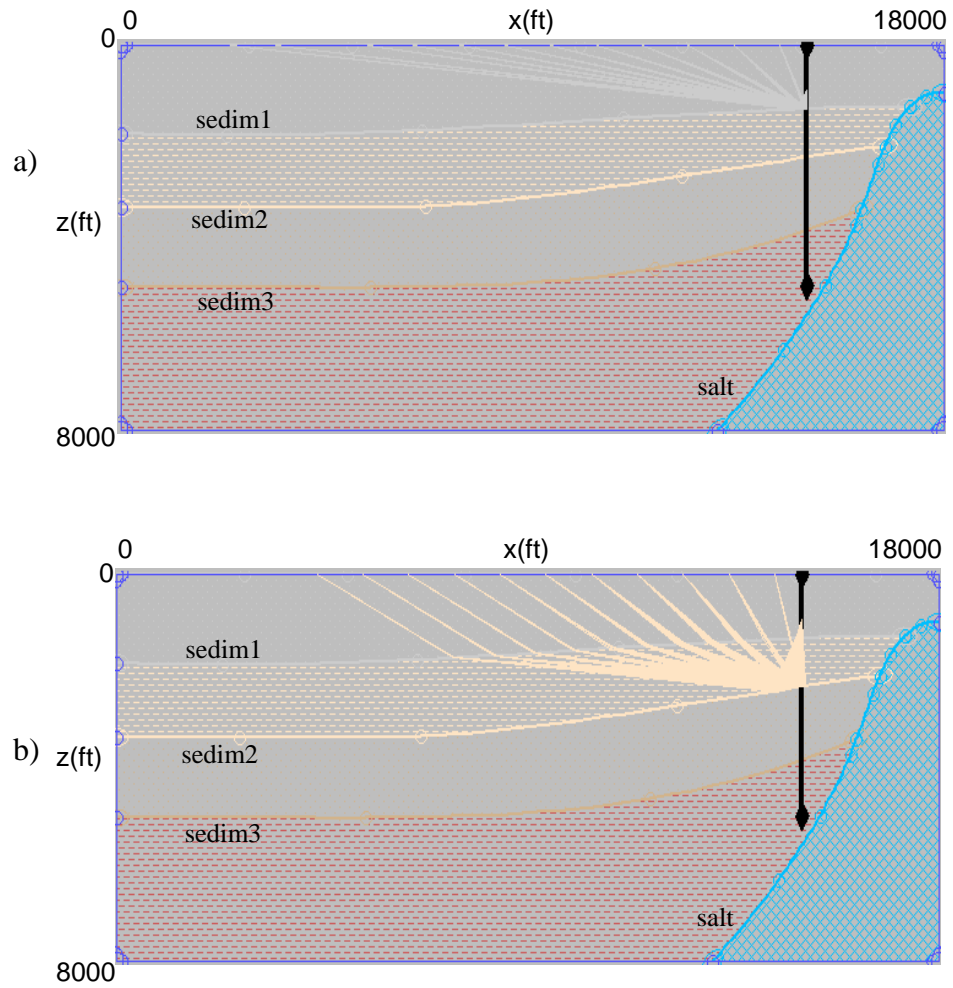


FIG. 4.3.6. PS reflection rays corresponding to a group of 14 shots. Note how the extent of subsurface illumination is greatly improved.

a) Reflections corresponding to the first sedimentary boundary (sedim 1); b) Reflections corresponding to the second sedimentary boundary (sedim 2); c) Reflections corresponding to the third sedimentary boundary (sedim 3); d) Reflections corresponding to the salt flank (salt).

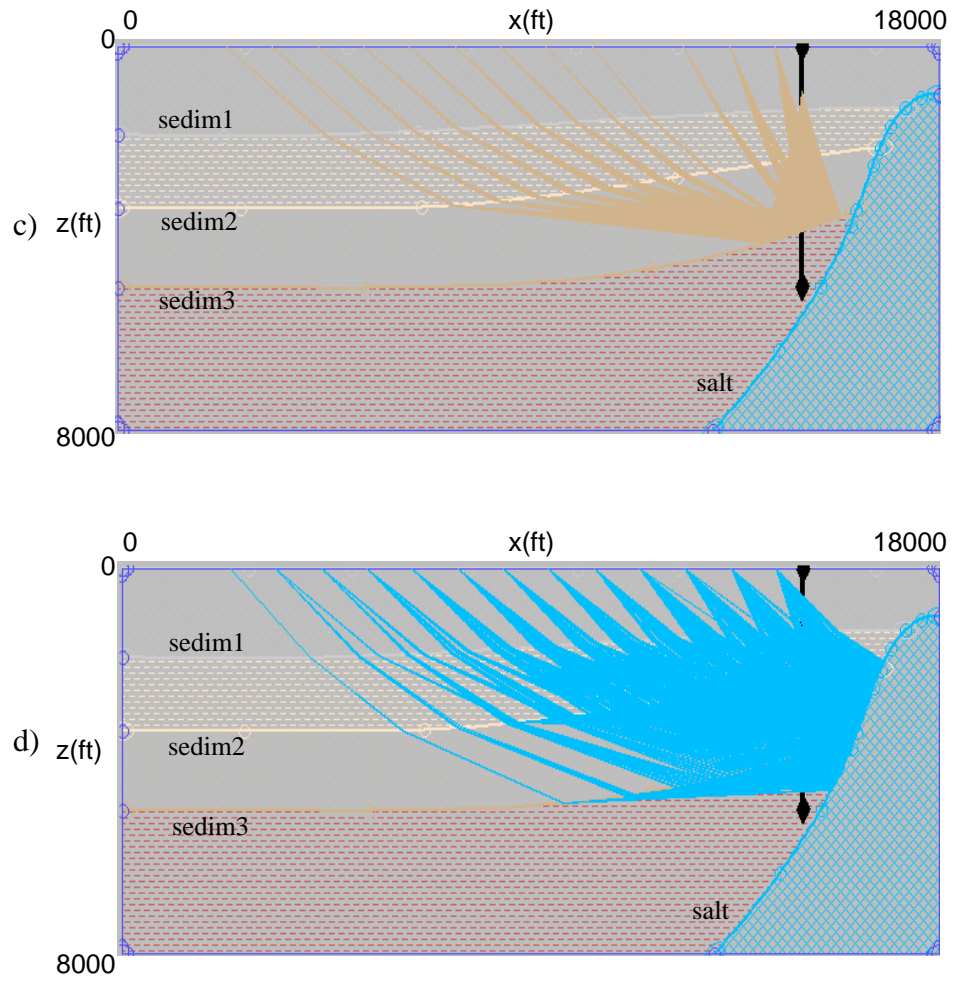


FIG. 4.3.6. (continued)

4.4. 2-D VSP subsurface illumination via elastic pseudospectral modeling

The second part of the VSP subsurface illumination study consists of modeling 2-D synthetic VSP data via an in-house elastic pseudo-spectral modeling algorithm. I modeled two shots selected from the group of shots described in the previous section. The multicomponent receiver array is located between 943 ft (287 m) and 3943 ft (1202 m), with 50 ft (15 m) group spacing. I present the acquisition geometry in Figure 4.4.1. Red stars indicate the shot locations while the solid blue line indicates the receiver array from the VSP well.

I first display snapshots of wavefront propagation recorded at 0.25 sec interval for the near-offset shot in Figures 4.4.2 – 4.4.3. This algorithm provides both vertical and horizontal components shot-gathers as well as snapshots in time that allow us to study the wavefront propagation in the subsurface. Analysis of the snapshots for both components indicates that there is a relatively good illumination of the sedimentary boundaries but only the portions of the reflected wavefront propagating towards the VSP well are recorded. This limitation of the VSP subsurface illumination to areas around the VSP well agrees with the ray-traced data. However, the PS wavefront seems to illuminate an area similar to the PP wavefront. Only the portion of the wavefront reflected from the salt flank area located at the level of receiver array is recorded.

One problem for the elastic pseudo-spectral modeling arises from the fact that by solving the wave equation on the grid we convert the smooth salt flank into a “stair-step”

surface. This “stair-step” shape of the salt flank will generate artificial reflections at every grid point (Figure 4.4.4), reflections that might generate migration artifacts.

Next, I present snapshots of wavefront propagation recorded at 0.5 sec interval for the far-offset shot in Figures 4.4.5 – 4.4.6. Note that this shot illuminates different areas of the sedimentary boundaries compared to the near-offset shot.

For convenience, I marked the direct P and S wavefronts with dark and light red arrows, the S* wave mode with yellow arrow, the PP and PS sediment reflections with dark and light green arrows and the PP and PS salt flank reflections with dark and light blue arrows, and the PP and PS artificial boundary reflections with pink arrows. The S* mode is considered to be a PS conversion due to a boundary located very close to the surface.

Both 2-D VSP studies provided similar conclusions regarding the extent of the lateral subsurface illumination. Sediments and salt flank reflections are about the same but diffractions and head-waves are poorly modeled by ray theory. For this reason, we need to generate synthetics by using wave equation solutions in order to calibrate the migration algorithms.

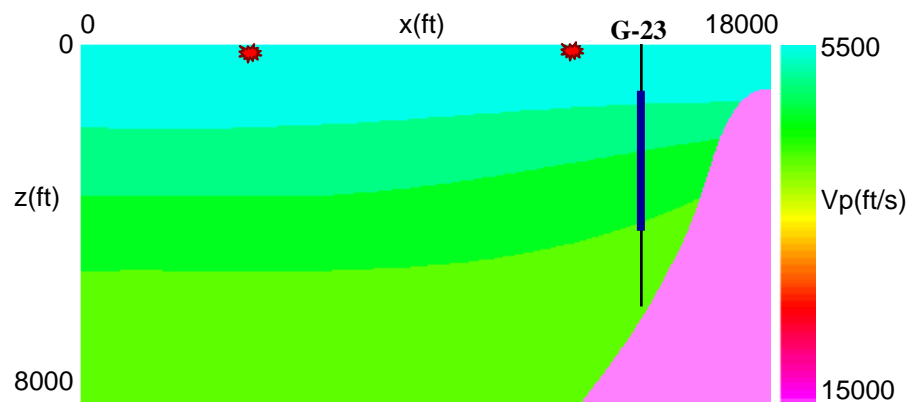


FIG. 4.4.1. 2-D P-wave velocity model used to perform elastic pseudo-spectral modeling. The red stars represent the shot locations and the solid blue line indicates the receiver location in the VSP well.

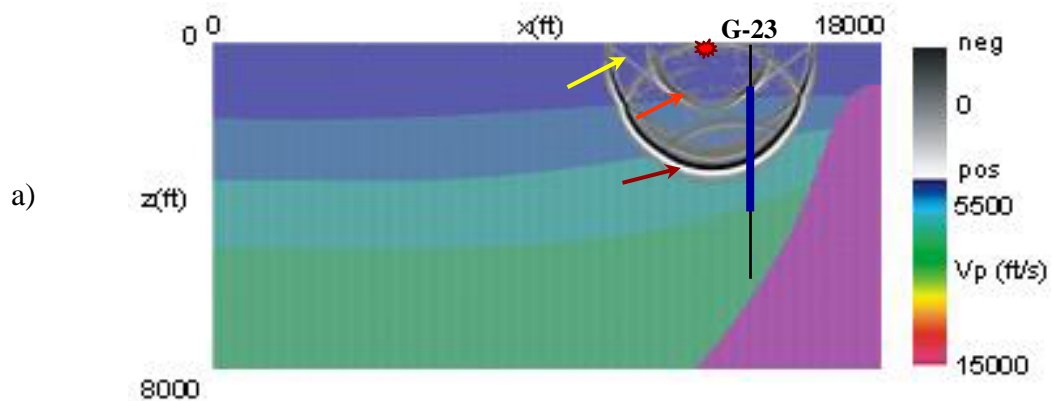


FIG. 4.4.2. Near-offset shot # 2 snapshots, vertical component, overlying the P-wave velocity model. The solid blue line indicates the receiver location in the VSP well. Dark and light red arrows points to the direct P and S wavefronts, yellow arrow points to the S* mode, dark and light green arrow points to the PP and PS sediment reflections, and dark and light blue arrows points to the PP and PS salt flank reflections. Snapshots at: a) 0.5 sec; b) 0.75 sec; c) 1.0 sec; d) 1.25 sec; e) 1.5 sec.

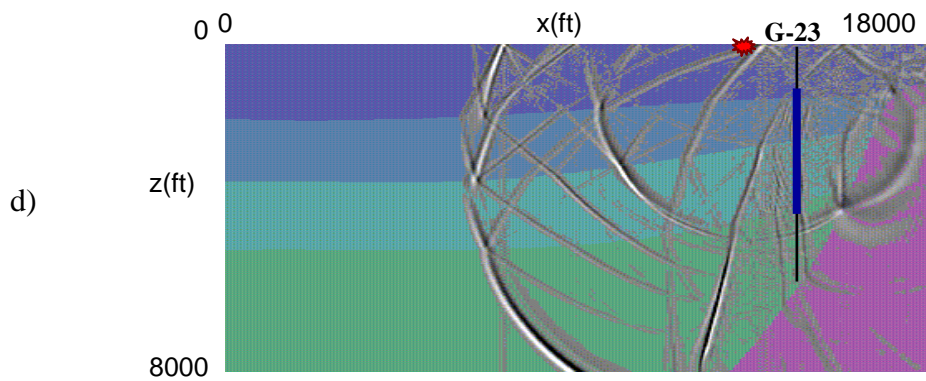
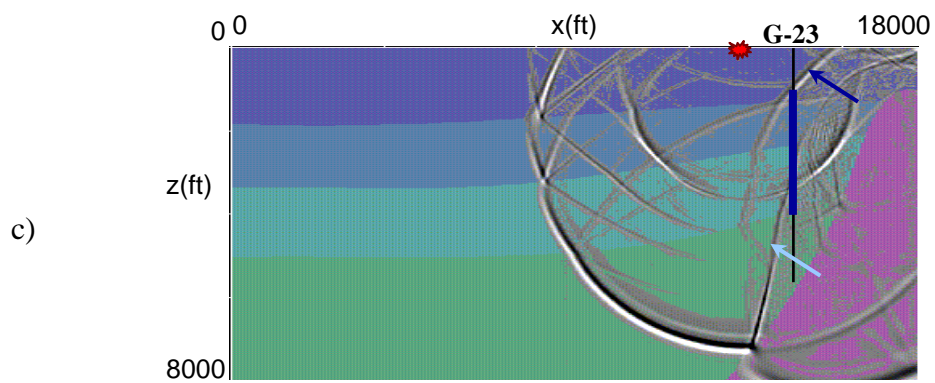
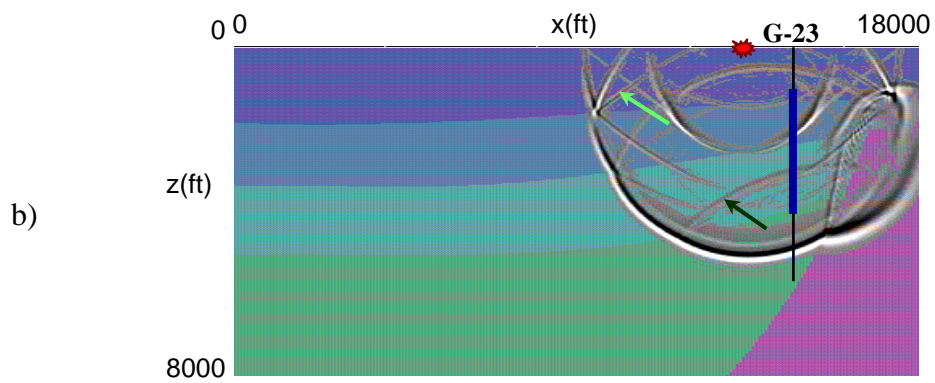


FIG. 4.4.2. (continued)

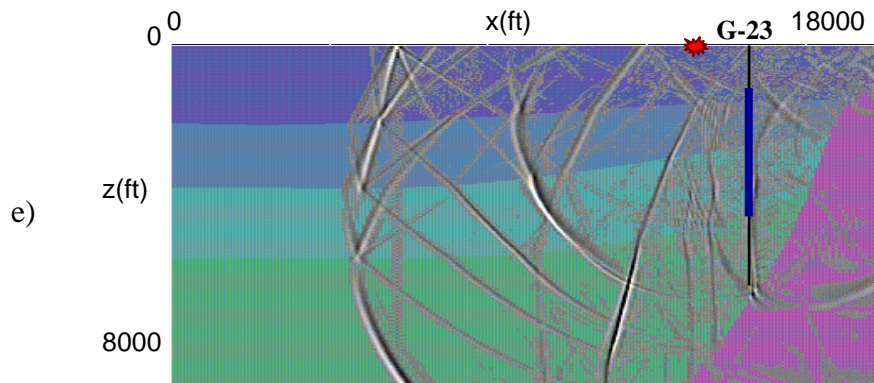


FIG. 4.4.2. (continued)

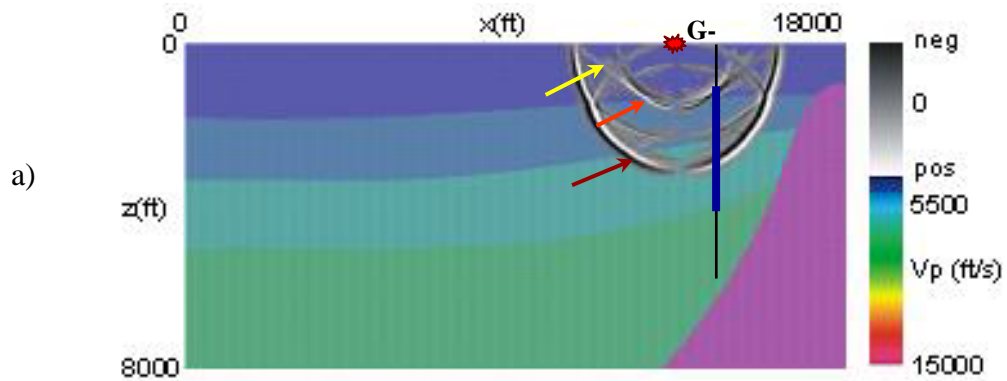


FIG. 4.4.3. Near-offset shot # 2 snapshots, horizontal component, overlying the P-wave velocity model. The solid blue line indicates the receiver location in the VSP well. Dark and light red arrows points to the direct P and S wavefronts, yellow arrow points to the S^* mode, dark and light green arrow points to the PP and PS sediment reflections, and dark and light blue arrows points to the PP and PS salt flank reflections. Snapshots at: a) 0.5 sec; b) 0.75 sec; c) 1.0 sec; d) 1.25 sec; e) 1.5 sec.

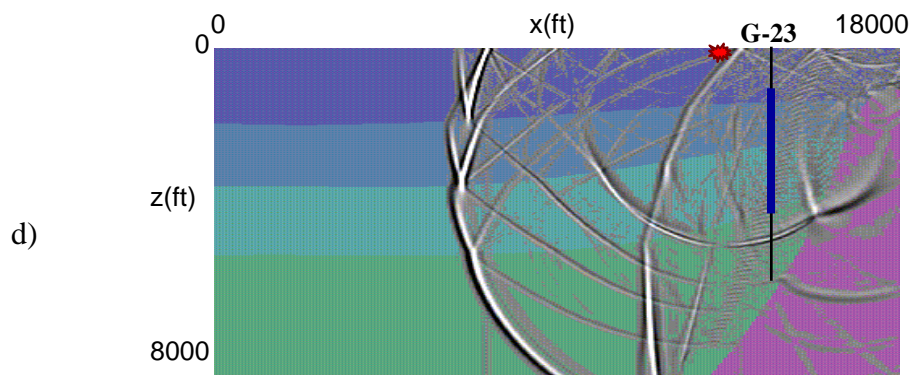
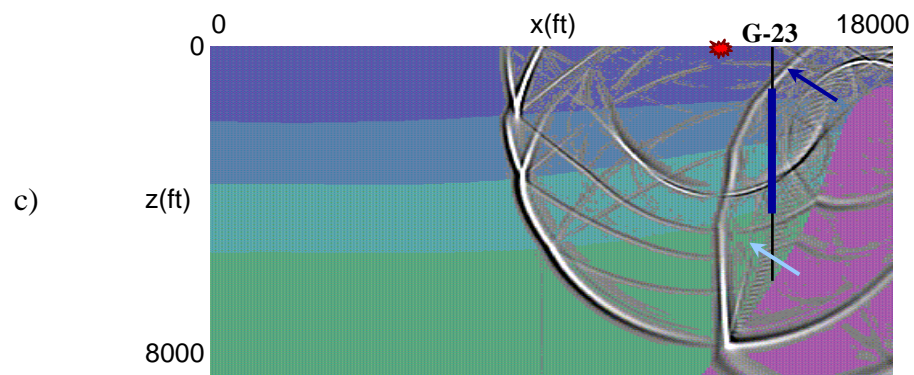
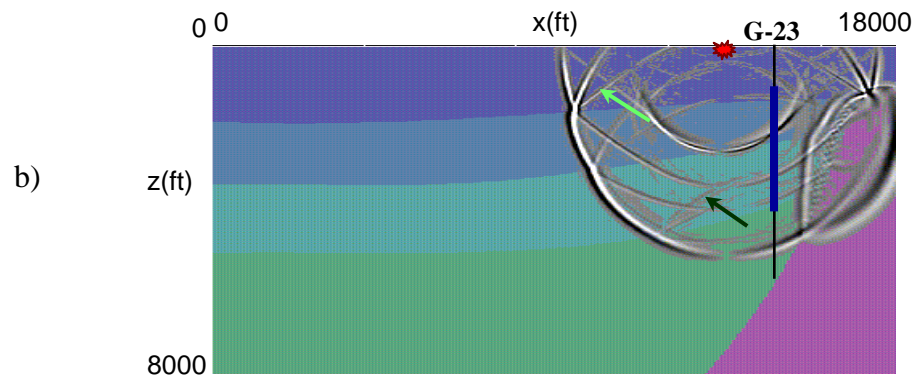


FIG. 4.4.3. (continued)

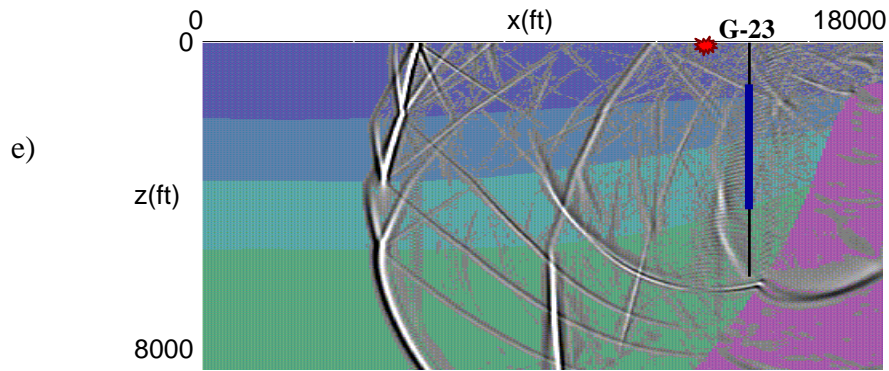


FIG. 4.4.3. (continued)

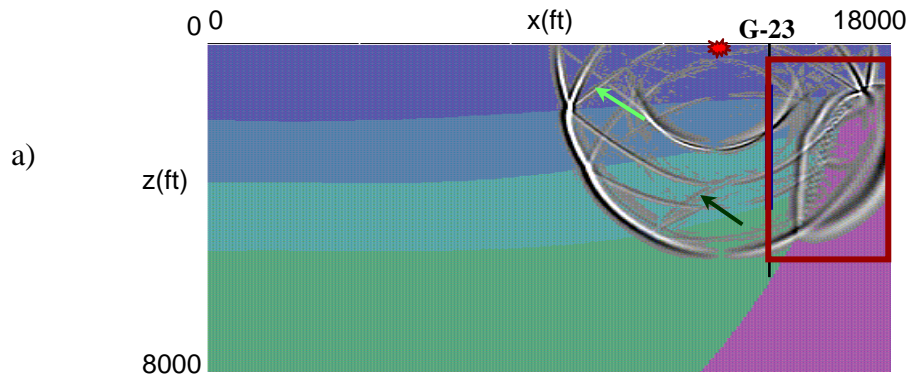


FIG. 4.4.4. a) Snapshot at 0.75 sec for near-offset shot # 2, horizontal component, overlying the P-wave velocity model. The red rectangle marks an area containing the artificial reflections generated by the “stair-step” shape of the salt flank. b) Zoom of the red rectangle area from Figure 4.4.4.a. The red arrows mark the artificial salt flank reflections.

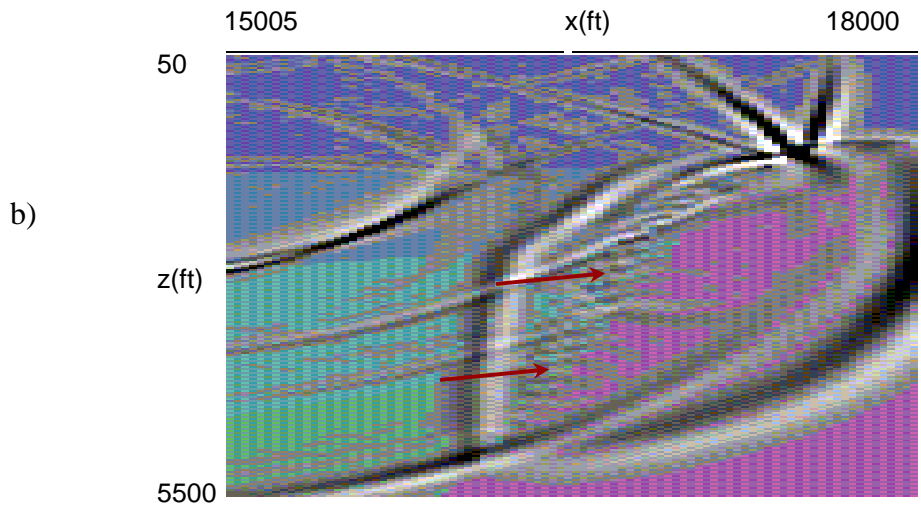


FIG. 4.4.4. (continued)

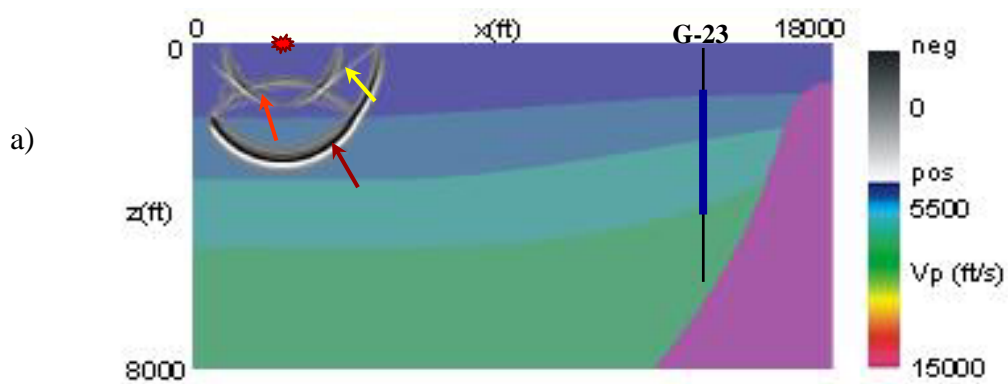


FIG. 4.4.5. Far-offset shot snapshots, vertical component, overlaying the P-wave velocity model. The solid blue line indicates the receiver location in the VSP well. Dark and light red arrows points to the direct P and S wavefronts, yellow arrow points to the S^* mode, dark and light green arrow points to the PP and PS sediment reflections, and dark and light blue arrows points to the PP and PS salt flank reflections. Snapshots at: a) 0.5 sec; b) 1.0 sec; c) 1.5 sec; d) 2.0 sec; e) 2.5 sec.

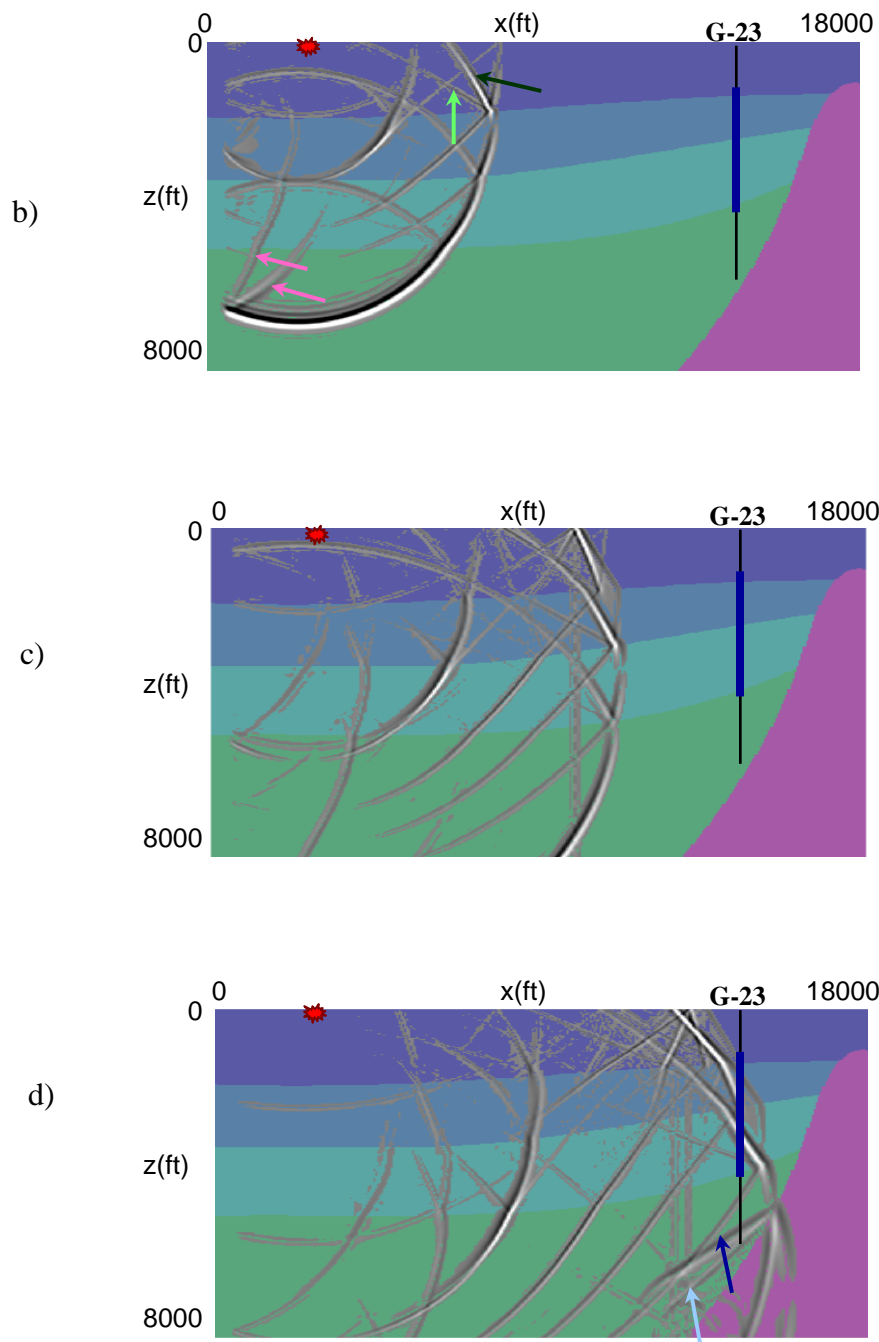


FIG. 4.4.5. (continued)

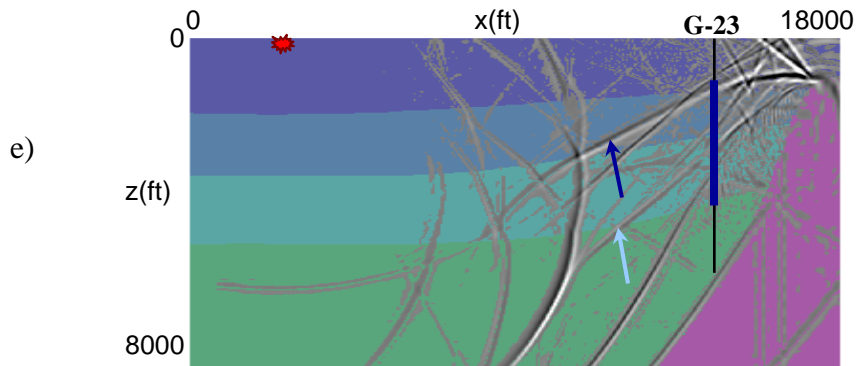


FIG. 4.4.5. (continued)

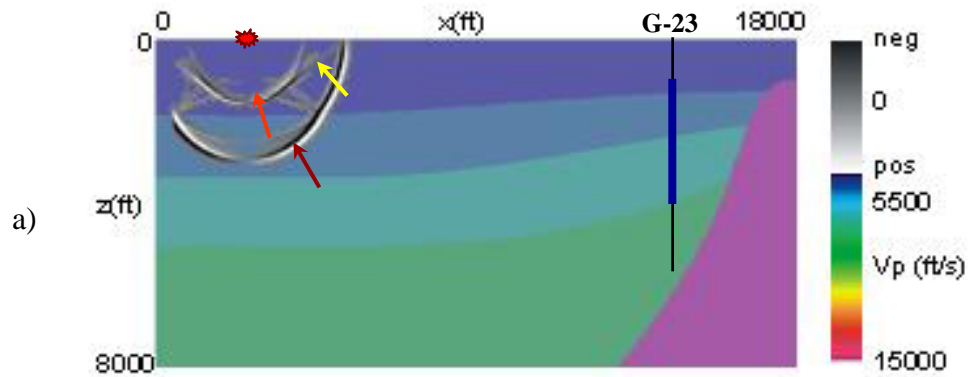


FIG. 4.4.6. Far-offset shot snapshots, horizontal component, overlying the P-wave velocity model. The solid blue line indicates the receiver location in the VSP well. Dark and light red arrows points to the direct P and S wavefronts, yellow arrow points to the S^* mode, dark and light green arrow points to the PP and PS sediment reflections, and dark and light blue arrows points to the PP and PS salt flank reflections. Snapshots at: a) 0.5 sec; b) 1.0 sec; c) 1.5 sec; d) 2.0 sec; e) 2.5 sec.

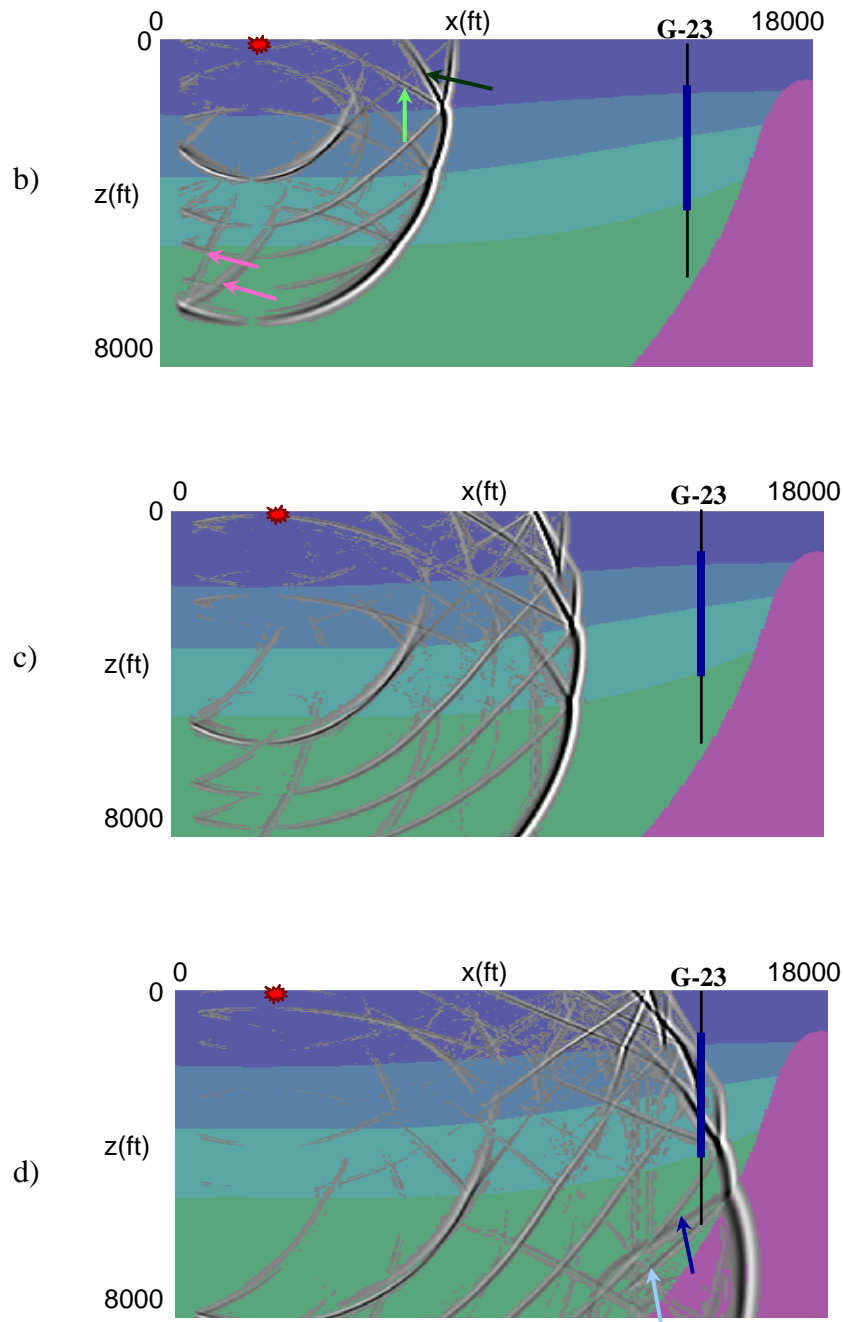


FIG. 4.4.6. (continued)

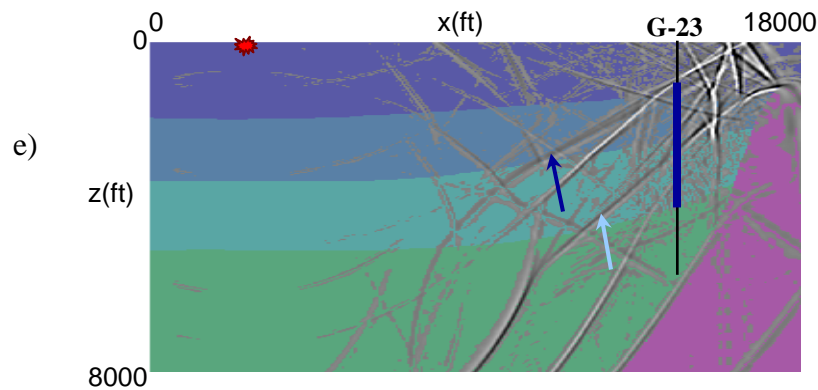


FIG. 4.4.6. (continued)

4.5. 3-D VSP subsurface illumination via acoustic pseudo-spectral modeling

The third part of the VSP subsurface illumination study consists of modeling 3D acoustic VSP data via an in-house 3d acoustic pseudo-spectral modeling algorithm. I built a 3-D P-wave velocity model that resembles the 2-D velocity model used in the previous two sections. I placed the salt dome in the lower right corner of the volume, based on the Vinton Dome depth migrated image (Figure 4.5.1). The P-wave velocities are the same as the values used in the 2-D illumination study. I calculated the densities based on Greenberg's equations.

$$\rho = 0.200 \cdot V_p^{0.261}. \quad (4.5.1)$$

Unlike the commercial 3-D ray-tracing software this wave equation modeling algorithm allows us to model the exact same source and receiver geometry extracted from the Vinton VSP field data. I set (x,y) volume coordinates based on the actual field one making sure that the location of the salt dome coincide with the location of the Vinton salt dome. Then, I extracted the geometry of the field shots falling inside the modeled volume and generated synthetic shot-gathers corresponding to these particular shot positions. I present a mapview of the Vinton Dome VSP acquisition geometry in Figure 4.5.2. The pink rectangle marks the area of the modeled volume. I modeled all shots enclosed by the pink rectangle. The VSP receiver array is located between 943 ft (287 m) and 3943 ft (1202 m), with 50 ft (15 m) group spacing. I display snapshots of the wavefront propagation for shot no. 2986 only. I recorded the snapshots with 0.1 sec time increment and display the significant ones, every 0.5 sec, in Figure 5.4.3. The coarse grid spacing of the velocity model causes the highest frequency to be quite small compared to the 2-D examples. Due to a 2 Gb memory restriction, I was limited to using 100 ft x 100 ft x 100 ft (30 m x 30 m x 30 m) grid spacing. I mark the shot location by the red star, the surface location of the VSP well by the green dot, and the receiver array by the dark blue line. I note the direct P wavefield by the dark red arrow, sediment PP reflected wavefield by dark green arrow, and salt PP reflected wavefield by dark blue arrow.

A quick analysis of the snapshots confirms the results obtained for the 2-D case. I noticed a good illumination of sedimentary interfaces and salt flank. However, only the portions of the sediment reflected wavefield located closer to the VSP well are recorded, which basically minimizes the amount of information received from the sedimentary boundaries.

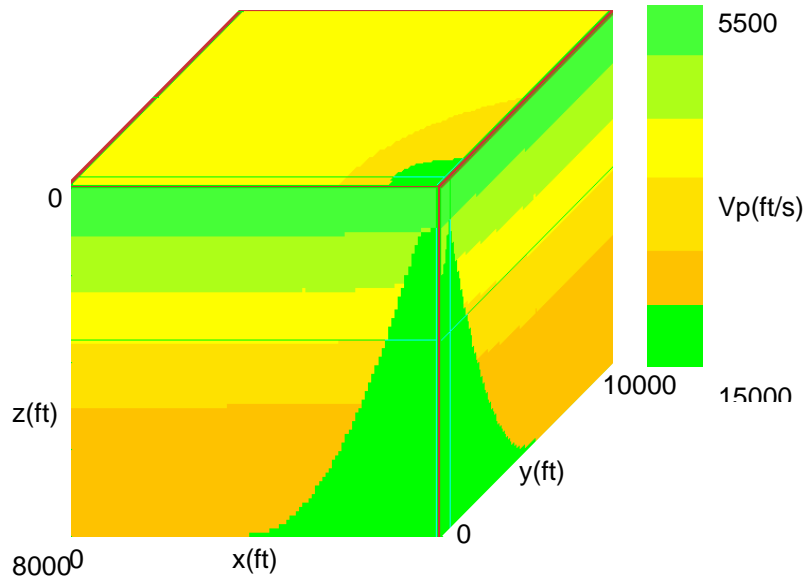


FIG. 4.5.1. 3-D P-wave velocity model.

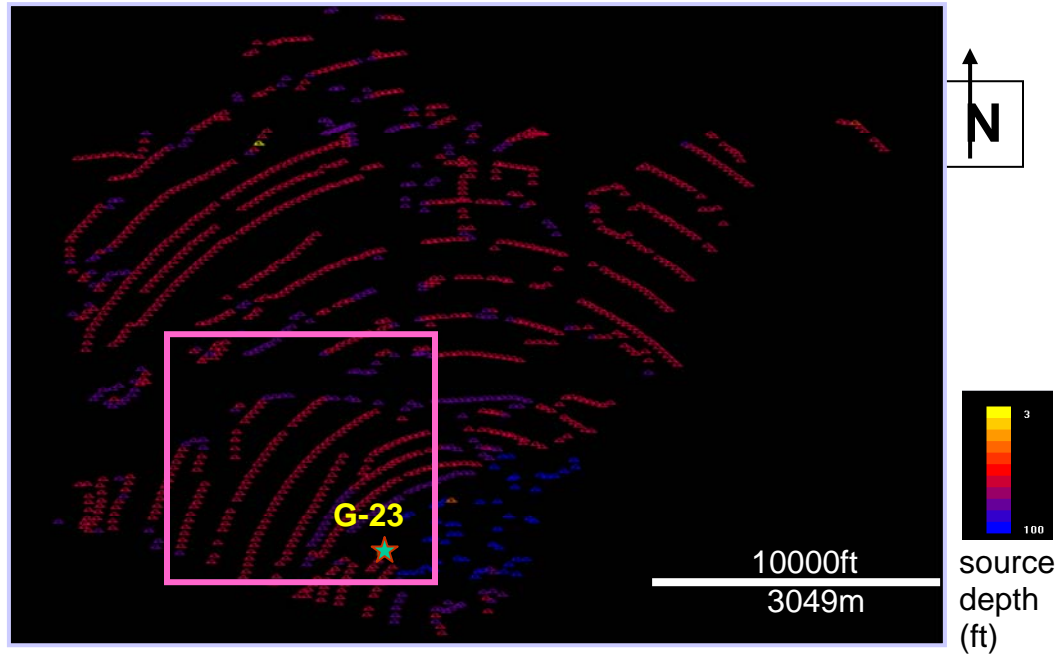


FIG. 4.5.2. Mapview of sources recorded in VSP well G-23. Color bar is shown on the lower right corner of the mapview. The pink rectangle marks the sources used in the 3-D VSP subsurface illumination study.

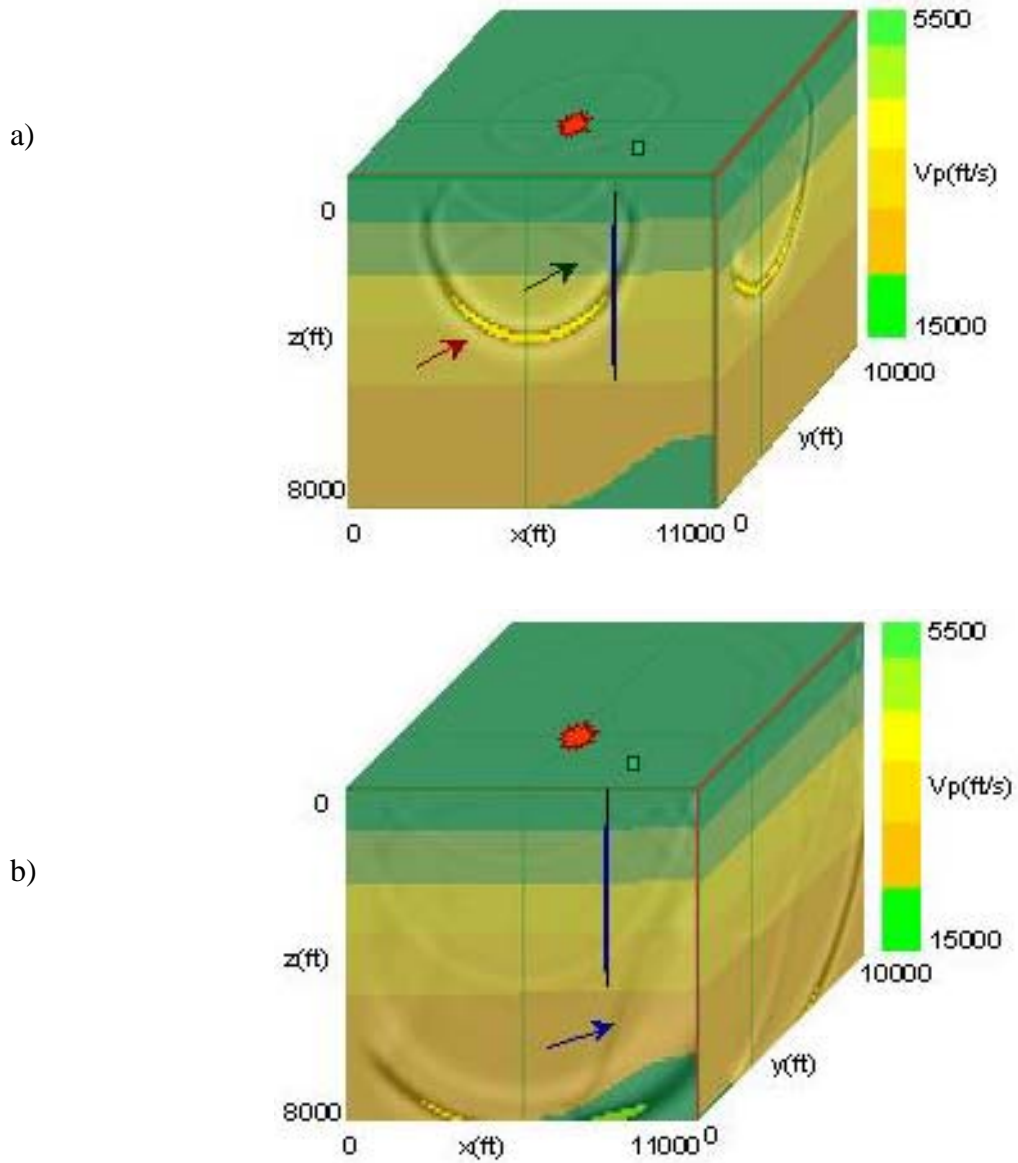


FIG. 4.5.3. 3-D P-wave snapshots recorded at 0.5 sec, 1.0 sec, and 1.5 sec. Red star marks the shot location, green dot marks the surface location of the well, and dark blue line marks the VSP receiver array. The dark red arrow marks direct P wavefield, the dark green arrow marks the sediment PP reflections, and the dark blue arrow marks the salt PP reflections.

c)

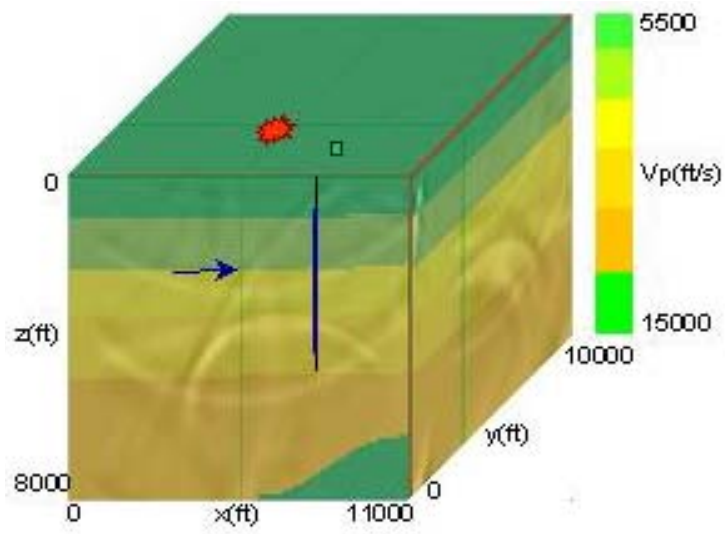


FIG. 4.5.3. (continued)

5. 3-D 3-C VSP KIRCHHOFF PRE-STACK DEPTH MIGRATION

5.1. Introduction

Kirchhoff migration operates on seismic data in the original space-time domain. It can be used for either time or depth migration and it is extremely versatile in the sense that any set of input traces from the unmigrated records can be migrated onto any output target of the migrated image (Gray, 2001). As new acquisition techniques have been developed in the last 20 years, migration methods needed to be adapted to be able to produce the proper information. Kirchhoff migration has proven to be one of the most adaptable algorithms to obtain time and depth images from single or multicomponent data.

There are two groups of Kirchhoff migration algorithms: scalar and elastic migration. Scalar migration is usually applied for reflected waves like PP- and PS-waves separated from the multicomponent data. Usually, for the surface data with a low-velocity weathering zone we assume that most of the PP reflections are found on the vertical geophone and most of the PS reflections are found on the horizontal geophones. Based on these assumptions, we migrate only data recorded by vertical geophone in order to obtain PP image and horizontal geophone to obtain the PS image.

Scalar migrations of PP-waves, will correctly image only the PP reflections. One of the processing steps required prior to scalar PP migration is separation of PP-waves from seismic data. There is a variety of P-/S-wave filters developed for the 2-D VSP data

based on f-k and Radon methods (Dankbaar, 1987; Foster, 1988) but not for 3-D VSP data.

If PP reflections are imperfectly separated from other events, scalar migration will treat these events as coherent noise, giving rise to spurious images (Zhe and Greenhalgh, 1997), with residual mismigrated PS- or SS-wave energy being on the PP-wave image (Hou and Marfurt, 2002). Sometimes, the mismigrated energy can be so strong that it can hide the correct images.

In contrast, elastic migration uses all components as input to the migration process and allows us to fully exploit the full information content in vector recording. In this manner, we eliminate the assumptions required by scalar migration. In 1991, Jackson *et al.* proposed a 2-D VSP “vector scalar” migration. By “vector” they mean that multicomponent data are migrated while by “scalar” they mean that each propagation step is based on a scalar wave equation. They begin by extracting P and S modes by projecting the data onto the expected polarization, which is obtained via ray-tracing. Their idea was extended by Takahashi (1995) for PP events in order to reduce the artifacts or false images in the migration images. Hou and Marfurt (2002) tested Jackson *et al.* idea on some 2-D OBC synthetic examples. In their method, the polarization was calculated directly from the migrated data.

In my dissertation, I image PP and PS via both scalar and elastic migration techniques. I perform 2-D scalar Kirchhoff pre-stack depth migration of previously separated PP and PS synthetic data generated by using ray-tracing. Next, I perform 2-D elastic Kirchhoff pre-stack depth migration of un-separated PP and PS synthetic data,

obtained by elastic pseudo-spectral methods, generating separate PP and PS images as output.

For the 3-D case, I show only scalar PP depth images of the 3-D acoustic synthetic data obtained via 3-D acoustic pseudo-spectral modeling algorithm. Finally, I present the field PP and PS depth images of the 3-D 3-C VSP Vinton data set obtained by 3-D elastic Kirchhoff pre-stack depth migration.

5.2. 2-D scalar synthetic VSP Kirchhoff pre-stack depth migration

2-D synthetic VSP data generated by ray-tracing

I used the 2-D model presented in Chapter 4 to generate the synthetics. Recall that I built the velocity model using a commercial modeling package and generated the synthetic data via ray-tracing. I maintained the same acquisition geometry as in the VSP subsurface illumination study. I present the 2-D V_p model indicating the source locations in Figure 5.2.1.

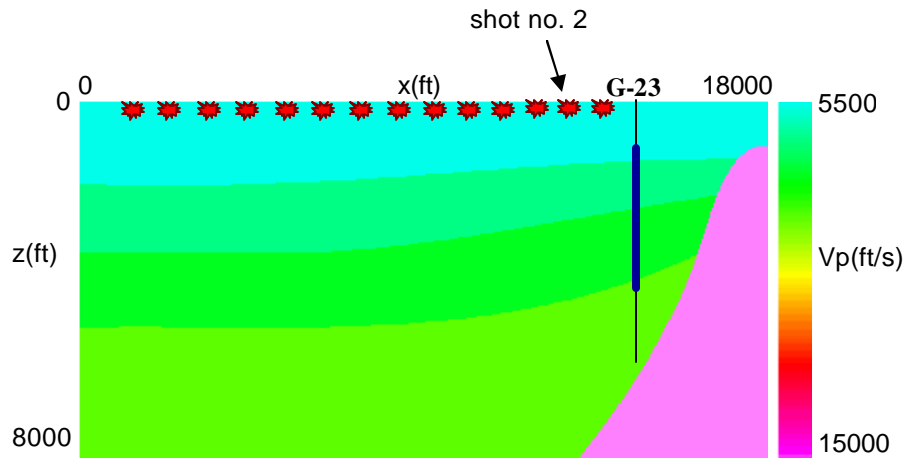


FIG. 5.2.1. Source locations used to generate the synthetics. There are 14 sources marked by the red stars, 1000 ft (304 m) apart. The solid blue line indicates the VSP receiver array located between 943 and 3943 ft, with 50 ft receiver spacing.

I first modeled PP and PS reflections separate for vertical and horizontal components using a 30 Hz Ricker wavelet, shot no. 2 that is the 2nd closest shot from the VSP well (Figures 5.2.2 – 5.2.3).

Based on the synthetic data, I observe that the salt flank reflection has a hyperbolic moveout in contrast to the linear moveout of the sedimentary boundaries. The PP salt flank reflection is stronger on the horizontal component than on the vertical component. The PS salt flank reflection appears to be stronger on the vertical component than on the horizontal component. In contrast the PP sediment reflections appear stronger on the vertical phone while PS sediment reflections appear stronger on the horizontal phone.

In order to evaluate migration aliasing, I generated synthetic shot-gathers (vertical and horizontal components) for groups of 14 and 65 shots. I obtained the groups of shots by maintaining the same minimum and maximum x source coordinates and decreasing the shot spacing from 1000 ft (304 m) to 200 ft (61 m).

In Chapter 4, I showed how the lateral extent of subsurface illumination increases as the number of shots included in the seismic survey increases, especially in the case of PP-waves. The next step is to migrate the synthetic data and see if I can accurately image these events.

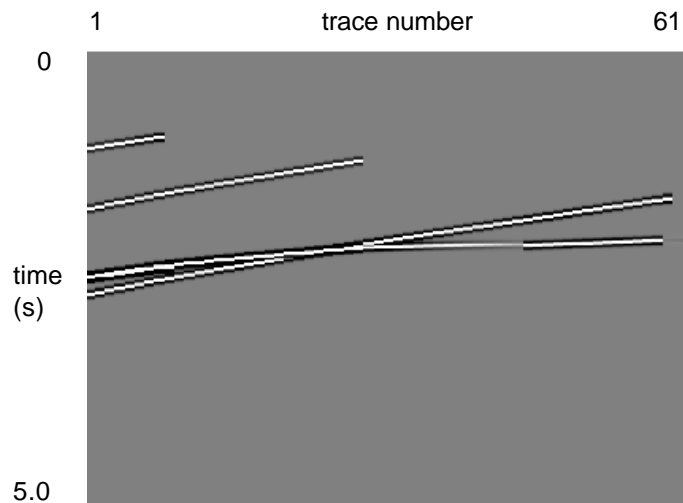


FIG. 5.2.2.a. Synthetic common-shot gather, shot no.2, offset = 1605 ft (490 m), vertical component, PP reflections only. Noise free. Trace no. 1 corresponds to receiver no. 1 located at depth = 943 ft (287 m), trace no. 61 corresponds to receiver no. 61 located at depth = 3943 ft (1202 m), with receiver depth spacing = 50 ft (15 m).

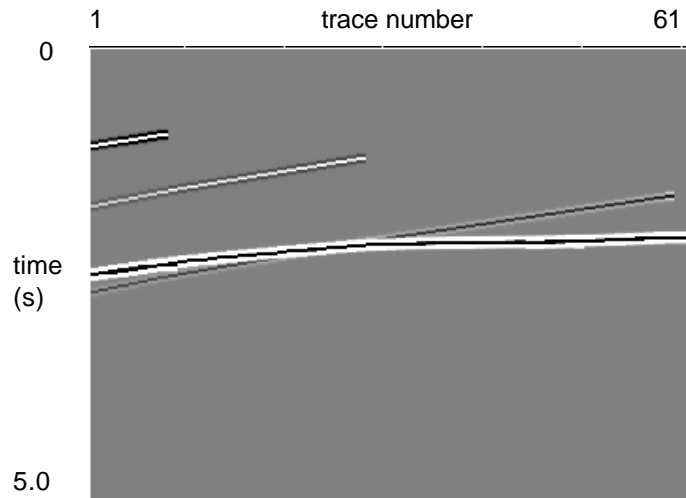


FIG. 5.2.2.b. Synthetic common-shot gather, shot no.2, offset = 1605 ft (490 m), horizontal component, PP reflections only. Noise free. Trace no. 1 corresponds to receiver no. 1 located at depth = 943 ft (287 m), trace no. 61 corresponds to receiver no. 61 located at depth = 3943 ft (1202 m), with receiver depth spacing = 50 ft (15 m).

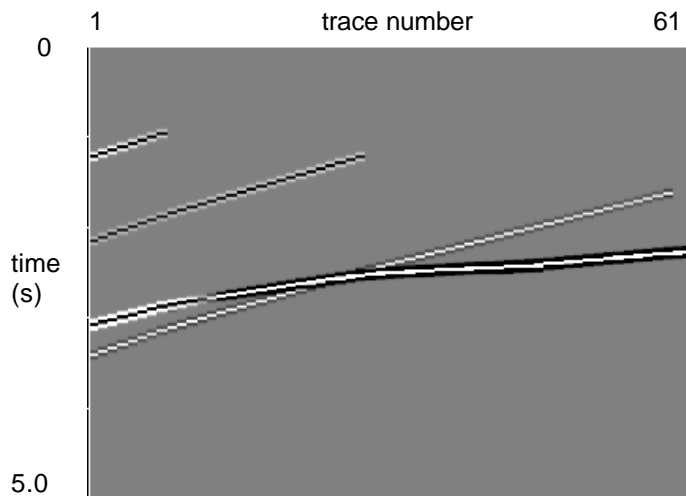


FIG. 5.2.3.a. Synthetic common-shot gather, shot no.2, offset = 1605 ft (490 m), vertical component, PS reflections only. Noise free. Trace no. 1 corresponds to receiver no. 1 located at depth = 943 ft (287 m), trace no. 61 corresponds to receiver no. 61 located at depth = 3943 ft (1202 m), with receiver depth spacing = 50 ft (15 m).

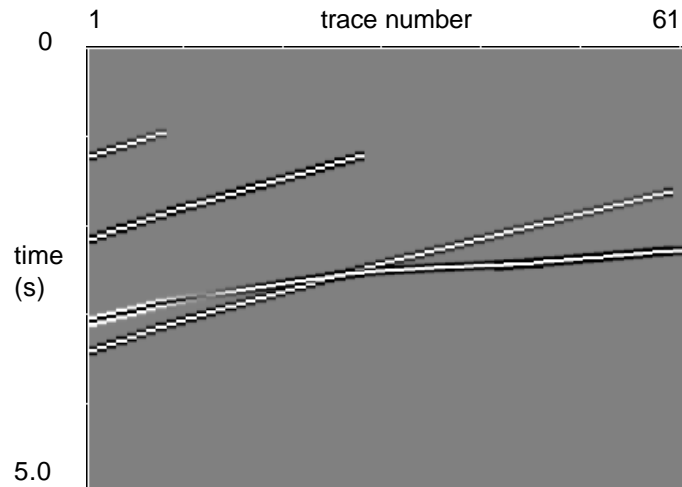


FIG. 5.2.3.b. Synthetic common-shot gather, shot no.2, offset = 1605 ft (490 m), horizontal component, PS reflections only. Noise free. Trace no. 1 corresponds to receiver no. 1 located at depth = 943 ft (287 m), trace no. 61 corresponds to receiver no. 61 located at depth = 3943 ft (1202 m), with receiver depth spacing = 50 ft (15 m).

Traveltime computation

Migration consists of wavefield downward continuation followed by an imaging condition. In the case of Kirchhoff migration, downward continuation of a given trace can be achieved by calculating the traveltime required by seismic wavefronts or seismic rays to travel between the source to each image point and back to the receiver.

There are various methods to calculate traveltimes, the most popular algorithms being based on ray-tracing and the eikonal equation. I selected an algorithm based on the eikonal equation and developed by SEP (Stanford Exploration Project). The algorithm created by Fomel and improved by Rickett (Fomel *et al.*, 2001) solves the eikonal

equation in three dimensions based on finite-difference methods. Their algorithm computes the transmission traveltimes from a point source through a predefined velocity model. The resulting traveltime field corresponds to the fastest wave traveling between the source point and any other point in the medium.

As stated in the previous section, the velocity model is composed of constant velocity layers in which case the traveltime contours should display a sharp change corresponding to the layer boundary. The smooth traveltime contours at the boundaries are due to the presence of head waves. At the critical angle of refraction, waves travel along the layer boundary with the faster velocity of the underlying layer. Eventually, these waves are refracted back into the overlying layer and are recorded in the form of head waves (Yilmaz, 2001).

Ideally, the traveltime contours should exhibit sharp changes at the layer boundary. Some of the eikonal solvers exclude the head waves (Reshef and Kosloff, 1986). The eikonal solver developed by SEP includes head waves, which for long offsets contaminate our traveltime tables.

The important advantages of the finite-differencing eikonal solvers are computational efficiency, algorithm simplicity, and generality of acceptable velocity fields, robustness and completeness of the solution whenever the arrival time is single-valued. Unfortunately, the traveltime solution fails to be single-valued in complex velocity models, which can affect the migration results.

A standard procedure in pre-stack depth migration of seismic data recorded over areas including salt formations has the following steps:

- 1- migrate using the sediment velocity,

- 2- pick the top of the salt and flood the velocity model with salt velocity the picked horizon,
- 3- remigrate with the new velocity model,
- 4- pick the bottom of the salt and flood with sediment velocity below it, and
- 5- remigrate to image the subsalt reflectors.

I followed this well-established workflow, calculating the traveltimes sections using only the sediment velocity. Salt present in the velocity model will generate an artifact in the final image by generating a strong head-wave in the traveltimes sections. Since I am only interested in imaging the salt flank, I stopped after step 1.

I display vertical traveltimes sections corresponding to shot no. 2 and receiver no. 1 in Figures 5.2.4 – 5.2.6. I calculated the receiver traveltimes necessary for migration of PP and PS reflections using both P- and S-wave velocity. I present the traveltimes overlying the sediment velocity model in order to check their accuracy.

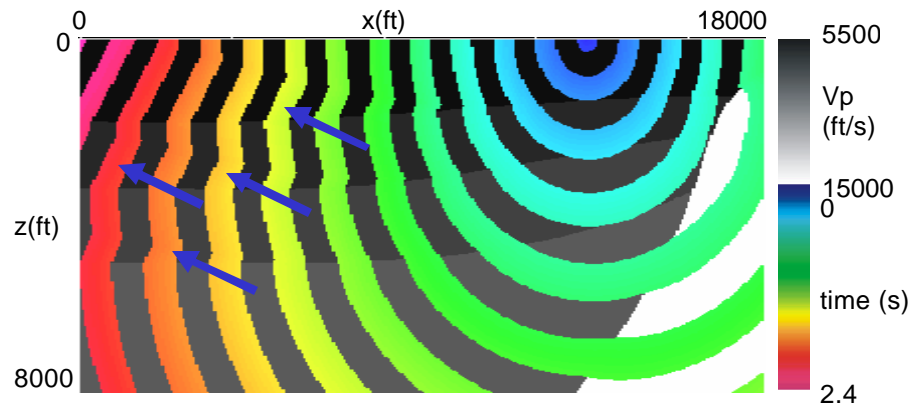


FIG. 5.2.4. 2-D vertical section of the source traveltimes (shot no. 2) overlying the P-wave velocity model, $\Delta t = 0.1$ sec. I calculated the source travel time using the P-wave velocity. Blue arrows point to the head waves.

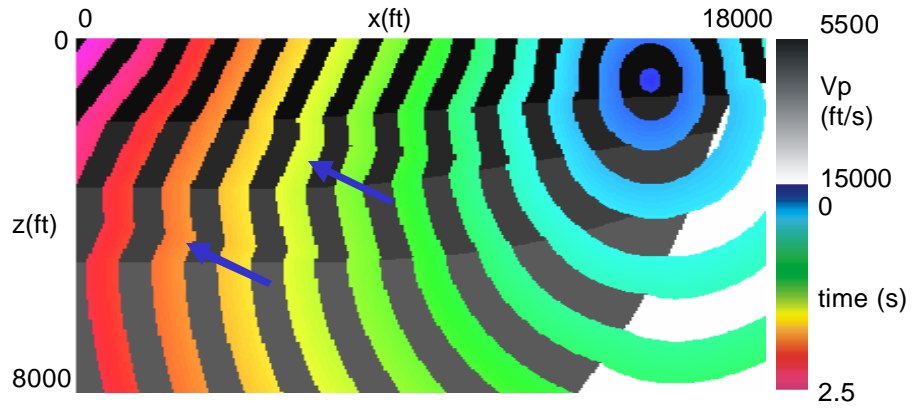


FIG. 5.2.5. 2-D vertical section of the receiver no. 1 traveltimes, overlying the P-wave velocity model, $\Delta t = 0.1$ sec. I calculated the receiver traveltimes using the P-wave velocity. Blue arrows point to the head waves.

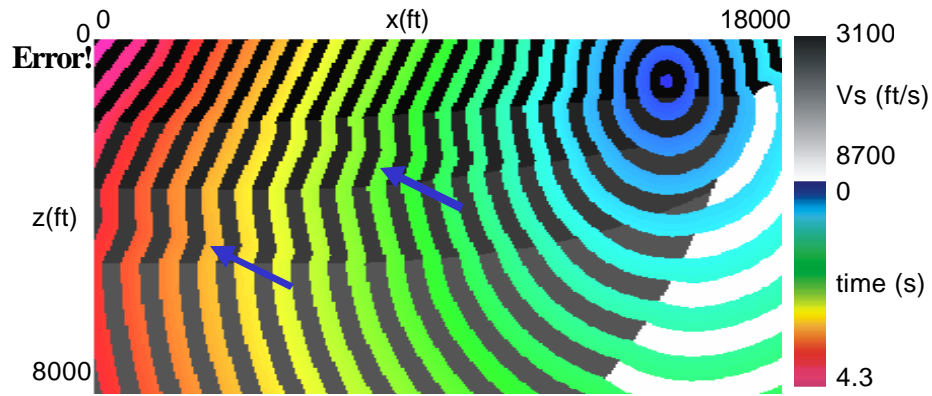


FIG. 5.2.6. 2-D vertical section of the receiver no. 1 traveltimes, overlying the S-wave velocity model, $\Delta t = 0.1$ sec. I calculated the receiver traveltimes using the S-wave velocity. Blue arrows point to the head waves.

2-D VSP synthetic scalar Kirchhoff pre-stack depth migration

After calculating the traveltimes, I focused my attention on developing the scalar pre-stack depth migration algorithm. I started with an in-house 3-D Kirchhoff pre-stack time migration code running under MPI created by Dr. Marfurt. I read in common-shot gathers, the source and receiver traveltimes tables, and performed the imaging. I migrated the seismic traces that fell within specified offset and azimuth limits. A second version of the pre-stack depth migration algorithm sorts the output into receiver depth bins.

I present the derivation of the Kirchhoff Integral in the Appendix A. Stolt and Benson (1986) presented the following simplified formula for the 3-D prestack Kirchhoff migration (eq. A-17 in Appendix A):

$$M(x) = \sum_{x_s, x_r} W(x_s, x_r, x) D_{sr}(t_s(x_s, x) + t_r(x, x_r)) \quad (5.2.1)$$

where $M(x)$ is the migrated image at 3-D location x , and where $W(x_s, x_r, x)$ represents the weighting factor or the amplitude compensation function which relates to the survey geometry, velocities along the raypath, and the geophone aperture, x_s and x_r are the source and receiver locations in 3-D, $D_{sr}(t_s(x_s, x) + t_r(x, x_r))$ is the recorded wavefield, and $t_s(x_s, x)$ and $t_r(x, x_r)$ are traveltimes from the source to image position and from the image position to the receiver.

The migration process spreads the recorded reflected energy at time t onto an ellipsoid. The resulting image at each location x consists of a superposition of weighted

energies WD_{sr} of all the ellipsoidal surfaces at x for each source x_s and each receiver x_r (Wang, 2004).

Bleistein (1987) derived a weight equation for pre-stack common-offset migration:

$$W = z \sqrt{1 + \frac{(x_s - x) \bullet (x_r - x)}{|x_s - x| |x_r - x|}} \sqrt{\frac{|x_s - x| + |x_r - x|}{|x_s - x| |x_r - x|}} \left[\frac{|x_r - x|}{|x_s - x|} + \frac{|x_s - x|}{|x_r - x|} \right] \quad (5.2.2)$$

where W – weighting factor, and where x_s – source X coordinate, x_r – receiver X coordinate, x – imaging point X coordinate, z – depth to the image point.

Gray (1998) rearranged Bleistein’s equation into a new formula that solely depends on the sum between the source and receiver traveltimes.

$$W = \frac{8}{(t_s + t_r)^2} \quad (5.2.3)$$

where W - weighting factor, and where t_s – source traveltime, t_r – receiver traveltime.

The major advantage of Gray’s (1998) formula is the minimum number of operations that needs to be performed in order to calculate the weighting factor, operations that can significantly increase the computation time when included inside the inner migration loop. In obtaining the new formula, Gray assumed constant velocity and ignored constant factors involving powers of 2, π and v .

Since most of the weight or amplitude factor equations are derived for the surface type of acquisition geometry, we preferred to use Gray’s (1998) formula.

Another important factor in migration techniques is the antialiasing filter (Gray, 1992; Lumley *et al.*, 1994; Abma *et al.*, 1999; Biondi, 2001).

Lumley *et al.*(1994) defined three types of aliasing:

- 1- Image aliasing occurs when the output sampling of the image space is too coarse to properly represent the migration dips,
- 2- Operator aliasing occurs when the operator dip along the migration summation trajectory is too steep for a given input seismic trace spacing and frequency content, and
- 3- Data aliasing occurs when the trace spacing is too coarse (Bardan, 1987).

Since “Image aliasing” can be easily avoided by using a proper output sampling, I will only focus on “Operator aliasing” and “Data aliasing”.

Operator aliasing

As stated before, the Kirchhoff migration method performs a sum over an aperture of input traces to obtain output at a single point. The length of the aperture is limited by a spatial Nyquist criterion, which typically prohibits imaging very steep dips at very high frequencies without generating severe migration artifacts (migration operator aliasing) (Gray, 1992). We followed Gray’s idea of creating three copies of the data. Given an aperture suitable for migrating out to a specified maximum dip, the frequencies in the data, which migrate out to the farthest offsets of the migration aperture, are restricted and all frequencies that migrate out to the shorter offsets are left intact.

Gray's antialiasing method is designed for migration in the time domain so we had to adjust it for the depth domain. In the pre-stack time migration algorithm, Nyquist frequency was defined as

$$f_N \leq \frac{1}{2 \cdot \Delta t} \quad (5.2.4)$$

The modified Nyquist formula that we used in the pre-stack depth migration is

$$f_N \leq \frac{V_{smooth}}{2 \cdot \Delta z} \quad (5.2.5)$$

Data aliasing

Kirchhoff migration spreads the energy of each time sample of a trace along a travelttime isochrone for each pair source-receiver corresponding to that trace. The final image represents a weighted sum of all the individual images. During the summation, events constructively and destructively interfere to form the image. I assume that the interference should act more successfully when having smaller source spacing.

Gardner *et al.* (1974) stated a similar idea by approximating a horizontal planar reflecting sheet with a set of horizontal cylindrical threads. Their experiment consisted of recording seismic data using constant offset source-receiver pairs along a surface line perpendicular to the axes of the set of parallel threads whose spacing decreases from one side to another. They proved that the resulting image looks smooth and continuous in the part corresponding to the closely spaced threads and is contaminated with migration tails in the part corresponding to the sparse threads.

Calibration

Since the migration program is designed to migrate 3-D data, I constructed a 2.5-D model by concatenating the 2-D velocity model five times. The resulting model is 18000 ft (5488 m) long in x direction, 240 ft (73 m) long in y direction and 8000 ft (2439 m) deep. I migrated only one line out of this volume, corresponding to the 2-D velocity model used to generate 2-D VSP synthetics and traveltimes.

I present a 3-D view of the 2.5-D P-wave velocity model in Figure 5.2.7. I first tested the program using shot no. 2, vertical and horizontal components, which contains PP reflections only. I display the result of the PP scalar Kirchhoff pre-stack depth migration in Figure 5.2.8.

In my data aliasing test, I started by migrating the group of 14 synthetic shot-gathers, vertical and horizontal components, PP reflections only. I display the PP depth images for both, vertical and horizontal components, in Figure 5.2.9. I mark with an arrow the location of the common-image gather displayed in Figure 5.2.10. As we can see, the aliasing effect is quite strong in both depth images. Since the shots are located too coarse and the subsurface illumination is concentrated around the well location, the constructive interference did not take place successfully.

We can remove the aliasing effect by combining two methods:

- a) semblance weighting during stacking;
- b) reducing shot spacing.

Semblance weighting

The similarity between two traces can be determined by the cross-correlation function. If we stack several channels together, the resulting amplitude is generally large when the individual channels are similar or coherent so that they stack in phase, and small where they are dissimilar or incoherent. The average amplitude of J stacked traces is given by

$$m_j(k \Delta z) \equiv m_{avg}(k \Delta z) = \frac{1}{J} \sum_{j=1}^J m_j(k \Delta z) \quad (5.2.6)$$

where m_j is the amplitude of an j^{th} migrated trace at depth $k \Delta z$, m_{avg} is the average amplitude at depth $k \Delta z$, and where J is the number of samples.

The energy of the stacked trace within a vertical window $(-w, +w)$ is given by

$$E = \sum_{z=z-w}^{z+w} m_{avg}(z). \quad (5.2.7)$$

where E is the energy of the stacked trace within a window, and where ζ is the length of the window.

The semblance within that window, $\sigma(z)$, is given by

$$s(z) = \frac{\sum_{k=-K}^{+K} \left(\sum_{j=1}^J m_j(k \Delta z) \right)^2}{(2K + 1) \sum_{k=-K}^{+K} \sum_{j=1}^J m_j^2(k \Delta z)}. \quad (5.2.8)$$

where $m_j(k \Delta z)$ is the migrated sample for bin j and depth sample k, and K is the number of depth samples in the window.

In our algorithm, we first calculate the semblance inside a running window of, let us say 7 traces and 5 samples in depth, for a common-image gather. Then, we reject the data that have a semblance smaller than a predefined minimum value and keep those for which semblance value exceeds a predefined passing semblance value. The semblance will not only tend to be large when a coherent event is present, but the magnitude of the semblance will be sensitive to the amplitude of event. Semblance values approach 1 for highly coherent events while for incoherent events they approach 0.

Gardner *et al.* (1974) have described a similar method based on coherency to remove the migration tails. The difference is that they applied the filter to the data prior to the migration. In the future, we recommend implementing the semblance weighting factor inside the migration algorithm, before the inner migration loop.

I show a comparison between the common-image gathers, obtained by migrating the group of 14 shots vertical component, before and after semblance weighting (Figure 5.2.10). Note how most parts of the migration smiles are removed after applying semblance weighting. The migration output, for this 2-D scalar migration algorithm, is sorted in offset-azimuth bins. I applied a bandpass filter to the common-image gather (CIG) before applying the semblance weighting to remove very low frequency noise.

I display the images presented in Figure 5.2.9 after applying semblance weighting in Figure 5.2.11. Next, I migrated the synthetic shot-gathers, vertical and horizontal components, PP reflections only for 65 shots. I display the PP depth images after bandpass filter and semblance weighting in Figure 5.2.12.

After calibrating the PP prestack depth migration algorithm, I moved on to the PS scalar prestack depth migration algorithm. The algorithm remains the same as for the PP

case. I used the same source traveltimes calculated with the P-wave velocity but I used the receiver traveltimes obtained using the S-wave velocity.

I followed a similar workflow analogous to that for PP migration. I started by migrating shot no. 2, vertical and horizontal components PS reflections only, and display the resulting PS depth images in Figure 5.2.13. Next, I generated the PS depth images for groups of 14 and 65 shots, both vertical and horizontal components. I show the PS depth image for group of 14 shots, both vertical and horizontal components, before applying the bandpass filter and semblance weighting in Figure 5.2.14. The arrow marks the location of the common-image gather, before and after semblance weighting, shown in Figure 5.2.15. In Figure 5.2.16 I present the resulting stacked image for 14 shots after bandpass and semblance weighting. Next, I present the PS depth images obtained for 65 shots after applying semblance weighting in Figures 5.2.17.

Analysis of the 2-D PS VSP images confirms the observation made in Chapter 4 that PS waves do not provide as good a lateral subsurface illumination of the sedimentary interfaces as PP waves. This small lateral subsurface illumination does not allow the constructive interference and semblance weighting during stacking to take place properly so, the PS depth images have more residual noise than PP depth images.

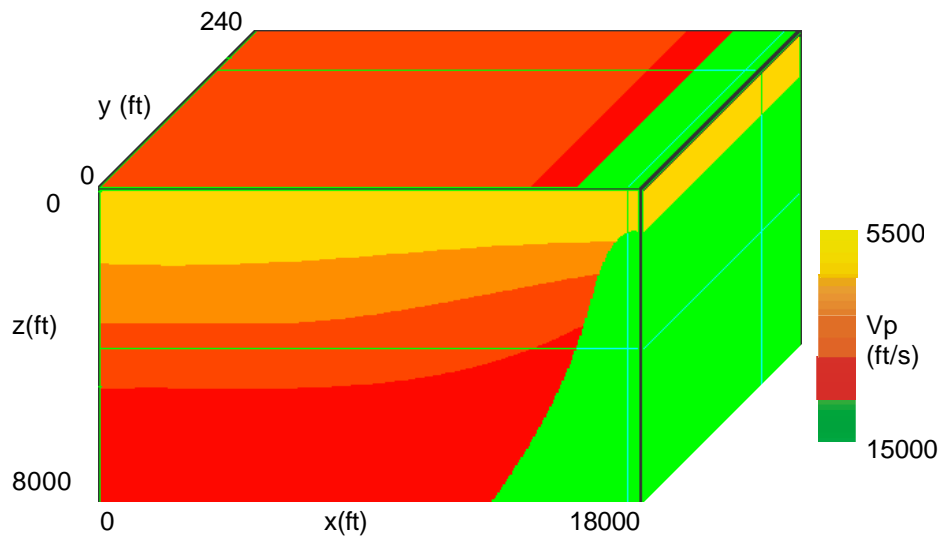


FIG. 5.2.7. 2.5-D velocity model used in migration. I only migrated one line corresponding to the 2-D velocity model used to generate the VSP synthetic data.

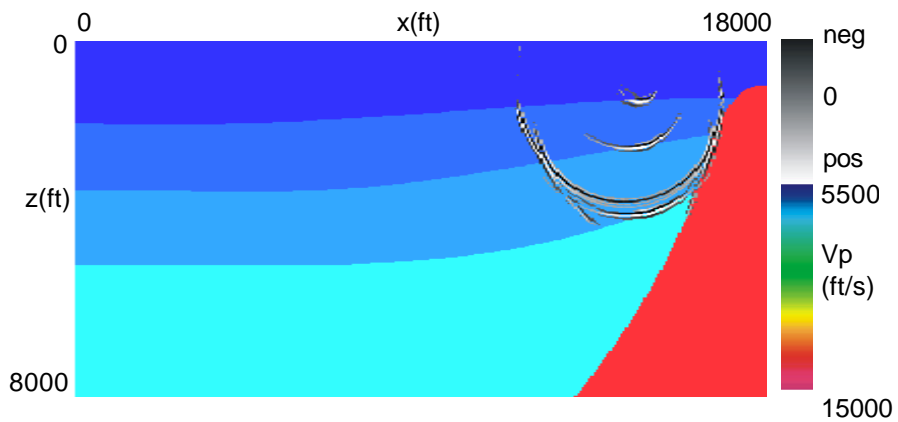


FIG. 5.2.8.a. 2-D scalar PP pre-stack depth image, shot no.2, vertical component, overlying the P-wave velocity model.

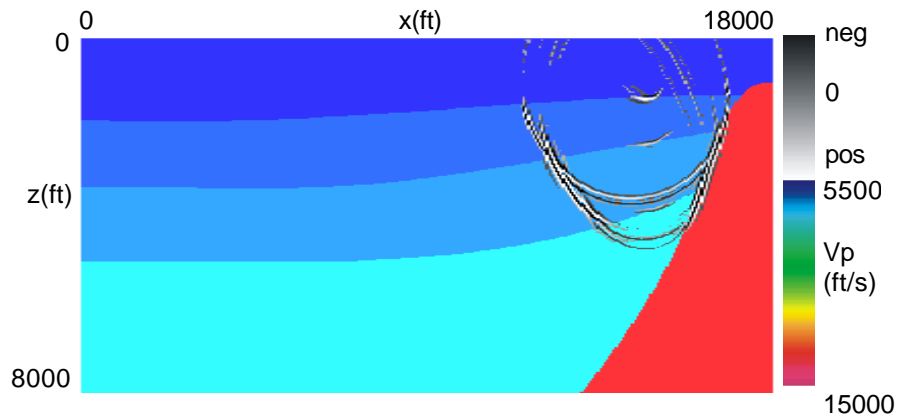


FIG. 5.2.8.b. 2-D scalar PP pre-stack depth image, shot no.2, horizontal component, overlying the P-wave velocity model.

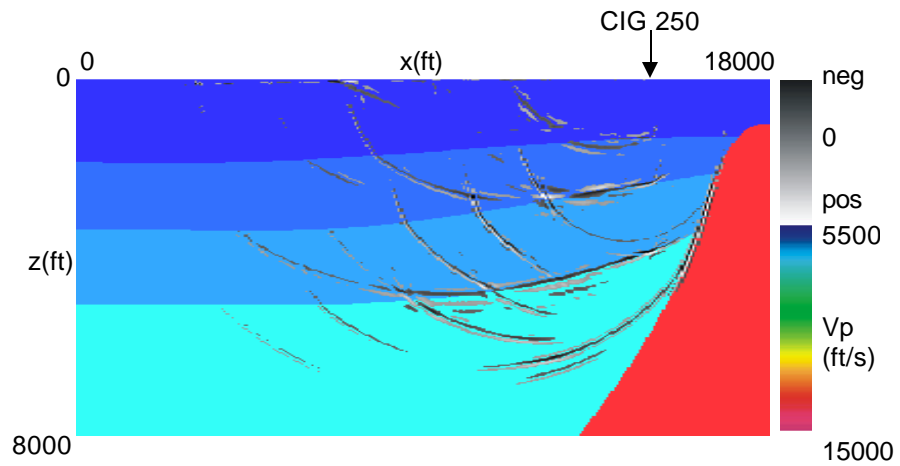


FIG. 5.2.9.a. 2-D scalar PP pre-stack depth image, 14 shots, vertical component, overlying the P-wave velocity model. No semblance weighting applied. The arrow marks the location of the common-image gather presented in Figure 5.2.14.

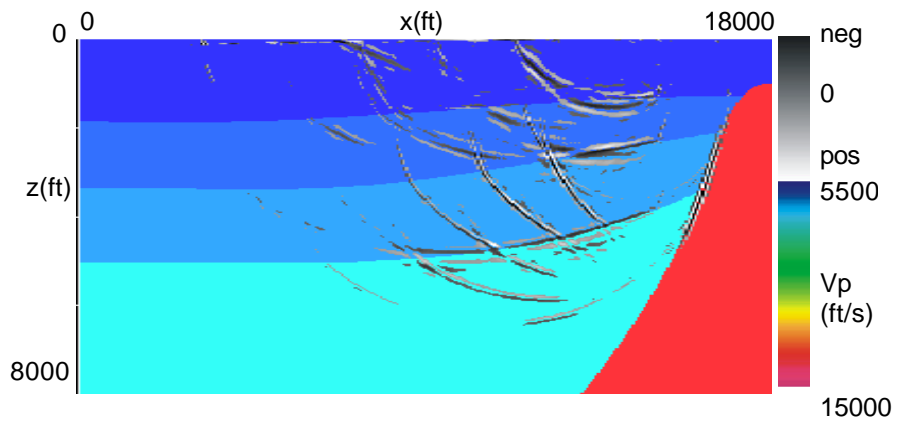


FIG. 5.2.9.b. 2-D scalar PP pre-stack depth image, 14 shots, horizontal component, overlying the P-wave velocity model. No semblance weighting applied.

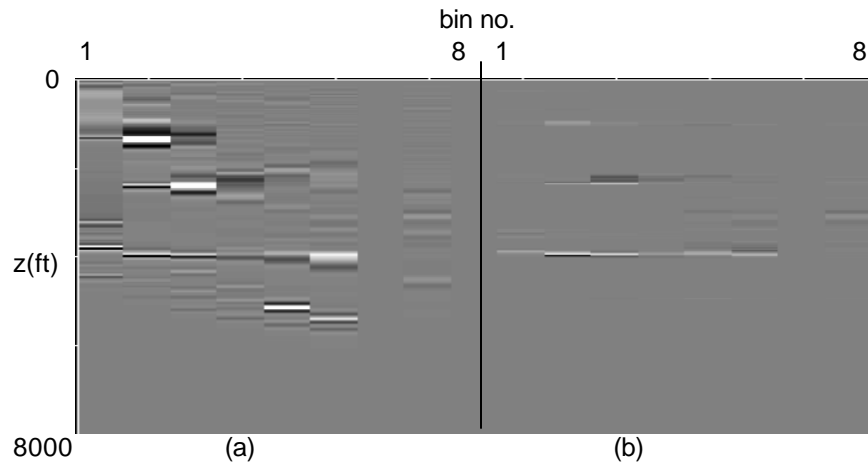


FIG. 5.2.10. Common-image gathers generated by migrating 14 shots, vertical component, PP events only. (a) before semblance weighting; (b) after BandPass and semblance weighting.

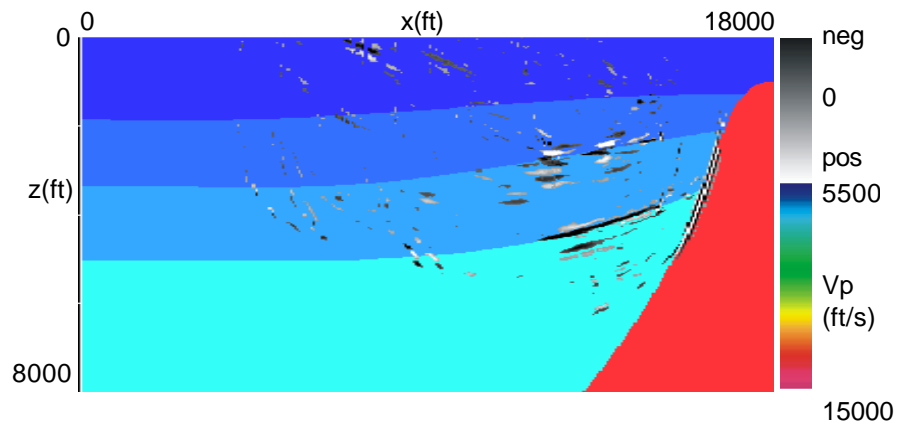


FIG. 5.2.11.a. 2-D scalar PP pre-stack depth image, 14 shots, vertical component, overlying the P-wave velocity model. Semblance weighting applied.

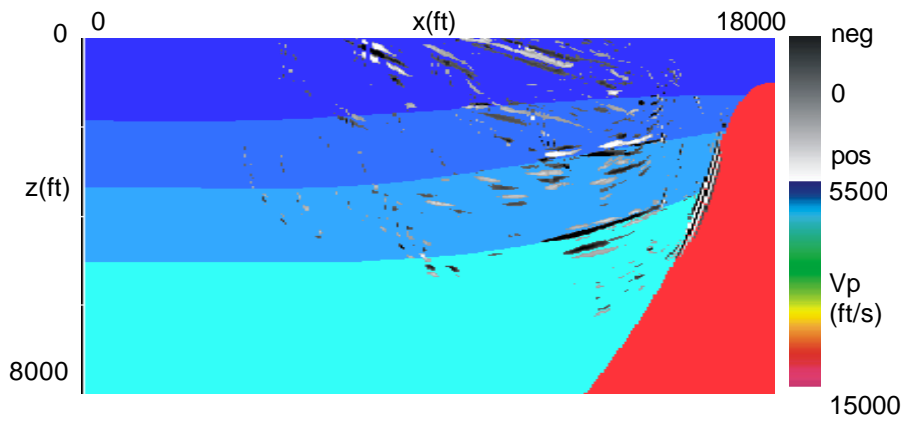


FIG. 5.2.11.b. 2-D scalar PP pre-stack depth image, 14 shots, horizontal component, overlying the P-wave velocity model. Semblance weighting applied.

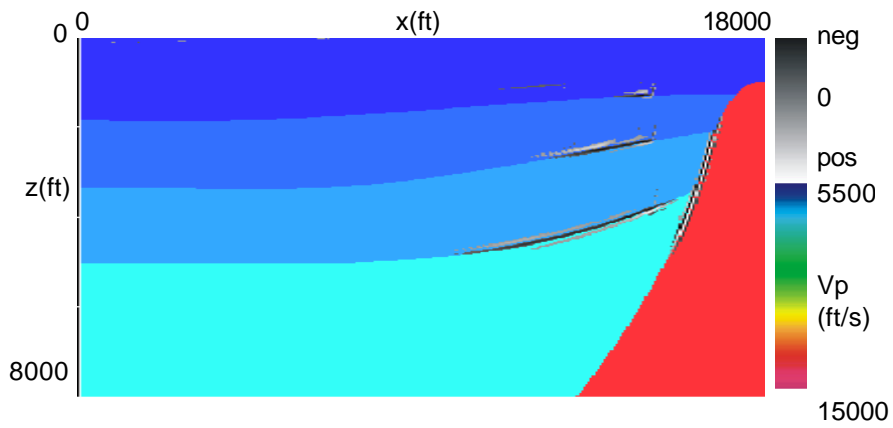


FIG. 5.2.12.a. 2-D scalar PP pre-stack depth image, 65 shots, vertical component, overlying the P-wave velocity model. Semblance weighting applied.

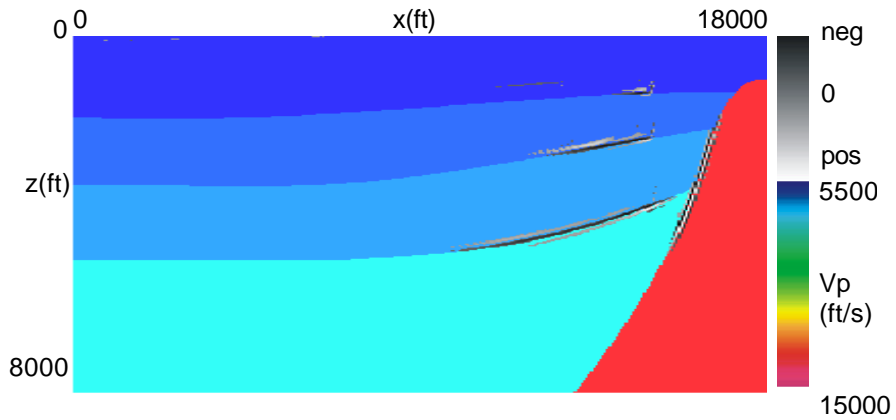


FIG. 5.2.12.b. 2-D scalar PP pre-stack depth image, 65 shots, horizontal component, overlying the P-wave velocity model. Semblance weighting applied.

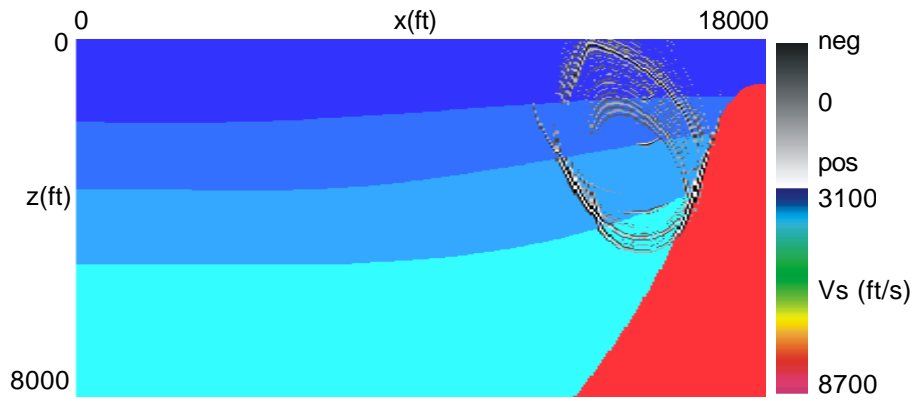


FIG. 5.2.13a. 2-D scalar PS pre-stack depth image, shot no.2, vertical component, overlying the S-wave velocity model.

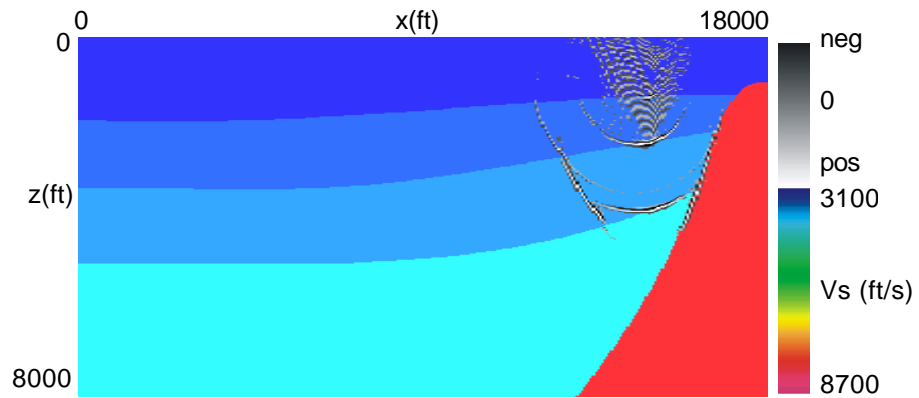


FIG. 5.2.13.b. 2-D scalar PS pre-stack depth image, shot no.2, horizontal component, overlying the S-wave velocity model.

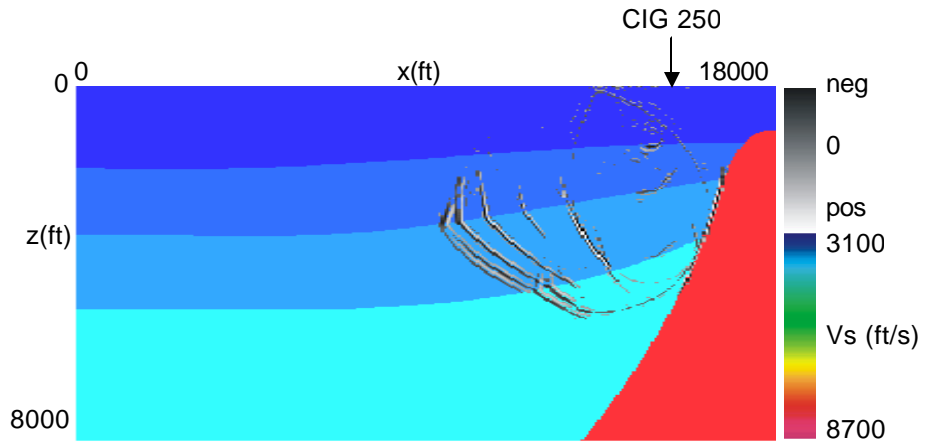


FIG. 5.2.14.a. 2-D scalar PS pre-stack depth image, 14 shots, vertical component, overlying the S-wave velocity model. No semblance weighting applied. The arrow marks the location of the common-image gather presented in Figure 5.2.14.

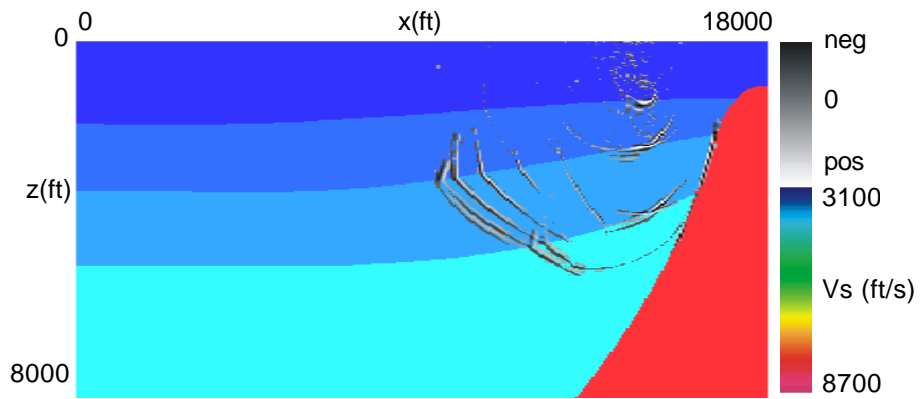


FIG. 5.2.14.b. 2-D scalar PS pre-stack depth image, 14 shots, horizontal component, overlying the S-wave velocity model. No semblance weighting applied.

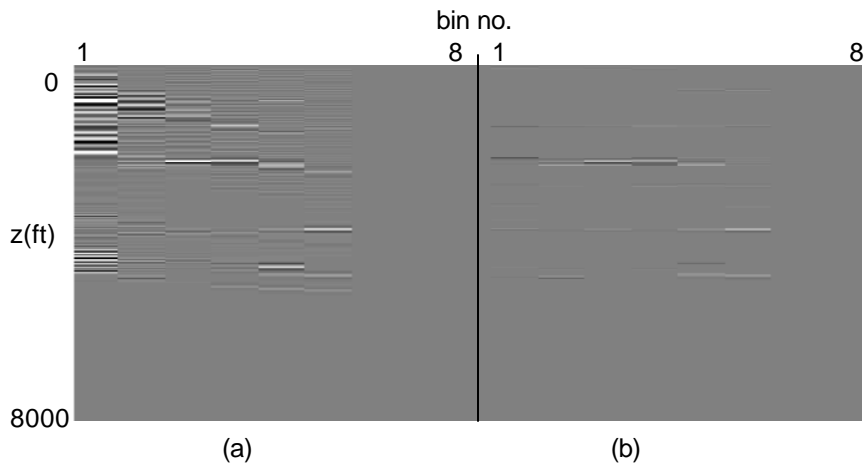


FIG. 5.2.15. Common-image gathers generated by migrating 14 shots, vertical component, PS events only. (a) before semblance weighting; (b) after BandPass and semblance weighting.

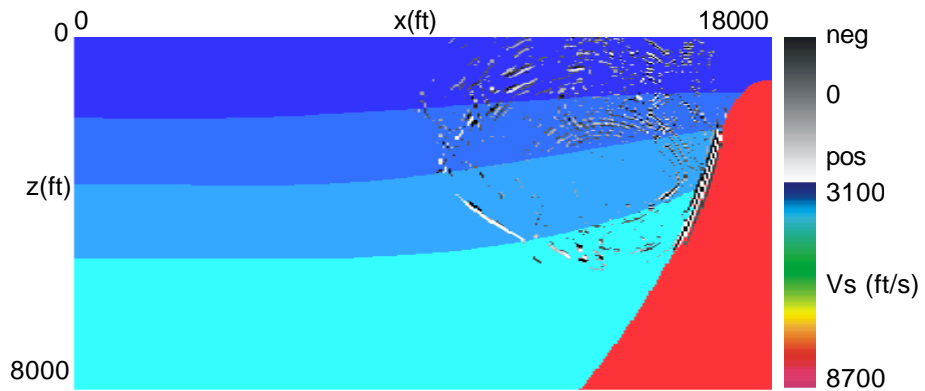


FIG. 5.2.16.a. 2-D scalar PS pre-stack depth image, 14 shots, vertical component, overlying the S-wave velocity model. Semblance weighting applied.

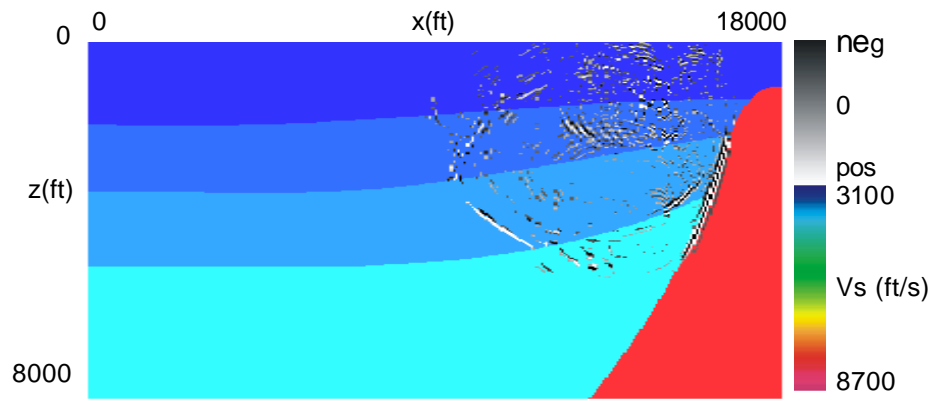


FIG. 5.2.16.b. 2-D scalar PS pre-stack depth image, 14 shots, horizontal component, overlying the S-wave velocity model. Semblance weighting applied.

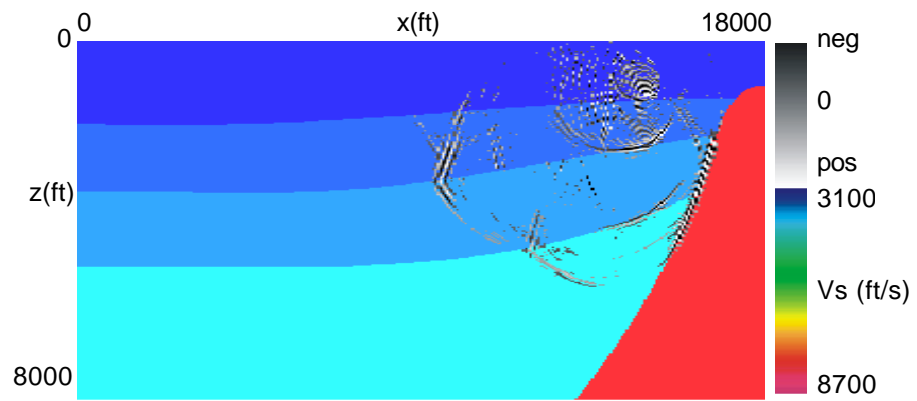


FIG. 5.2.17.a. 2-D scalar PS pre-stack depth image, 65 shots, vertical component, overlying the S-wave velocity model. Semblance weighting applied.

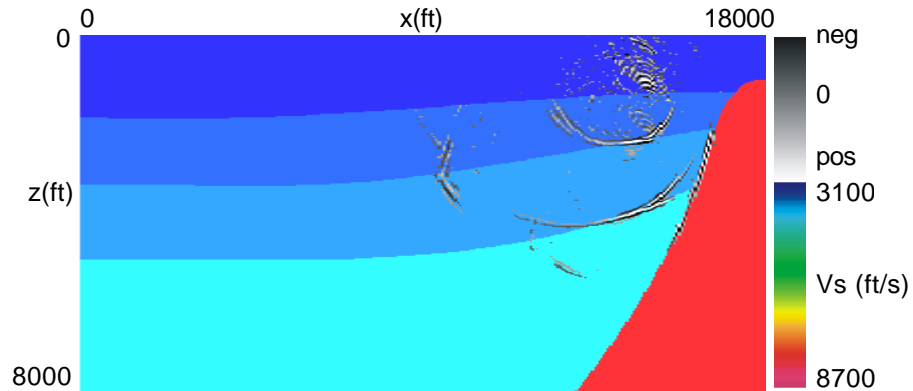


FIG. 5.2.17.b. 2-D scalar PS pre-stack depth image, 65 shots, horizontal component, overlying the S-wave velocity model. Semblance weighting applied.

5.3. 2-D elastic synthetic VSP Kirchhoff pre-stack depth migration

2-D synthetic VSP data generated by elastic pseudo-spectral modeling

I used the same 2-D velocity model (Figure 5.3.1) presented in Chapter 4 to generate 2-D elastic VSP synthetic data via an in-house elastic pseudo-spectral modeling algorithm. I started by modeling one shot only, shot no.2 (Figure 5.3.2).

Synthetic VSP data have a reasonably high frequency, which is due to the small cell size of the velocity model. I used 15 ft (4.5 m) cell size that ensured a frequency of 75 Hz. The only pre-processing step I performed before elastic migration is muting the first-breaks. Based on the previous modeling results, the up-going/down-going wave

separation prior to migration is not suitable for my project. I show the synthetic shot-gather displayed in Figure 5.3.2 after muting the first-breaks in Figure 5.3.3.

Based on the synthetic data, I observe that the salt flank reflection has a hyperbolic moveout in contrast to the linear moveout of the sedimentary boundaries. The PP salt flank reflection is stronger on the horizontal component than on the vertical component. The PS salt flank reflection appears to be stronger on the vertical component than on the horizontal component. In contrast, the PP sediment reflections appear stronger on the vertical phone while PS sediment reflections appear stronger on the horizontal phone.

As described in Chapter 4, the VSP synthetic data obtained by elastic pseudo-spectral modeling are perturbed by artificial salt flank reflections that are stronger on the horizontal phone. These reflections are due to solving the wave equation at each grid point, which consider the salt flank having a “star-step” shape instead of a smooth one (Figure 5.3.4).

In order to evaluate migration aliasing, I generated synthetic shot-gathers (vertical and horizontal components) for groups of 14 and 65 shots. I obtained the groups of shots by maintaining the same minimum and maximum x source coordinates and decreasing the shot spacing from 1000 ft (304 m) to 200 ft (61 m).

In Chapter 4, I showed how the lateral extent of subsurface illumination increases as the number of shots included in the seismic survey increases, especially in the case of PP-waves. The next step is to migrate the synthetic data and see if I can accurately image these events.

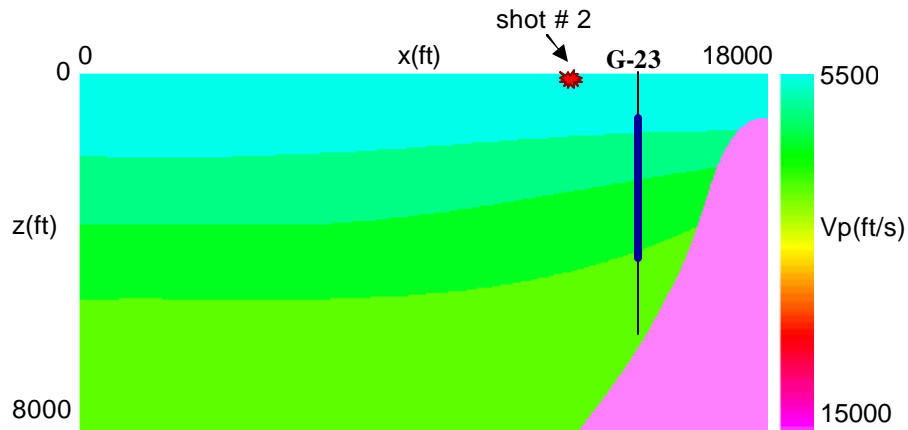


FIG. 5.3.1. Source location used to generate the synthetics. The red star indicates the shot location, offset = 1565 ft (477 m), which corresponds to shot no. 2 presented in the ray-traced data. The solid blue line indicates the VSP receiver array located between 943 and 3943 ft, with 50 ft receiver spacing.

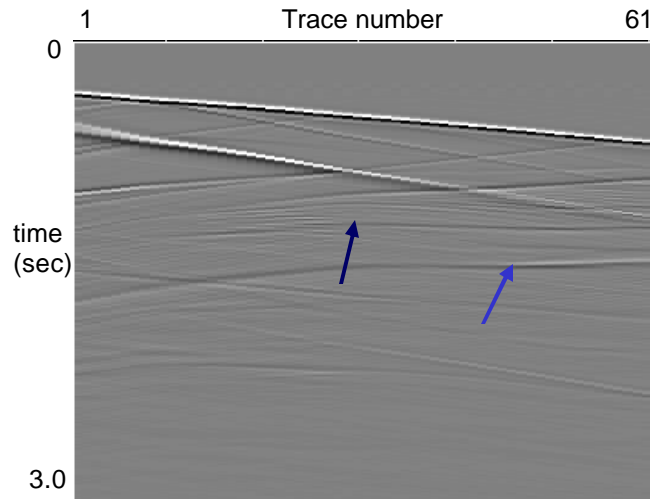


FIG. 5.3.2.a. Synthetic shot-gather, vertical component, shot no. 2, offset = 1565 ft (477 m). Dark blue arrow points to the PP salt flank reflection, light blue arrow points to the PS salt flank reflection. Trace no. 1 corresponds to receiver no. 1 located at depth = 943 ft (287 m), trace no. 61 corresponds to receiver no. 61 located at depth = 3943 ft (1202 m), with receiver depth spacing = 50 ft (15 m).

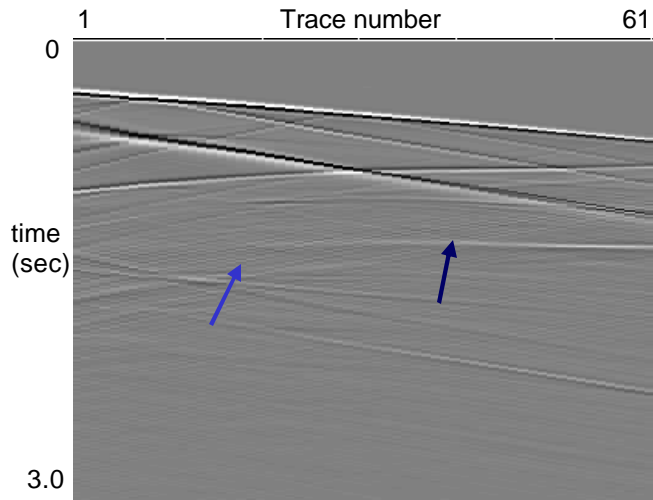


FIG. 5.3.2.b. Synthetic shot-gather, horizontal component, shot no. 2, offset = 1565 ft (477 m). Dark blue arrow points to the PP salt flank reflection, light blue arrow points to the PS salt flank reflection. Trace no. 1 corresponds to receiver no. 1 located at depth = 943 ft (287 m), trace no. 61 corresponds to receiver no. 61 located at depth = 3943 ft (1202 m), with receiver depth spacing = 50 ft (15 m).

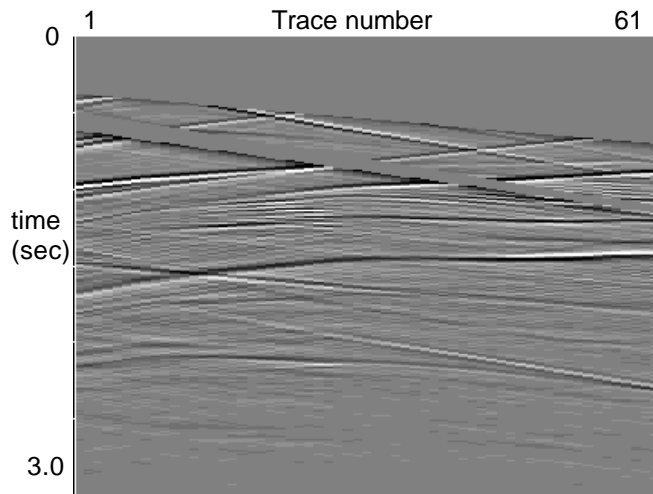


FIG. 5.3.3.a. Synthetic shot-gather, vertical component, shot no. 2, offset = 1565 ft (477 m). First breaks muted. Trace no. 1 corresponds to receiver no. 1 located at depth = 943 ft (287 m), trace no. 61 corresponds to receiver no. 61 located at depth = 3943 ft (1202 m), with receiver depth spacing = 50 ft (15 m).

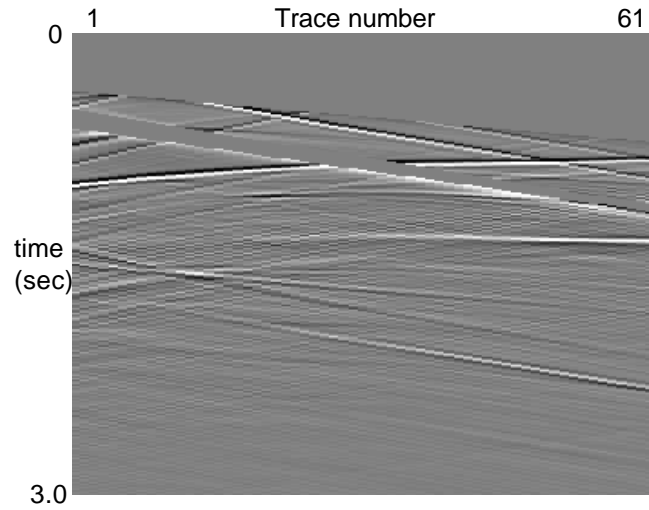


FIG. 5.3.3.b. Synthetic shot-gather, horizontal component, shot no. 2, offset = 1565 ft (477 m). First breaks muted. Trace no. 1 corresponds to receiver no. 1 located at depth = 943 ft (287 m), trace no. 61 corresponds to receiver no. 61 located at depth = 3943 ft (1202 m), with receiver depth spacing = 50 ft (15 m).

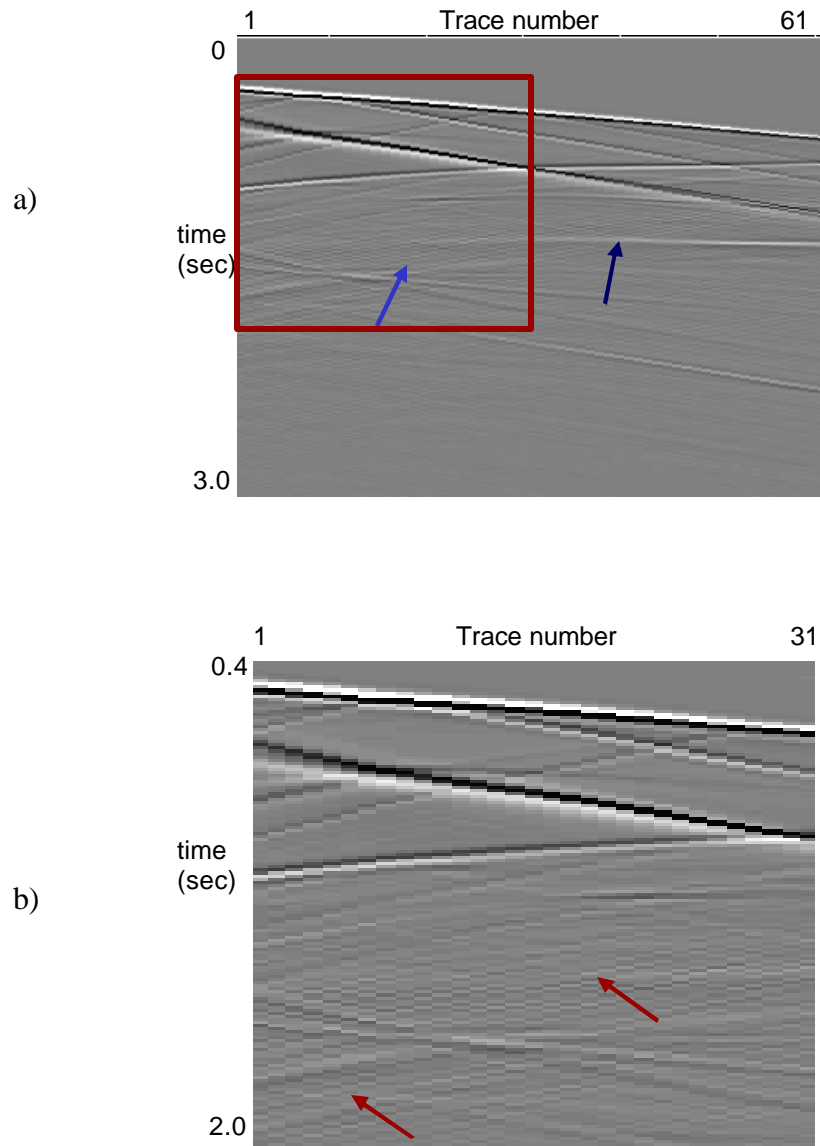


FIG. 5.3.4. a) Synthetic shot-gather, horizontal component, shot no. 2, offset = 1565 ft (477 m). Dark blue arrow points to the PP salt flank reflection, light blue arrow points to the PS salt flank reflection. Red rectangle marks the zoomed area shown in Figure 5.3.4.b. Trace no. 1 corresponds to receiver no. 1 located at depth = 943 ft (287 m), trace no. 61 corresponds to receiver no. 61 located at depth = 3943 ft (1202 m), with receiver depth spacing = 50 ft (15 m).

b) Zoomed area from (a), red arrows point to the artificial salt flank reflections.

Traveltime computation

I use the same traveltime tables generated for the 2-D synthetic VSP scalar Kirchhoff pre-stack depth migration (Figures 5.2.4 – 5.2.6).

2-D VSP synthetic elastic Kirchhoff pre-stack depth migration

I built my elastic migration algorithm based on Jackson *et al.* (1991) method which assume the interaction between the wavefields occurs only once in the far-field of both source and receiver. Extraction of P, SV and SH wavefields is achieved within the depth migration (if we assume isotropy in the neighborhood of the downhole receiver) by a projection onto the polarization for the desired mode. The extraction of the desired mode is performed for each depth migration bin after the separate scalar migration of each receiver gather component. They obtained the expected polarization necessary for the post-migration projection via ray-tracing.

I also perform the elastic migration by projecting the data onto the expected polarization to separate the P- and S-waves. The difference is that, in my case, I perform the projection during the prestack depth migration.

I explain the idea of elastic migration in Figure 5.3.5. The red arrow represents the migration ray unit vector calculated using the direction cosines. The dot product between this migration ray vector and the VSP vector data give the P-waves, which are waves with particle displacement along the propagation direction, and the cross-product

gives the S-waves, which are waves with particle displacement normal to the direction of propagation.

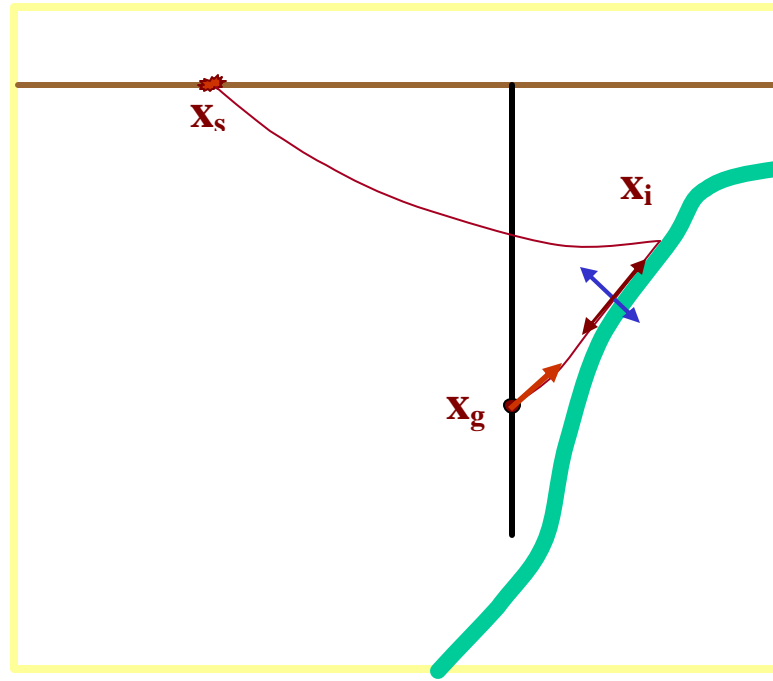


FIG. 5.3.5. Elastic migration using direction cosines. Red arrow represents the migration ray unit vector calculated using the direction cosines. Maroon double arrow represents the P polarization (along the direction of propagation) and the blue double arrow represents the S-wave polarization (perpendicular to the direction of propagation).

I use the same 3-D Kirchhoff pre-stack depth migration algorithm given by equation (5.3.1):

$$M_p(x) = \sum_{x_s, x_r} W(x_s, x_r, x) P(x_s, x_r, x) \quad (5.3.1)$$

but where I have replaced D_{sr} by P where P is given by:

$$P(x_s, x_r, x) = \hat{a} \bullet \overrightarrow{D_{sr}}(t_s(x_s, x) + t_r(x, x_r)). \quad (5.3.2)$$

In these equations, $M_P(x)$ represents the PP-wave image at location x , $W(x_s, x_r, x)$ represents the same weighting factor used in the scalar migration, $\overrightarrow{D_{sr}}(t_s(x_s, x) + t_r(x, x_r))$ represents the seismic data, and \hat{a} represents the migration ray vector calculated using the direction cosines (Figure 5.3.6).

I calculated the direction cosines using the x , y and z coordinates of the image point and receivers, an approach that does not take into account any ray bending. An improvement is to finish the 3-D ray-tracing algorithm presented in Section 5.5 to obtain the ray take-off angle at the receivers. I expect less leakage of the S-waves into PP image and P-waves into PS image when using take-off angles computed via ray-tracing.

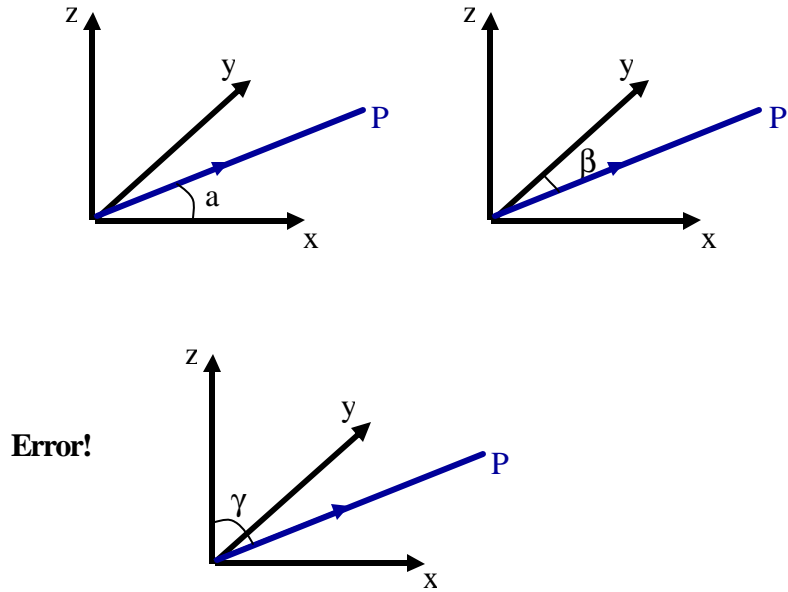


FIG. 5.3.6. Direction cosines of a vector in 3-D domain.

For the PS image case, I use the following migration formula:

$$M_S(x) = \sum_{x_s, x_r} W(x_s, x_r, x) S(x_s, x_r, x) \quad (5.3.3)$$

where

$$S(x_s, x_r, x) = \hat{a} \times \overline{D_{sr}}(t_s(x_s, x) + t_r(x, x_r)) \quad (5.3.4)$$

and where $M_S(x)$ represents the PS-image at location x , $W(x_s, x_r, x)$ represents the same weighting factor used in the scalar migration, $\overline{D_{sr}}(t_s(x_s, x) + t_r(x, x_r))$ represents the

seismic data, and $\hat{\mathbf{a}}$ represents the migration ray vector calculated using the direction cosines.

Wang (2004) has presented a 3-D 3-C VSP pre-stack Kirchhoff migration, which also uses the dot product inside the migration loop. His algorithm uses a dynamic, vector energy mapping method to image a reflection position and maps each time sample only to its reflected image point. An advantage of this method is that it does not require a rotation of the data to a preferred orientation prior migration. The dynamic rotation of the data allows the migration to use directional mapping and therefore distribute the reflection energy only to its true reflection position. This enhances reflection images and reduces noise in the image.

To calibrate the elastic Kirchhoff migration algorithm, I followed a workflow analogous to the scalar migration case. The advantage of Kirchhoff pre-stack depth migration is that we can use the same traveltimes sections that we already calculated for the scalar migration case.

I first test the program using shot no. 2, vertical and horizontal components, and generate PP and PS elastic depth images. I display the images in Figure 5.3.7. The elastic pre-stack depth migration suffers from similar types of aliasing like the pre-stack scalar depth migration. Since earlier I provided a detailed explanation of “Data Aliasing” and “Operator Aliasing” for the 2-D scalar pre-stack depth migration case, I will directly present the results of the elastic pre-stack depth imaging of groups of 14 and 65 shots. The migration output, for this 2-D elastic migration algorithm, is sorted in offset-azimuth bins.

I show the PP and PS elastic depth images generated for the group of 14, before applying the bandpass filter and semblance weighing, in Figure 5.3.8. The arrows mark the location of the common-image gathers presented in Figure 5.3.9 – 5.3.10. As we can see from these figures, the incoherent noise seen in common-image gathers before using the bandpass filter and the semblance weighting is suppressed. In Figure 5.3.11, I present the 2-D elastic PP and PS depth images for 14 shots after bandpass filter and semblance weighting.

Next, I show depth images obtained for the group of 65 shots before bandpass and semblance weighting (Figure 5.3.12). The arrow marks the location of the common-image gathers presented in Figures 5.3.13 – 5.3.14, before and after bandpass and semblance weighting. In Figure 5.3.15, I show the final 2-D PP and PS elastic depth images for 65 shots, after bandpass and semblance weighting.

In Chapter 4, I showed that using the same acquisition geometry, PP-waves provide a much better lateral subsurface illumination than PS-waves. The migration artifacts from the elastic depth images are mainly due to the poor job in removing the first breaks and other events, e.g. multiples. The artificial salt flank reflections generated a high-frequency migration artifact, which was successfully removed by the bandpass filter. The analysis of the previous images indicates the presence of PS-waves leakage in the PP images and PS-waves leakage in the PS images. I expect the leakage to disappear once we use the take-off angles calculated during ray-tracing.

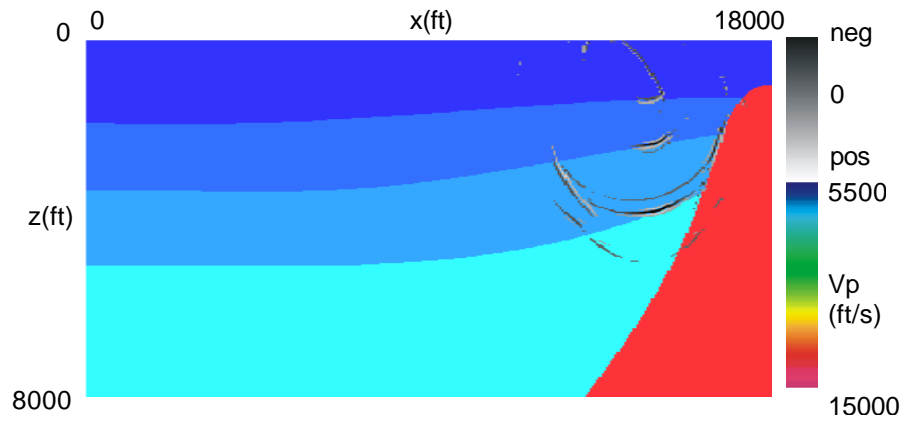


FIG. 5.3.7.a. 2-D elastic PP pre-stack depth image, shot no.2, overlaying the P-wave velocity model.

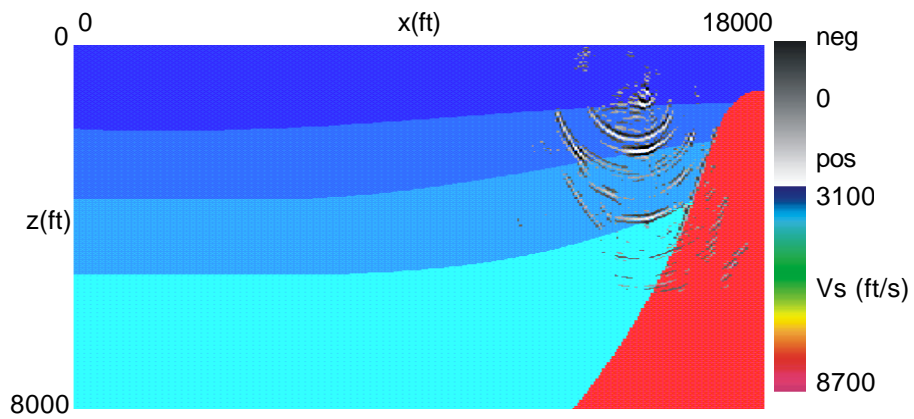


FIG. 5.3.7.b. 2-D elastic PS pre-stack depth image, shot no.2, overlaying the S-wave velocity model.

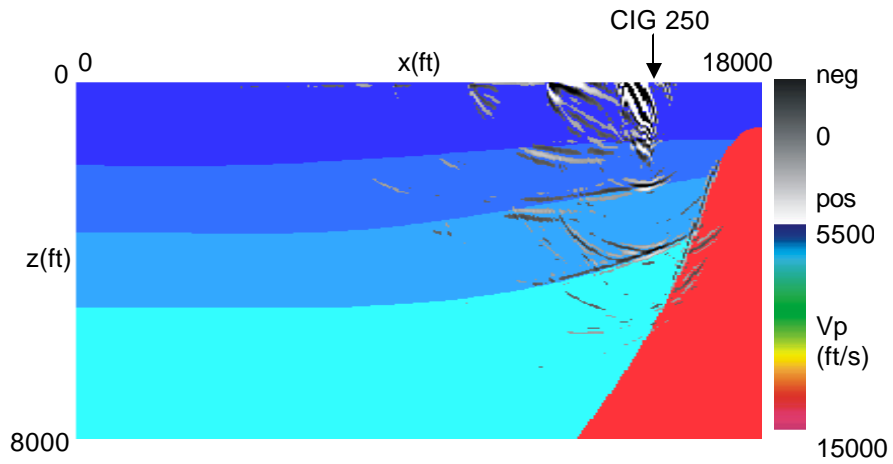


FIG. 5.3.8.a. 2-D elastic PP pre-stack depth image, 14 shots, overlying the P-wave velocity model. No bandpass and semblance weighting applied.

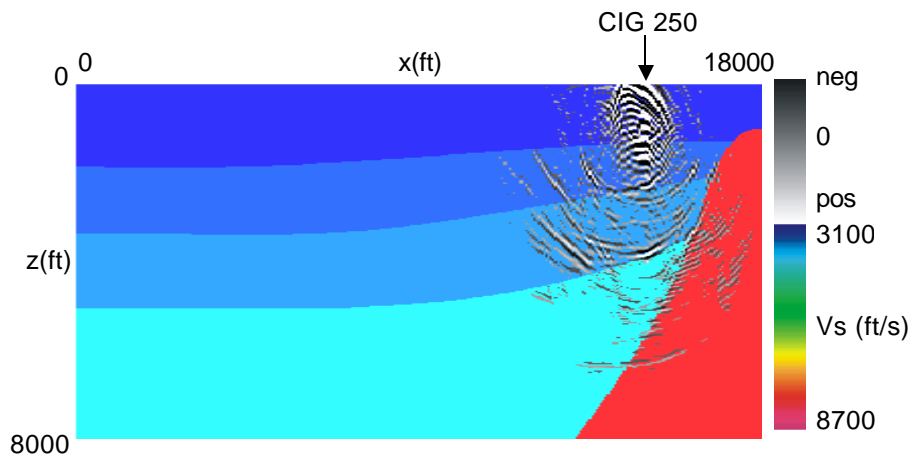


FIG. 5.3.8.b. 2-D elastic PS pre-stack depth image, 14 shots, overlying the S-wave velocity model. No bandpass and semblance weighting applied. Note the high-frequency migration artifacts located along the salt flank, generated by the artificial salt flank reflection.

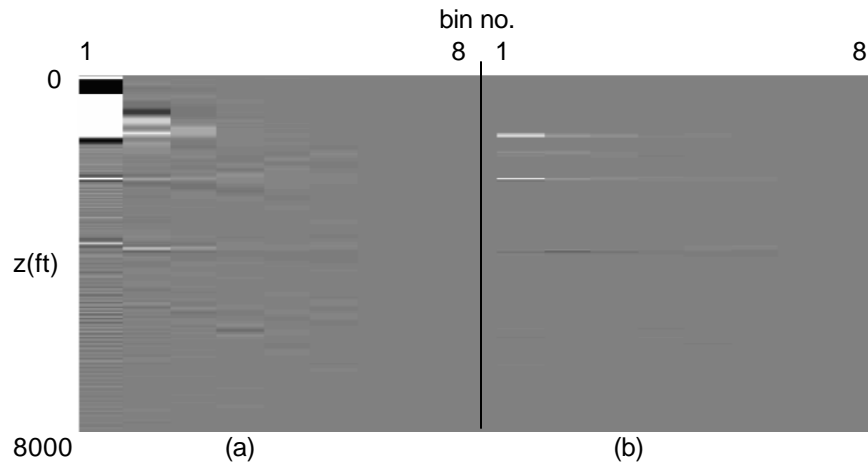


FIG. 5.3.9. Common-image gathers before and after bandpass and semblance weighting generated by elastic PP migration of 14 shots. (a) before bandpass and semblance weighting, (b) after bandpass and semblance weighting

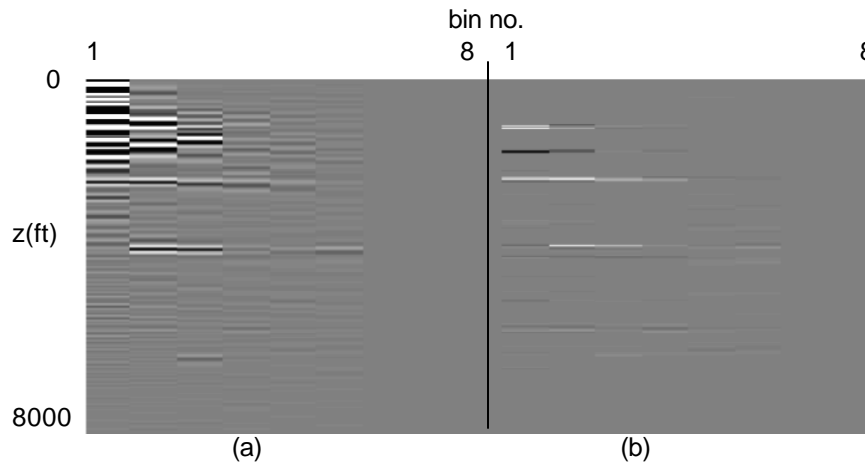


FIG. 5.3.10. Common-image gathers before and after bandpass and semblance weighting generated by elastic PS migration of 14 shots. (a) before bandpass and semblance weighting, (b) after bandpass and semblance weighting

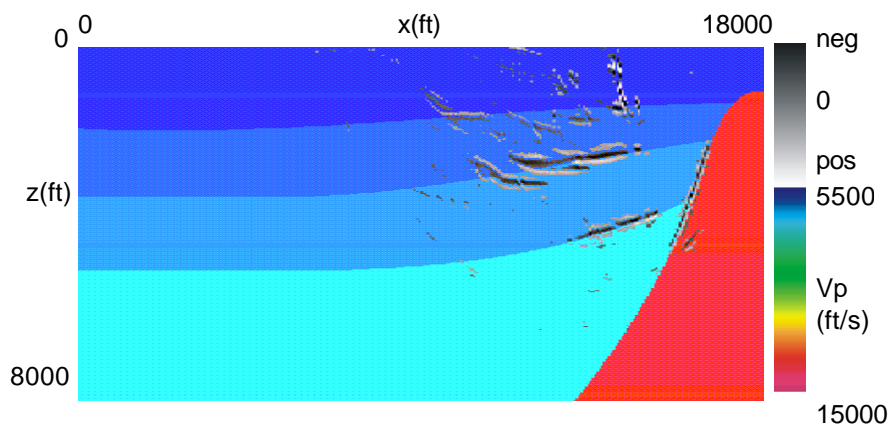


FIG. 5.3.11.a. 2-D elastic PP pre-stack depth image, 14 shots, overlying the P-wave velocity model. Bandpass and semblance weighting applied.

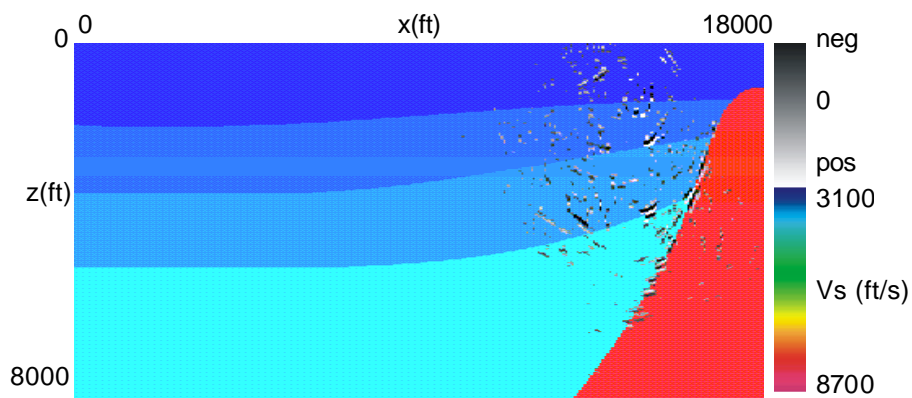


FIG. 5.3.11.b. 2-D elastic PS pre-stack depth image, 14 shots, overlying the S-wave velocity model. Bandpass and semblance weighting applied.

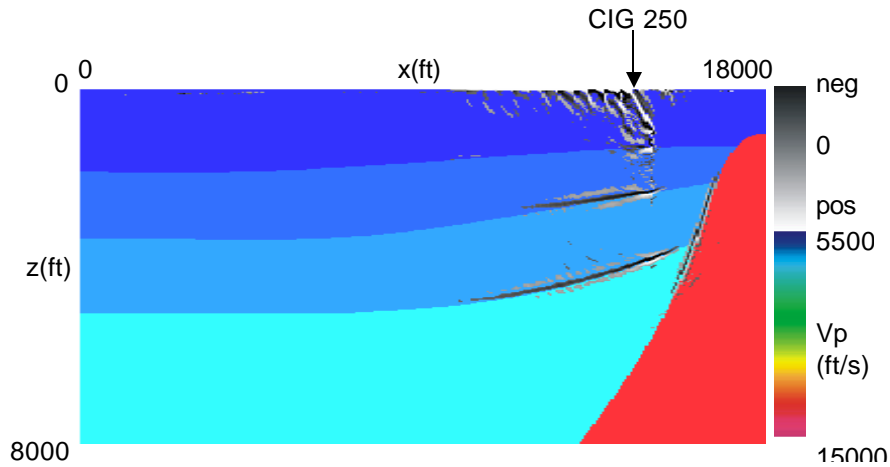


FIG. 5.3.12.a. Elastic 2-D PP depth image, 65 shots, overlying P-wave velocity model. No semblance weighting applied. Note the migration artifacts present in the shallow part of the image, which are due to parts of first breaks left in the common-shot gathers.

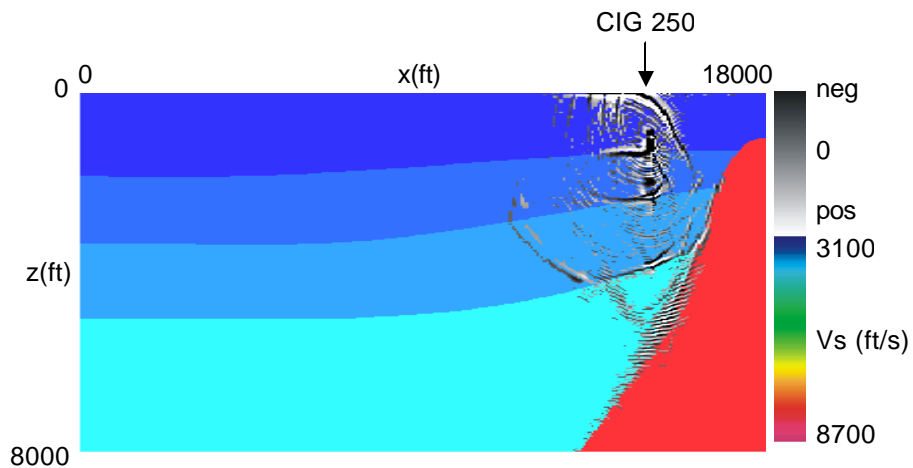


FIG. 5.3.12.b. Elastic 2-D PS depth image, 65 shots, overlying S-wave velocity model. No semblance weighting applied. Note the migration artifacts present in the shallow part of the image, which are due to parts of first breaks left in the common-shot gathers. Note the high-frequency artifacts due to the artificial salt flank reflections. The arrow marks the location of the common-image gather displayed in Figure 5.3.13.

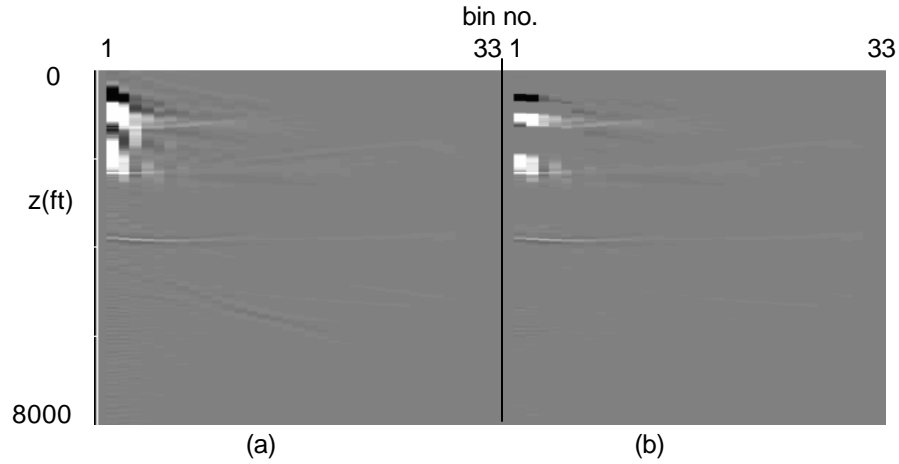


FIG. 5.3.13. Common-image gathers resulting from the elastic PP migration of 65 shots, before and after bandpass filter and semblance weighting. The migration artifacts present in the shallow part of the gather and small offsets are due to parts of first breaks left in common-shot gathers. Note the absence of the incoherent events from the common-image gather obtained after applying semblance weighting.

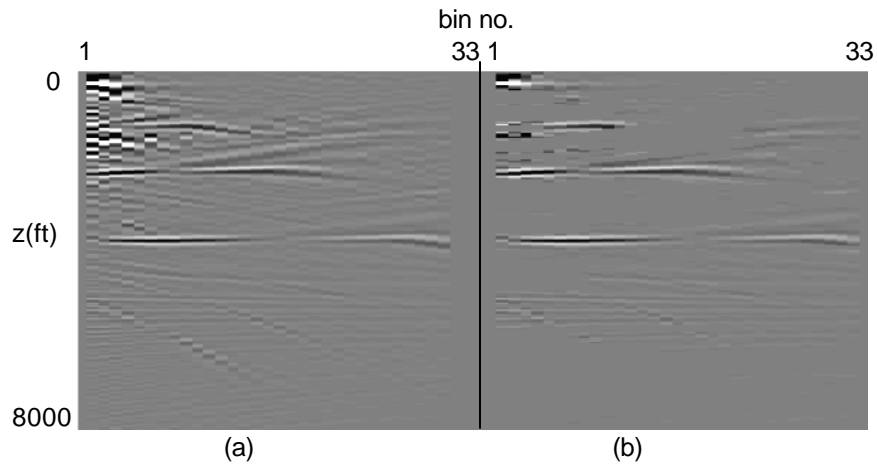


FIG. 5.3.14. Common-image gathers resulting from the elastic PS migration of 65 shots, before and after bandpass filter and semblance weighting. The migration artifacts present in the shallow part of the gather and small offsets are due to parts of first breaks left in common-shot gathers. Note the absence of the incoherent events from the common-image gather obtained after semblance weighting.

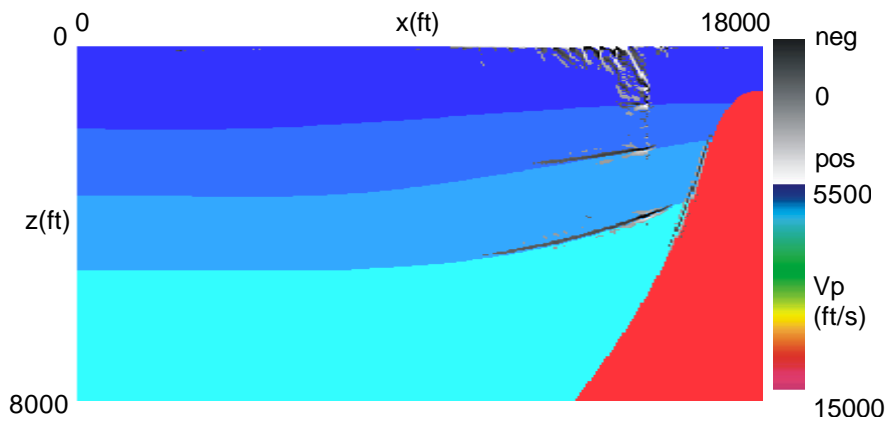


FIG. 5.3.15.a. Elastic 2-D PP depth image, 65 shots, overlying P-wave velocity model. Note the migration artifacts present in the shallow part of the image, which are due to parts of first breaks left in the common-shot gathers. Band pass and semblance weighting applied.

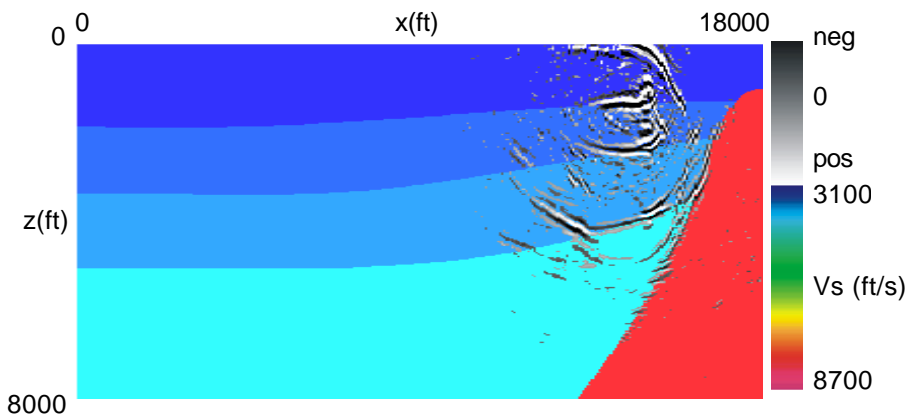


FIG. 5.3.15.b. Elastic 2-D PS depth image, 65 shots, overlying S-wave velocity model. Note that the high-frequency migration artifacts are removed. Bandpass and semblance weighting applied.

5.4. 3-D scalar synthetic VSP pre-stack Kirchhoff depth migration

3-D synthetic acoustic VSP data generation

I built a 3-D P-wave velocity model that resembles the 3-D field P-wave velocity model by placing the salt dome in the lower right corner of the model (Figure 5.4.1). I explained the modeling process in detail in Chapter 4. Since I selected the (x,y) corner coordinates of the velocity model to match the field coordinates, I obtained synthetic shot-gathers for the same space locations like the field shot-gathers. I show a mapview of the field VSP data indicating the location of the synthetic velocity model in Figure 5.4.2.

I generated synthetic shot-gathers, vertical component, for all shots included into the synthetic velocity model. I present an example of a synthetic shot-gather in Figure 5.4.3. The only pre-processing step I performed prior to migration was the first-break removal. I display in Figure 5.4.4 the same shot presented in Figure 5.4.3 after muting the first-breaks. I mark the salt flank reflection by the red arrow.

One important observation is the low frequency of the data, which is determined by the size of the cell grid used during the modeling phase. It is obvious to see that the salt flank reflection is low in amplitude compared to sediment reflections and some multiples, especially the multiple seen right below the salt flank reflection that has high amplitude.

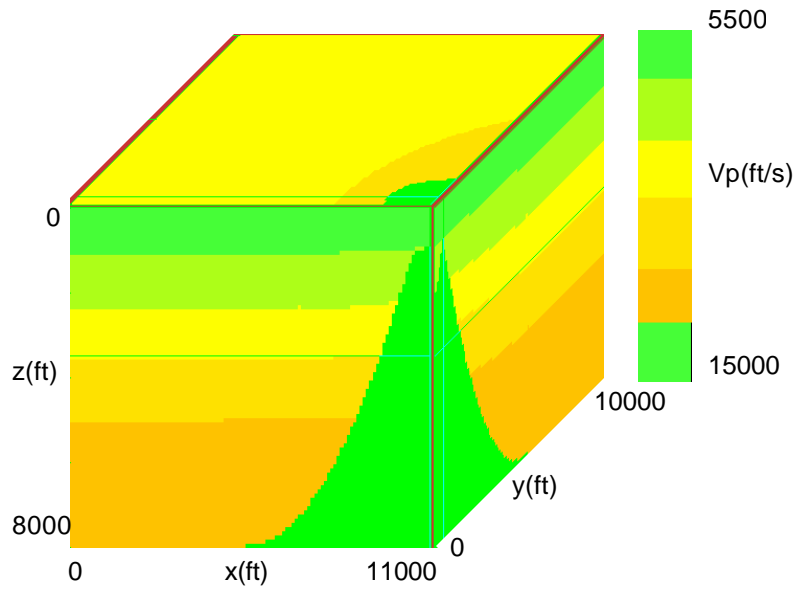


FIG. 5.4.1. 3-D P-wave velocity model used to generate the 3-D acoustic synthetic VSP data. The thin green lines observed on those three faces of the volume mark the location of the sections throughout the volume.

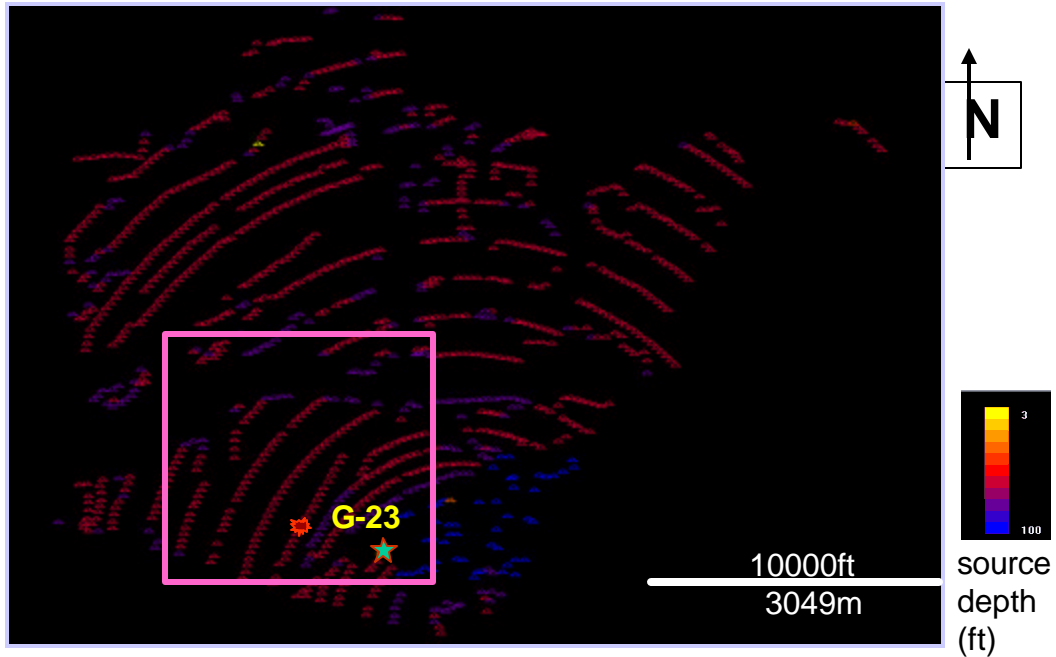


FIG. 5.4.2. Mapview of field sources recorded by VSP well G-23. Color bar is shown on the lower right corner of the mapview. The pink rectangle marks the source locations used in the 3-D VSP subsurface illumination study. The red star marks the location of the synthetic shot presented in the following figures, corresponding to shot no. 2986 from the field VSP data.

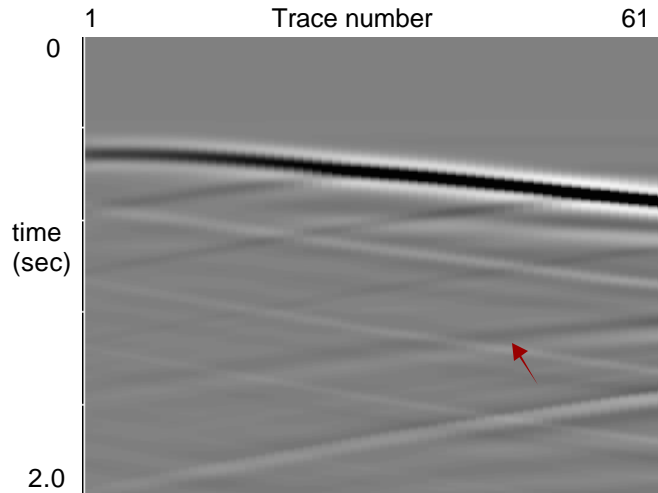


FIG. 5.4.3. Synthetic shot-gather, vertical component, corresponding to shot no. 2986, offset = 2640 ft (805 m). Red arrow marks the salt flank reflection. Trace no. 1 corresponds to receiver no. 1 located at depth = 943 ft (287 m), trace no. 61 corresponds to receiver no. 61 located at depth = 3943 ft (1202 m), with receiver depth spacing = 50 ft (15 m).

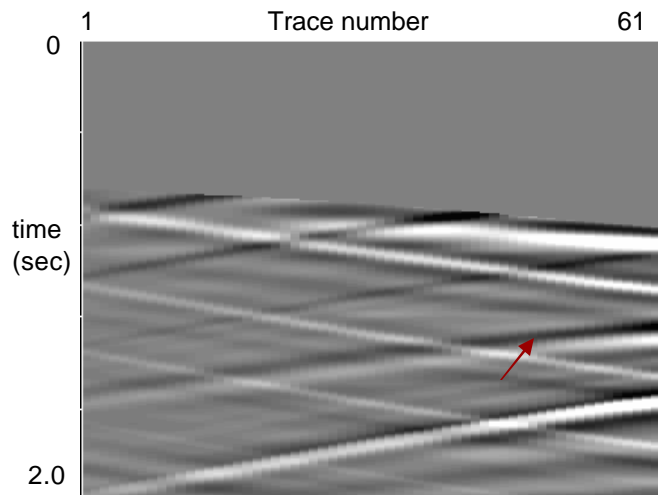


FIG. 5.4.4. Synthetic shot-gather, vertical component, corresponding to shot no. 2986, offset = 2640 ft (805 m). First-break muted. Red arrow marks the salt flank reflection. Note the strong multiple bellow the salt reflection. Trace no. 1 corresponds to receiver no. 1 located at depth = 943 ft (287 m), trace no. 61 corresponds to receiver no. 61 located at depth = 3943 ft (1202 m), with receiver depth spacing = 50 ft (15 m).

Traveltime computation

I calculated the traveltimes using the same algorithm as in the 2-D case, the algorithm based on the Fermat equation. Following a similar idea explained in Section 5.2, I generated the traveltimes using sediment velocity only.

I display the traveltimes corresponding to shot 2986, offset = 2640 ft (805 m) colored by the traveltimes measured in sec, in Figure 5.3.2.1. I also display the receiver traveltimes volume (receiver no. 1), colored by the traveltimes measured in sec, in Figure 5.3.2.2. The thin white lines observed on top face of the cube marks the location of the sections displayed on the side faces of the cube.

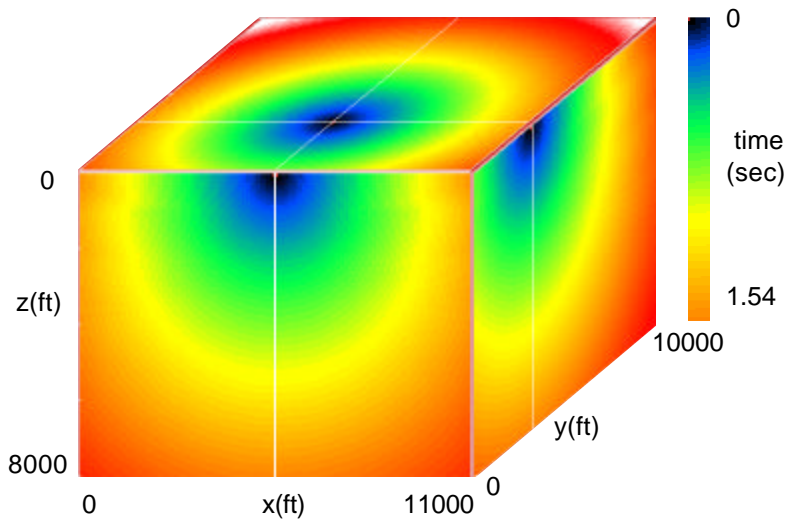


FIG. 5.4.5. Source traveltimes volume calculated using P-wave velocity, colored by traveltimes measured in sec. Shot no. 2986, offset = 2640 ft (805 m). The side cube faces show the inline and crossline sections through the 3-D traveltimes volume intersecting at location of shot 2986.

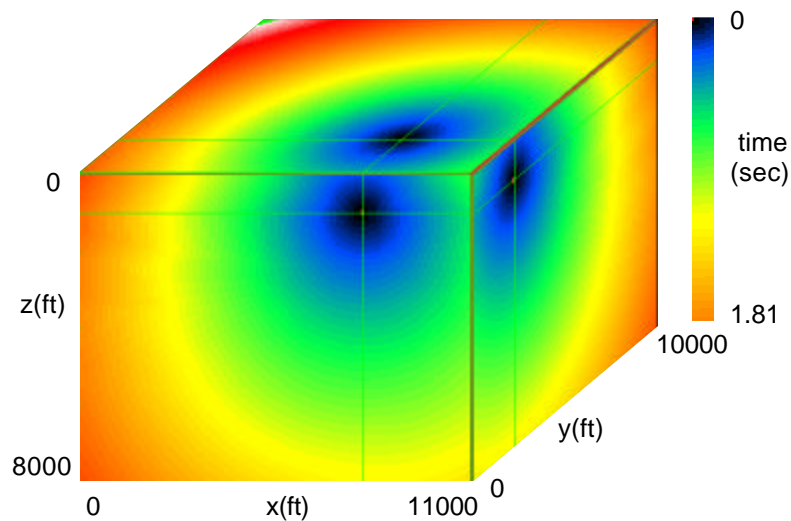


FIG. 5.4.6. Receiver traveltime volume calculated using P-wave velocity, colored by traveltime measured in sec. Receiver no. 1, depth = 943 ft (288 m). The side cube faces show the inline and crossline sections through the 3-D traveltime volume intersecting at the location of the 1st receiver from VSP well.

3-D synthetic scalar VSP Kirchhoff pre-stack depth migration

I migrated the 3-D acoustic synthetic VSP data using the scalar Kirchhoff pre-stack depth migration algorithm described in detail in Section 5.2. I first migrated shot no. 2986 and then I migrated the rest of the shots encompassed by the synthetic velocity model. I display the resulting images in Figures 5.4.7- 5.4.8. These 3-D PP images are displayed before applying semblance weighting stacking. For the 3-D case, I chose to sort the migration output with respect to the receiver depth, grouping 5 receivers into one bin.

Since the 3-D VSP synthetic data have basically the same acquisition geometry like the VSP field data, those synthetic images should give me an insight about the field VSP images. Notice that the depth images are centered at the well location, as expected based on the 2-D tests, and that the lateral extent of the image increases with depth. The salt flank image has low amplitude, almost indistinguishable from the other events. The multiples noticed in the synthetic shot-gather, located right below the salt reflection, create a strong artifact in the depth image updip the salt flank image.

To remove the migration smiles, I applied the semblance weighting stacking on the common-image gathers generated by the scalar 3-D pre-stack depth migration. I show an example of common-image gather before and after semblance weighting in Figure 5.4.9 and the final image in Figure 5.4.10. The semblance weighting has proven to be very effective especially in removing the migration artifacts presented around the sedimentary boundary images. Note how clean these particular interface images look after semblance weighting.

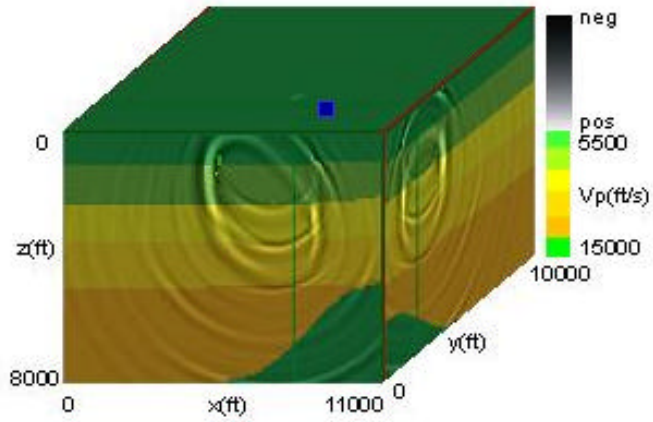


FIG. 5.4.7. 3-D PP depth image generated by migrating synthetic shot-gather corresponding to shot no. 2986. The depth image overlays the P-wave velocity model. The blue dot indicates the VSP well location. The side cube faces show the inline and crossline sections through the 3-D migrated volume intersecting at the VSP well.

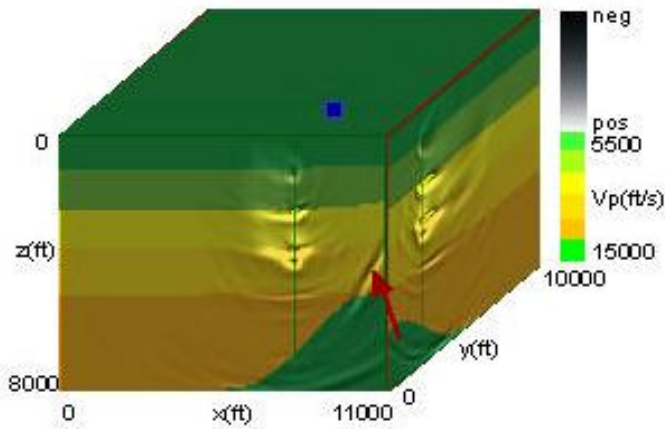


FIG. 5.4.8. 3-D PP depth image generated by migrating the synthetic shot-gathers. The depth image overlays the P-wave velocity model. The blue dot indicates the VSP well location. The side cube faces show the inline and crossline sections through the 3-D migrated volume intersecting at the VSP well. Red arrow points to an image artifact created by multiples. Note the migration artifacts around sedimentary boundary images created by multiples.

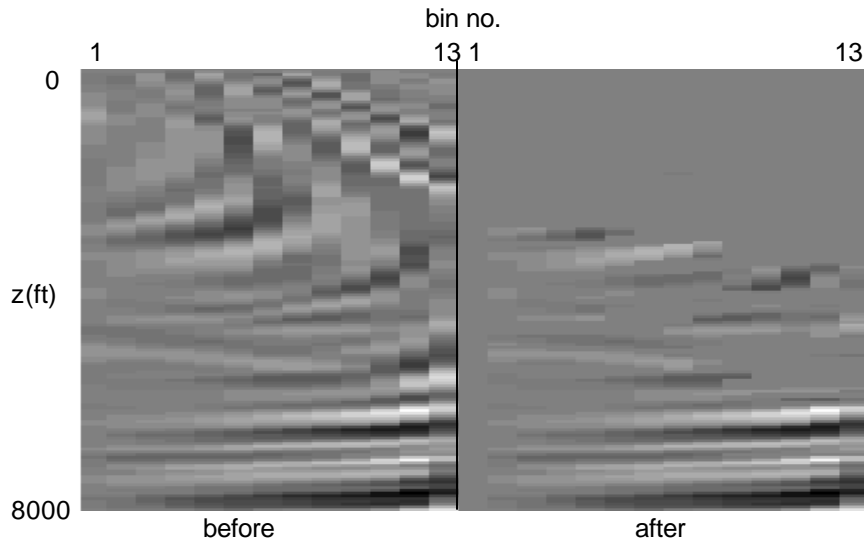


FIG. 5.4.9. Common-image gathers before and after applying semblance weighting stacking. Note how most of the incoherent events are removed.

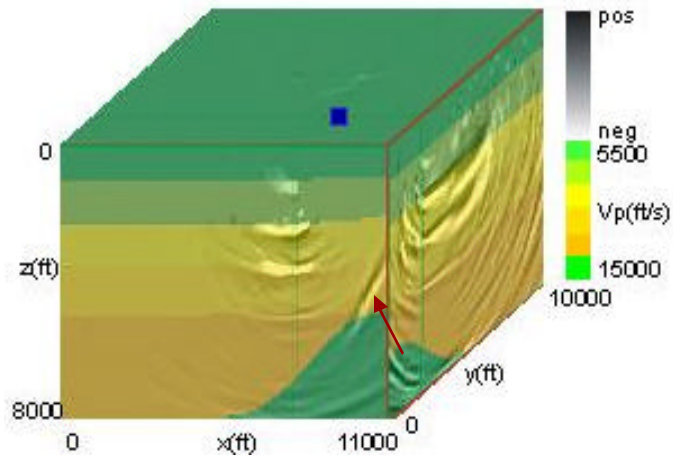


FIG. 5.4.10. 3-D PP synthetic depth image overlaying P-wave velocity model. The blue dot indicates the VSP well location. The side cube faces show the inline and crossline sections through the 3-D migrated volume intersecting at the VSP well. Red arrow points to an image artifact created by multiples. Semblance weighting applied.

5.5. 3-D 3-C VSP elastic Kirchhoff pre-stack depth migration –

Vinton Dome, Louisiana

3-D 3-C VSP Vinton Dome, Louisiana

I presented in great detail the acquisition and processing of the 3-D 3-C VSP Vinton Dome data set. For this reason, I will only show in this section the mapview of the Vinton Dome field survey with the location of shot no. 3068 marked by a red star (Figure 5.5.1) and shot no. 3068, as it was input into the elastic migration program (Figure 5.5.2). Due to the absence of a 3-D 3-C P-/S-wave separation algorithm, I will not perform 3-D scalar Kirchhoff pre-stack depth migration on the field data.

For convenience, I excluded shots 2856 to 2986 because of the inconsistent number of channels in the shot-gathers. I decided to migrate only shots having the same number of traces (61). Also, I excluded shots that had offset greater than 16000 ft. In these particular shots, most of the energy is represented by turning waves and not by reflections. Since this elastic depth migration algorithm is not designed to handle turning waves, their presence in the data will generate migration artifacts.

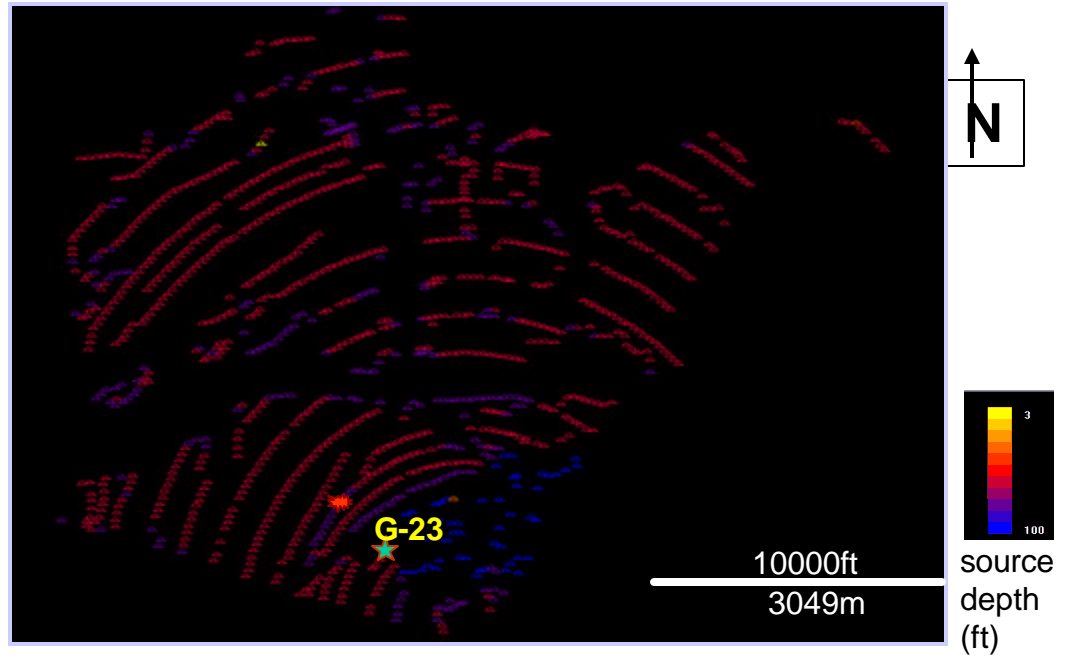


FIG. 5.5.1. Mapview of field sources recorded by VSP well G-23. Color bar is shown on the lower right corner of the mapview. The red star marks the location of shot no. 3068, offset = 1989 ft (606 m) presented in the previous figure.

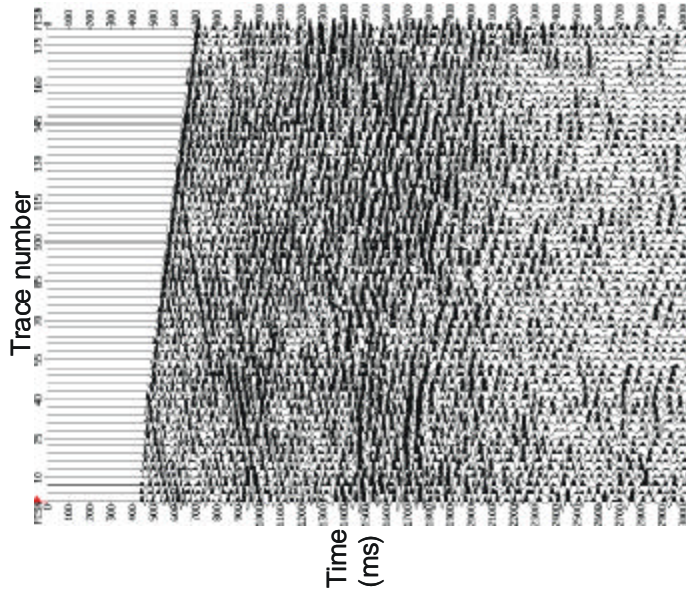


FIG. 5.5.2.a. Field common-shot gather, vertical component. Shot no. 3068, offset = 1989 ft (606 m). First breaks muted.

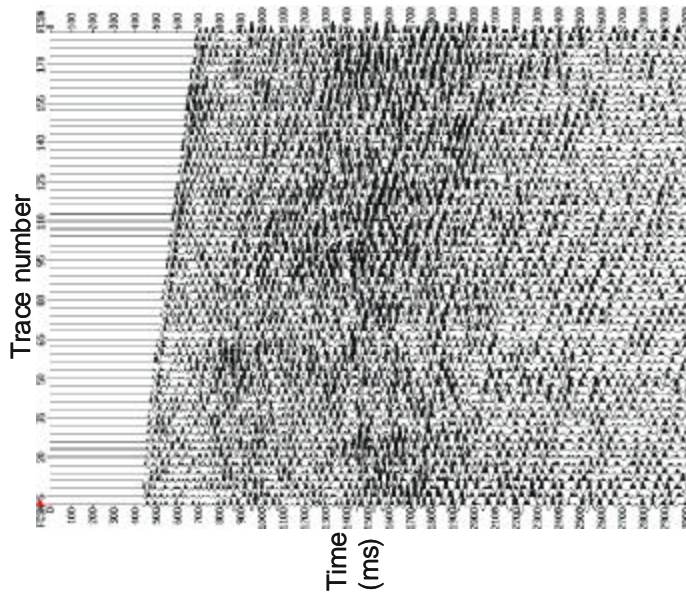


FIG. 5.5.2.b. Field common-shot gather, east component. Shot no. 3068, offset = 1989 ft (606 m). First breaks muted.

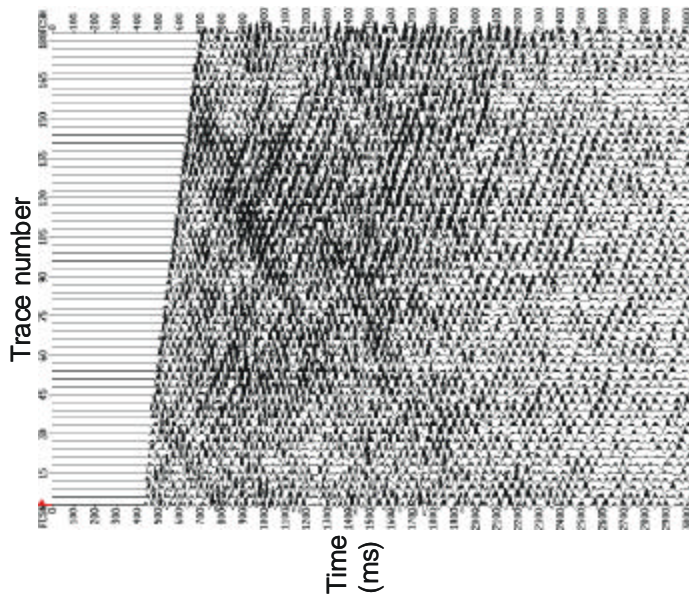


FIG. 5.5.2.c. Field common-shot gather, north component. Shot no. 3068, offset = 1989 ft (606 m). First breaks muted.

Traveltime computation

I calculated the source and receiver traveltimes using the same FMEikonal algorithm described in the previous sections. I followed the same procedure as in the synthetic data case, meaning I calculated traveltimes using sediment velocity only.

The first step consists of analyzing the 3-D P-wave velocity model created by Duncan (Duncan, 2005) for the surface seismic survey. The second step consists of windowing the 3-D velocity model according to the size of the VSP survey. The third step consists of calculating the S-wave velocity model. A brief analysis of Gamma-Ray logs recorded in the Vinton field area indicated that the majority of layers are composed

of sand with shale intercalations. For simplicity, I used only the V_p/V_s castagna's relationship derived for sand lithology.

$$V_s = -0.856 + 0.804 \cdot V_p \quad (5.5.1)$$

I first present a mapview of the entire velocity model created by my colleague Duncan (Duncan, 2005) overlaid by a rectangle that marks the velocity model selected for the VSP survey (Figure 5.5.3). Next, I display 3-D P- and S-wave velocity models used to calculate the source and receiver traveltimes volumes (Figures 5.5.4 – 5.5.5). I computed the source traveltimes volumes using P-wave velocity (Figure 5.5.6) and receiver traveltimes volumes using both, P- and S-wave velocity (Figure 5.5.7 – 5.5.8).

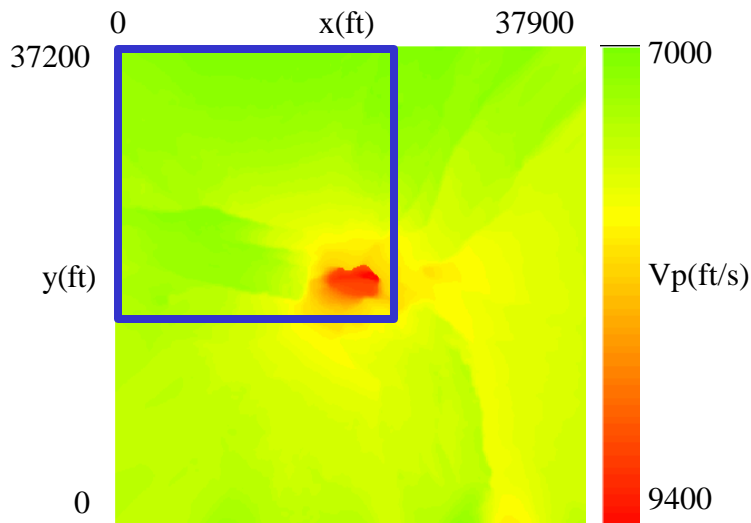


FIG. 5.5.3. Mapview of original P-wave velocity model colored by P-wave velocity. Blue rectangle marks the VSP velocity model. Depth slice = 2490 ft.

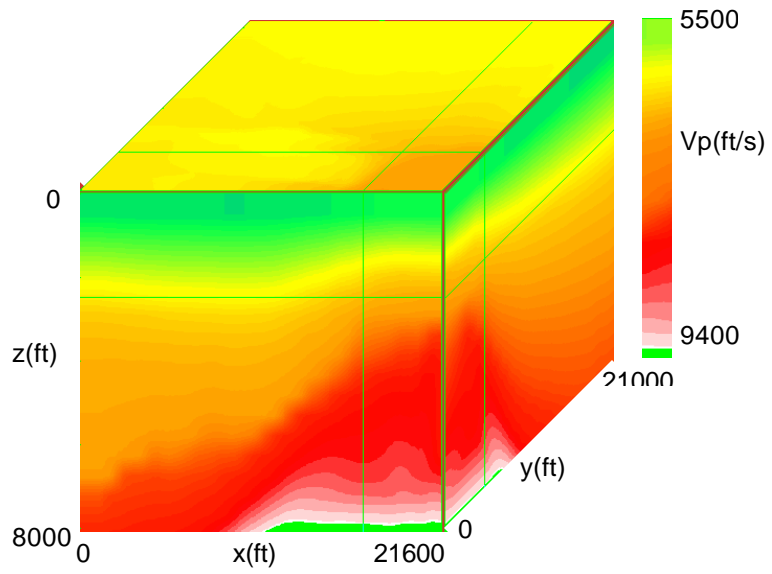


FIG. 5.5.4. 3-D P-wave velocity model colored by P-wave velocity.

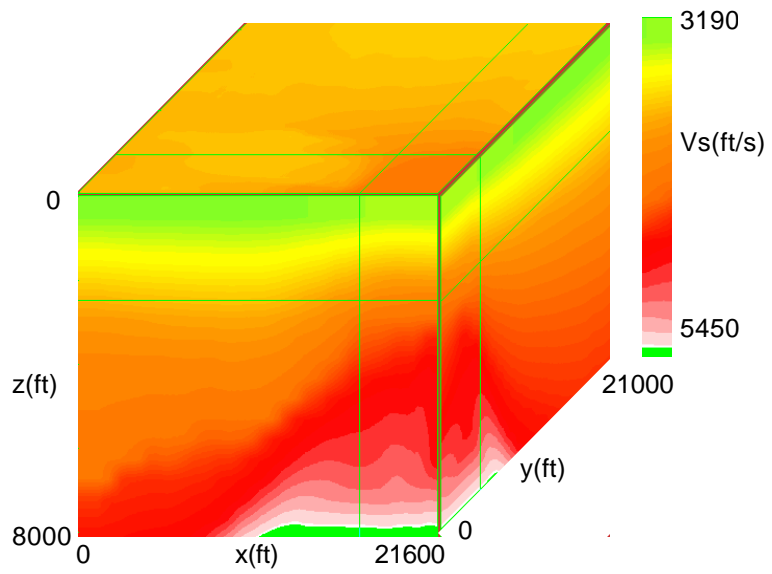


FIG. 5.5.5. 3-D S-wave velocity model colored by S-wave velocity.

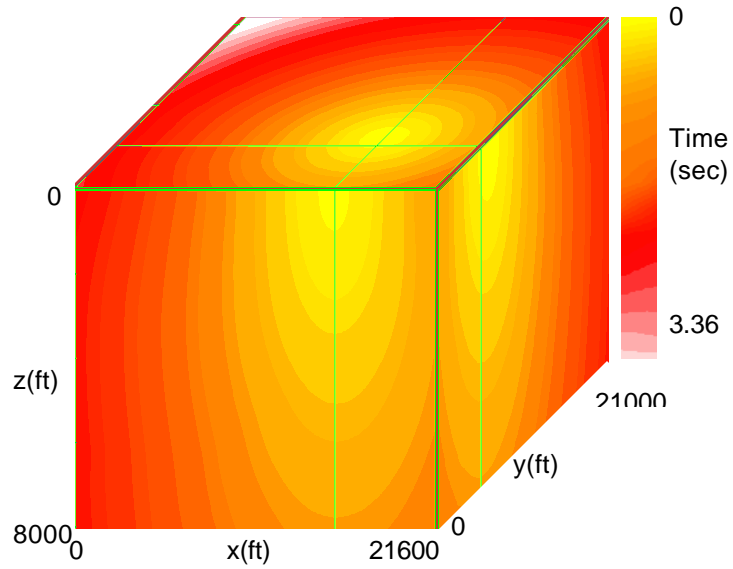


FIG. 5.5.6. Source traveltime volume calculated using P-wave velocity, measured in seconds. Shot no. 3068, offset = 1989 ft (606 m).

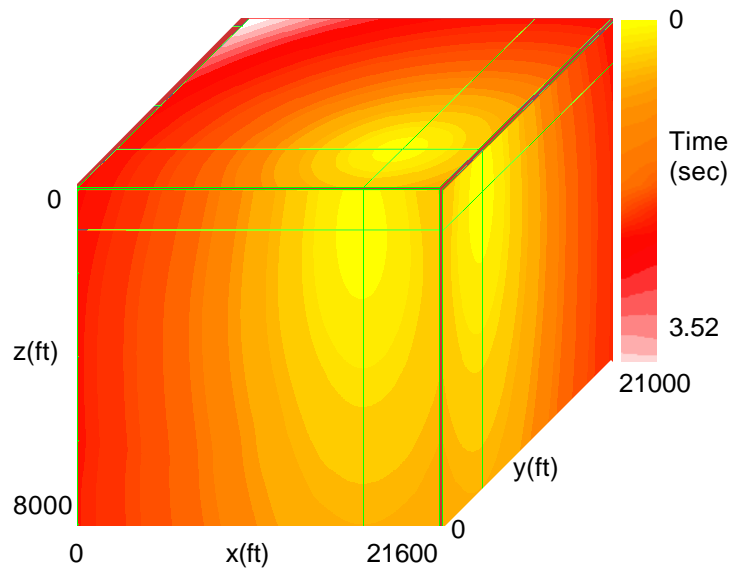


FIG. 5.5.7. Receiver traveltime volume calculated using P-wave velocity, measured in seconds. Receiver no. 1, depth = 943 ft (287 m).

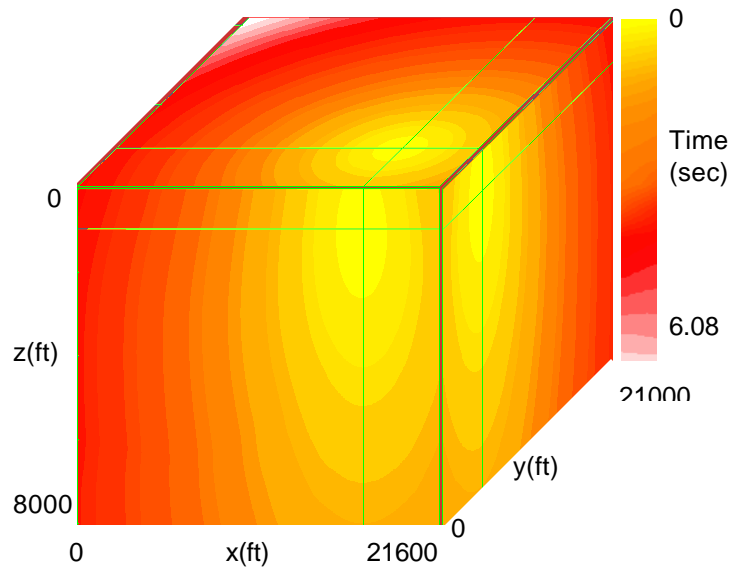


FIG. 5.5.8. Receiver traveltime volume calculated using S-wave velocity, measured in seconds. Receiver no. 1, depth = 943 ft (287 m).

3-D 3-C VSP Kirchhoff pre-stack depth migration – Vinton Dome, Louisiana

I followed the same workflow as for the synthetic case. I started by performing elastic PP and PS depth migration on a single common-shot gather, shot no. 3068. I present the elastic PP and PS depth images in Figure 5.5.9. I also chose to sort the migration output with respect to the receiver depth, grouping 5 receivers into one bin.

Based on the 2-D and 3-D modeling results, we know that the VSP subsurface illumination concentrates around the well location, so I created the depth images only for a small cube located around the VSP well. The dimensions of the VSP velocity model are

21600 ft x 21000 ft x 8000 ft (6585 x 6402 x 2439 m), while the dimensions of the output image volume are 12600 x 4800 x 8000 ft (3840 x 1463 x 2439 m). Since the subsurface illumination does not extend too much laterally, I expect a low constructive interference away from the well that allows the presence of the migration smiles in the final image.

To test the data aliasing problem, I selected a group of shots located along a radial line and a concentric arc marked by red stars in Figures 5.5.10 - 5.5.11. I generated elastic PP and PS depth images without (Figure 5.5.12 – 5.5.13) and with semblance-weighting factor (Figure 5.5.14 – 5.5.15). I also show an example of PP and PS common-image gathers before and after semblance weighting (Figure 5.5.16). Analysis of the depth images indicated that the PP and PS depth images generated for the concentric arc case show better continuity of the reflectors than in 2-D radial line case.

Next, I selected a group of 600 shots marked by the red polygon in Figure 5.5.17 with offset varying between 500 ft (152 m) and 15000 ft (4573 m) and generated elastic PP and PS depth images (Figure 5.5.18). The thin green lines mark the location of the inline, crossline and depth slices intersecting at the level of the first receiver in the well.

As specified in the previous sections, semblance weighting factor proves to be efficient in removing parts of the migration smiles. We can remove more or less incoherent energy from the image-gathers by selecting different values for the “semb_cut” and “semb_pass” parameters. “Semb_cut” represents the minimum semblance value of the removed data and “semb_pass” represents the minimum semblance value of the preserved data. The events with a lower semblance value than “semb_cut” will be removed and with a higher semblance values than “semb_pass” will be preserved. I present an example of common-image gathers before and after semblance

weighting in Figure 5.5.19 and the final elastic PP and PS depth images, after semblance weighting, in Figure 5.5.20.

The elastic PP depth image shows a better continuity of the reflectors compared to the elastic PS depth image. One problem I noticed in the final depth image is the lack of continuity of the shallow reflectors, which is due to muting the first breaks. One way to improve the quality of the depth images is using another solution to first break removal instead of muting. The first break removal does not pose a problem when applying up-going/down-going separation filter. I performed the wavefield separation on the field common-shot gathers via f-k filter. I display an example of common-shot gather, up-going events only, in Figure 5.5.21. I present the PP and PS depth images for the group of 600 shots, up-going events only, after semblance weighting, in Figure 5.5.22. I noticed an improved image of the shallow reflectors.

To calibrate my VSP depth images I checked the similarity between my PP VSP elastic depth migrated volume with Duncan's PP scalar depth migrated volume generated using surface data. I noticed quite a good similarity at the VSP well location between those two depth migrated volumes. I also interpreted a few horizons on the surface migrated volume and plotted the picks on the VSP migrated volume, picks that matched perfectly with the surface migrated volume. I display a section through the surface and VSP depth migrated volumes, located at the VSP well, showing the interpreted horizons in Figure 5.5.23.

An extra piece of information present on the VSP images represents the reflectors marked by the red arrows, which might indicate the salt flank image. Previous information (Duncan, 2005) suggests a "Christmas-tree" shape of the salt dome, a shape

that I consider is confirmed by the portion of the image located around 3000 - 4000 ft (915 – 1220 m). If accurate, this “Christmas-tree” shape of the salt dome will make the salt flank imaging more difficult.

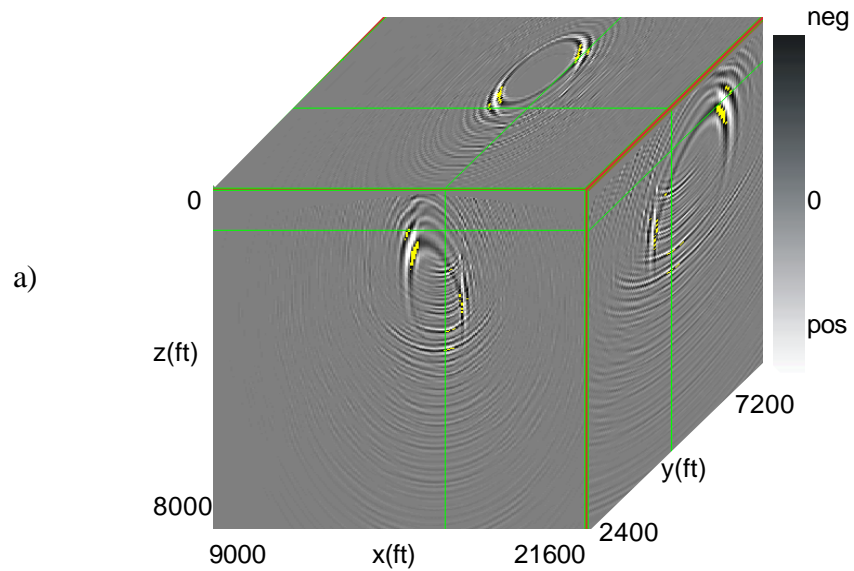


FIG. 5.5.9. a) 3-D PP elastic depth image; b) 3-D PS elastic depth image. Shot no. 3068, offset = 1989 ft (606 m). No semblance weighting applied. The migration artifacts present in the shallow part of the image, relatively closed to the well location, are due to multiples and leaks of first breaks. Green lines represent the inline, crossline and depth slices intersecting at the receiver no. 1 location.

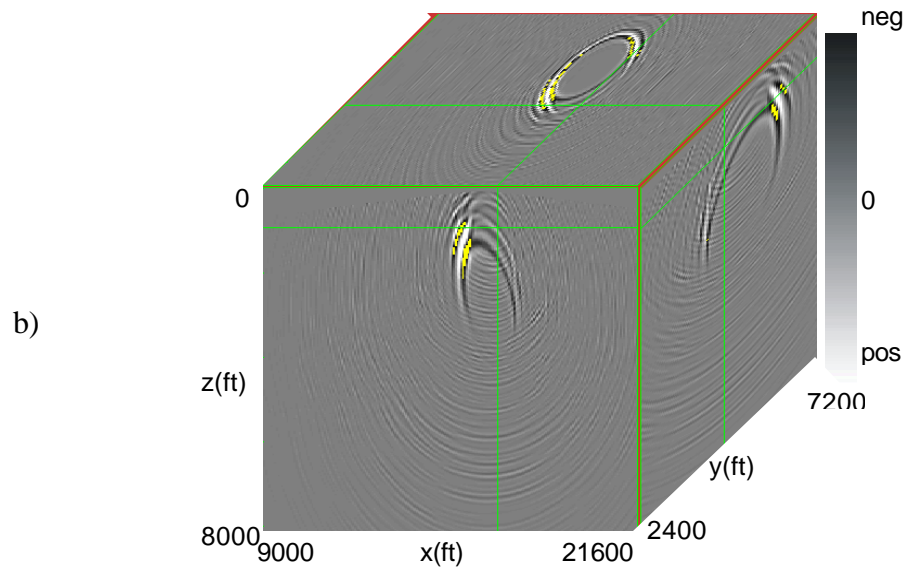


FIG. 5.5.9. (continued)

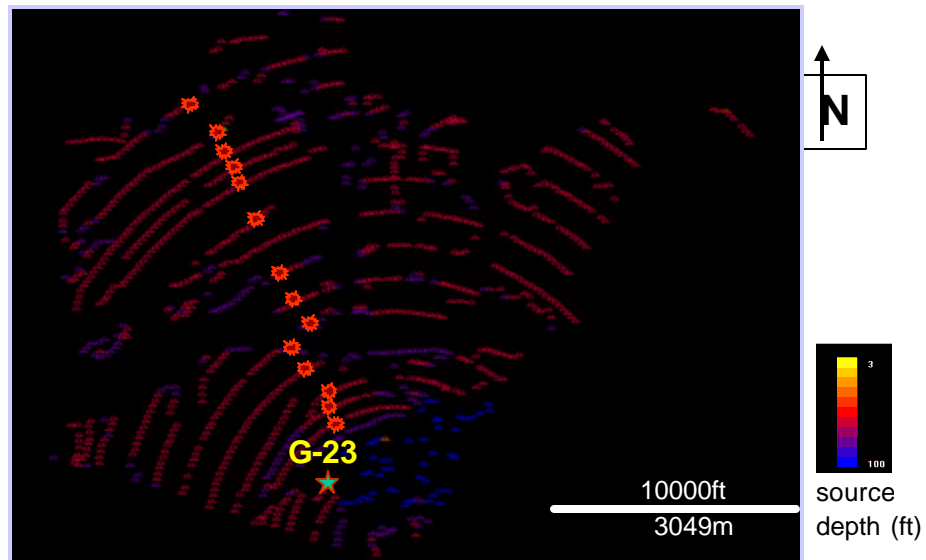


FIG. 5.5.10. Mapview of field sources recorded by the G-23 VSP well. Red stars mark a group of 14 shots located along a radial line used in migration.

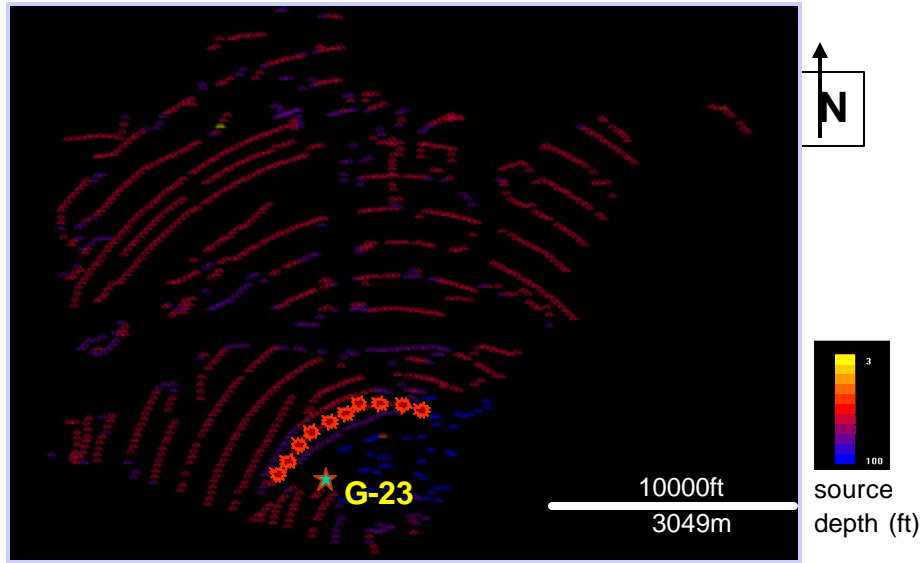


FIG. 5.5.11. Mapview of field sources recorded by the G-23 VSP well. Red stars mark a group of 36 shots located along a concentric arc used in migration.

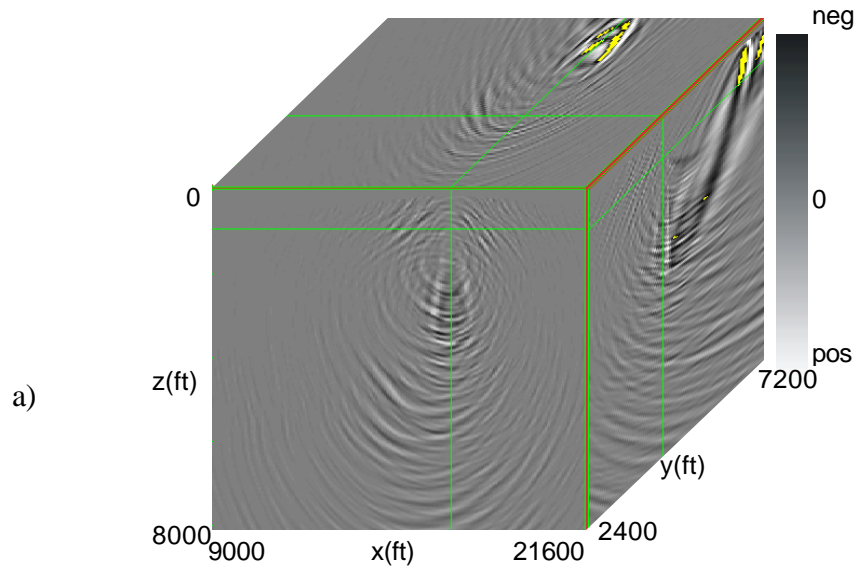


FIG. 5.5.12. a) 3-D PP elastic depth image; b) 3-D PS elastic depth image. 14 shots migrated. Green lines represent the inline, crossline and depth slices intersecting at the receiver no. 1 location. No semblance weighting applied.

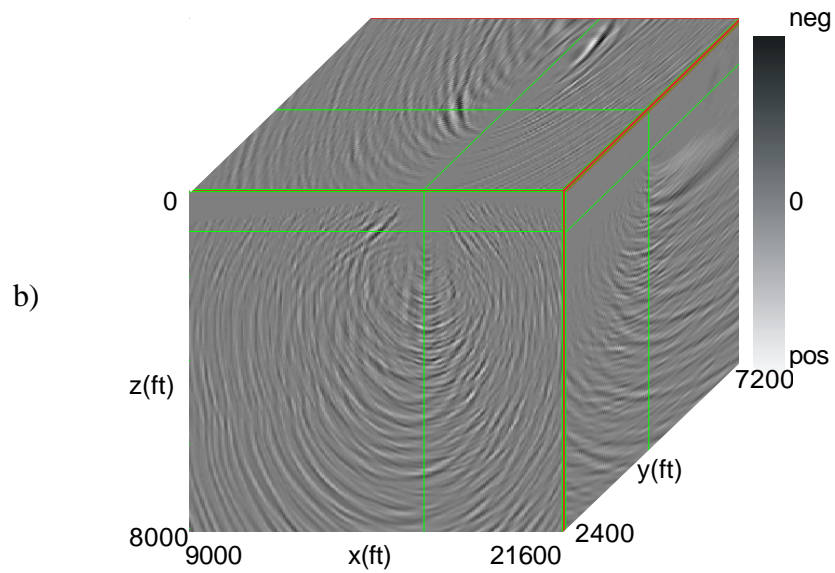


FIG. 5.5.12. (continued)

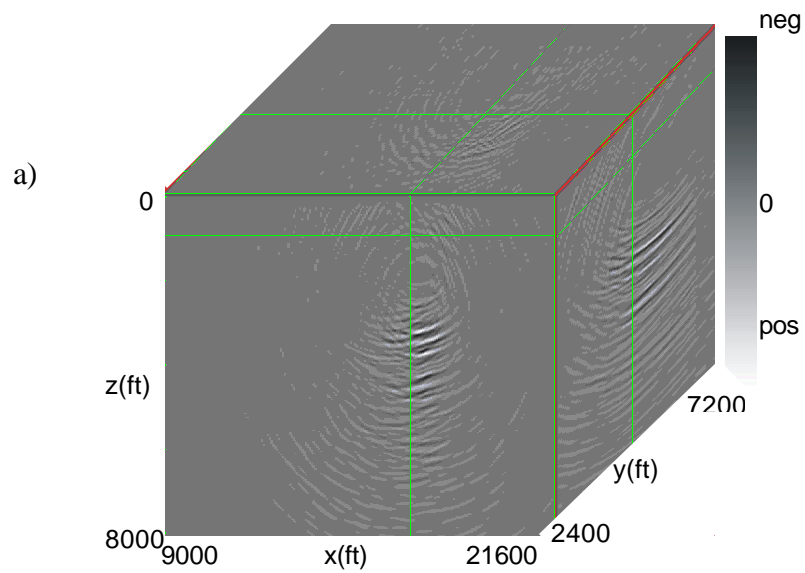


FIG. 5.5.13. a) 3-D PP elastic depth image; b) 3-D PS elastic depth image. 36 shots migrated. Green lines represent the inline, crossline and depth slices intersecting at the receiver no. 1 location. No semblance weighting applied.

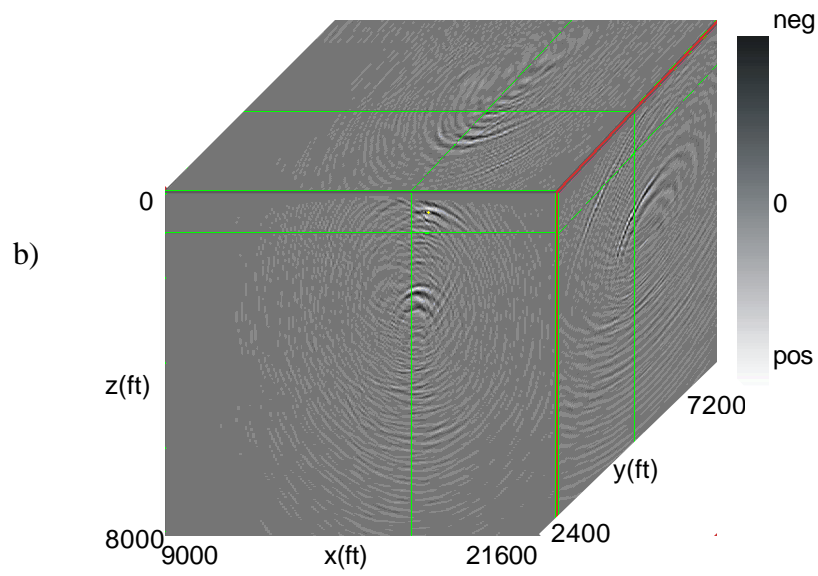


FIG. 5.5.13. (continued)

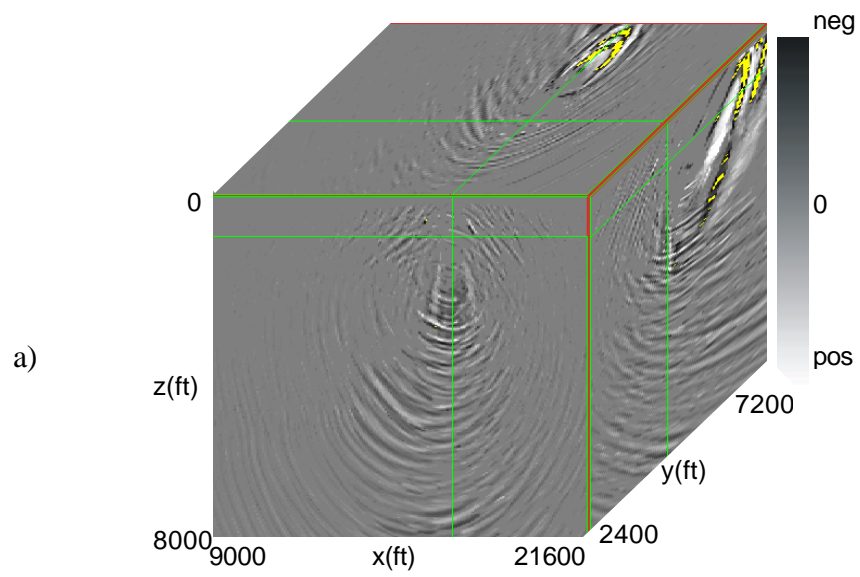


FIG. 5.5.14. a) 3-D PP elastic depth image; b) 3-D PS elastic depth image. 14 shots migrated. Green lines represent the inline, crossline and depth slices intersecting at the receiver no. 1 location. Semblance weighting applied.

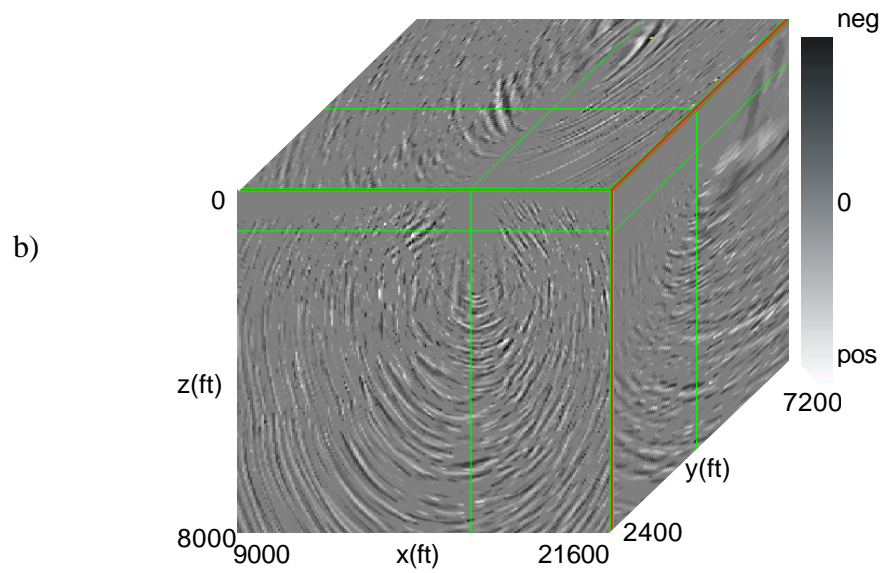


FIG. 5.5.14. (continued)

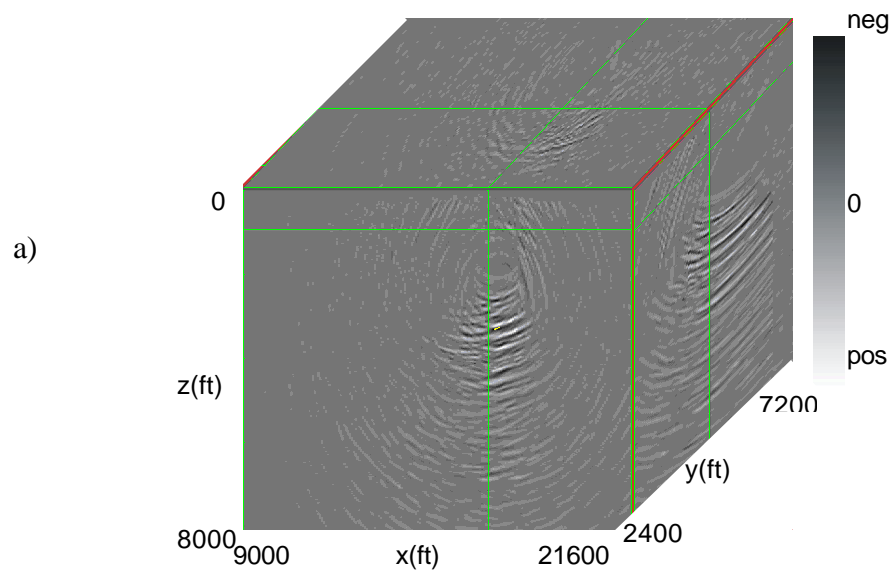


FIG. 5.5.15. a) 3-D PP elastic depth image; b) 3-D PS elastic depth image. 36 shots migrated. Green lines represent the inline, crossline and depth slices intersecting at the receiver no. 1 location. Semblance weighting applied.

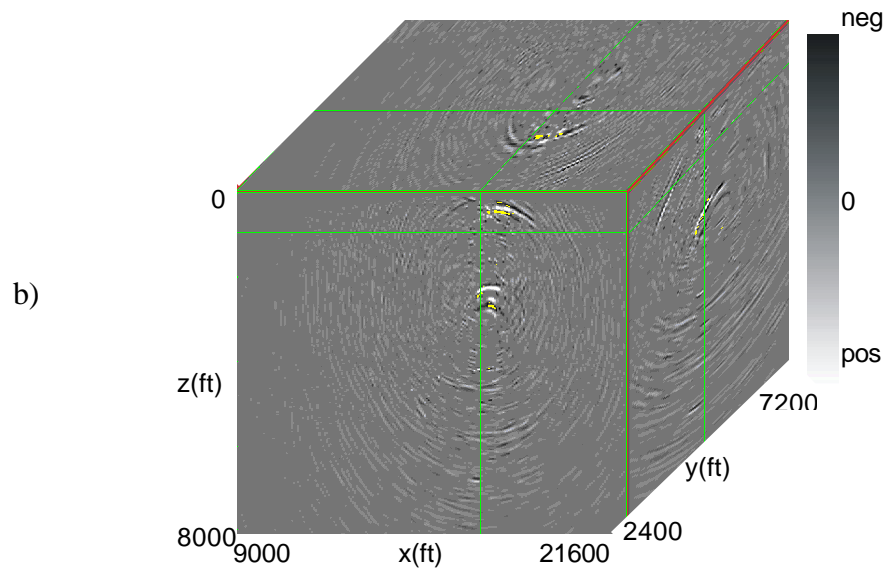


FIG. 5.5.15. (continued)

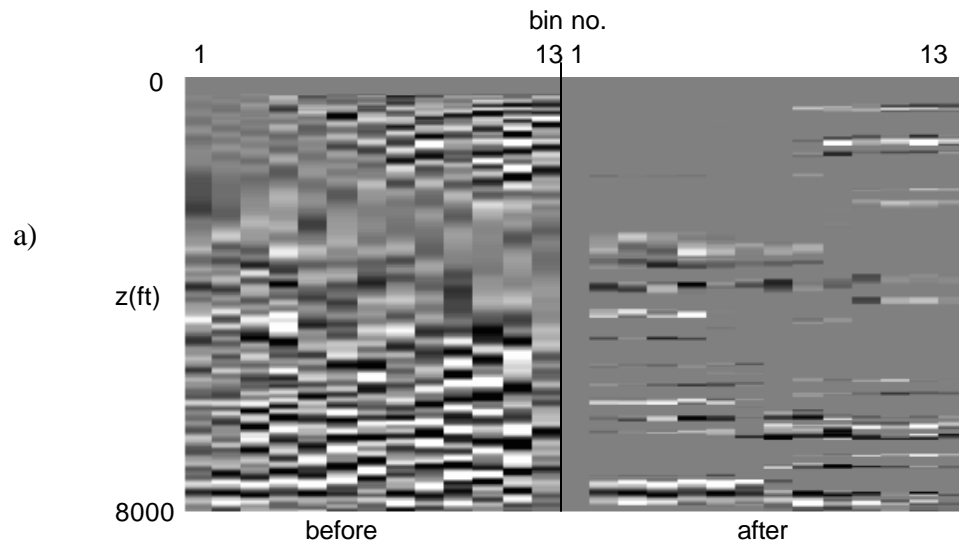


FIG. 5.5.16. a) PP common-image gathers; b) PS common-image gathers before and after applying semblance weighting stacking. 14 shots migrated. Note how most of the incoherent events are removed.

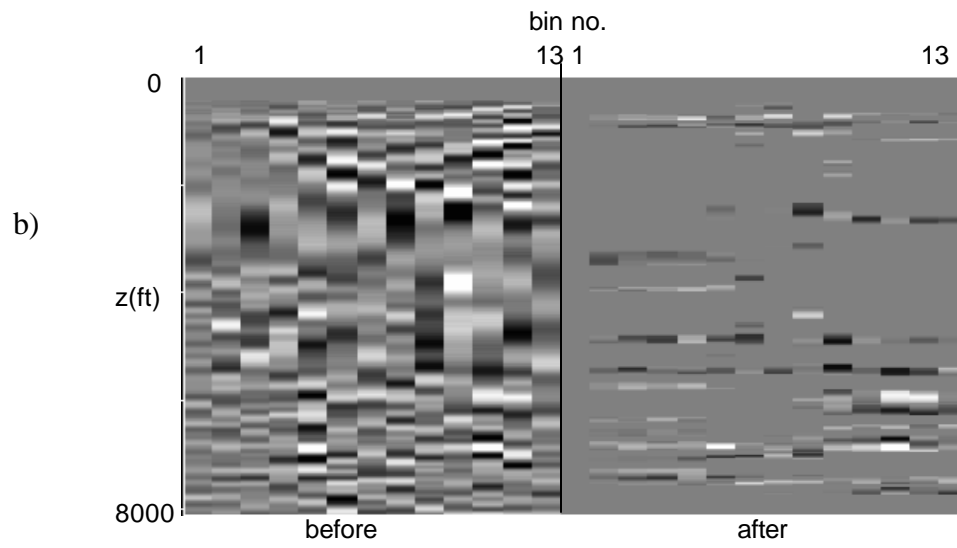


FIG. 5.5.16. (continued)

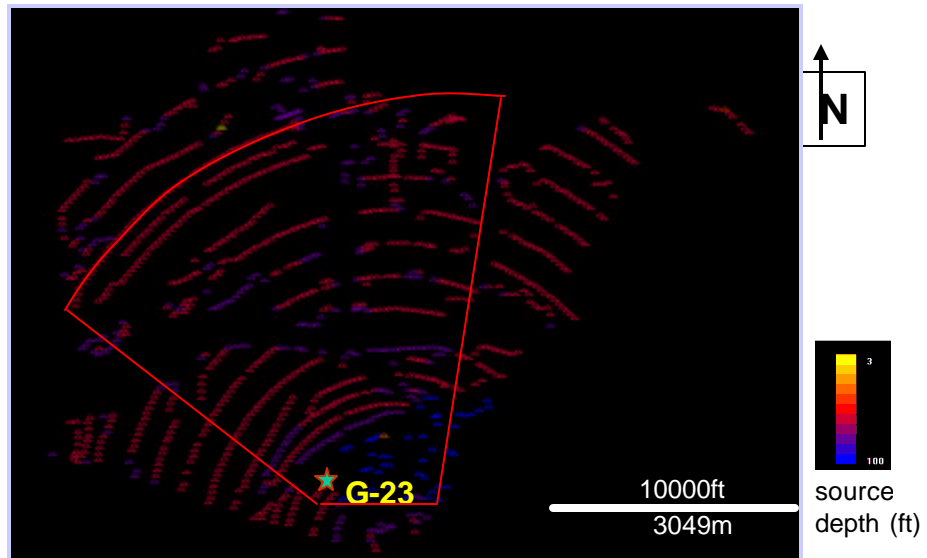


FIG. 5.5.17. Mapview of field sources recorded by the G-23 VSP well. Red polygon mark a group of 600 shots used in migration.

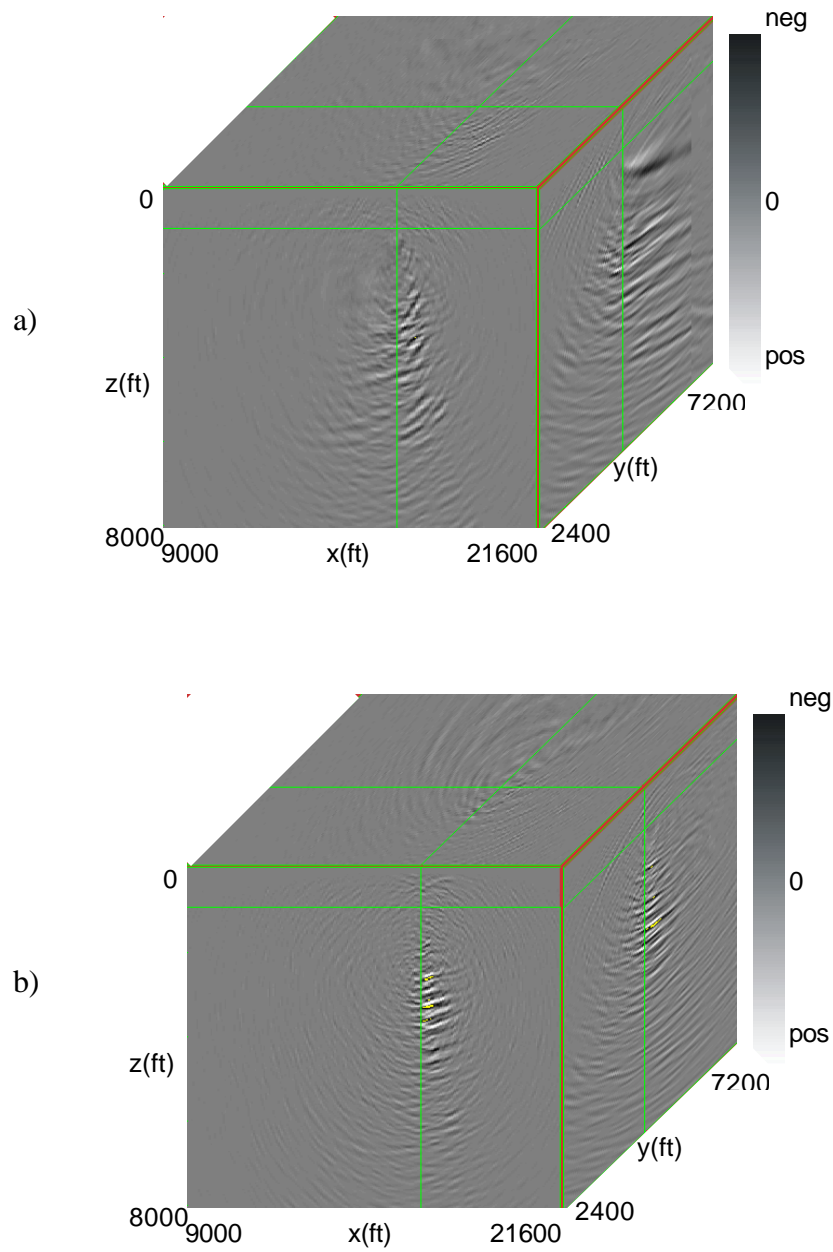


FIG. 5.5.18. a) 3-D PP elastic depth image; b) 3-D PS elastic depth image obtained by migrating 600 shots. Green lines represent the inline, crossline and depth slices intersecting at the receiver no. 1 location. No semblance weighting applied.

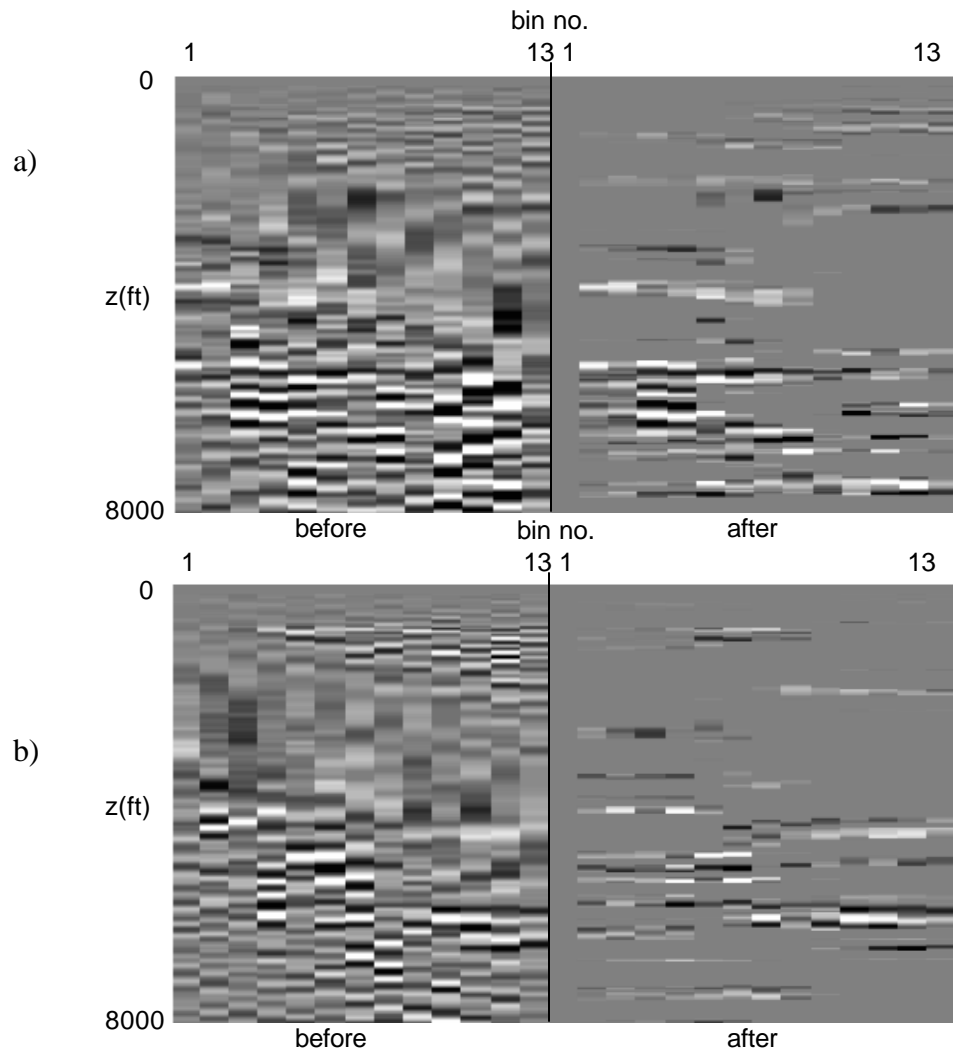


FIG. 5.5.19. a) PP common-image gathers; b) PS common-image gathers before and after applying semblance weighting stacking. 600 shots migrated. Note how most of the incoherent events are removed.

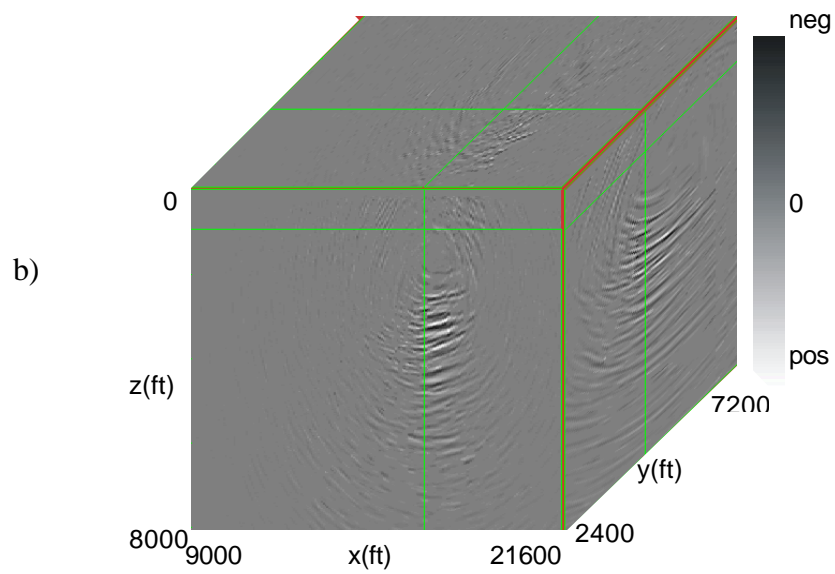
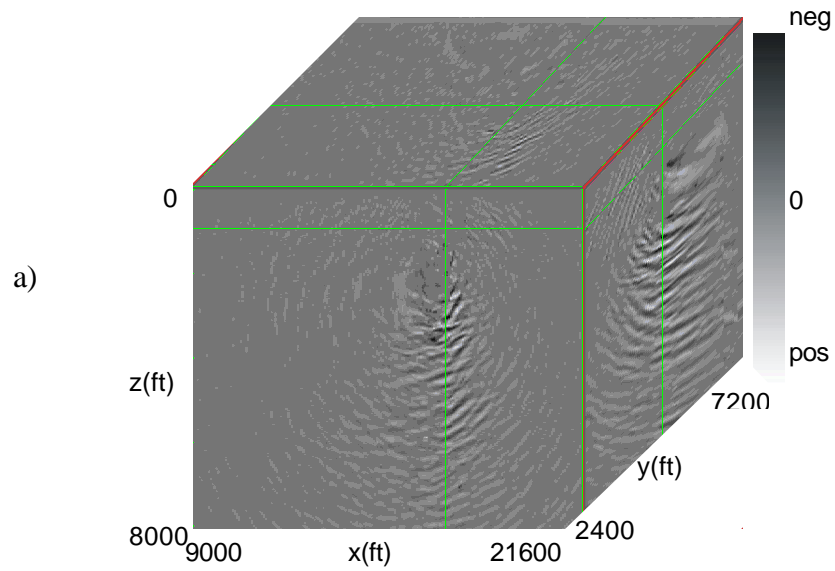


FIG. 5.5.20. a) 3-D PP elastic depth image; b) 3-D PS elastic depth image obtained by migrating 600 shots. Green lines represent the inline, crossline and depth slices intersecting at the receiver no. 1 location. Semblance weighting applied.

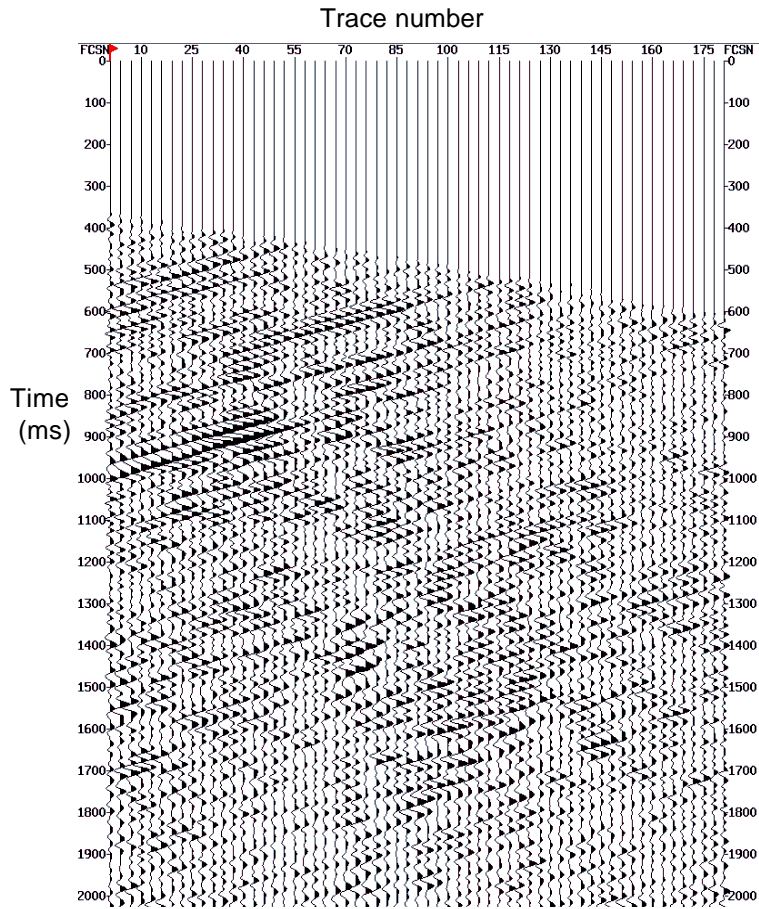


FIG. 5.5.21. Field common-shot gather, shot no. 3068, offset = 1989 ft (606 m).

Up-going events only. a) vertical component; b) east component; c) north component.

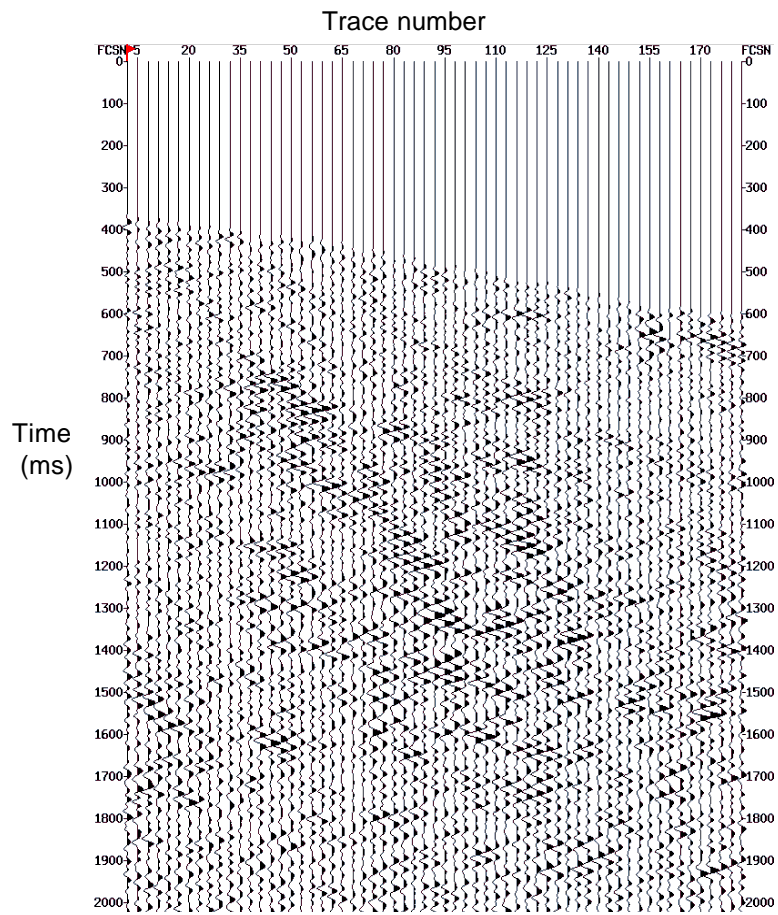


FIG. 5.5.21. (continued)

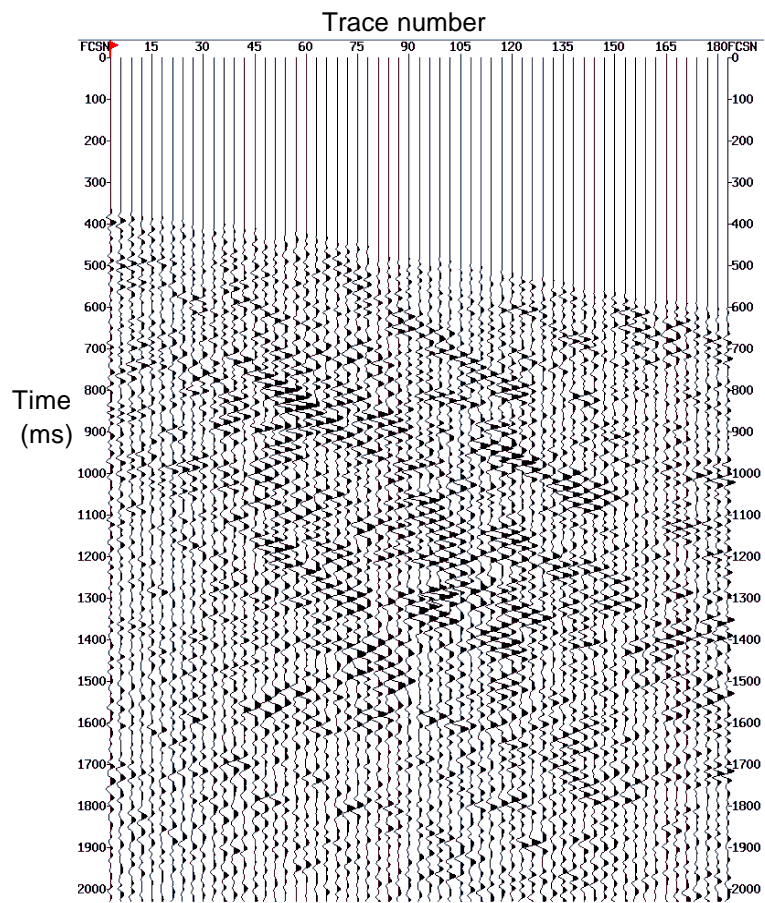


FIG. 5.5.21. (continued)

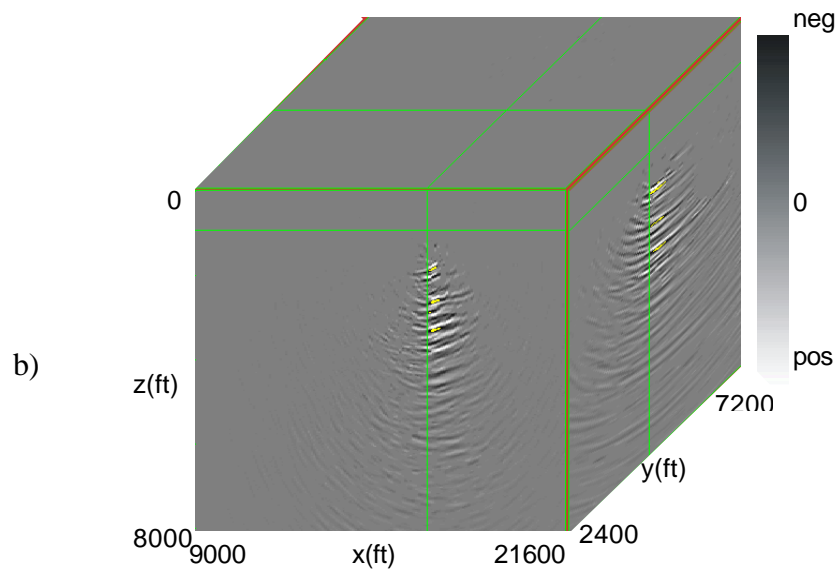
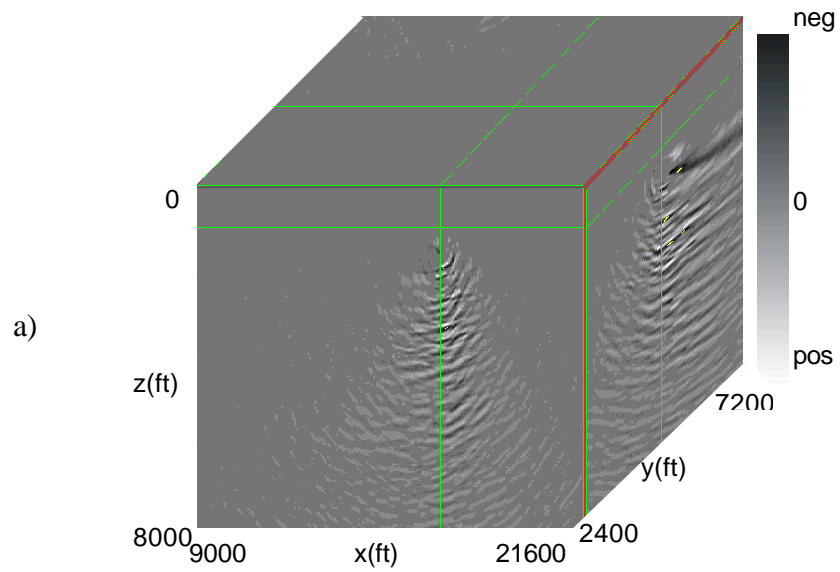


FIG. 5.5.22. a) 3-D PP elastic depth image; b) 3-D PS elastic depth image obtained by migrating 600 shots, up-going events only. Green lines represent the inline, crossline and depth slices intersecting at the receiver no. 1 location. Semblance weighting applied.

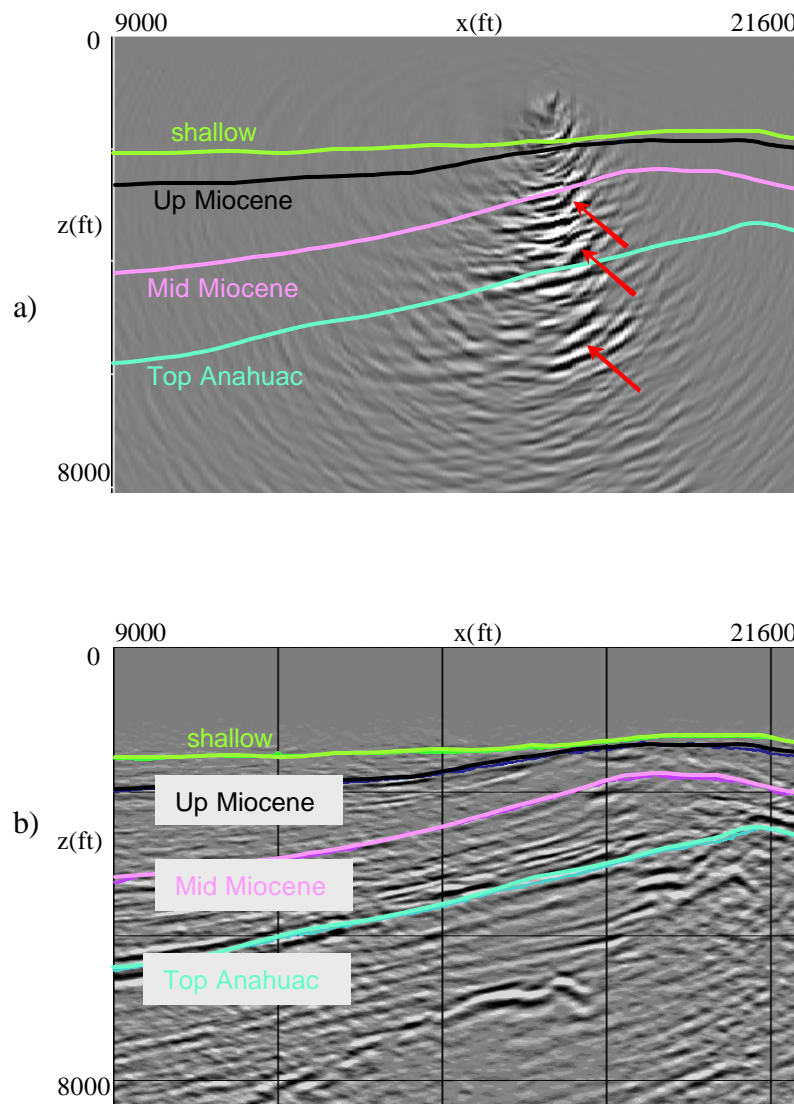


FIG. 5.5.23. a) 2-D section through the 3-D VSP PP elastic depth image located at the VSP well location; b) 2-D section through the 3-D surface PP acoustic depth image located at the VSP well location. VSP depth image obtained when migrating 600 shots, up-going events only. Both sections show the interpreted sedimentary boundaries that match perfect on both, VSP and surface images. Red arrows mark the probable image of the “Christmas-tree” shape of the salt flank. Note the higher frequency and better continuity of the reflectors in the VSP image compared to the surface image.

5.6 Traveltime and take-off angle estimation using wavefront construction

Traditionally, we performed traveltime and amplitude calculations by dynamic ray tracing (Cerveny, 2001). Another set of methods calculates the traveltimes by using the eikonal solver (Sethian and Popovici, 1999). The disadvantage of the dynamic ray tracing is that produces shadow zones in areas of large velocity contrasts. Vinje *et al.* (1993) described another way of computing the traveltimes and amplitudes for a 2-D case via wavefront construction. Later, Vinje *et al.* (1996, 1999) extended the method to the 3-D case.

The basic idea of the wavefront (WF) construction approach is to use ray tracing to estimate a new wavefront from the old one. The WF is defined as a curve (in 2-D) or a triangle (in 3-D). The ray direction and amplitude are functions of s , the distance along the front. To maintain a sufficiently small sampling distance along the WF, it is scanned at every time step and new rays are interpolated whenever the distance between two rays becomes larger than a predefined limit (Figure 5.6.1). We need to interpolate at the new location the following parameters: start position of the ray, unit ray tangent vector, geometrical spreading, amplitude coefficient and ray entrance direction at the source.

In the 3-D case, the rays are maintained in a triangular network and are traced stepwise in traveltime through the model (Figure 5.6.2). As the wavefronts are constructed, the data (i.e. traveltimes, amplitude coefficients, take-off angles etc) are transferred to the receivers by interpolation within the ray cells (Figure 5.6.3). The walls

of the ray cell consist of pairs of rays and wavefronts. Since we know the seismic parameters in the four corners of the ray cell, we can estimate the parameters in the receiver point: the distances d_1 and d_2 from the receiver perpendicular to the two rays; the normalized distance s' along the WF $s' = d_1/(d_1+d_2)$; the distance l_r from $X_i(s')$ to the receiver. By using the velocity v_{mid} in the midpoint of the line l_r , the traveltimes through the receiver is estimated to be:

$$t_{rec} = t + \frac{l_r}{v_{mid}} \quad (5.6.1)$$

where t is the accumulated traveltimes of the old wavefront (Vinje *et al.*, 1993).

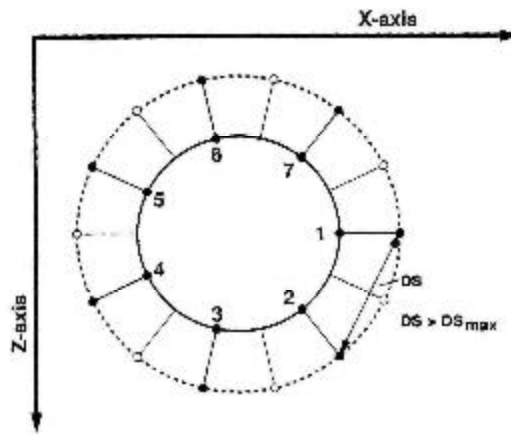


FIG. 5.6.1. In 2-D case, a new WF (dashed line) is constructed by ray tracing from the previous one (solid line). New rays are interpolated between each of the points (1 to 7) in the old front because DS exceeds DS_{max} (after Vinje *et al.*, 1993).

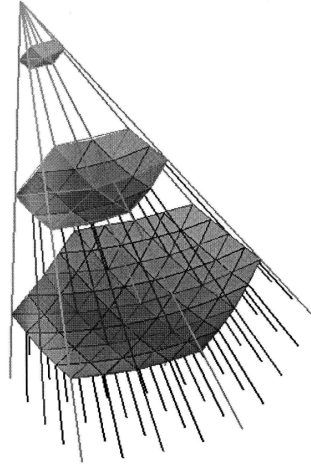


FIG. 5.6.2. In 3-D case, the ray tracing algorithm has criteria to check and keep the size of each triangle and the propagation-direction derivation of every two adjacent rays within pre-defined values (after Wang, 1999).

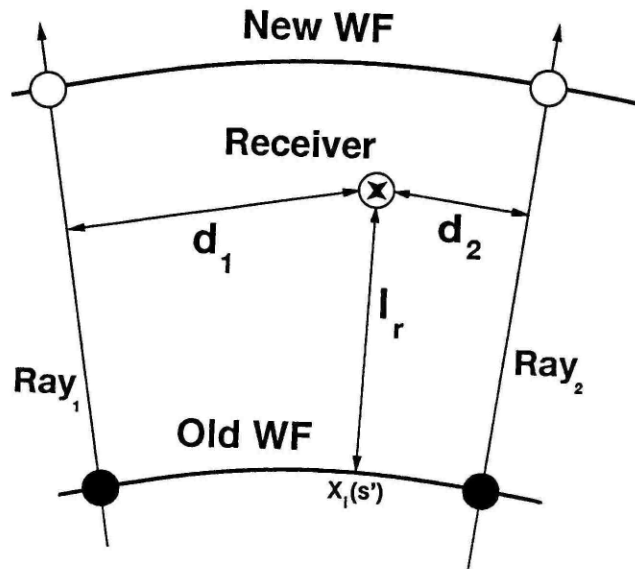


FIG. 5.6.3. The receiver parameters are found by interpolation within each ray cell (after Vinje *et al.*, 1993).

Advantages of this method are its flexibility, robustness and accuracy. Also, we can calculate multiple arrivals. One condition of the wavefront construction is having a smooth velocity model. Drawbacks are as in conventional ray-tracing methods: large velocity contrasts, caustics and near-critical incidence angle of rays onto interfaces give less accurate solutions.

Wang (1999) implemented a 3-D ray-tracing algorithm for the surface case based on wavefront construction method described above. The program provided the traveltimes, amplitudes, phase and the polar and the azimuthal angle at each grid point.

I modified the 3-D raytracing algorithm to the VSP type of acquisition in order to calculate the traveltimes and the take-off angles at the receiver. In the modified version, I calculated the traveltimes, amplitudes and phase and also, the take-off polar and azimuthal angles at the receiver. I obtained partially good results for the VSP case.

For algorithm calibration, I used a 2.5-D velocity model from which I display a vertical slice in Figure 5.6.4, colored by the P-wave velocity. The velocity model is 2500m wide along x and y axis and 2500m deep. I calculated the traveltime and the polar and azimuthal take-off angles for a source located at the surface of the model ($x = 0$, $y = 0$, $z = 0$). I display the results in Figures 5.6.5 – 5.6.7. Next, I calculated the traveltime and the polar and azimuthal take-off angles for a receiver located at $z = 1000\text{m}$. Note that while the traveltime and take-off angle values look good for the portion of the model below $z = 1000\text{m}$, the values above the receiver depth level are mostly equal to zero (Figures 5.6.8 – 5.6.10). Due to time constraints, I leave the program for the future improvements.

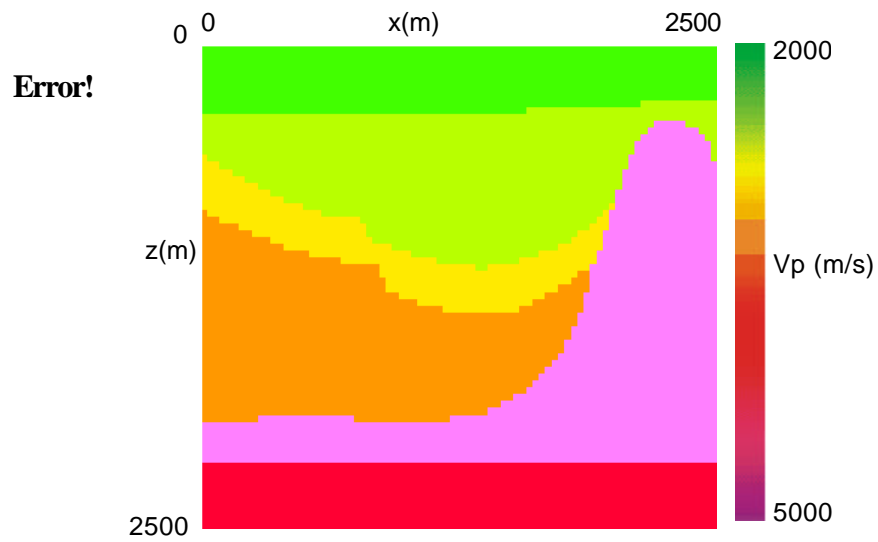


FIG. 5.6.4. 2-D vertical slice through the 2.5-D velocity model colored by V_p .

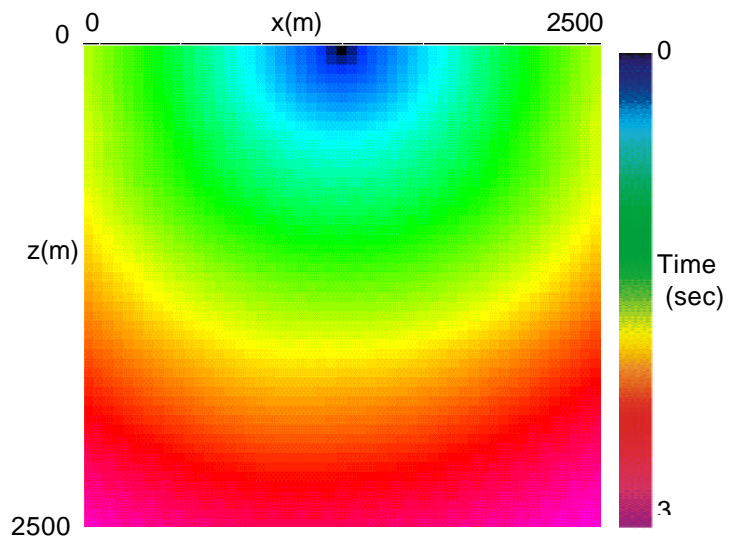


FIG. 5.6.5. 2-D vertical slice through the 2.5-D traveltimes volume colored by traveltime values. Source is located at $x = y = z = 0$.

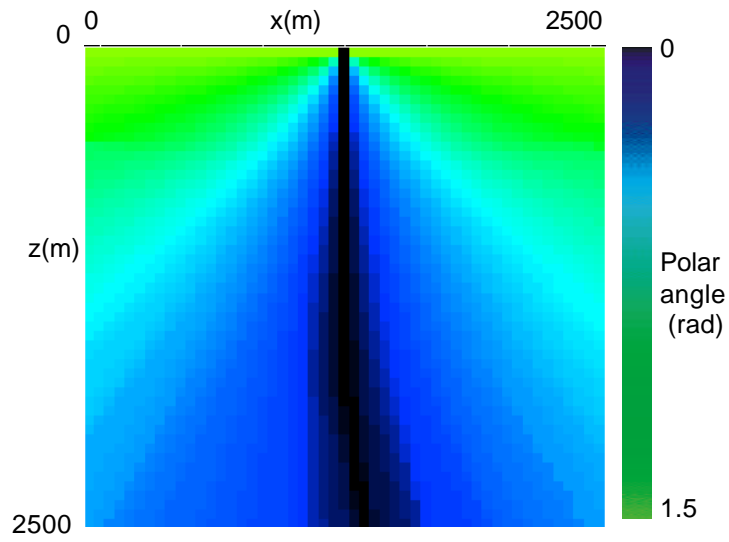


FIG. 5.6.6. 2-D vertical slice through the 2.5-D polar take-off angle volume colored by the polar angle values in radians. Source is located at $x = y = z = 0$.

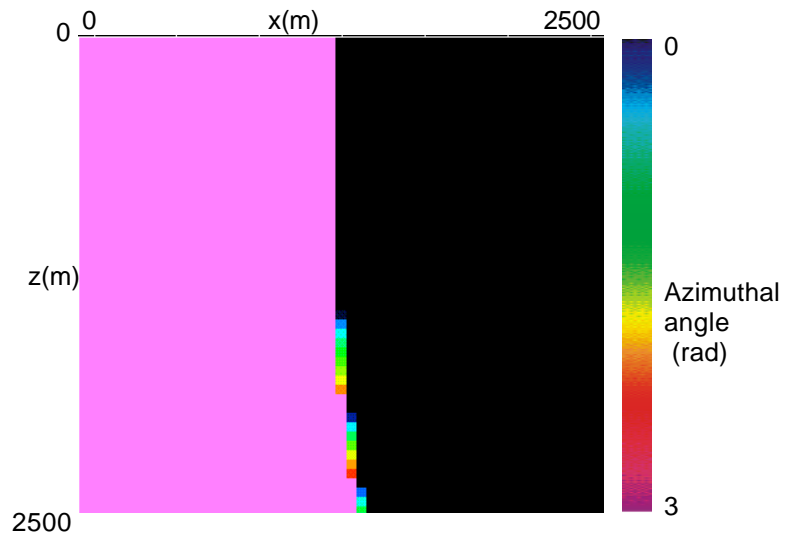


FIG. 5.6.7. 2-D vertical slice through the 2.5-D azimuthal take-off angle volume colored by the polar angle values in radians. Source is located at $x = y = z = 0$

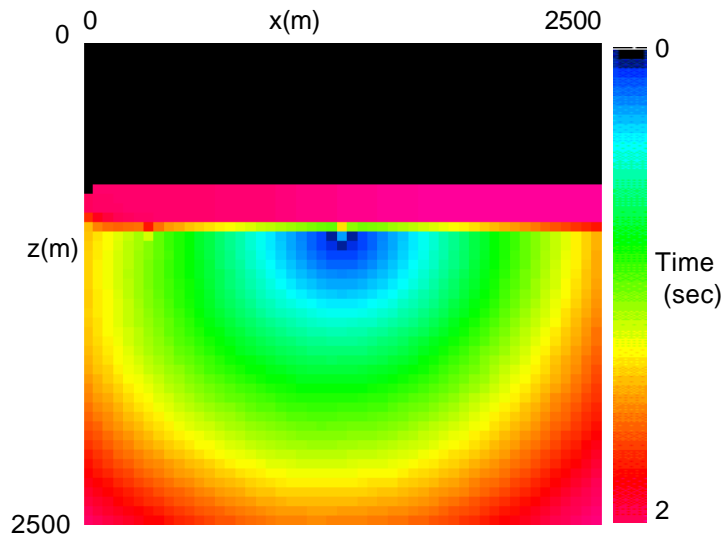


FIG. 5.6.8. 2-D vertical slice through the 2.5-D traveltimes volume colored by traveltimes values. Receiver is located at $x = y = 0$ and $z = 1000$ m.

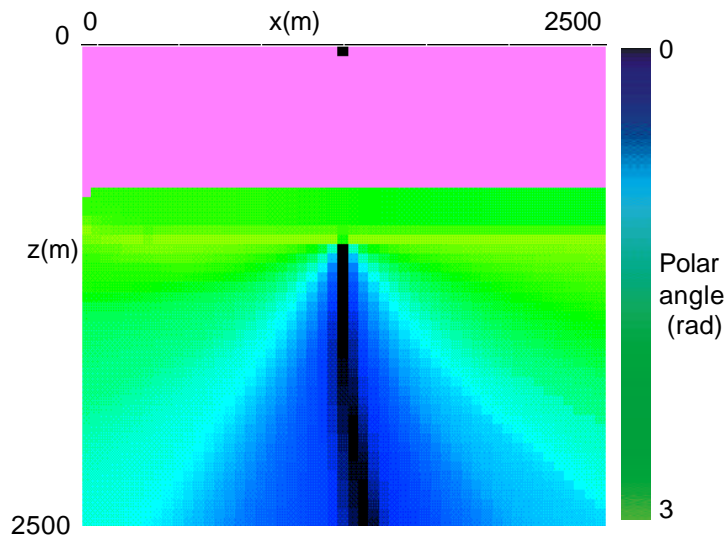


FIG. 5.6.9. 2-D vertical slice through the 2.5-D polar take-off angle volume colored by polar angle values. Receiver is located at $x = y = 0$ and $z = 1000$ m.

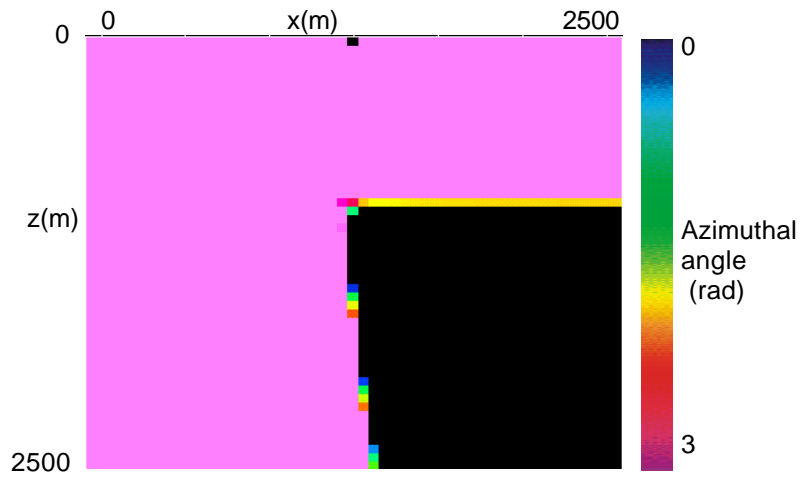


FIG. 5.6.10. 2-D vertical slice through the 2.5-D azimuthal take-off angle volume colored by the azimuthal angle values. Receiver is located at $x = y = 0$ and $z = 1000\text{m}$.

6. FORT WORTH BASIN – 2-D ELASTIC SYNTHETIC DEPTH MODELING

6.1. Summary

I have created a 2-D elastic synthetic depth model corresponding to a publicly available 2-D 3-C line acquired in Fort Worth Basin for use in calibration of multicomponent processing and imaging algorithms. The model, generated from a conventional 3-D “P-wave” survey and well logs over the same area, includes collapsed features identified as karsts and a series of relatively thin layers. I employed a hierarchal modeling approach of ray tracing followed by finite difference scalar wave equation and pseudospectral elastic wave equation modeling to provide a suite of models of increasing complexity.

These synthetics will be made available to the geophysical community to form the one of what we hope will be a suite of shared seismic data sets. I conclude by comparing and contrasting the synthetic common-shot gathers, from the three modeling techniques, with a shot gather from the field data.

6.2. Introduction

The goal of seismic modeling is to provide synthetic data that will help to better understand seismic wave propagation and the impact of seismic processing, velocity

analysis, and migration on the final subsurface image. This 2-D elastic model is a part of a project that includes academia, national laboratories and oil companies (House *et al.*, 2002). In the past years research has proven that converted-waves can be used to solve problems that could not be solved using conventional P-wave seismic. Although a great deal of progress has been made in both processing and imaging, we do not yet have a freely available model that allows researchers and interpreters to quantitatively compare the results of alternative processing algorithms and work flows. The choice of this model is dictated by the availability of a corresponding real multicomponent data set previously donated to the SEG by what was then Mitchell Energy (Van Dok and Gaiser, 2001). This particular data set will allow us to evaluate the usefulness of converted-waves in identifying or imaging thin sands and limestones containing hydrocarbons.

Unlike the commonly used Marmousi model (Versteeg, 1994; Martin *et al.*, 2002), my model only contains “mild” structural features. Nevertheless, processing of the real data is quite challenging, with considerable interference from headwaves, backscattered ground roll, statics, and out of the plane reflections complicating our analysis. The elastic wave equation synthetics contain converted-wave reflections of non-geometrical events (e.g. S*- wave) as well as surface waves. These synthetics should be useful for calibrating processing flows to attenuate surface waves, address problems of polarization, and enhance converted-wave reflections of both geometrical and non-geometrical events.

Perhaps the most important objective of this kind of study is to determine if we can sufficiently constrain 2-D multicomponent seismic data with conventional 3-D “P-

wave” data to provide us with accurate estimates of shear velocity for use in more accurate AVO and fracture analysis.

6.3. Geologic framework

The study area falls in the Bend Arch-Fort Worth Basin. The asymmetrical, wedge-shaped Fort Worth Basin is a peripheral Paleozoic foreland basin with about 12000 ft (3659 m) of strata preserved in its deepest northeast portion and is adjacent to the Ouachita structural belt. The basin formed in front of the advancing Ouachita structural belt as it was thrust onto the margin of North America. Thrusting occurred during a late Paleozoic (Late Mississippian and Early Pennsylvanian time) episode of plate convergence (Flippin, 1982).

The stratigraphy of the area (Figure 6.3.1) begins with the Riley, Wilberns and Ellenburger formations that are carbonate shelf deposits of Cambro-Ordovician age. During the late Mississippian, Barnett and Comyn formations were deposited. These vary from limestone in the West of the Basin to shale and sandstones in the East of the basin (Walper, 1982). Pennsylvanian time is characterized by the deposition of carbonate formations such as Comyn, Marble Falls and Caddo.

6.4. 2-D 3-C field data

A 3-D vertical component and 2-D 3-C simultaneous acquisition was performed in the Fort Worth basin, North Texas. The 2-D 3-C line is oriented approximately SW-NE across the 3-D survey, cutting across major faults. The total number of dynamite shots for the 3-D survey was 7100 but the 2-D 3-C line recorded only 471. Each shot-gather has 161 traces, with 220 ft shot spacing. Examples of field shot-gathers, vertical, inline and crossline horizontal components are presented in Figure 6.4.1.

6.5. Model construction and synthetic generation

The modeling study can be divided in four steps. First, I picked horizons along a traverse from the time migrated, 3-D surface seismic volume. I used the formation tops from wells located on or very close to the 2-D line to identify the horizons that needed to be picked. I also picked other strong reflectors that correspond to major velocity discontinuities. The traverse line extracted from the 3-D survey and the picked horizons are shown in Figure 6.5.1.

The second and third steps consisted in the time-to-depth conversion of the picked horizons using sonic log information and generation of the 2-D depth model. The depth horizons were imported into a commercial model building and ray-tracing package, where the layers were assigned a lithology consistent with the stratigraphy shown in Figure 6.3.1. The model consists primarily of sands, shale and limestone. Alternating

strata of sand and shale compose the shallow part of the model. A sequence of limestones corresponding to Caddo lime, Atoka and Marble Falls lime, Barnett shale and Ellenburger limestone formations underlies the sand/shale section. Vertical collapse structures are noticed at the top of the Ellenburger formation, which are believed to be a result of bottoms-up karsting (Sullivan *et al*, 2003). The bottom of the model represents what we believe to be basement or at least the base of the Ellenburger.

P-wave velocities were obtained from sonic logs. Since the elastic modeling also requires shear-wave velocities, I used Castagna's relationships to calculate the Vs and densities based on the P-wave velocity section, which was derived from the depth model for

sandstone:

$$V_s = -0.856 + 0.804 \cdot V_p,$$

$$\rho = 0.200 \cdot V_p^{0.261},$$

shale:

$$V_s = -0.867 + 0.770 \cdot V_p,$$

$$\rho = 0.204 \cdot V_p^{0.265},$$

and limestone:

$$V_s = -1.030 + 1.017 \cdot V_p - 0.055 \cdot V_p^2,$$

$$\rho = 0.243 \cdot V_p^{0.225}.$$

I indicate tops of the main formations in the resulting 55000 ft (16768 m) long and 9400 ft (2866 m) deep model in Figure 6.5.2. I inserted several hydrocarbon (gas)

traps in the model, which are displayed in red in Figure 6.5.2. Gas parameters were calculated using standard fluid substitution modeling (Hilterman, 2001).

The fourth step is to generate synthetic surface seismic data. The 2-C elastic synthetic data were generated using a commercial ray-tracing algorithm, courtesy of GX Technology. The beauty of ray tracing is that it provides an easy identification of the events. Thus we can examine the PP, PS, SS, and multiple reflections for each reflector, one at a time, superposing them as a last step to obtain a complete seismic section. Nevertheless, ray theory solutions do not accurately model diffractions, head waves and interface waves. These events are more accurately modeled by the acoustic and elastic wave equation synthetics using finite-difference and pseudospectral algorithms implemented at AGL.

The split-spread acquisition parameters are specified to closely approximate the field acquisition. Receiver spacing is 82.5 ft (25 m), with 161 receivers per shot. Shot locations are chosen to be similar to their location in the field data set. I display the depth model with overlain seismic rays for shot 182 in Figure 6.5.3. I show corresponding vertical and horizontal components shot-gathers in Figures 6.5.4-6.5.5.

The P-wave velocity and density sections were used to generate an acoustic finite difference synthetic data set. The acquisition geometry is identical to the ray-traced data. Acoustic synthetic data were generated with an in-house finite-difference algorithm that uses a scalar two-way wave equation that is fourth order accurate in space and second order accurate in time (Figure 6.5.6). Snapshots recorded at 0.5, 1.0, 1.5 and 2.0 sec are displayed in Figure 6.5.7.

Figures 6.5.8 and 6.5.10 show the shot-gathers for vertical and horizontal components obtained using the elastic pseudospectral algorithm. The vertical artifacts near the source location are due to method of source insertion used in our pseudospectral algorithm. These artifacts will vanish after upgrading the algorithm to a staggered grid formulation. Snapshots were output at every 10th shot with 0.05 sec time step. Snapshots of the Vz and Vx modes of the elastic wavefield at 0.5, 1.0, 1.5, and 2.0 sec after source initiation are shown in Figure 6.5.9 and Figure 6.5.11.

6.6. Data interpretation

I employed a hierarchal modeling approach of ray tracing followed by finite difference scalar wave equation and pseudospectral elastic wave equation modeling to provide a suite of models of increasing complexity.

I started with the ray tracing modeling because it provides a means to check the accuracy of the velocity model by correlating the events observed on the field shot-gathers with the events observed on the synthetic data. According to Prasad's interpretation (Prasad, 2003), PP reflection from the top of Atoka layer can be identified around 0.7 sec on the field data. The PP reflection from the top of Caddo interval appears around 0.85 sec and the PS reflection are found at 1.4 sec (Figure 6.4.1). The PP reflection coming from Ellenburger is observed around 1.13 sec and the PS reflection is spotted around 1.62 sec (Figure 6.4.1). Due to the high velocity contrast between the basement and the limestone interval, Ellenburger, I identified a very strong PP reflection

from the basement measured at 1.7 sec, a PS reflection at 2.4 sec, and a SS reflection at 3.2 sec (Figure 6.5.4).

All these events were correlated between the field and synthetic data and seemed to appear at approximately the same time. I cannot say there is a perfect match between the events due to the small discrepancy between the true velocity and the velocity model I generated.

The ray theory solutions are high-frequency approximations and do not accurately model diffractions, head waves and interface waves. These events are more accurately modeled by the acoustic and elastic wave equation synthetics using finite-difference and pseudospectral algorithms implemented at AGL.

In the next step of the modeling effort, I generated synthetic shot-gathers using the finite-difference acoustic modeling program. I noticed an overall better continuity of the PP reflections comparing to the events observed in the ray-traced data. There is a kind of diagonal event showing up on the right side of the shot gather but not on the left side, which I think might be due to the edge of the model. The shot location is very close to the right edge of the velocity model. This algorithm models P-waves only.

In the final step, I generated the elastic synthetic data using the pseudospectral elastic modeling code. I analyzed the snapshots to understand the behavior and characteristics of events like S* mode and PS head waves (Figure 6.5.9). To avoid modeling artifacts, I decided not to use the free surface option from the elastic pseudospectral algorithm, which resulted in the absence of the Rayleigh waves.

The main goal of this project is to provide acoustic and elastic synthetic data along with the existing field data to the geophysical community. Although this depth

model is simpler than the Marmousi or the SEG models and it does not pose a challenge for imaging, it can have an impact on designing new processing algorithms especially for converted-waves. The field data contain headwaves and non-geometrical events (S*-waves), which are also found in these synthetics. We can use the synthetic data to calibrate processing methods that address polarization problems, enhance converted-wave reflections of both geometrical and non-geometrical events. Another objective of this study is to determine if we can sufficiently constrain the 2-D multicomponent seismic data with conventional 3-D “P-wave” data to provide us with accurate estimates of shear velocity for use in more accurate AVO and fracture analysis.

6.7. Conclusions

I have generated a 2-D elastic synthetic depth model based on a 2-D 3-C line acquired in the Fort Worth Basin. Acoustic and 2-C elastic synthetic data were recorded using a surface geometry. I was able to correlate the reflections present in the time interval 0.8 – 1.5 sec from the field data with the events from the synthetics. Using the snapshots, I identified the events indicated by red arrows on the elastic synthetic shot gathers as S mode reflections from the non-geometrical S* event. If these events exist in the field data and they can be separated from the ground roll noise cone, they would be useful in deriving an estimate of the Vs stacking velocity.

SYSTEM	SERIES	Group or Formation
K	UNDIVIDED	
P	WOLFCAMP	Cisco Group
IP	UPPER	VIRGIL
		MISSOURI
	MIDDLE	DES MOINES
		ATOKA
	LOWER	MORROW
M	CHESTER	Chester Formation
	MERAMEC	Barnett and Chappel Formations
	OSAGE	
	KINDERHOOK	
E-O	CANADIAN	Viola and Simpson Formations
		Ellenburger Group
		Wilberns and Riley Formations
PE	UNDIVIDED	

Subsurface Formation/Facies
Atoka-Caddo
Atoka sand "facies"
Smithwick
Big Saline

FIG. 6.3.1. Stratigraphic column of the Fort Worth Basin (after Walper, 1982).

Error!

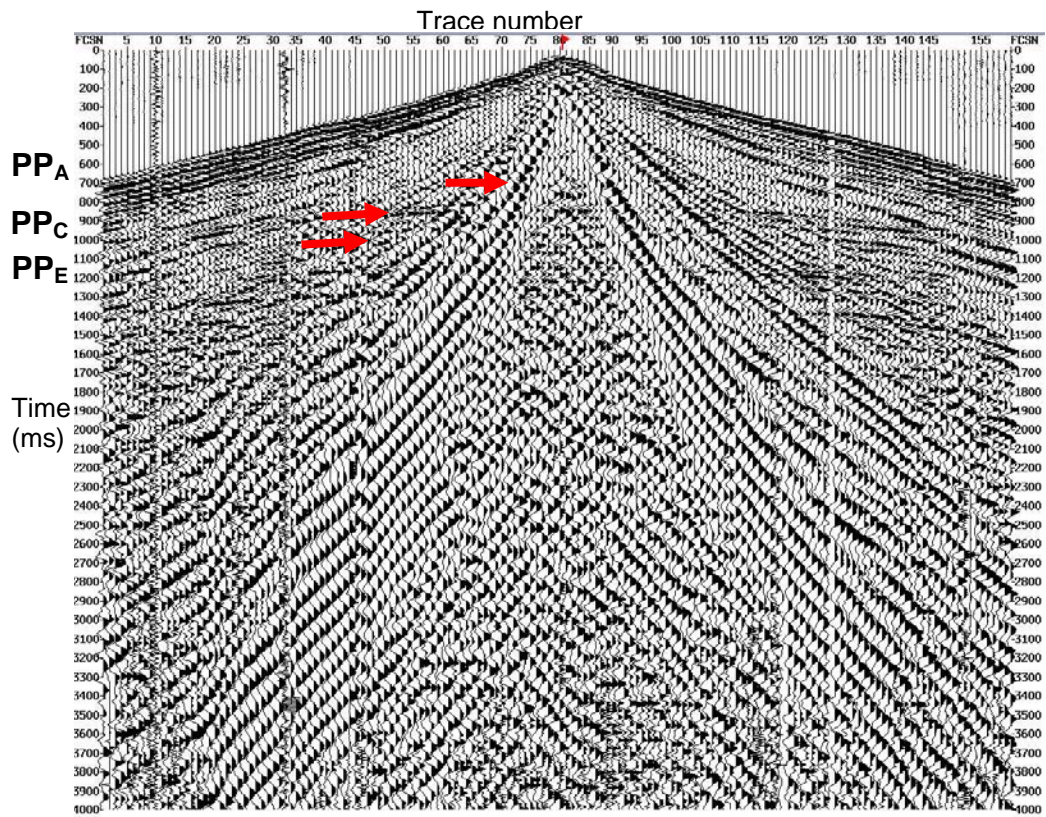


FIG. 6.4.1.a. Field common-shot gather, vertical component. Shot no.: 182. AGC applied. PP reflections coming from the top of Atoka (PP_A), Caddo (PP_C) and Ellenburger (PP_E) layers are indicated by the red arrows.

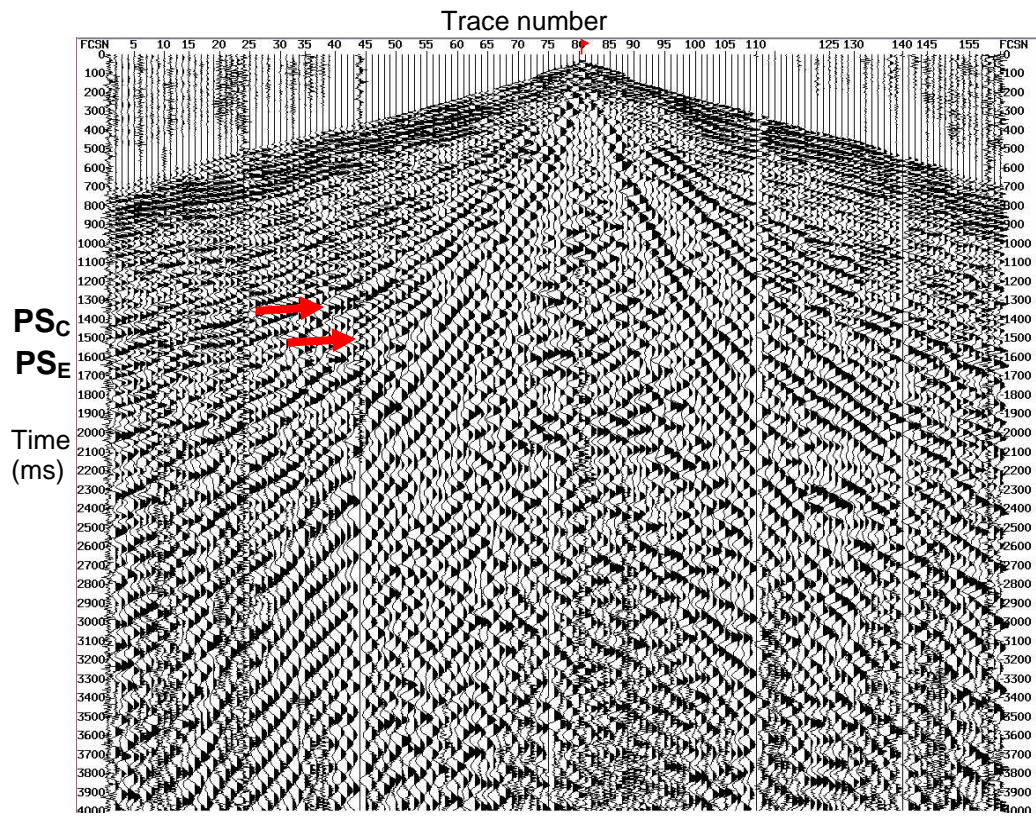


FIG. 6.4.1.b. Field common-shot gather, inline horizontal component. Shot no.: 182. AGC applied. PS reflections coming from the top of Caddo (PS_C) and Ellenburger (PS_E) layers are indicated by the red arrows.

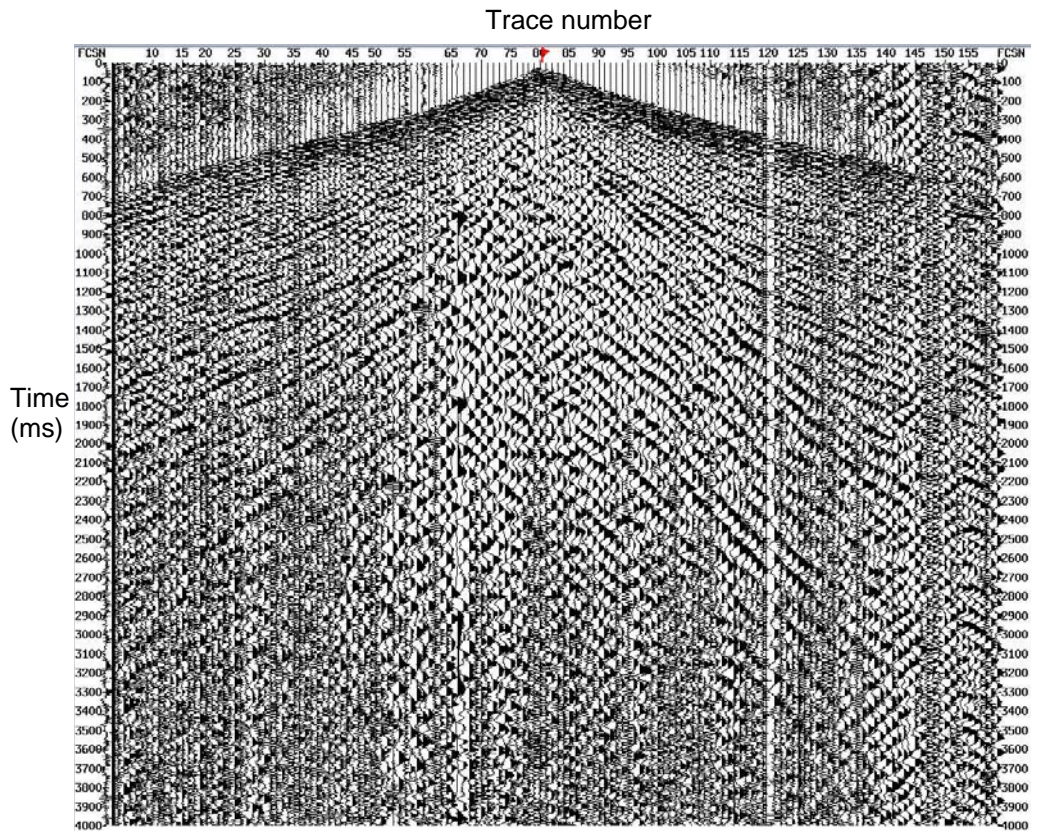


FIG. 6.4.1.c. Field common-shot gather, xline horizontal component. Shot no.: 182. AGC applied.

Error! 55000

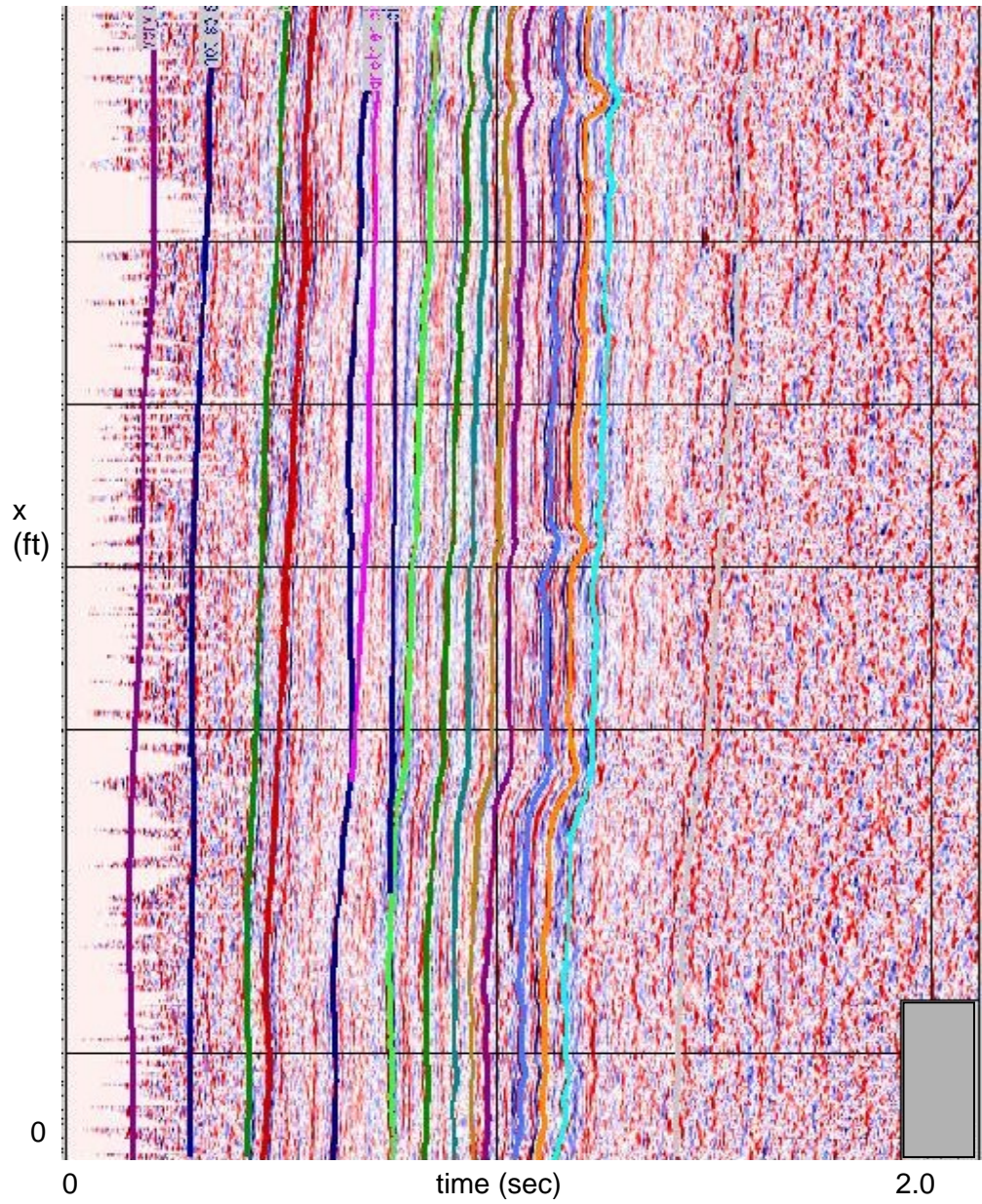


FIG. 6.5.1. 2-D traverse through the 3-D time migrated surface data. Picked horizons used to build the synthetic model are displayed in color.

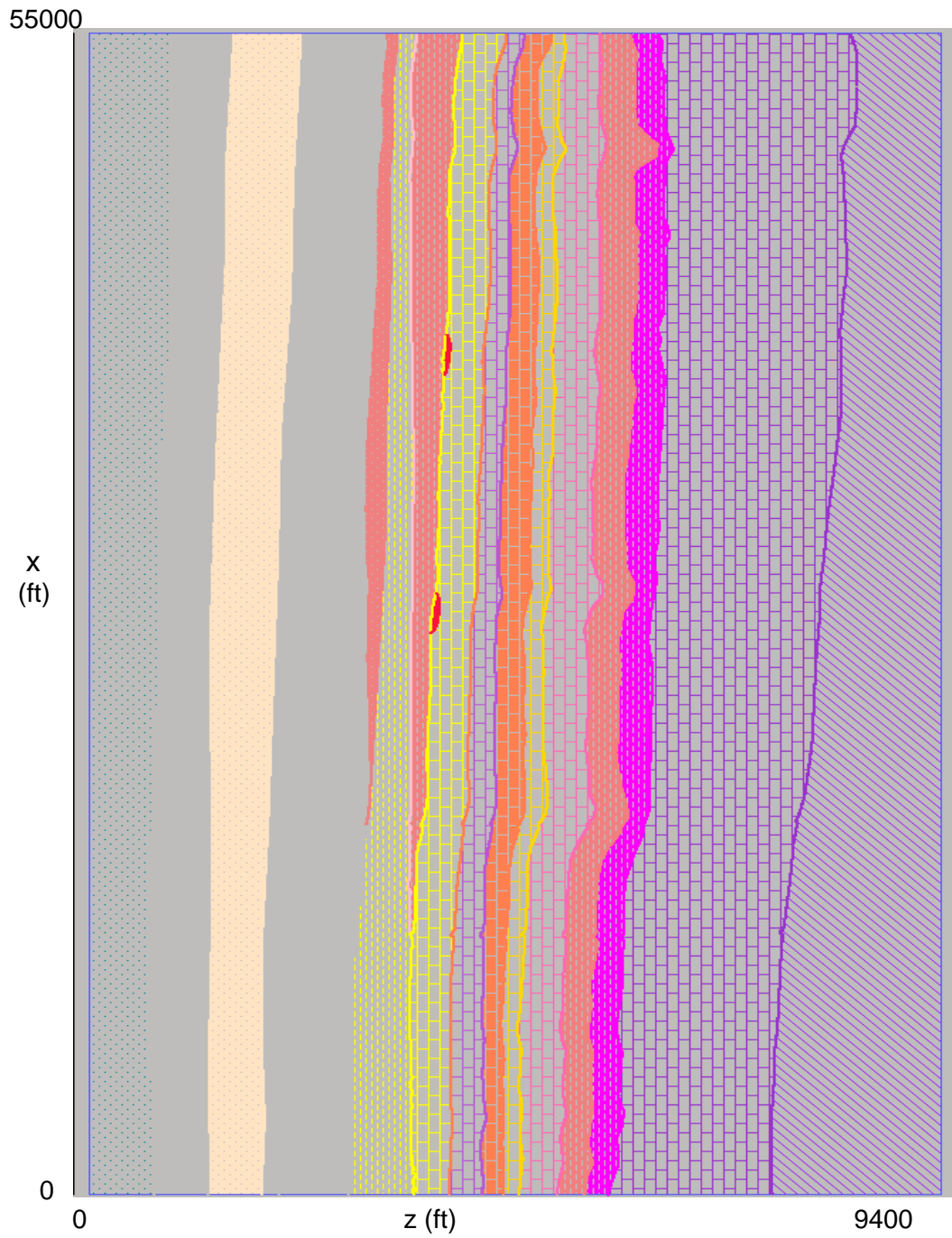


FIG. 6.5.2. 2-D depth model built using the horizons displayed in previous figure.

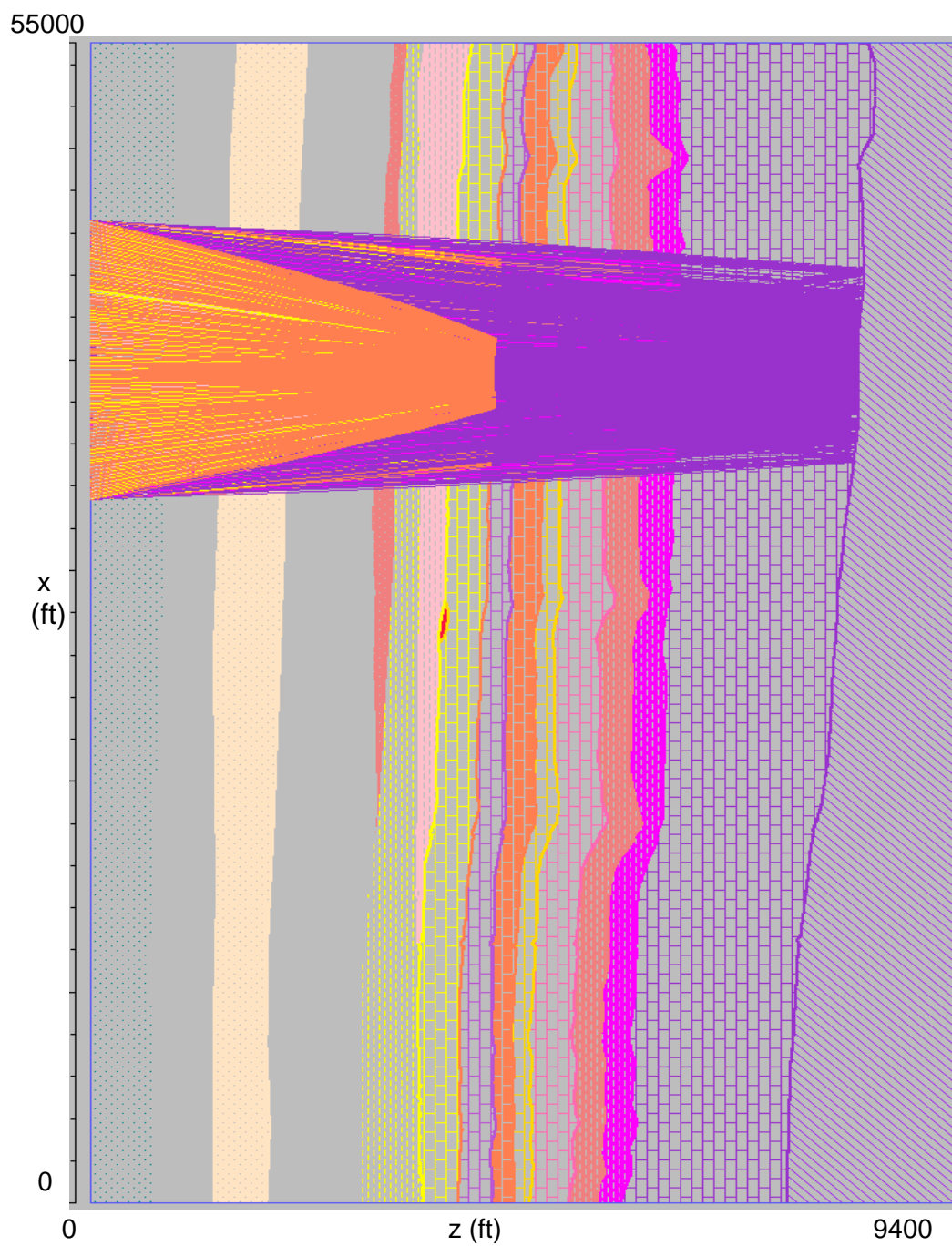


FIG. 6.5.3. 2-D depth model with rays displayed for shot no 182.

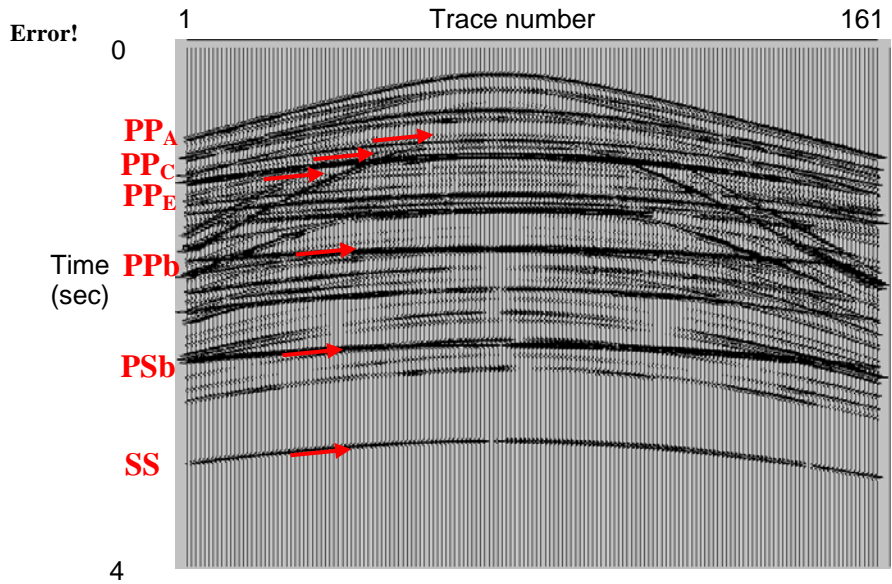


FIG. 6.5.4. Synthetic common-shot gather, vertical component, generated by ray-tracing at shot point 182. Shot depth = 0 ft. The PP reflections for the top of Atoka (PP_A), Caddo (PP_C), and Ellenburger (PP_E) are indicated by the red arrows. The PP-, PS-, and SS-wave reflections for basement are marked by red arrows (PP_b , PS_b , SS_b).

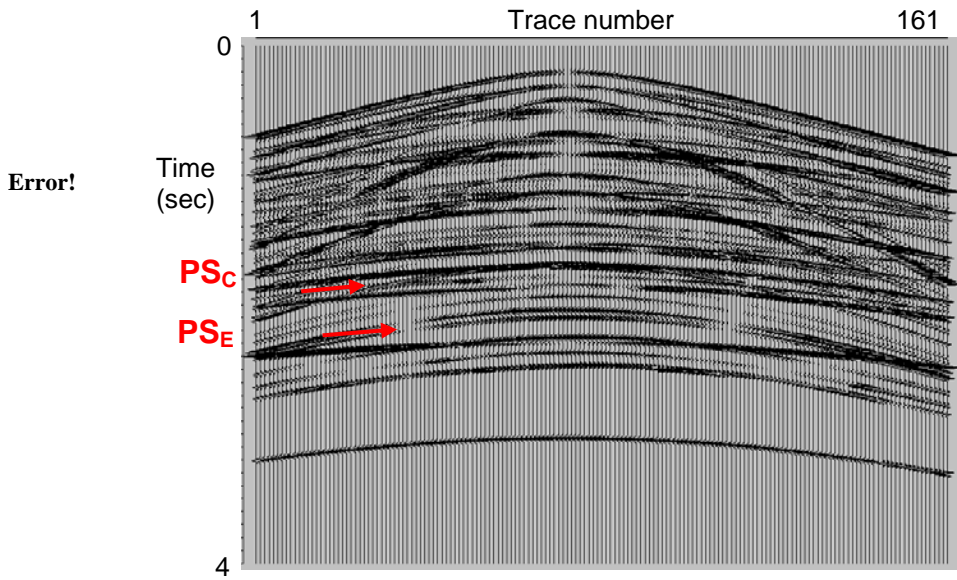


FIG. 6.5.5. Synthetic common-shot gather, inline horizontal component, generated by ray-tracing at shot point 182. Shot depth = 0 ft. PS reflections coming from the top of Caddo (PS_C) and Ellenburger (PS_E) layers are indicated by the red arrows.

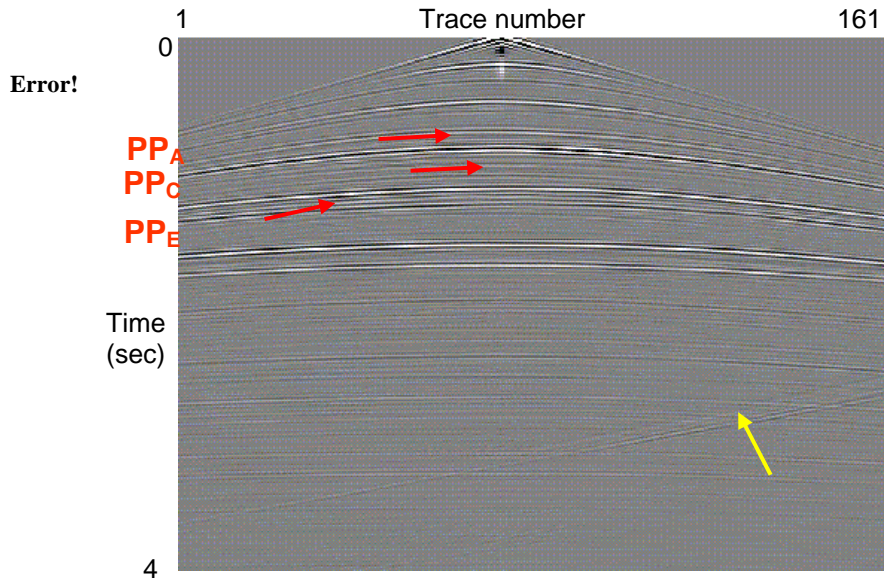


FIG. 6.5.6. Synthetic common-shot gather generated at shot point 182 using an acoustic finite-difference modeling code. The acoustic modeling algorithm models only PP events. PP reflections from the top of Atoka (PP_A), Caddo (PP_C), and Ellenburger (PP_E) are indicated by the red arrows. The diagonal event showing up on the right side of the shot gather (yellow arrow) might be an edge model artifact since the shot location is very close to the right edge of the velocity model.

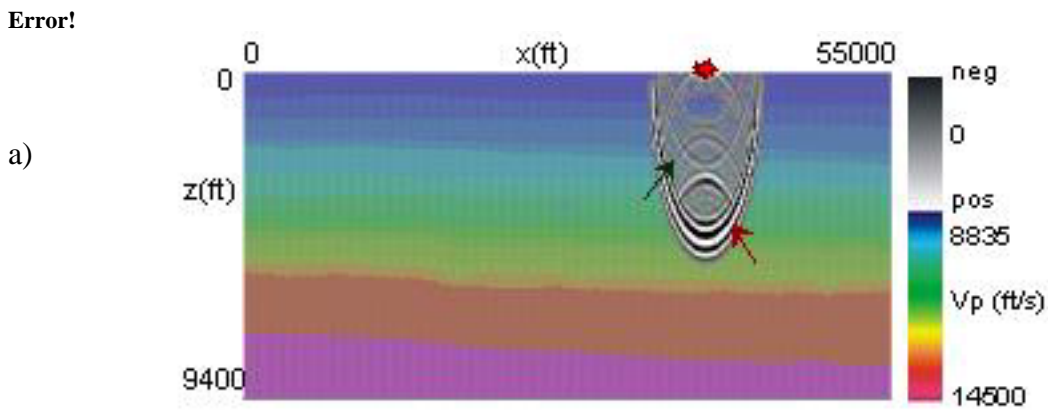


FIG. 6.5.7. P-wave only snapshots for the acoustic data generated at shot point 182 using an acoustic finite-difference modeling code. Dark red arrow marks the direct P-wave, dark green arrow marks the PP sedimentary reflection. Red star marks the shot location. Background color is represented by P-wave velocity. a) 0.5 sec; b) 1.0 sec; c) 1.5 sec; d) 2.0 sec.

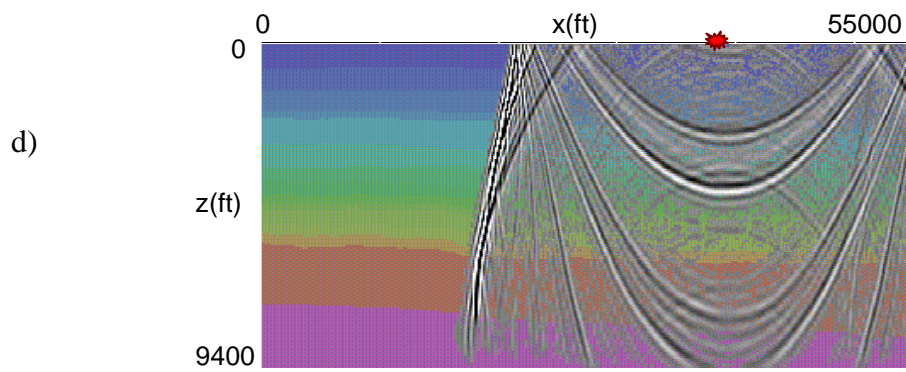
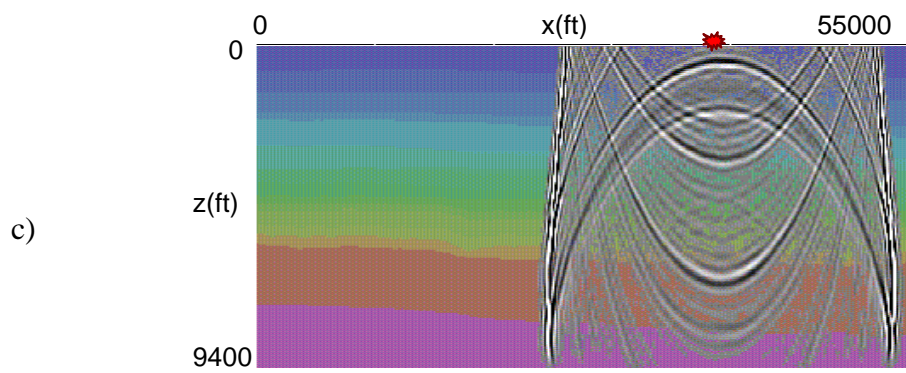
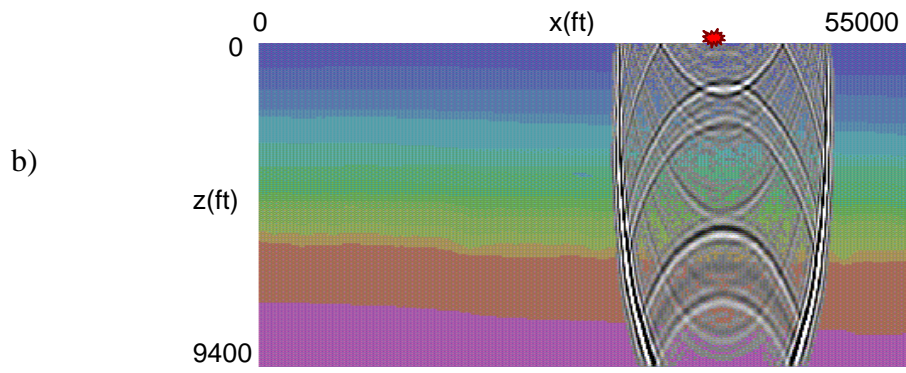


FIG. 5.6.7. (continued)

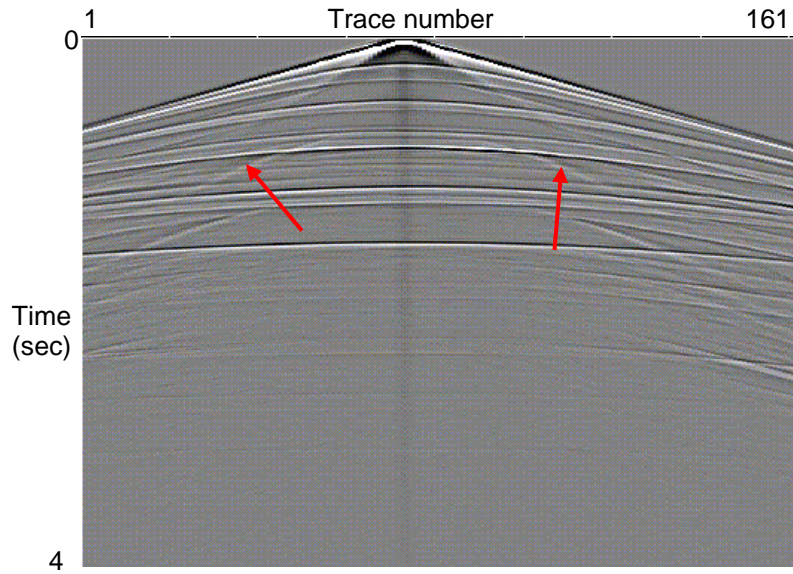


FIG. 6.5.8. Synthetic common-shot gather, vertical component, at shot point 182 obtained by elastic pseudo-spectral modeling algorithm. Note the S mode reflections marked by the red arrows. I didn't include the option of free surface, which means I do not generate the surface waves.

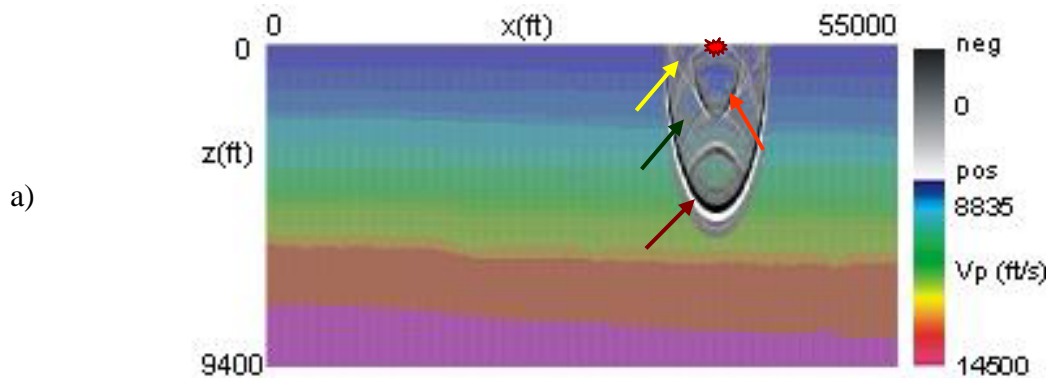


FIG. 6.5.9. Snapshots obtained from the elastic simulation of the vertical component. Dark red marks the direct P-wave, light red arrow points to the S* mode, yellow arrow points to the PS head-wave, and dark green arrow marks the PP sediment reflection. Red star marks the shot location. Background color is represented by P-wave velocity. a) 0.5 sec; b) 1.0 sec; c) 1.5 sec; d) 2.0 sec.

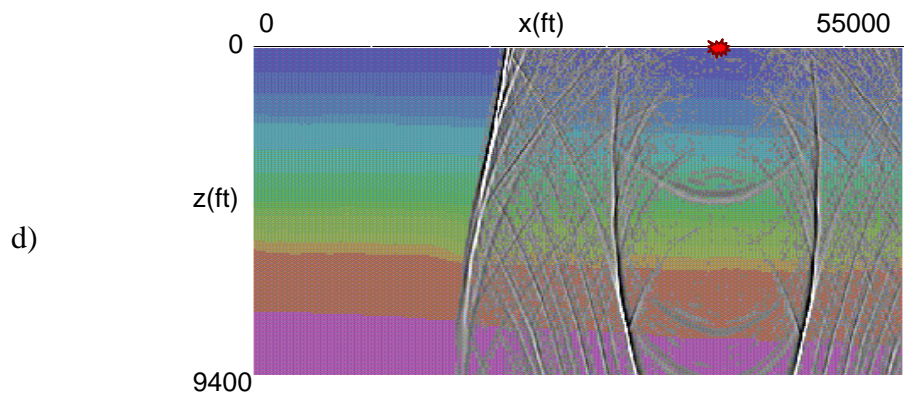
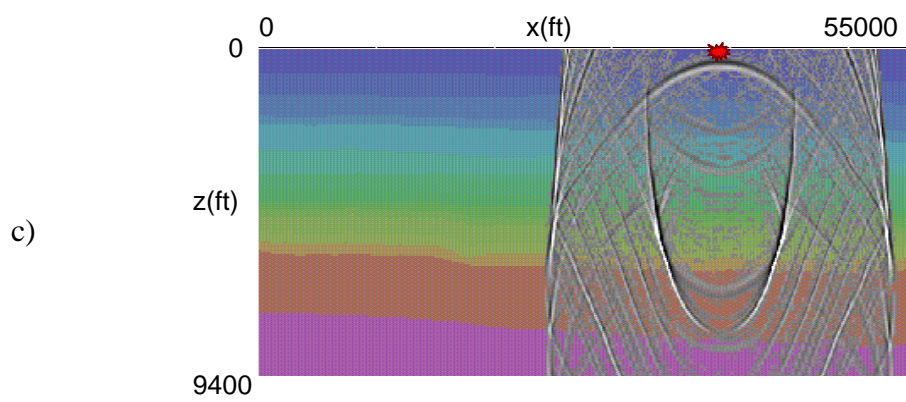
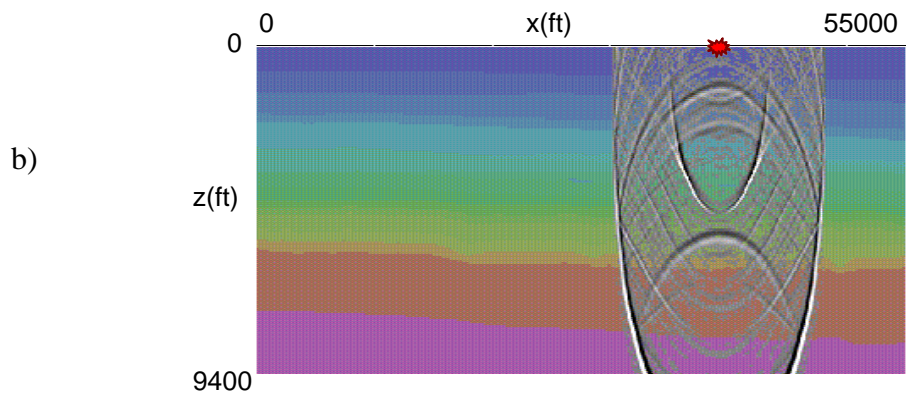


FIG. 5.6.9. (continued)

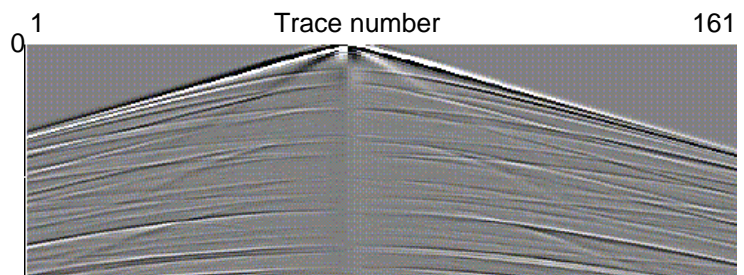


FIG. 6.5.10. Synthetic common-shot gather, horizontal component, generated by the elastic pseudo-spectral modeling algorithm.

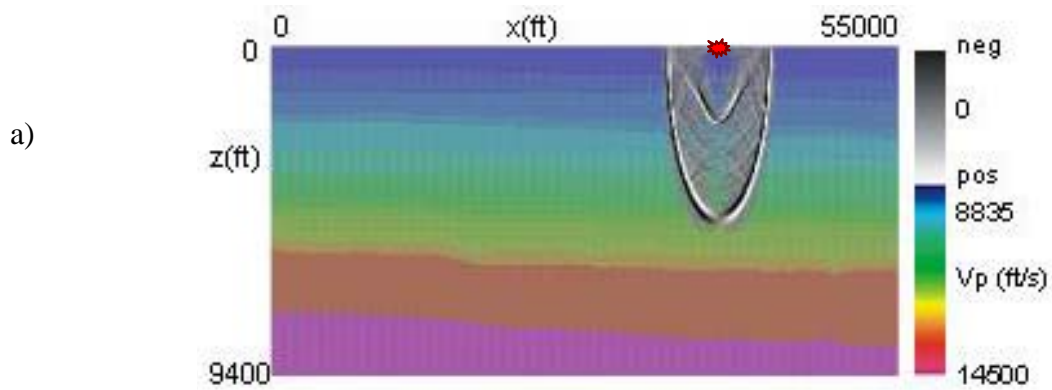
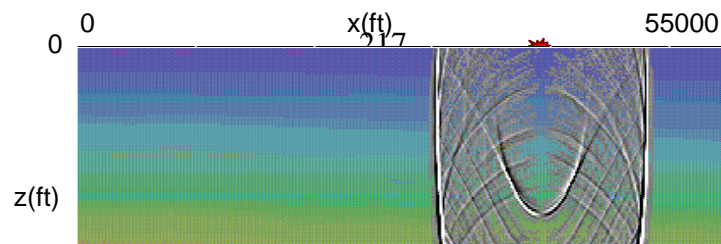


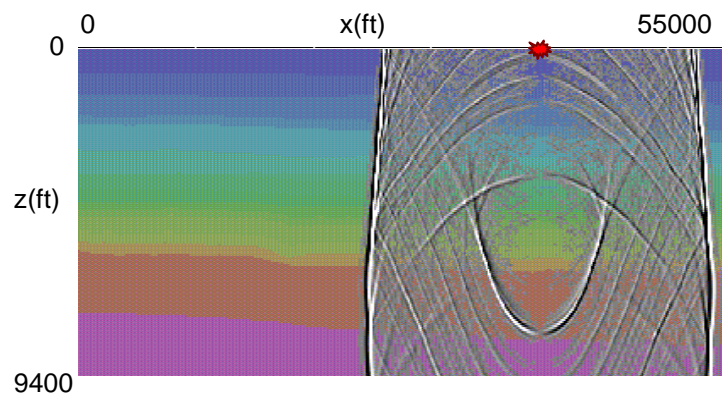
FIG. 6.5.11. Snapshots obtained from the elastic simulation of the horizontal component. Red star marks the shot location. Background color is represented by P-wave velocity. a) 0.5 sec; b) 1.0 sec; c) 1.5 sec; d) 2.0 sec.

Error!



b)

c)



d)

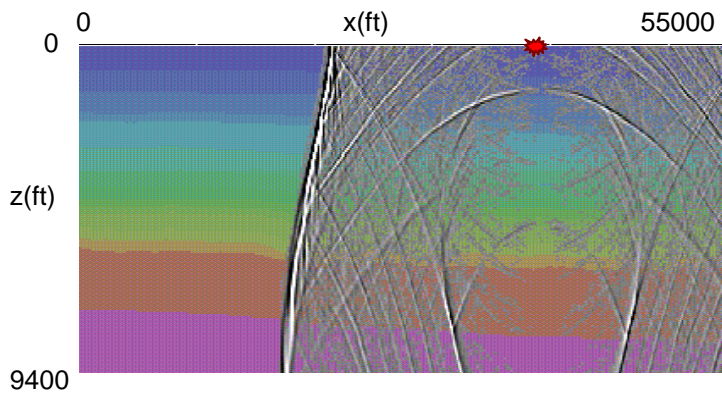


FIG. 5.6.11. (continued)

7. CONCLUSIONS

My dissertation consists of a major effort dedicated to the 3-D 3-C VSP Vinton data set and a secondary effort dedicated to the 2-D 3-C surface seismic data set (Fort Worth Basin). The main goal of my thesis was to develop a 3-D elastic VSP imaging algorithm that avoids some of the simple assumptions present in the current algorithms, and thereby fully exploits the information content in vector recording. A secondary goal was to design a new type of stacking of common-image gathers based on semblance weighting, which will replace the common “mute” operation applied to VSP images to remove migration artifacts. I end my dissertation with a separate chapter dedicated to the 2-D elastic modeling of the Fort Worth Basin data.

My VSP effort consisted of three steps: a subsurface illumination study via 2-D/3-D multicomponent VSP modeling, 3-D 3-C VSP processing, and 2-D/3-D scalar and elastic imaging. The first two steps were performed simultaneously, since the models were built and modified to answer some of the questions raised during data processing. My modeling experiments made a critical contribution to my understanding wavefield propagation during VSP acquisition.

The first and most important conclusion is that the salt flank reflection is made of both up-going and down-going wavefields. In this situation, the typical VSP processing step involving the up-going/down-going wavefield separation prior to migration is not optimal for generating a high fidelity salt flank image. This typical VSP processing step of separation is valid for sedimentary layers that are horizontal or moderately dipping but fails in case of steeply dipping structures, such as salt dome flanks.

My second conclusion is that the PP-wave salt flank reflection is found mainly on the horizontal phone and the PS-wave salt flank reflection mainly on the vertical phone. In contrast, PP sediment reflections are mainly recorded by the vertical phone and PS sediment reflections are primarily recorded by the horizontal phone. This conclusion is important in that it contradicts the current assumption that P-waves are recorded by the vertical components while the PS-waves by the horizontal components in the presence of low-velocity weathering zone.

My third conclusion is related to the subsurface illumination. VSP acquisition offers good illumination around the well, which makes it suitable for imaging of specific targets that cannot be properly imaged with the surface seismic data. One way to increase the lateral subsurface illumination is to perform walk-away VSPs; but even so, there is a limited area that can be illuminated. In theory, the advantage of VSP data over surface data is that the higher frequency content that allows higher resolution imaging. This high frequency can be best exploited by locating the geophones below the low-velocity weathering zone, which makes the wavefield travel only once through that zone and makes it less affected by attenuation compared to surface seismic acquisition. Having access to both surface and VSP field data sets, I was able to confirm this theory. Spectral analysis of my VSP pre-stack data set showed a higher frequency content (115 HZ) compared than surface data (100 Hz). Also, my final VSP depth images showed a higher frequency content than the surface depth images although slightly lower frequency than the input prestack data. Part of the high frequency is lost during processing due to trace balancing, wavelet shaping, band pass filtering, and stacking of the partial images with imperfect velocities.

The results of modeling directly influenced my VSP processing workflow. I followed the conventional processing methods involving geometry building, trace re-numbering and sorting, rotation of the horizontal geophones, wavelet shaping and time scaling. However, I purposely did not separate the up-going and down-going wavefields prior to migration.

The last step of my dissertation was to develop an elastic Kirchhoff pre-stack depth migration algorithm. My task was to create a new algorithm that avoids simple assumptions commonly used in scalar migration, and thereby more fully exploits the full information content in vector recording. I developed a 3-D scalar Kirchhoff pre-stack depth migration algorithm based on preexisting in-house 3-D Kirchhoff pre-stack time migration algorithm. The traveltimes are calculated with an Eikonal solver. The major difficulty was to read and distribute the source and receiver traveltime volumes in MPI environment. Other than I/O, the difference between the scalar and elastic migrations is limited to the imaging condition. The input to the scalar migration consists of separated PP- and PS-waves, which are migrated independently. In this workflow, we migrate the PP-waves using the P-wave source and receiver traveltime tables while we migrate the PS-waves using P-wave source traveltime tables and S-wave receiver traveltime tables. Prior wavefield separation is not necessary in elastic migration. Instead, I separate the P-waves by taking the dot-product inside the migration loop between the vector VSP data and a calculated migration ray vector, and separate the PS-waves by taking one component of the cross-product. Currently, I calculate the migration ray vector using the direction cosines without considering ray bending.

The output of both migrations is filtered using a semblance weighted stack to remove large amplitude “cabbage leaves” associated with sparse shots migration.

Due to the absence of a 3-D VSP elastic modeling algorithm, I first calibrated the scalar and elastic Kirchhoff pre-stack depth migration algorithms with 2-D scalar and elastic synthetic VSP data computed via ray-tracing and elastic pseudo-spectral techniques. I also calibrated my 3-D scalar Kirchhoff pre-stack depth migration using a 3-D acoustic synthetic VSP data set that I generated by a newly developed in-house acoustic pseudo-spectral modeling algorithm. The results of synthetic 2-D elastic and 3-D scalar wave equation models are excellent.

For the real data, I excluded those that had offset greater than 16000 ft. In these particular shots, most of the energy is represented by turning waves and not by reflections and do not satisfy the imaging condition implemented in my algorithm.

The final elastic PP and PS depth images, especially the PP images, show a coherent high frequency image at the well location. However, the shallow part of those depth images is affected by lack of events that were muted along with the first breaks. One way to improve the shallow part of the image is to separate the up-going and down-going events by using an f-k filter and migrate only the up-going events. In this case, the final PP and PS images showed a much better continuity in the shallow part.

To test the accuracy of my VSP images, I compared my VSP PP elastic depth image at the VSP well location with the PP scalar depth image obtained by Duncan (2005) for the surface data set. A quick analysis confirms the presence of higher frequency and more details on the VSP depth image compared to the surface depth image. I was able to correlate horizons interpreted on the surface migrated volume with

the horizons interpreted on the VSP migrated volume. I also noticed some steeply dipping reflectors that might represent partial images of the salt flank.

Still, I was not able to obtain a clear salt flank image from the VSP data. There are a few possible reasons for this. Duncan (2005), interpreted the surface seismic and well logs, suggested a possible “Christmas-tree” shape of the salt flank, which makes the imaging process more difficult particularly for VSPs. Second, my field data velocity model was constructed from well control and surface seismic reflector picks designed to focus horizontal reflectors. I believe that an improved image will require a more accurate, tomographically-driven velocity model designed to focus the vertical salt flank. Also, we should perform migration velocity analysis on the surface migrated volume as a secondary way to improve the velocity model. Another reason is anisotropy caused by the shale from the Vinton Dome area. Once we include the anisotropy information in the velocity model, I expect an improvement in our images. A last reason might be pre-processing of the VSP data. Since salt dome reflections were almost invisible in the field data, I believe we should design a processing workflow to enhance the salt flank reflections.

As future work, I would like to finish the 3-D ray-tracing algorithm that calculates the take-off angle at the receiver. These angles should allow a more accurate determination of polarization and reduce the PP-wave leakage currently observed in the PS elastic depth images. We would also like to finish the 3-D 3-C P-/S-wave filter based on Radon technique developed by Jovanovich (2004) and then migrate the separated P- and S-waves using the 3-D scalar Kirchhoff pre-stack depth migration algorithm. Finally,

I would like to investigate methods of removing first-breaks instead of surgical mute, which removes part of the useful energy.

Another part of my dissertation represented building a 2-D velocity model for a 2-D 3-C surface seismic data set from the Forth Worth basin, and generating synthetic data sets by various modeling techniques. These synthetic data sets, along with the corresponding field data set, will be made available to the geophysical community through the CAGE/AGL website.

APPENDIX A

The Kirchhoff Integral

Kirchhoff's integral solution to the scalar wave equation

$$\left[\frac{\partial^2}{\partial x^2} + \frac{\partial^2}{\partial y^2} + \frac{\partial^2}{\partial z^2} - \frac{1}{v^2(x, y, z)} \frac{\partial^2}{\partial t^2} \right] P(x, y, z; t) = 0 \quad (\text{A-1})$$

is a mathematical statement of Huygen's principle (Yilmaz, 2001),

where $P(x, y, z; t)$ – pressure wavefield propagating in a medium with velocity $v(x, y, z)$.

Huygen's principle states that the pressure disturbance at time $t + \Delta t$ is the superposition of the spherical waves generated by point sources at time t .

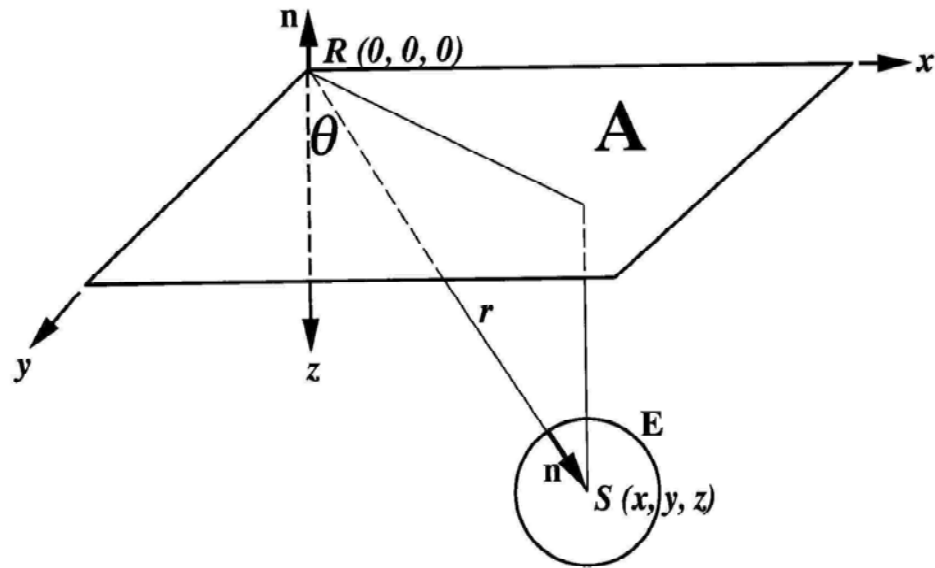


FIG. A.1. Geometry of a point diffractor to derive the Kirchhoff integral solution to the scalar wave equation (after Yilmaz, 2001).

Consider the geometry from Figure A.1. of a point diffractor at a location $S(x,y,z)$ and an observation surface A for the diffraction wavefield generated by the source at the diffractor. The surface area, A is only a portion of a closed surface and is the aperture of the observation made over that closed surface. We choose the receiver location $R(0,0,0)$ on the observation area to be at the origin of our coordinate system.

For convenience, we apply the Fourier transform to the wavefield in the time direction

$$P(x, y, z; \omega) = \int P(x, y, z; t) e^{(-i\omega t)} dt, \quad (\text{A-2a})$$

where ω is the angular frequency.

The inverse transform is given by

$$P(x, y, z; t) = \int P(x, y, z; \omega) e^{(i\omega t)} d\omega. \quad (\text{A-2b})$$

Now apply the Fourier transform to equation (A-1) in the time direction to obtain

$$\left(\nabla^2 + \frac{\omega^2}{v^2} \right) P(x, y, z; \omega) = 0, \quad (\text{A-3})$$

where ∇^2 is the Laplacian operator

$$\nabla^2 P = \left(\frac{\partial^2}{\partial x^2} + \frac{\partial^2}{\partial y^2} + \frac{\partial^2}{\partial z^2} \right) P.$$

We may intuitively state that what we observe at the surface A is what is generated at the source S (Yilmaz, 2001). This statement is mathematically expressed by Gauss's divergence theorem as (Coulson, 1965)

$$\int_V \nabla^2 P dV = \int_A \frac{\partial P}{\partial n} dA, \quad (\text{A-4})$$

where V is the volume of the region enclosed by the surface A and the derivative $\frac{\partial P}{\partial n}$ is taken normal to the surface A in the outward direction.

We solve equation (A-3) for each frequency component ω and sum the resulting solutions over all frequency components to compute the wavefield at the source $P(x,y,z;t=0)$.

The solution obtained by Kirchhoff in 1882 requires Green's function that describes the propagation outward from a point source with spherical symmetry as (Coulson, 1965)

$$G(r, \omega) = \frac{1}{r} e^{\left(-i\frac{\omega}{v}r\right)}, \quad (\text{A-5a})$$

where

$$r = \sqrt{x^2 + y^2 + z^2} \quad (\text{A-5b})$$

is the distance between the observation point and the source location. Green's function given by equation (A-5a) is also a valid solution to equation (A-3):

$$\left(\nabla^2 + \frac{\omega^2}{v^2}\right)G(x, y, z; \omega) = 0. \quad (\text{A-6})$$

If we rewrite the equation (A-4) by multiplying both sides with Green's function G of equation (A-5a) as

$$\int_V G \nabla^2 P dV = \int_A G \frac{\partial P}{\partial n} dA, \quad (\text{A-7a})$$

and rewrite equation (A-7a) by interchanging our wave function P with Green's function G we obtain

$$\int_V P \nabla^2 G dV = \int_A P \frac{\partial G}{\partial n} dA. \quad (\text{A-7b})$$

Then we subtract equation (A-7b) from (A-7a) and get

$$\int_V (G \nabla^2 P - P \nabla^2 G) dV = \int_A \left(G \frac{\partial P}{\partial n} - P \frac{\partial G}{\partial n} \right) dA. \quad (\text{A-8})$$

If we substitute equations (A-3) and (A-6) into the left-hand side of equation (A-8)

$$\int_V (G \nabla^2 P - P \nabla^2 G) dV = \int_V \left(-G \frac{\omega^2}{v^2} P + P \frac{\omega^2}{v^2} G \right) dV,$$

we note that

$$\int_V (G \nabla^2 P - P \nabla^2 G) dV = 0. \quad (\text{A-9})$$

Next, because Green's function defined by equation (A-5a) becomes infinite at the source location S, we need to place it inside an infinitesimally small enclosed surface E. This would then require computing the right-hand side of equation (A-8) in two parts: once for the surface E and once for the surface A.

Substitute equation (A-5a) into the right-hand side of equation (A-8) and note, from

Figure A.1, that for the surface E, $\left(\frac{\partial}{\partial n}\right) = -\left(\frac{\partial}{\partial r}\right)$:

$$\int_E \left(G \frac{\partial P}{\partial n} - P \frac{\partial G}{\partial n} \right) dE = \int_E \left[-\frac{1}{r} e^{\left(-i\frac{\omega}{v}r\right)} \left(\frac{\partial P}{\partial r} \right) + P \frac{\partial}{\partial r} \left(\frac{1}{r} e^{\left(-i\frac{\omega}{v}r\right)} \right) \right] r^2 d\Omega, \quad (\text{A-10a})$$

where $dE = r^2 d\Omega$ and Ω is the solid angle around the source point S in Figure A.1.

After differentiating with respect to r and simplifying the right-hand side of equation (A-10a) we obtain

$$\int_E \left(G \frac{\partial P}{\partial n} - P \frac{\partial G}{\partial n} \right) dE = -\int_E e^{\left(-i\frac{\omega}{v}r\right)} \left(r \frac{\partial P}{\partial r} + P + i \frac{\omega}{v} r P \right) d\Omega. \quad (\text{A-10b})$$

Next, we take the limit $r \rightarrow 0$ and obtain the contribution of the surface E:

$$\int_E \left(G \frac{\partial P}{\partial n} - P \frac{\partial G}{\partial n} \right) dE = -4\pi P. \quad (\text{A-11})$$

Then, substitute again equation (A-5a) into the right-hand side of equation (A-8) and note from Figure A.1 that for the surface A, $\left(\frac{\partial}{\partial n} \right) = -\left(\frac{\partial}{\partial z} \right)$:

$$\int_A \left(G \frac{\partial P}{\partial n} - P \frac{\partial G}{\partial n} \right) dA = \int_A \left\{ -\frac{1}{r} e^{\left(-i\frac{\omega}{v}r \right)} \frac{\partial P}{\partial z} + P \frac{\partial}{\partial z} \left[\frac{1}{r} e^{\left(-i\frac{\omega}{v}r \right)} \right] \right\} dA. \quad (\text{A-12})$$

We differentiate with respect to z while noting from Figure A.1 that $\frac{\partial r}{\partial z} = \cos \theta$, and

simplify the right-hand side of equation (A-12) to obtain

$$\int_A \left(G \frac{\partial P}{\partial n} - P \frac{\partial G}{\partial n} \right) dA = -\int_A e^{\left(-i\frac{\omega}{v}r \right)} \left(\frac{1}{r} \frac{\partial P}{\partial z} + \frac{\cos \theta}{r^2} P + i \frac{\omega \cos \theta}{v r} P \right) dA. \quad (\text{A-13})$$

The total contribution to the right-hand side of equation (A-8) is the sum of equations (A-11) and (A-13). The left-hand side of equation (A-8) vanishes by way of equation (A-9).

Hence, the resulting expression from equation (A-9) is

$$4\pi P = \int_A e^{\left(-i\frac{\omega}{v}r \right)} \left(\frac{1}{r} \frac{\partial P}{\partial z} + \frac{\cos \theta}{r^2} P + i \frac{\omega \cos \theta}{v r} P \right) dA. \quad (\text{A-14})$$

We know that $P = P(x,y,z;\omega)$ in equation (A-14) and multiply both sides by $e^{i\omega t}$ and integrate over the frequency ω . The left-hand side of the equation becomes $P(x,y,z;t)$ by way of the inverse Fourier transform. Thus the resulting expression is

$$P(x, y, z; t) = \frac{1}{4\pi} \int_{\omega} \int_A \left(\frac{1}{r} \frac{\partial P}{\partial z} + \frac{\cos \theta}{r^2} P + i \frac{\omega \cos \theta}{v r} P \right) e^{[-i\omega(t - \frac{r}{v})]} dA d\omega. \quad (\text{A-15})$$

If we define the variable $\tau = t - \frac{r}{v}$ as retarded time and some properties of the Fourier transform we obtain after incorporating them into equation (A-15) and applying the inverse Fourier transform to the right-hand side

$$P(x, y, z; \tau) = \frac{1}{4\pi} \int_A \left\{ \frac{1}{r} \left[\frac{\partial P}{\partial z} \right] + \frac{\cos \theta}{r^2} [P] + \frac{\cos \theta}{vr} \left[\frac{\partial P}{\partial t} \right] \right\} dA, \quad (\text{A-16})$$

where $[P]$ means that the integration over the area A is done using the wavefield P at retarded time $\tau = t - \frac{r}{v}$.

The first term depends on the vertical gradient of the wavefield $\frac{\partial P}{\partial z}$. The second term is called the *near-field term* since it decays with $1/r^2$.

Both terms are neglected in seismic migration. The remaining term is called the *far-field term* and it is the foundation of Kirchhoff migration.

If we write it in the discrete form, we have:

$$P_{out} = \frac{\Delta x \Delta y}{4\pi} \sum_A \frac{\cos \theta}{vr} \frac{\partial}{\partial t} P_{in} \quad (\text{A-17})$$

where Δx and Δy are inline and crossline trace spacings,

$P_{out} = P\left(x_{out}, y_{out}, z; \tau = \frac{2z}{v}\right)$ is the output of migration using the input wavefield

$P_{in} = P\left(x_{in}, y_{in}, z = 0, \tau = t - \frac{r}{v}\right)$ within an areal aperture A.

References

Abma, R., Sun, J., and Bernitsas, N., 1999, Antialiasing methods in Kirchhoff migration: *Geophysics*, **64**, 1783-1792.

Ahmed, H., Dillon, P.B., Johnstad, S.E., and Johnston, C.D., 1986, Northern Viking graben multilevel three-component walkaway VSP – A case history: *First Break*, **04**, 9-27.

Ahmed, H., 1987, Mode-Converted shear waves in 3-Component VSP data: 57th Ann. Internat. Mtg., Soc. Expl. Geophys., Expanded Abstracts, 700-702.

Amano, H., 1995, An analytical solution to separate P-waves and S-waves in VSP wavefields: *Geophysics*, **60**, 955-967.

Amery, G.B., 1969, Structure of Sigsbee Scarp, Gulf of Mexico: *A.A.P.G. Bulletin*, **53**, 2480-2482.

Amundsen, L., and Reitan, A., 1995, Decomposition of multicomponent sea-floor data into upgoing and downgoing P- and S-waves: *Geophysics*, **60**, 563-572.

Bardan, V., 1987, Trace interpolation in seismic data-processing: *Geophysical Prospecting*, **35**, 343-358.

Berkhout, A.J., and Wapenaar, C.P.A., 1988, Delft philosophy on Inversion of elastic data: 58th Ann. Internat. Mtg., Soc. Expl. Geophys., Expanded Abstracts, 831-833.

Bevc, D., 1997, Imaging complex structures with semirecursive Kirchhoff migration: *Geophysics*, **62**, 577-588.

Biondi, B., 2001, Kirchhoff imaging beyond aliasing: *Geophysics*, **66**, 654-666.

Bleistein, N., 1987, On the imaging of reflectors in the earth: *Geophysics*, **52**, 931-942.

Bleistein, N., 1987, Kirchhoff inversion for reflector imaging and soundspeed and density variations: *Proceedings of the First Joint EAGE/SEG Workshop on Deconvolution and Inversion*, Rome, Italy, 1986. Blackwell Scientific Publications, Oxford.

Calandra, H., Baina, R., Hanitzsch, C., and LeRousseau, J. H., 2001, Improving 3D Kirchhoff prestack depth migration: why not use regularization and multipathing?: 71st Ann. Internat. Mtg., Soc. Expl. Geophys., Expanded Abstracts, 1049-1052.

Cassell, B.R., 1984, Vertical seismic profile – An introduction: *First Break*, **2**, 9-19.

- Cerveny, J., 2001, *Seismic Ray Theory*, Cambridge University Press.
- Chang, H., VanDyke, J.P., Solano, M., McMechan, G., and Epili, d., 1998, 3-D prestack Kirchhoff depth migration: From prototype to production in a massively parallel processor environment: *Geophysics*, **63**, 546-556.
- Chopra, S., Alexeev, V., Manerikar, A., and Kryzan, A., 2004, Processing/integration of simultaneously acquired 3D surface seismic and 3D VSP data: *The Leading Edge*, **23**, 422-432.
- Claerbout, J.F., and Doherty, S.M., 1972, Downward continuation of moveout-corrected seismograms: *Geophysics*, **37**, 741-768.
- Combes, J.M., 1993, The Vicksburg Formation of Texas: depositional systems distribution, sequence stratigraphy, and petroleum geology: *A.A.P.G. Bulletin*, **77**, 1942-1970.
- Constance, P. E., Roche, S., Bicquart, P., Bryans, B., Gelinsky, S., Ralph, J. G., and Bloor, R. I., 1999, Simultaneous acquisition of 3-D surface seismic data and 3-C, 3-D VSP data: 69th Ann. Internat. Mtg., Soc. Expl. Geophys., Expanded Abstracts, 104-107.
- Coulombe, C.A., Stewart, R.R., and Jones, M.J., 1991, AVO analysis using the VSP: 61st Ann. Internat. Mtg., Soc. Expl. Geophys., Expanded Abstracts, 1080-1083.
- Coulombe, C.A., Stewart, R.R., and Jones, M.J., 1992, Elastic wave AVO using borehole seismic data: 62nd Ann. Internat. Mtg., Soc. Expl. Geophys., Expanded Abstracts, 864-866.
- Coulombe, C.A., 1993, Amplitude-versus-offset analysis using vertical seismic profiling and well-log data: M. Sc. Thesis, Univ. of Calgary.
- Coulson, C.H., 1965, *Waves: A mathematical account of the common type of wave motion*: Oliver and Boyd.
- Dankbaar, J. W. M., 1985, Separation of P- and S-waves: *Geophysical Prospecting*, **33**, 970-986.
- Dankbaar, J. W. M., 1987, Vertical seismic profiling – separation of P- and S-waves: *Geophysical Prospecting*, **35**, 803-814.
- Deregowski, S.M., and Brown, S.M., 1983, A theory of acoustic diffractors applied to 2-D models: *Geophysical Prospecting*, **31**, 293-333.
- Dellinger, J., Murphy, G., Etgen, J., Fei, T., and Gray, S., 1999, Efficient 2.5-D true-amplitude migration: *The Leading Edge*, **18**, 946-949.

- Dellinger, J., Gray, S.M., Murphy, G., and Etgen, J.T., 2000, Efficient 2.5-D true-amplitude migration: *Geophysics*, **65**, 943-950.
- Devaney, A.J. and Oristaglio, M.L., 1986, A plane-wave decomposition for elastic wave fields applied to separation of P-waves and S-waves in vector seismic data: *Geophysics*, **51**, 419-423.
- Dillon, P.B., Ahmed, H. and Roberts, T., 1988, Migration of mixed-mode VSP wavefields: *Geophysical Prospecting*, **36**, 825-846.
- DiSiena, J.P., Gaiser, J.E., and Corrigan, D., 1981, Three-component vertical seismic profile – orientation of horizontal components for shear-wave analysis: 51st Ann. Internat. Mtg., Soc. Expl. Geophys., Expanded Abstracts, 1990-2011.
- DiSiena, J.P., Gaiser, J.E., and Corrigan, D., 1984, Horizontal components and shear wave analysis of three-component VSP data, in Toksoz, M.N., and Stewart, R.R., Eds., *Vertical Seismic Profiling: Advanced concepts*: Geophysical Press, 177-188.
- Duncan, W., 2005, A Deterministic evaluation of seismic fidelity using velocity modeling and attribute analysis to improve surface seismic imaging around Vinton Dome, Louisiana: Ph.D. Thesis, University of Houston, A.G.L.
- Dupal, L., and Miller, D.E., 1985, Reef delineation by reef multiple offset borehole seismic profiles: 55th Ann. Internat. Mtg., Soc. Expl. Geophys., Expanded Abstracts, 105-107.
- Fails, T.G., 1990, Variation in salt dome faulting, Coastal Salt Basin: *Transactions, Gulf Coast Association of Geological Societies*, **40**, 181-193.
- Flippin, J.W., 1982, The stratigraphy, structure, and economic aspects of the Paleozoic strata in earth County, North-Central Texas, in C.A. Martin, ed., *Petroleum Geology of the Fort Worth Basin and Bend Arch Area*: Dallas Geological Society, 129-155.
- Fomel, S., and Alkhalifah, T., 2001, Implementing the fast marching eikonal solver: spherical versus Cartesian coordinates: *Geophysical Prospecting*, **49**, 165-178. *Geophysical Society of America*, **86**, 234-246.
- Foster, D. J., and Gaiser, J. E., 1986, Elastic wavefield decomposition of offset VSP data: 66th Ann. Internat. Mtg., Soc. Expl. Geophys., Expanded Abstracts, 563-565.
- Foster, D. J. and Mosher, C. C., 1988, Up and Downgoing wave field separation for multioffset single level VSP data: 68th Ann. Internat. Mtg., Soc. Expl. Geophys., Expanded Abstracts, 816-818.

Gaiser, J.E., Ward, R.W., and DiSiena, J.P., 1982, Three Component Vertical Seismic Profiles: Polarization Measurements of P-wave particle motion for velocity analysis: 52nd Ann. Internat. Mtg., Soc. Expl. Geophys., Expanded Abstracts, 162-165.

Gaiser, J.E., 1999, Applications for vector coordinate systems of 3-D converted-wave data: The Leading Edge, **18**, no. 11, 1290-1300.

Gardner, G.H.F., French, W.S., and Matzuk, T., 1974, Elements of migration and velocity analysis: Geophysics, **39**, 811-825.

Gazdag, J., 1978, Wave equation migration with the phase-shift method: Geophysics, **43**, 1342-1351.

Gazdag, J. and Sguazzero, P., 1984, Migration of seismic data by phase-shift plus interpolation: Geophysics, **49**, 124-131.

Gherasim, M., Hoelting, C., Duncan, W., Zhou, H-w, Marfurt, K., 2002, A preliminary study of slat flank illumination at Vinton Dome, Louisiana: do we need lateral wavefield continuation?: 72nd Ann. Internat. Mtg., Soc. Expl. Geophys., Expanded Abstracts, 1368-1371.

Gray, S.H., 1992, Frequency-selective design of the Kirchhoff migration operator: Geophysical Prospecting, **40**, 565-572.

Gray, S.H., 1998, Speed and accuracy of seismic migration methods: Mathematical Geophysics Summer School at Stanford University.

Gray, S.H., 2001, Seismic imaging: Geophysics, **66**, 15-17.

Gray S.H., Etgen, J., Dellinger, J. and Whitmore, D., 2001, Seismic migration problems and solutions: Geophysics, **66**, 1622-1640.

Gray, S. H., Notfors, C. and Bleistein, N., 2002, Imaging using multi-arrivals: Gaussian beams or multi-arrival Kirchhoff?: 72nd Ann. Internat. Mtg., Soc. Expl. Geophys., Expanded Abstracts, 1117-1120.

Guevara, S. E. and Stewart, R. R., 2001, 3-C geophone orientation and wave modes polarization: 71st Ann. Internat. Mtg., Soc. Expl. Geophys., Expanded Abstracts, 799-801.

Gulati, J. S., Stewart, R. R., Hoffe, B. H. and Bland, H. C., 1998, Land vertical cable acquisition and analysis: Results from the Blackfoot high-resolution 3-C seismic survey, 68th Ann. Internat. Mtg: Soc. Expl. Geophys., Expanded Abstracts, 308-311.

Guo, J., and Yang, H-J., 1998, Rough topography and complex structure band-limited energy travelttime Kirchhoff prestack dept-migration: 68th Ann. Internat. Mtg., Soc. Expl. Geophys., Expanded Abstracts, 1908-1912.

Hagedoorn, J.G., 1954, A process of seismic reflection interpretation: Geophysical Prospecting, **02**, 85-127.

Halbouty, M. T., 1972, Salt Domes Gulf Region, U.N. and Mexico: 2nd Edition, Gulf Publishing Company, Houston.

Hildebrand, S., Roberts, P., Huang, L.-J., Burch, C., and Fehler, M., 1997, Prestack depth migration for complex 2-D structure using phase-screen propagators: 67th Ann. Internat. Mtg., Soc. Expl. Geophys., Expanded Abstracts, 1121-1124.

Hilterman, F., 2001, Seismic Amplitude Interpretation: 2001 Distinguished Instructor Short Course, Distinguished Instructor Series, No. 4, SEG.

Hinds, R.C., Anderson, N.L. and Kuzmiski, R.D., 2001, VSP Interpretive Processing: Theory and Practice: Short Course Notes, Open File Publications No.3, SEG.

Hoelting, C., Gherasim, M., House, L. and Marfurt, K., 2003, Elastic modeling and steep dips: unraveling the reflected wavefield: 73rd Ann. Internat. Mtg., Soc. Expl. Geophys., Expanded Abstracts, 1833-1836.

Hokstad, K., 2000, Multicomponent Kirchhoff migration: Geophysics, **65**, 861-873.

Hou, A., and Marfurt, K., 2002, Multicomponent prestack depth migration by scalar wavefield extrapolation: Geophysics, **67**, 1886-1894.

House, L., Marfurt, K., Larsen, S., Martin, G., and Wiley, R., 2002, 2D and 3D elastic modeling with shared seismic models: 72nd Ann. Internat. Mtg., Soc. Expl. Geophys., Expanded Abstracts, 1975-1978.

Humphris, C.C., Jr., 1978, Salt movement on continental slope, northern Gulf of Mexico, in A.H. Bouma, G.T. Moore, and J.M.Coleman, eds., Framework, facies, and oil-trapping characteristics of the upper continental margin: A.A.P.G. Studies in Geology, **7**, 69-86.

Jackson, G. M., Mason, I. M. and Lee, D., 1991, Multicomponent common-receiver gather migration of single-level walk-away seismic profiles: Geophysical Prospecting, **39**, 1015-1030.

Jackson, M.P.A., and Galloway, W.E., 1984, Structural and Depositional styles of Gulf Coast Tertiary Continental Margins: Application to Hydrocarbon Exploration: Continuing Education Course Note Series, **25**.

- Jackson, M.P.A., and Cramez, C., 1989, Seismic recognition of salt welds in salt tectonics regimes (abs.): S.E.P.M. Gulf coast Section, 10th Ann. Research Conference, Program and Extended Abstracts, Houston, Texas, 66-71.
- Jackson, M.P.A., Roberts, D.G. and Snelson, S., 1995, Salt Tectonics: A global perspective: A.A.P.G. Memoir **65**.
- Jones, M.J., and Fung, M., 1988, Case history using a multioffset VSP to map Devonian reef: 58th Ann. Internat. Mtg., Soc. Expl. Geophys., Expanded Abstracts, 180-183.
- Jovanovic, K., 2004, P and SV wave separation for VSP data, Vinton Dome: M.Sc. Thesis, University of Houston, Department of Geosciences, A.G.L.
- Keho, T. H. and Wu, R-S., 1987, Elastic Kirchhoff migration for Vertical Seismic Profiles: 67th Ann. Internat. Mtg., Soc. Expl. Geophys., Expanded Abstracts, 774-776.
- Keho, T.H., and Beydoun, W.B., 1988, The paraxial ray method: Geophysics, **53**, 1540-1546.
- Kuo, J. T. and Dai, T-f, 1984, Kirchhoff elastic wave migration for the case of noncoincident source and receiver: Geophysics, **49**, 1223-1238.
- Leaney, P.W.S. and Esmersoy, C., 1989, Parametric decomposition of offset VSP wavefields: 59th Ann. Internat. Mtg., Soc. Expl. Geophys., Expanded Abstracts, 26-29.
- Lumley, D.E., Claerbout, J., and Bevc, D., 1994, Anti-aliased Kirchhoff 3-D migration: 64th Ann. Internat. Mtg., Soc. Expl. Geophys., Expanded Abstracts, 1282-1285.
- Martin, G.S., Marfurt, K.J., and Larsen, S., 2002, marmousi-2: an updated model for the investigation of AVO in structural complex areas: 72nd Ann. Internat. Mtg. Soc. Expl. Geophys., Expanded Abstracts, 1979-1982.
- Martin, R.G., 1978, Northern and eastern Gulf of Mexico continental margin: stratigraphic and structural framework, in A.H. Bouma, G.T. Moore, and J.M.Coleman, eds., Framework, facies, and oil-trapping characteristics of the upper continental margin: A.A.P.G. Studies in Geology, **7**, 25-32.
- Miller, D., Oristaglio, M. and Beylkin, G., 1987, A new slant on seismic imaging: Migration and integral geometry: Geophysics, **52**, 943-964.
- Pao, Y.H., and Varatharajulu, V., 1976, Huygen's principle, radiation conditions, and integral formulas for the scattering of elastic waves: J. Acoust. Soc. Of Am., **59**, 1361-1371.

- Prasad, S.J., 2003, Azimuthally dependent seismic attribute analysis: M.Sc. Thesis, University of Houston, Department of Geosciences, A.G.L.
- Reshef, M. and Kosloff, D., 1986, Migration of common shot gathers: *Geophysics*, **51**, 324-331.
- Schneider, W.A., 1978, Integral formulation for migration in two and three dimensions: *Geophysics*, **43**, 49-76.
- Schuster, D.C., 1995, Deformation of allochthonous salt and evolution of related salt-structural systems, eastern Louisiana Gulf Coast, in M.P.A. Jackson, D.G. Roberts, and S. Snelson, eds., *Salt Tectonics: a global perspective: A.A.P.G. Memoir* **65**.
- Sethian, J., and Popovici, A.M., 1999, 3-D travelttime computation using fast marching method: *Geophysics*, **64**, 516-523.
- Sheriff, R.E., and Geldart, L.P., 1995, *Exploration Seismology: 2nd Edition*, Cambridge University Press.
- Stewart, R.R., and DiSiena, J.P., 1989, The values of VSP in interpretation: *The Leading Edge*, **8**, 16-23.
- Stolk, C. C. and Symes, W. W., 2002, Artifacts in Kirchhoff common image gathers: 72nd Ann. Internat. Mtg., Soc. Expl. Geophys., Expanded Abstracts, 1129-1132.
- Stolt, R.H., 1978, Migration by Fourier Transform: *Geophysics*, **43**, 23-48.
- Stolt, R., and Benson, A., 1986, *Seismic Migration, Theory and Practice: Handbook of Geophysical Exploration*, **5**, Geophysical Press.
- Sullivan, E., Marfurt, K. and Ammerman, M., 2003, Bottoms-up karst: New 3-D seismic attributes shed light on the Ellenburger (Ordovician) carbonates in the Fort Worth Basin (north Texas, USA), 73rd Ann. Internat. Mtg. Soc. of Expl. Geophys. Expanded Abstracts, 482-485.
- Sumner, H.S., Robison, B.A., Dirks, W.K., and Holliday, J.C., 1990, Morphology and evolution of salt/minibasin systems: lower shelf and upper slope, central offshore Louisiana (abs.): *G.S.A. Ann. Mtg., Programs with Abstracts*, Dallas, Texas, 48.
- Sun, R., and McMechan, G.A., 2001, Scalar reverse-time depth migration of prestack elastic seismic data: *Geophysics*, **66**, 1519-1527.
- Sun, R., McMechan, G., Hsiao, H.-H. and Chow, J., 2004, Separating P- and S-waves in prestack elastic seismograms using divergence and curl: *Geophysics*, **69**, 286-297.

- Takahashi, T., 1995, Prestack migration using arrival angle information: *Geophysics*, **60**, 154-163.
- Tatham, R.H. and Goolsbee, V., 1984, Separation of S-wave and P-wave reflections offshore western Florida: *Geophysics*, **49**, 493-508.
- Thompson, S.A., and Eichelberger, O.H., 1928, Vinton salt dome, Calcasieu Parish, Louisiana: *Amer. Assoc. of Petrol. Geol. Bull.*, **12**, 385-394.
- Toksoz, M.N., and Stewart, R.R., 1984, *Vertical Seismic Profiling part B: Advanced concepts*: Geophysical Press.
- Vanderfeen, M.J., 1988, Salt flank imaging using VSP: 58th Ann. Internat. Mtg., Soc. Expl. Geophys., Expanded Abstracts, 545-547.
- Van Dok, R. and Gaiser, J., 2001, Stratigraphic description of the Morrow Formation using mode-converted shear waves: Interpretation tools and techniques for three land surveys: *The Leading Edge*, **20**, 1042-1047.
- Versteeg, R., 1994, The Marmousi experience: Velocity model determination on a synthetic complex data set: *The Leading Edge*, **13**, 927-936.
- Vinje, V., Iversen, E. and Gjoystdal, H., 1993, Traveltime and amplitude estimation using wavefront construction: *Geophysics*, **58**, 1157-1166.
- Vinje, V., Astebol, K., Iversen, E. and Gjoystdal, H., 1996, Estimation of multivalued arrivals in 3-D models using wavefront construction –Part I: *Geophysical Prospecting*, **44**, 819-842.
- Vinje, V., Astebol, K., Iversen, E. and Gjoystdal, H., 1999, 3-D ray modeling by wavefront construction in open models: *Geophysics*, **64**, 1912-1919.
- Walper, J.L., 1982, Plate Tectonic evolution of the Forth Worth Basin, in Martin, C. A., *Petroleum Geology of the Fort Worth Basin and Bend Arch Area*: Dallas Geological Society, 237-251.
- Wang, D., 2004, Vector 3C3D VSP Kirchhoff Migration: 74th Ann. Internat. Mtg., Soc. Expl. Geophys., Expanded Abstracts, 1455-1458.
- Wang, L., 1999, Estimation of Multi-valued Green's function by dynamic ray-tracing and true amplitude Kirchhoff inversion in 3-D heterogeneous media: Ph.D. Thesis, Colorado School of Mines, Department of Mathematics and Computer Sciences.

- Wang, Y., and Nemeth, T., 1997, Multicomponent separation of PP and SS by least-squares migration method: Synthetic and field data tests: 67th Ann. Internat. Mtg., Soc. Expl. Geophys., Expanded Abstracts, 1222-1225.
- Wapenaar, C.P.A., and Haime, G.C., 1990, Elastic extrapolation of primary seismic P- and S-waves: Geophysical Prospecting, **38**, 23-60.
- Wapenaar, C.P.A., Herrmann, P., Verschuur, D.J. and Berkhour, A.J., 1990, Decomposition of multicomponent seismic data into primary P- and S-wave responses: Geophysical Prospecting, **38**, 633-662.
- Warren A.D., 1957, The Anahuac and Frio sediments in Louisiana: Transactions, Gulf Coast Association of Geological Societies, **7**, 221-237.
- Weimer, P., and Buffler, R.T., 1992, Structural geology and evolution of the Mississippi Fan foldbelt, deep Gulf of Mexico: A.A.P.G. Bulletin, **76**, 225-251.
- Whitmore, N.D. and Marfurt, K.J., 1988, Method for depth imaging multicomponent seismic data: U.S. Patent 4 766 574.
- Wiggins, J.W., 1984, Kirchhoff integral extrapolation and migration of nonplanar data: Geophysics, **49**, 1239-1248.
- Wilson, F., and Noel, J.A., 1983, A gravity analysis of west-central Calcasieu Parish, Louisiana: Transactions, Gulf Coast Association of Geological Societies, **33**, 243-250.
- Worall, D.M., and Snelson, S., 1989, Evolution of the northern Gulf of Mexico, with emphasis on Cenozoic growth faulting and the role of salt, in A.W.Bally and A.R. Palmer, eds., The Geology of North America: an overview: G.S.A. Decade of North American Geology, **A**, 97-138.
- Wu, R.S. and Huang, L.-Y., 1992, Scattered field calculation in heterogeneous media using phase-screen propagation: 62nd Ann. Internat. Mtg., Soc. Expl. Geophys., Expanded Abstracts, 1289-1292.
- Wu, S.A., Bally, A.W., and Cramez, C., 1990, Allochthonous salt, structure, and stratigraphy of the northeastern Gulf of Mexico, part II: structure: Marine and Petroleum Geology, **7**, 334-370.
- Yan, Y-S., Yi, M-L., Wei, X., Xu, Z-k, Zhou, Z., 2004, C-wave processing of 3-D VSP data: 74th Ann. Internat. Mtg., Soc. Expl. Geophys., Expanded Abstracts, 1244-1247.
- Yilmaz, O., 2001, Seismic Data Analysis: Processing, Inversion and Interpretation of Seismic Data: Investigations in Geophysics No. 10. SEG.

Zhao, P., Uren, N. F., Wenzel, F., Hatherly, P. J. and McDonald, J. A., 1998, Kirchhoff diffraction mapping in media with large velocity contrasts: *Geophysics*, **63**, 2072-2081.

Zhe, J., and Greenhalgh, S.A., 1997, Prestack multicomponent migration: *Geophysics*, **62**, 598-613.

Zhou, H.-W., 2002, Quarterly Report – Vinton Dome: A.G.L., University of Houston.